Universität Münster

Kern- und Teilchenphysik

Property and Optimization Studies at Münster Cluster-Jet Targets

Doctoral Thesis

vorgelegt von

Sophia Vestrick

aus Heiden
Münster, November 2024

living.knowledge

Dekan: Prof. Dr. Bratschitsch
Erstgutachter: Prof. Dr. Khoukaz
Zweitgutachter: Prof. Dr. Klein-Bösing

Tag der mündlichen Prüfung:
Tag der Promotion:

Zusammenfassung

In Münster Cluster-Jet Targets wird flüssiger, kryogener Wasserstoff durch eine de Lavaldüse gepresst, um ein vakuumbeständiges Target in Form eines Cluster-Jets für z.B. Beschleuniger- oder Laserexperimente bereitzustellen. Der Fokus dieser Arbeit liegt auf der Fertigung und Beurteilung der de Lavaldüsen. Das umfasst auch die Charakterisierung der erzeugten Cluster-Jets.

Mit der erstmaligen vollkommen hausinternen Fertigung der de Lavaldüsen innerhalb dieser Arbeit konnte die Ausschussrate deutlich reduziert werden. Dies ermöglicht ausführliche Studien zur optimalen Düsengeometrie und der zugrundeliegenden Clusterproduktionsprozesse. Mit der winkelabhängigen Analyse von Cluster-Jets wurden Einblicke in die Eigenschaften und Herkunft von hochintensitven Kernstrahlen innerhalb der Cluster-Jets gewonnen.

In der Analyse der Cluster-Jets nimmt die Größenmessung eine wichtige Rolle ein. Messungen mittels Shadowgraphie zeigten Durchmesser zwischen $2\,\mu\mathrm{m}$ und $10\,\mu\mathrm{m}$ für Cluster, die aus flüssigem Wasserstoff entstehen. Mit der Messung von Mie-Streuung für kleine Winkel wurden neben der generellen Durchführbarkeit in einem großen Abstand zur Düse auch erste Ergebnisse erzielt, die auf größere Cluster hindeuten.
Auch die Messung der Temperatur des Cluster-Jets ist eine wichtige Charakterisierung. Hier wurde festgestellt, dass kurz hinter der Düse die Cluster als unterkühlte Flüssigkeit vorliegen, welche in der weiteren Flugstrecke ausfrieren.

Weiterhin wurden neue bzw. aktualisierte Detektionsmethoden studiert. Insbesondere ein MCP-System mit YAG:Ce Schirm mit zusätzlicher Aluminiumschicht zeigt gute Ergebnisse. Außerdem wurde der Pumpstand für den neuen MCT-$\overline{\mathrm{P}}$ANDA Beam Dump aufgebaut und in Betrieb genommen. Über verschiedene Eigenschaften des Cluster-Jets, insbesondere die Breite der Geschwindigkeitsverteilung, konnte die Widomlinie das erste Mal für Wasserstoff vermessen werden. Über die gleiche Methode kann nun auch die Temperaturmessung an der Clusterquelle kalibriert werden.

Abstract

In Münster Cluster-Jet Targets, liquid, cryogenic hydrogen is pressed through a de Laval nozzle to provide a vacuum-resistant target in the form of a cluster-jet for, e.g., accelerator or laser experiments. The focus of this work is on the production and evaluation of de Laval nozzles. This also includes the characterization of the cluster-jets obtained.

With the first completely in-house production of the de Laval nozzles within this thesis, the rejection rate could be significantly reduced. This enables detailed studies on the optimum nozzle geometry and the underlying cluster production processes. The angle-dependent analysis of cluster-jets provided insights into the properties and origin of high intensity core beams within the cluster-jet.

Size measurement plays an important role in the analysis of cluster-jets. Measurements using shadowgraphy showed diameters between $2\,\mu m$ and $10\,\mu m$ for clusters formed from liquid hydrogen. With the measurement of Mie scattering for small angles, in addition to the general feasibility at a large distance to the nozzle, initial results were also obtained that indicate larger clusters.
Measuring the temperature of the cluster jet is also an important characterization. Here it was found that the clusters are present as a supercooled liquid shortly behind the nozzle, which freeze out in the further flight path.

New or updated detection methods were also studied. In particular, an MCP system with a YAG:Ce screen with an additional aluminum layer showed good results. In addition, the pumping station for the new MCT-$\overline{P}$ANDA beam dump was set up and put into operation. Different properties of the cluster-jet, in particular the width of the velocity distribution, were used to measure the Widom line for hydrogen for the first time. The same method can now be used to calibrate the temperature measurement at the cluster source.

Contents

Chapter 1

Introduction

Münster Cluster-Jet Targets (MCTs) are high performance targets for a broad variety of physical experiments. The basic principle of a *Cluster-Jet Target* (CJT) is injecting a pressurized, cooled fluid, in most cases hydrogen, through a specially shaped de Laval nozzle into vacuum. The resulting jet consisting of clusters, i.e., hydrogen micro droplets with a diameter in the order of nano- up to micrometers, can then be tailored to fit special requirements or can be used even directly for several experiments.

The application possibilities of these targets reach from laser, to lepton and hadron experiments. MCTs were or are continuously in operation at the laser facilities of the Heinrich Heine University in Düsseldorf, at the electron accelerator facilities MAMI at the Johannes Gutenberg University in Mainz, and at the proton accelerator facility COSY at the Forschungszentrum Jülich. In the future, MCTs will be installed at MESA and $\overline{P}ANDA$ for more in-depth studies of the standard model of particle physics.

Even though MCTs are already "state-of-the-art", the development and optimization process never ends, willing to fulfill even higher expectations of planned and further future experiments. In order to determine if an optimization is successful, cluster-jet characterization is necessary. This leads to the main topics of this thesis: **Study and optimize existing parts of a CJT while characterizing the properties of the resulting clusters and cluster-jets**.

As a first basis, the working principle of MCTs and existing characterization methods for cluster-jets are introduced in chapter 3. Further, two setups developed within this thesis are presented: An existing system for monitoring the two-dimensional shape of the cluster-jet was evolved to be more robust against environmental influences without loosing its excellent performance. Also, a pumping station for a future implementation at the $\overline{P}ANDA$ experiment was developed and constructed.

Subsequently, the following main questions are going to be answered in detail within this thesis:

The de Laval nozzle is the origin of a cluster-jet and thus the centerpiece of every CJT. **What characterizes an optimal nozzle and how can it be reliably produced?** Chapter 4 covers de Laval nozzles and their working principle. Furthermore, the used and optimized nozzle production techniques are presented along with the nozzles fabricated within this thesis. Their characteristics and especially the properties of the resulting cluster-jets form the main basis for decision making, whether the production technique is reliable.

With the cluster-jet resulting from de Laval nozzles a new experimental method was developed to probe the fluid upstream of the nozzle. Apart from the commonly known liquid and gaseous phase of a fluid, the supercritical phase above the critical point can be separated into a liquid-like and a gas-like region. **With which cluster-jet properties can the liquid(-like) and the gas(-like) phases be separated?** And subsequently, **where is this separation, the so-called Widom line located?** Chapter 5 answers this question for hydrogen, as this is the fluid currently used at the utilized setup.

Even though the probing methods developed by previous researchers are comprehensive and thus sufficient to determine, e.g., the Widom line, additional methods are necessary for further optimizations of CJTs and especially the de Laval nozzles. Hence, an even closer look at the clusters and the cluster-jet is required. **Which size(-distribution) have the clusters within the cluster-jet especially originating from liquid hydrogen?** And **which temperature has the cluster-jet close to the nozzle exit?** Even-though both questions seem to be easily answerable, there are many side-effects and obstacles to be considered which are addressed in chapter 6 along with first results.

Chapter 2

The $\overline{P}$ANDA Experiment

The standard model of particle physics is the basis to modern day particle experiments. It was formed over the past decades and describes today's knowledge of the fundamental particles and forces. As still pressing, fundamental questions remain unanswered, the *Facility for Antiproton and Ion Research* (FAIR) is currently under construction. It comprises particle sources and accelerators as well as four large research pillars. One of these pillars of FAIR is the future $\overline{P}$ANDA experiment (*antiProton ANnihilation at DArmstadt*). Here, some of the open fundamental questions will be addressed, e.g., "What is the theory behind the confinement?" and "What is the origin of the hadron masses?". The importance of CJTs for the $\overline{P}$ANDA experiment will conclude this introductory chapter.

2.1 Theory of Particle Physics

The modern perception of the atom was formed in the early 20th century, mainly due to experiments by Rutherford. In the 1930s the known phenomena of nuclear physics have been described with the four particles proton, neutron, electron and neutrino [Pov+14]. Even though these particles form most of the known matter, today the model is much more complex as presumed at that time. Especially with experiments at particle accelerators in the 50s and 60s many new particles of the hadron family, which includes proton and neutron, were discovered. The quark model, introduced in the 1960s and valid until today, brought structure to all the hadrons. [Pov+14]

As the perception of standard particles changed, knowledge of the fundamental forces was gained. Gravitation, electricity, magnetic force and the force between atoms and molecules were considered as fundamental around 1800 [Pov+14]. Towards the end of the 20th century electricity and the magnetic force were found to be based on the same

three generations of matter   gauge bosons
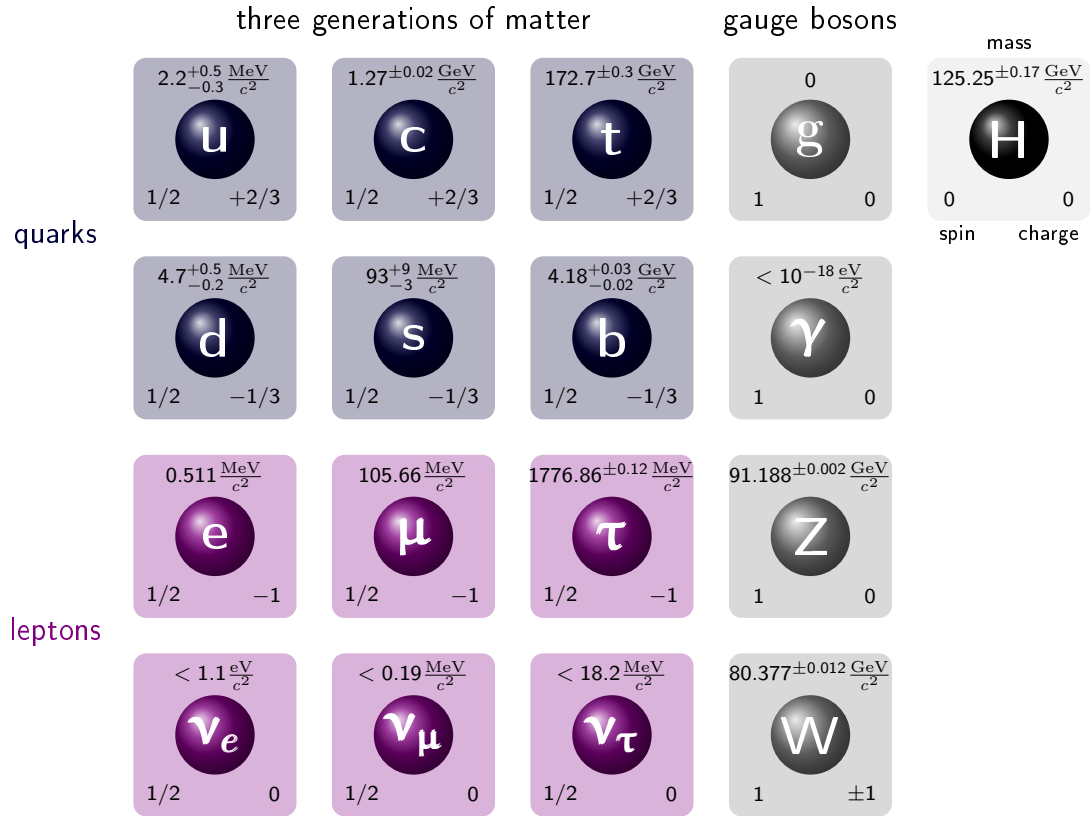
quarks				mass

Figure 2.1: Standard Model of particle physics. Each fundamental particle is pictured as square with its mass, spin, and charge in units of e. In blue and purple the three generations of matter, i.e., the three generations of quarks and leptons, respectively, are presented. The gauge vector bosons are pictured in dark gray, while the scalar Higgs boson is shown in light gray. The graviton as exchange particle for the gravitational force is not shown. Figure generated by E. Köhler [Köh15], updated with masses from [Wor$^+$22].

force: electromagnetism. With the discovery of the inner structure of the atom the force between atoms and molecules could be traced back to the electromagnetism of the constituents. As nuclear physics was researched, two further forces were discovered: the nuclear force, which is based on the strong force as discovered later, and the weak force. This gave rise to today's concept of four fundamental forces: gravitation, electromagnetism, weak force and strong force. [Pov$^+$14]

2.1.1 Standard Model of Particle Physics

Today's standard model of particle physics includes the two fundamental particle classes, the quarks and the leptons with their anti-particles, as well as three of the four fundamental forces: the electromagnetism, the weak force, and the strong force with their exchange particles (see fig. 2.1).

Leptons, including the most prominent electron and (electron) neutrino, and quarks are smaller than 10^{-18} m, thus they are considered to be point-like. With a spin of $^1/_2$ they are fermions. The six leptons and six quarks are subdivided into three generations [Pov$^+$14].

The interactions between these particles are mediated by vector bosons, i.e., particles with spin 1. For the electromagnetic force there are photons, for the strong interaction gluons, and for the weak interaction W$^+$, W$^-$, and Z^0 bosons. A particle only interacts with these bosons and is thus subject to the interaction, if it carries the corresponding charge: Leptons and quarks carry a weak charge and can thus interact weakly by means of the W$^+$, W$^-$, and Z^0 bosons, quarks and some leptons carry an electric charge and can thus interact with the photon, and only quarks carry a color charge (short: color) and are thus subject to the strong force. The large masses of W and Z bosons lead to a very short life time for these virtual exchange particles based on the uncertainty principle and hence a short range of the weak interaction. In contrast, the photon has no mass and thus the range of the electromagnetic force is infinite. Although the gluon also has a mass of zero, the range of the strong interaction is strongly limited due to the color of the gluons themselves and the necessity of color-neutral particles [Pov$^+$14]. All these interactions have underlying symmetries and conservations. An example from classical mechanics is the momentum conservation. For more fundamental interactions, such as the strong and weak force, other numbers are conserved, e.g., the baryon or the lepton number, i.e., quarks and leptons can only be created, when an corresponding anti-particle is also generated (electron and anti-electron neutrino or positron; upquark and anti-upquark, ...).

2.1.2 Hadrons, Exotics, and Their Color

Quarks only occur in bundles called hadrons. The two most prominent hadrons are the nucleons proton and neutron, which are to be more precise baryons. The other subgroup of hadrons are mesons.

Baryons consist of three quarks and are fermions, i.e., they have a half-integer spin. Proton and neutron are only some of the ground states of a rich spectrum of excited states. When creating a new baryon an anti-baryon is created as well, leading to the introduction of the conserved "baryon number", which is 1 for baryons and thus $^1/_3$ for quarks with negative values for the anti-particles. [Pov$^+$14]

Mesons on the other hand consist of a quark and an anti-quark. Thus, it has a baryon number of 0 and an integer spin [Pov$^+$14]. The lightest mesons are the three pions with positive, negative, and neutral charge, consisting of up and anti-down ($|u\overline{d}\rangle$), down and

anti-up ($|\overline{\text{u}}\text{d}\rangle$), or the mixed state $1/\sqrt{2}\,|\text{u}\overline{\text{u}}\rangle - |\text{d}\overline{\text{d}}\rangle$, respectively.

Later on, the color charge was introduced to maintain the Pauli principle for some particles, e.g., the Delta resonance Δ^{++}. Each quark has one out of three colors (red, blue, or green) and each anti-quark has one out of three anti-colors (anti-red, anti-blue, or anti-green), thus the quarks within one hadron are distinguishable [Pov$^+$14].

As mentioned before, the strong interaction is mediated by gluons, which couple to the color charge of particles. The corresponding field theory is the *Quantum Chromo Dynamic* (QCD), which is similar to the *Quantum Electro Dynamic* (QED) from electroweak interaction. Importantly, each gluon has a color and an anti-color itself, meaning gluons not only couple to quarks but also to other gluons [Pov$^+$14]. In general, the colors need to be combined to color-neutral states, e.g., all three colors for baryons, or one color with its corresponding anti-color for mesons. When trying to separate for example the quark and anti-quark of a meson, the necessary energy rises infinitely, which is called confinement and is based on the interactions between gluons. With enough energy within the field the creation of a quark anti-quark state is more favorable than further separation. This also explains, why combinations like quark-quark-anti-quark ($|\text{qq}\overline{\text{q}}\rangle$) or $|\text{qq}\rangle$ are not possible; they cannot be color-neutral [Pov$^+$14].

But still, particles like $|\text{qq}\overline{\text{qq}}\rangle$ or $|\text{qqqq}\overline{\text{q}}\rangle$ would be possible. These particles are called tetraquarks or pentaquarks, respectively, and belong to the particle group of exotic hadrons. It also includes hybrids, i.e., hadrons with additional gluons, or glueballs consisting only of gluons [Bar$^+$21]. Studying exotic hadrons, quarkonia (consisting of a quark and its anti-quark, e.g., a charm anti-charm pair), and exited states is mandatory to understand and further develop the QCD. This is one main research topic of the $\overline{\text{P}}$ANDA experiment at FAIR.

2.2 The $\overline{\text{P}}$ANDA Experiment at FAIR

Besides the open questions addressed by $\overline{\text{P}}$ANDA, there are three more research pillars of FAIR addressing not only nuclear physics related but a broad variety of phenomena. For these experiments FAIR is currently under construction. At the moment there are some delays [GSI22], leading to the possibility to reevaluate some of the components not quite as developed. The considered components could be updated with newly emerging methods and components or could be replaced with already existing and optimal working hardware. The status presented here is based on the plans in 2022 and preceding.
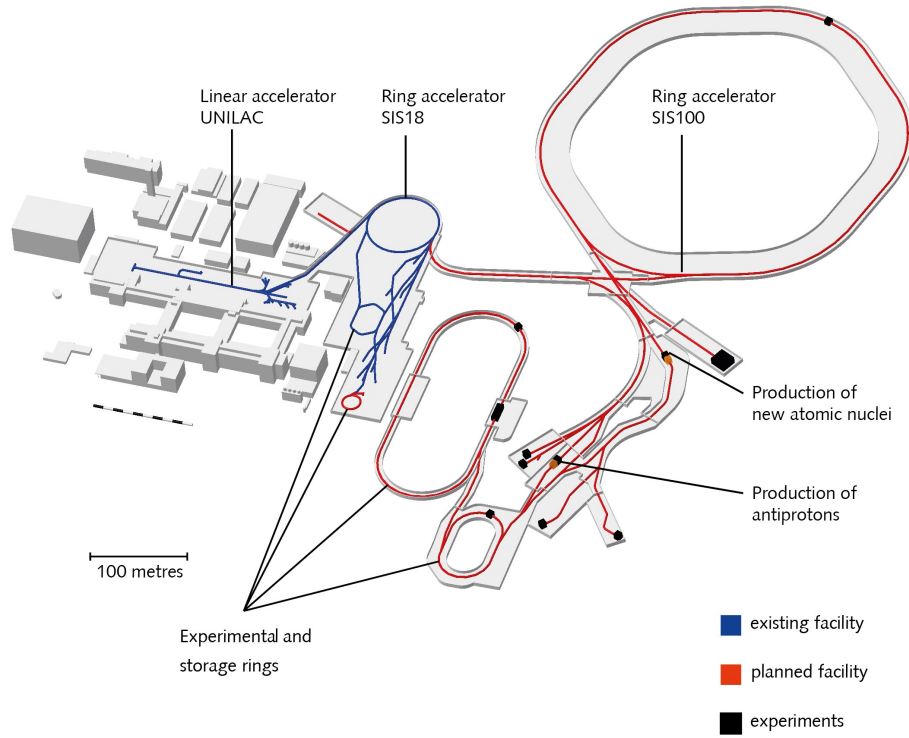
Figure 2.2: Schematic overview of the GSI-FAIR complex. The existing and the planned facility is shown in blue and red, respectively, as well as the intended experiments shown in black. Copyright by GSI/FAIR [GSI].

2.2.1 GSI & FAIR

In 2002 the conceptual development of a new-generation multi-purpose facility started leading to new requirements on quality and intensity of ion and antiproton beams in order to investigate under previously unattainable conditions [FSS12]. With this the heavy-ion accelerator complex and broad experimental program of the *Gesellschaft für Schwerionenforschung* (GSI) in Darmstadt will be expanded. With the groundbreaking in 2017 the massive civil construction work of FAIR began [GSI]. Today, first buildings are undergoing interior work while others have not been started, yet [GSI]. When finalized, FAIR will have a complicated and economically sound arrangement of several accelerator systems and thus will be able to produce particle beams with an unprecedentedly wide range of parameters [FSS12]. A schematic overview of the GSI/FAIR facility is shown in fig. 2.2.

The GSI *UNIversal Linear ACcelerator* (UNILAC) and the *SchwerIonen-Speicherring* (SIS18) synchrotron together with the new *proton LINear ACcelerator* (p-LINAC) will serve as preaccelerators [Küm21]. At the SIS100 synchrotron the protons and heavy ions will be accelerated to energies of 29 GeV and 2.7 GeV, respectively [Küm21]. These beams can be used as high-quality particle beams and by directing them onto targets for

the production of secondary particles, i.e., antiprotons and (un-)stable nuclei. Utilizing a secondary complex system of storage rings the antiprotons or nuclei can be formed into beams with the required parameters for the experiments. [FSS12]

With this complex setup a variety of experiments can pursue their own but also combined research focuses. The science of FAIR can be divided into four research pillars [FSS12]:

APPA: *Atomic, Plasma Physics, and Applications*

At APPA several research collaborations are combined: BIOMAT (*BIOlogy and MATerial Science*), FLAIR (*Facility for Low-energy Antiproton and heavy Ion Research*), HED@FAIR (*High Energy Density science at FAIR*), and SPARC (*Stored Particles Atomic Research Collaboration*). The research covers the range from the fundamental processes in atoms to applications in technology and medicine including biophysics, materials research, atomic physics, and plasma physics. Despite this broad variety of research fields, the participating groups share experimental techniques and installations. [FAI24]

CBM: *Compressed Baryonic Matter*

CBM will investigate the QCD phase diagram at high net-baryon densities by heavy-ion collisions with the SIS100 beam in order to explore the relevant degrees of freedom here. With this one can search for phase transitions from hadronic to quark-gluon matter with a possible region of coexistence and for exotic QCD phases. Furthermore, questions regarding modified properties of hadrons in dense baryonic matter are addressed, as well as indications for chiral symmetry restoration. The boundaries of extending the chart of strange nuclei by producing single and double strange hypernuclei are also tested. [Abl+17]

NUSTAR: *Nuclear STructure and AstRophysics*

NUSTAR is subdivided into eight experiments in three branches. The central element is the Super-FRS, a super-conducting fragment separator in which secondary exotic isotope beams can be produced and separated. Furthermore, it can be used as a high-resolution spectrometer system for nuclear physics experiments. NUSTAR will focus its researches on exotic atomic nuclei by studying their structure and reactions, and use these results to answer astrophysical questions. [GHN12]

$\overline{P}$ANDA: *antiProton ANihilation in DArmstadt*

For the $\overline{P}$ANDA experiment a beam of antiprotons is directed onto a hydrogen or an other nuclear target to annihilate. The annihilation process allows for the production of a broad variety of hadrons compared to other experimental probes. Furthermore, the well defined initial state is flavor-blind with a high precision in mass. Thus, annihilation is known as an universal tool for the fundamental understanding of hadrons [Pet$^+$17]. The broad experimental program and the elemental questions of hadron physics aimed to answer at $\overline{P}$ANDA are described in the next section. Even though the program presented in the following is already broad, the anticipated detector is so elaborate and precise, one is not limited to the presented program as one can extend it by questions emerging in the future.

2.2.2 Physics of $\overline{P}$ANDA

With the details of the $\overline{P}$ANDA setup to come, at first it is important to understand with which intention such a large scale experiment is set up. Which fundamental questions can be addressed by $\overline{P}$ANDA?

$\overline{P}$ANDA is designed in a staged approach. Not all detectors will be ready for day-1 operation and the antiproton production rate will be limited at first, leading to a limited rate of reactions for the first operation. Still, the possibilities in this *Phase One setup* cover a broad range of physic topics. With the gained knowledge, the full detector layout, and the high luminosity mode, even deeper and further studies will be addressed in the Phases Two and Three. [Bar$^+$21]

Even though the Standard Model of Particle Physics is the commonly agreed theory to describe the elementary particles and their interaction, challenging questions remain unanswered. In detail, the QCD is used to describe the strongly interacting quarks and gluons. At the high energy frontier, i.e., for small distances in the order of hadrons, the strong coupling is sufficiently weak to treat QCD perturbatively. Here, the asymptotic freedom applies and quarks act within, e.g., hadrons as free particles (H. Fritzsch, M. Gell-Mann, H. Leutwyler (1973); H.D. Politzer (1973); D.J. Gross, F. Wilczek (1973); and S. Weinberg (1973); as cited in [Bar$^+$21]).

The strong coupling constant α_S rises for low and intermediate energies due to the self-interaction of gluons, as can be seen in fig. 2.3. α_S is dependent on the momentum
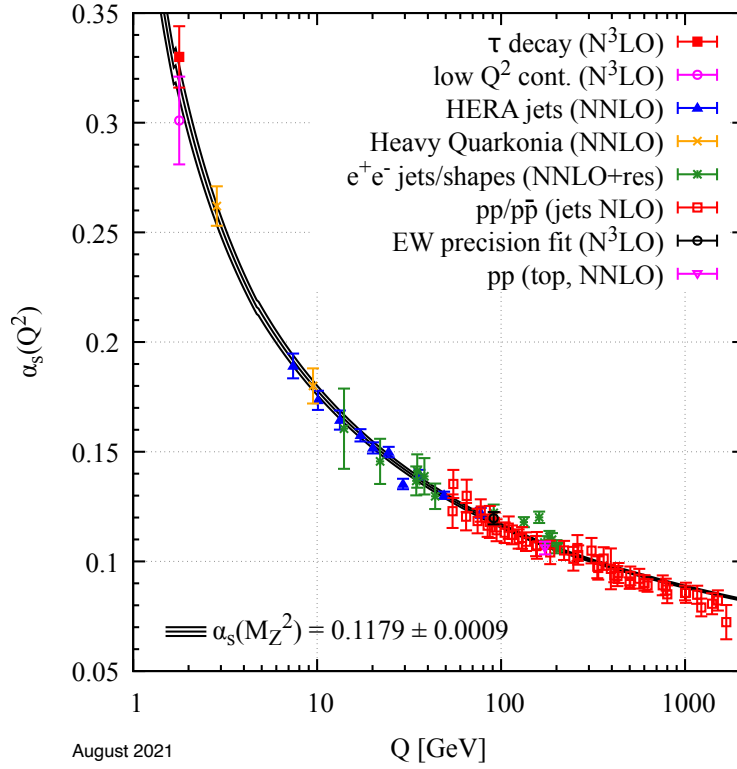
Figure 2.3: Strong coupling constant as a function of the energy scale Q. Especially in the low energy regime more measurements are desirable. Figure from [Wor$^+$22].

transfer Q in a given process which can be given in the first order by [Wor$^+$22] (simplified):

$$\alpha_{\text{S}}(Q^2) = \frac{12\pi}{\left(33 - 2n_f\right)\ln\!\left(\frac{Q^2}{\Lambda^2}\right)} \tag{2.1}$$

with the re-normalization group invariant Λ-parameter and the number of flavors n_f. However, for distances larger than the size of hadrons the possibility for pertubative treatment vanishes. Quarks and gluons are confined into hadrons. Understanding, e.g., the spin of a nucleon requires knowledge about the inner structure of hadrons, i.e., the distribution and motion of the quarks and gluons. For the research at $\overline{\text{P}}$ANDA this can be subdevided in four main physics domains: Nucleon structure, strangeness physics, charm and exotics, and hadrons in nuclei [Bar$^+$21].

In general there are many advantages in using the intense and precise antiproton beam foreseen in $\overline{\text{P}}$ANDA. Hadronic interactions have in general large cross sections and there are no severe limitations to spin and parity combinations in produced meson-like states, in opposition to the production in, e.g., electron-positron colliders where the quantum numbers are given by the in the first order necessary intermediate virtual photon (with $J^{PC} = 1^{--}$) ([Abl$^+$22] and as cited therein: J. Kühn, J. Kaplan, and E.

Safiani (1979); J. Kaplan and J. Kühn (1978); among others). Furthermore, various baryons (in flavor, spin, and parity) can be produced in two-body reactions, and due to the possibility of an annihilation via gluons, there is a gluon-rich environment, which is favorable especially for the investigation of exotics and glueballs. [Bar+21]

Nucleon Structure

With the structure of hadrons the QCD can be tested in the confinement domain. It is parameterized in terms of observables as form factors and structure functions. Especially electromagnetic probes as, e.g., the electromagnetic form factor (EMFF), have been studied in the past 60 years. [Bar+21]

EMFFs are defined over the four-momentum transfer squared q^2 and for the whole complex q^2 plane. They can be distinguished in time-like for $q^2 > 0$ and space-like for $q^2 < 0$. At low energies, the distance to be probed is approximately the size of a hadron. Studying time-like EMFFs at $\overline{\text{P}}$ANDA at low energies with different baryonic reactions can give insight into direct and transition form factors. With rising energy the probed distances are getting much smaller than the size of a hadron. Thus, not the hadron as total but its building blocks are probed. By applying the factorization theorem, the interaction can be divided into a hard, reaction-specific, but pertubative and calculable part, and a soft, reaction-universal and measurable part. [Bar+21]

With the desired resolution of $\overline{\text{P}}$ANDA especially the precision of proton EMFFs will be improved and with the high luminosity of $\overline{\text{P}}$ANDA reasonable statistics can be accumulated to study the building blocks of hadrons. [Bar+21]

Strangeness Physics

In physics with strangeness one of the light quarks of a hadron is replaced by a strange quark. The resulting hadron is then called hyperon. When such a hyperon is bound in a nucleus, it is called a hypernucleus.

The strange quark is significantly heavier than up and down quark, so that interesting knowledge in addition to the standard model based on nucleons can be gained. On the other hand, the strange quark mass is sufficiently light to link knowledge about hyperons and nucleons. Especially within $\overline{\text{P}}$ANDA Phase One the hyperon production and hyperon spectroscopy will be studied, providing basics to later experiments in $\overline{\text{P}}$ANDA, i.e., hyperon decays [Bar+21]. These decays will give insight into CP violation and thus allow for searches beyond the standard model and investigations regarding baryogenesis (A.D. Sakharov (1967), as cited in [Bar+21]). Furthermore,

the strangeness in hypernuclei introduces an additional degree of freedom (see also "Hadrons in Nuclei"), which will be investigated in later stages of $\overline{\text{P}}$ANDA [Bar+21].

Charm and Exotics

Apart from the original *Constituent Quark Model* (CQM) describing mesons and baryons, there is the sector of exotics like glueballs, hybrids, and multi quark states as introduced in section 2.1.2. The search for exotic hadrons can be divided into subtopics.

Excited light hadrons can either be described by quarks and gluons or by various dynamical effects. Due to the broad resonances of these excitations the masses overlap and can mix. Based on the large production cross sections and especially with large statistics, e.g., partial-wave analysis can be performed to determine mixing. [Bar+21]

Since the higher mass of the charm quark, hidden-charm physics, i.e., with a charm number of 0, like charmonium states are of highest interest. With a strong coupling constant of $\alpha_S \approx 0.3$ the pertubative treatment is at its limits as quark and gluon degrees of freedom become relevant. Charm systems can be considered non-relativistic with relativistic corrections as the velocity of the charm quark is in the order of half the speed of light. The aim is to determine the impact of these relativistic corrections. [Bar+21]

Furthermore, open-charm meson-like states, i.e., with a charm number other than 0, provide a different point of research. Experimental observations hint to narrow resonances that do not fit into the conventional heavy-light meson patterns. The spectroscopy and the ground-state decays of these open-charm states may give insight into, e.g., semi-leptonic form factors, which will also be relevant in the later stages of $\overline{\text{P}}$ANDA. [Bar+21]

Hadrons in Nuclei

Using nuclear targets in hadron reactions gives the additional opportunity to investigate nuclear forces. This includes the color transparency at intermediate energies, the short-distance structure of the nuclear medium, and the effects of the nuclear potential on hadron properties. [Bar+21]

Particles produced close to production threshold are rather slow in the laboratory frame leading to an interaction of these particles with the nuclear residue as ordinary hadrons. Thus, using an antiproton beam gives access to hadron channels at low momenta, which are difficult to study at other experiments. In this nuclear environment, the effect of

the nuclear potential on the masses and lifetime of produced antibarions or mesons can be studied, giving crucial insights into neutron stars. [Bar⁺21]

Furthermore, at higher beam momenta there is probably the onset of color transparency with varying momentum transfer, as well as the nuclear medium itself. Here, also the three research topics presented above come into play, each in the presence of the nuclear repulsive core. [Bar⁺21]

2.2.3 $\overline{\mathrm{P}}$ANDA Setup

First, for the annihilation experiments of $\overline{\mathrm{P}}$ANDA the antiprotons need to be generated. Initially the already operating UNILAC and later on the p-LINAC will be used to inject protons into the SIS18 [FSS12, Küm21]. Afterwards they are injected into the SIS100 with a perimeter of approximately $1100\,\mathrm{m}$ and a magnetic rigidity of $100\,\mathrm{T\,m}$ which accelerates them to $29\,\mathrm{GeV}$ with up to 4×10^{13} protons per pulse [FSS12, Küm21]. This proton beam is directed onto a solid state target to produce antiprotons [Küm21]. Using a pulsed magnetic horn these antiprotons are focused and selected in a magnetic channel at approximately $3\,\mathrm{GeV}$ and directed into the *Collector Ring* (CR) with a rate of $\dot{N}_{\overline{\mathrm{p}}}^{+} \leq 2 \times 10^{7}\,\overline{\mathrm{p}}/\mathrm{s}$ [Bar⁺21, Küm21, PAN22]. Within the CR the antiprotons are stochastically cooled [Küm21] and are then injected in bunches of 10^{8} antiprotons into the *High Energy Storage Ring* (HESR) [Bar⁺21, Küm21] where the $\overline{\mathrm{P}}$ANDA experiment is located.

High Energy Storage Ring (HESR)

An overview of the HESR is shown in fig. 2.4. Here, the racetrack shaped design is shown, as well as the location of the experiments, magnets, injection, stochastic cooling, and the *RadioFrequency* (RF) cavities.

With several antiproton bunches being injected within $1000\,\mathrm{s}$ into the HESR within Phase One, 10^{10} antiprotons can then be accelerated or decelerated to momenta from $1.5\,\mathrm{GeV/c}$ to $15\,\mathrm{GeV/c}$ [Bar⁺21] with the RF cavity. For compensating energy losses within the measurement cycle a barrier bucket cavity is installed [Pet⁺17]. The number of stored antiprotons will be enlarged to 10^{11} in a later phase [Bar⁺21, Küm21]. The anticipated antiproton production rate of $2 \times 10^{7}\,\overline{\mathrm{p}}/\mathrm{s}$ leads to a maximum cycle-averaged interaction rate of just that $2 \times 10^{7}\,\mathrm{s}^{-1}$ [PAN22]. For proton-antiproton reactions the total cross section for the HESR momentum range is approximately $\sigma_{\mathrm{tot}} \approx 100\,\mathrm{mb}$ [Wor⁺22]. From this the luminosity can be determined. Luminosity $L = \dot{N}/\sigma_{\mathrm{tot}}$ is the ratio of the reaction rate $\dot{N}$ and the total cross section σ_{tot}. Thus, it defines the rate
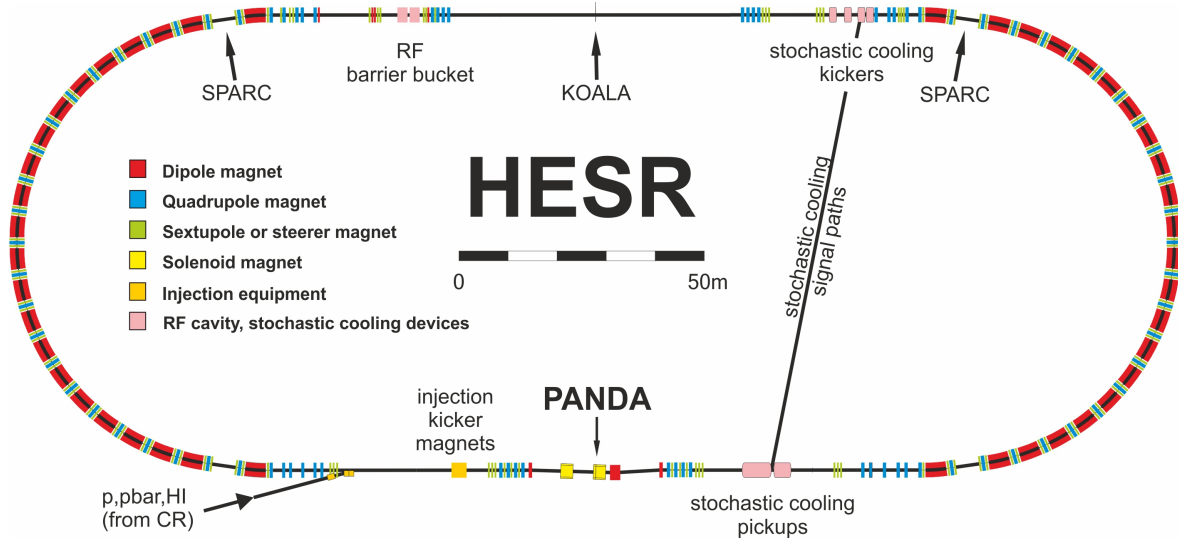
Figure 2.4: Schematic overview of the HESR in racetrack shaped design. It consists of two 180° arcs and two straight sections. The magnets are displayed as well as the RF cavity and the stochastic cooling system (pickups and kickers). On one straight section the $\overline{P}$ANDA detector is located while on the other straight section the KOALA experiment takes place. Figure from [Fri17].

of produced particles depending on the reaction studied and is given here by the upper limit $L_{\max} = 2 \times 10^{32}\,\mathrm{cm^{-2}\,s}$.

The stored beam is cooled by means of a stochastic cooling in beam direction (momentum spread) and transversal (horizontal, vertical). Within Phase One the *high resolution mode* will be accessible. Here, the luminosity is reduced to $L = 2 \times 10^{31}\,\mathrm{cm^2\,s^{-1}}$ but the low beam momentum spread $\delta p/p < 10^{-5}$ is foreseen [Küm21, PAN22]. In the later Phases of $\overline{P}$ANDA also the *high luminosity mode* will become available, allowing for high statistics. With a momentum spread of $\delta p/p < 10^{-4}$ the desired maximum luminosity of in average $L = 2 \times 10^{32}\,\mathrm{cm^2\,s^{-1}}$ is reached. [PAN22]

One important input to the $\overline{P}$ANDA experiment is the differential cross section of (anti)proton-proton elastic scattering to reach the desired precision in luminosity and thus to obtain absolute cross sections of measured reactions. Therefore, the *Key experiment fOr pAnda Luminosity determinAtion* (KOALA), which is also located at the HESR, measures the total kinetic energy of recoil protons near 90° and elastically scattered beam particles in the forward direction near 0° [Zho$^+$21]. Here, a MCT in a similar but simpler manner to the MCT-$\overline{P}$ANDA will be used [Eic24].
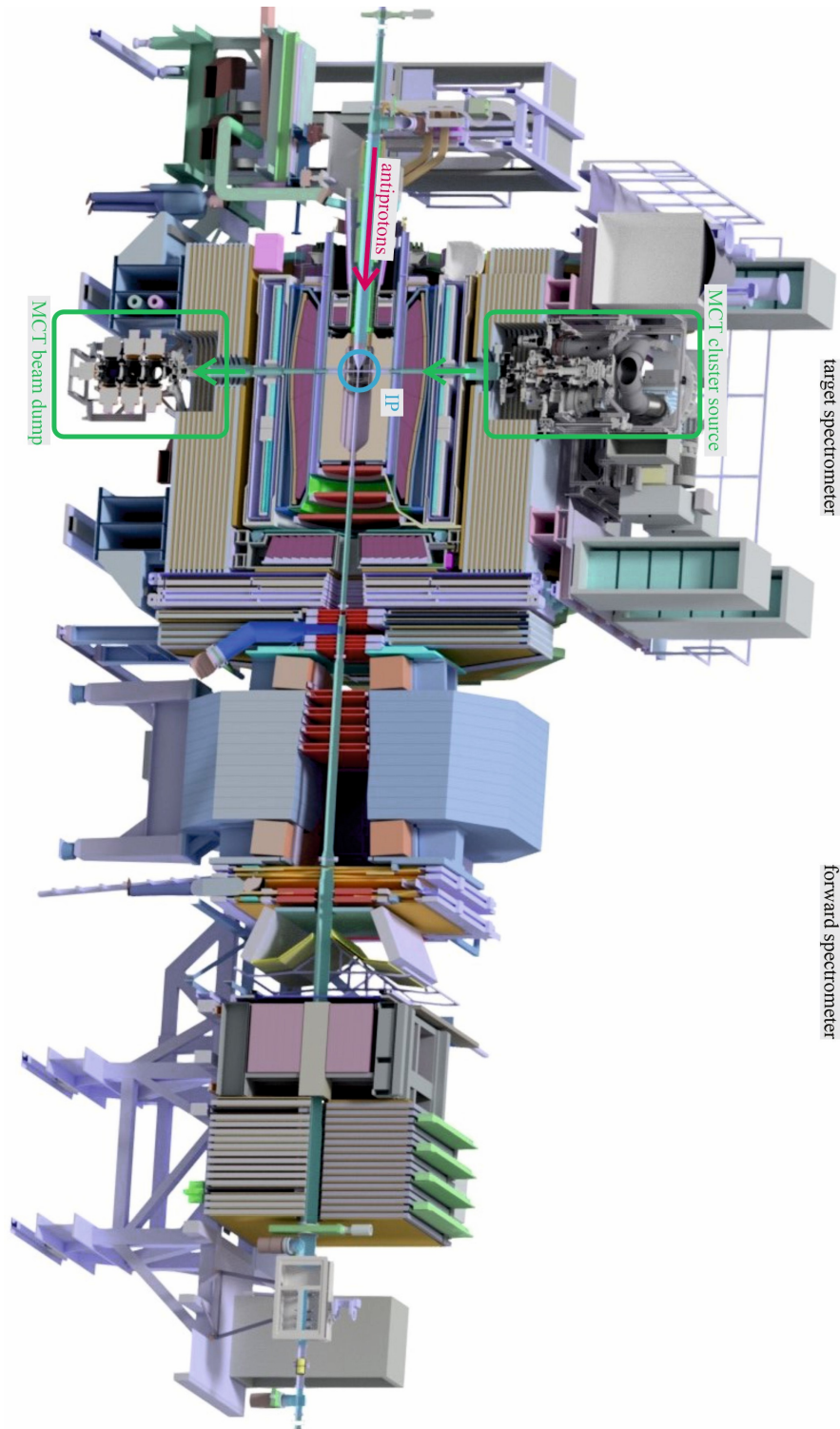
Figure 2.5: Cross sectional view of the $\overline{\text{P}}$ANDA detector. The accelerated antiproton beam propagates from left to right passing the *Interaction Point* (IP) where they might interact with the protons delivered by, e.g., the cluster-jet of the MCT propagating from top to bottom. Surrounding the IP, a target spectrometer is equipped with several subdetectors. Due to the forward boost an additional forward spectrometer (right) is foreseen consisting of further subdetectors. In total a close to 4π detector coverage is obtained, leading to large distances of the MCT cluster source and the MCT beam dump to the IP, each connected with narrow target beam pipes.

$\overline{\text{P}}$ANDA Detector System

At the $\overline{\text{P}}$ANDA experiment an internal target will be used. An internal target means the target is installed within the accelerator ring and thus interacts with the accelerator beam each circulation, in contrast to an external experiment where the beam is extracted and only used once. Furthermore, an internal target is at rest when the high energy antiprotons interact in opposition to a collider experiment where two accelerated particle beams interact. This leads to a massive forward boost, which further results in the design of the detector as target spectrometer and forward spectrometer [PAN22] (see fig. 2.5).

The **target spectrometer** surrounds the interaction point (IP) in an onion shell like manner. All detector components are placed close to each other, avoiding solid angle gaps and resulting in a close to 4π coverage. This also results in the source and beam dump placement of the foreseen cluster-jet or pellet target in a distance of more than 2 m to the IP. [PAN12, PAN22]

The innermost detector of the target spectrometer is the *MicroVertex Detector* (MVD). It provides a secondary vertex sensitivity for particles with decay lengths in the order of 100 μm and strongly improves the transverse momentum resolution. Surrounding the MVD is the *Straw Tube Tracker* (STT) with a resolution of ≤ 150 μm and, in forward direction, several *Gas Electron Multipliers* (GEMs). The three presented subdetectors combined are the *central tracker*. With these a momentum resolution for charged particle tracks on the percent level is reached. [PAN12, PAN22]

Surrounding, Cherenkov and *Time-of-Flight* (TOF) detectors are used to identify charged particles over a large range of angle and momenta. Using the *Detection of Internally Reflected Cherenkov* (DIRC) light instead of other types of ring imaging cherenkov counters gives the possibility to use thin radiators and place the readout elements outside the acceptance. Here, the Barrel DIRC covers the polar angles from 22° to 140° and the Forward DIRC from 10° to 22°. Cylindrically surrounding is the Barrel TOF, which gives precise timing information below 100 ps and good spatial resolution, which enables, e.g., the separation of kaons and pions below 1 GeV/c. The surrounding detector, the *ElectroMagnetic Calorimeter* (EMC) is separated into backward endcap, barrel, and forward endcap. It identifies and measures electrons, photons, and hadrons. [PAN12, PAN22]

The subsequent *MUOn detectors* (MUO) are embedded into the yoke for the solenoid magnet in barrel direction and in the downstream door in forward direction. In the layered design (alternating muon and iron layers) the innermost muon layer can detect low energy muons. The cumulated iron layer thickness provides enough hadronic

material to stop high energy pions. The solenoid magnet will provide a magnetic field of $2\,T$ which is necessary for the functionality of the detection principles. [PAN12, PAN22]

Due to the forward boost, most of the reaction products are ejected into the forward direction. To minimize the angular gap and to detect nearly all particles completely, the **forward spectrometer** is designed with an angular acceptance of $\pm 10°$ horizontally and $\pm 5°$ vertically. Tracking is performed with a *Forward Tracker* (FT) partly in front of, partly within the dipole magnet which provides a bending power of $2\,T\,m$. Further downstream additional tracking stations are placed. The RICH detector, a TOF Wall, and a forward EMC each provide the same diagnostics as the corresponding detectors in the target spectrometer. [PAN12, PAN22]

Even further downstream a luminosity monitor will be installed. It is used to reconstruct the angle of scattered antiprotons to obtain a luminosity precision of about 3%. [PAN12]

Differentiation of Possible Jet Targets

In general, cryogenic fluids can be pressed through a nozzle expanding into vacuum. Depending especially on the stagnation condition and partly on the nozzle geometry one can **distinguish between gas-jet, cluster-jet, droplet, and pellet targets** (see fig. 2.6):

For a gas-jet target cryogenic gas is pressed through a de Laval nozzle. Several orifices reduce residual gas background until the jet interacts with, e.g., an accelerator beam. With decreasing temperature a clustering process commences. The gas accumulates towards clusters, i.e., accumulations of the gas molecules. The target is now called cluster-jet target. Here, less orifices are needed to reduce the residual gas background because the jet is more directed and stable within vacuum. With further decreasing the temperature and finally crossing the vapor pressure curve upstream to the nozzle, the cluster size rises significantly until one can speak rather of micro droplets rather than clusters (but still speaking of a cluster-jet target). Changing the nozzle to a simple orifice and with significantly smaller pressures and temperatures the target is known as droplet target. A filament of the liquid forms at the nozzle and then breaks up into a string of small liquid drops, i.e., droplets. These droplets can freeze out in vacuum or within a triple point chamber, then being called (frozen) pellets, leading to the name pellet target. For all of these target systems a dedicated beam dump is needed to ensure the desired vacuum conditions.
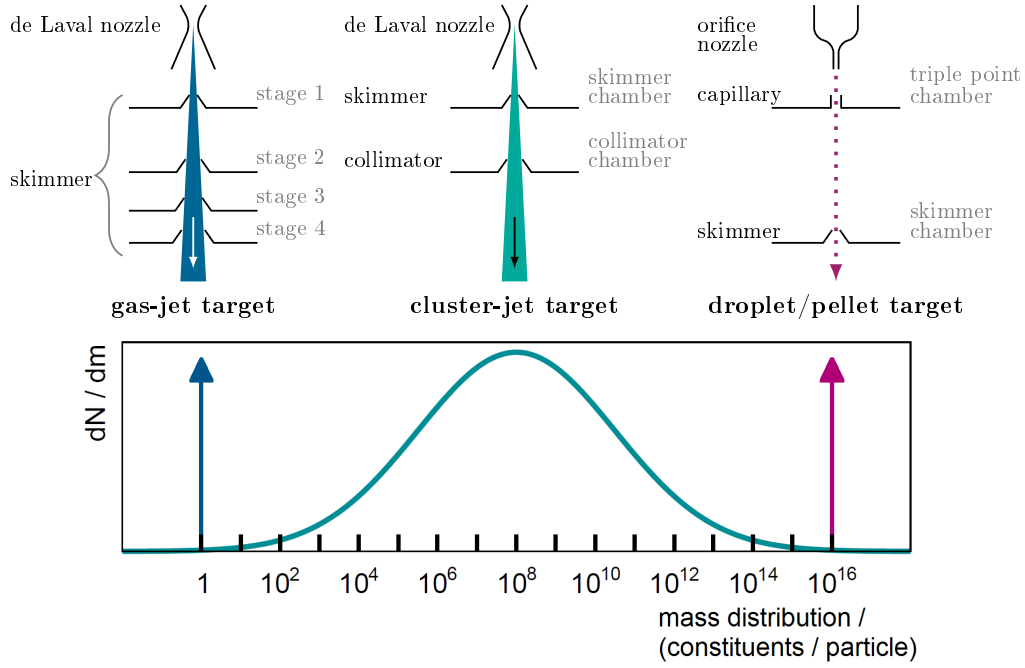
Figure 2.6: Schematic overview of gas-jet, cluster-jet, droplet, and pellet targets. The different production process for gas-jet, cluster-jet, and droplet or pellet targets depend mainly on pressure and temperature of the fluid as well as on the nozzle choice. This results in different regions of (micro-)droplet sizes, whereas the numbers are only an initial approximation. Figure from S. Grieser [Gri18], generated by E. Köhler (top) and A. Khoukaz (bottom), edited.

When using the clusters, droplets, or pellets in laser, lepton, or hadron experiments, the clear separation between the target beam definition vanishes. All three are molecule accumulations within vacuum. After a flight path of only a few centimeters or less the initial liquid clusters or (micro) droplets are frozen when they interact with any kind of experiment. The difference between cluster-jet and droplet-/pellet-jet is the size distribution for clusters instead of a single droplet or pellet diameter and the arrangement of the droplets or pellets on a single line.

Requirements on Internal Targets and Foreseen Candidates

Now considering the $\overline{\text{P}}$ANDA experiment, different targets are foreseen. Depending on the physics studied the requirements on the target and the target material changes. For studying antiproton-nucleus reactions, nuclear targets are an option. Here, a thin fiber overlaps with the antiproton beam. [PAN12]

For many physics cases a more dilute, but localized target within an ultra high vacuum is required. Even the thinnest window of gaseous target cells introduces background

and is thus prohibited. Such an elaborate target at $\overline{\text{P}}$ANDA is realized by a CJT and a pellet target. [PAN12] Within this thesis CJTs are studied and optimized, which is anticipated as Phase One target. At a later stage the second anticipated target, a pellet target, will become available. The requirements on these targets and why they are perfectly suited for the high-precision $\overline{\text{P}}$ANDA experiment is presented in the following.

The **target material is exchangeable** over a broad spectrum of elements and compounds. The main target material will be hydrogen serving as a pure proton target. As an effective neutron target, deuterium will be used. For nuclear targets a very pure environment is required to minimize background reactions. The **purity of the target material** of cluster-jet and pellet-targets is very high and thus perfectly suited, as opposed to target cells with windows, or foils with support structures. [PAN12]

The antiproton production rate at FAIR will be limited to approximately $2 \times 10^7 \,\overline{\text{p}}/\text{s}$ so that these costly particles should not be wasted to background reactions, e.g., with residual gas, but only react with the target material in the vertex zone. In contrast to conventional (supersonic) gas-jets, the cluster-jet or pellet beams do not broaden in the ultra high vacuum of a storage ring, hence they maintain the **good vacuum conditions**. Instead, they have very low beam divergence, which allows them to be guided through the $5\,\text{m}$ of target beam pipe. [PAN12]

Further, the **areal target density** (or target thickness) needs to be significantly below $10^{16}\,\text{nucleons}/\text{cm}^2$ to avoid beam heating larger than the available cooling and to avoid multi-scattering and secondary interactions of the ejectiles in the target material. A lower limit in target density is given by the desired luminosity of $L_\text{max} = 2 \times 10^{32}\,\text{cm}^{-2}\,\text{s}$. Using the number of beam particles $N_\text{beam} = 10^{11}\,\overline{\text{p}}$ and the revolution frequency $f_\text{beam} = 443\,\text{kHz}$, the maximum useful target thickness is $\rho_\text{target,max} = {}^{L_\text{max}}/_{N_\text{beam} \cdot f_\text{beam}} = 4.5 \times 10^{15}\,\text{atoms}/\text{cm}^2$. For the high resolution mode the luminosity and the number of beam particles are both reduced by a factor of 10 leading to the same desired target thickness. With this the beam cooling systems are sufficient. [PAN12]

For different physic cases a lower luminosity is desired. This can either be realized by reducing the number of antiprotons, or the reduction of a **variable target density**. The latter is preferable, because thus there is reduced beam heating and smearing, as well as a reduced probability of secondary interactions with the target material. Furthermore, with a smaller target density better vacuum conditions are obtained leading to minimized interactions with residual gas background. And lastly, the consumption of antiprotons within one cycle can be compensated by increasing the target density leading to a constant luminosity and event rate. [PAN12]

Due to the cooling of the antiproton beam a beam diameter below 100 µm is possible. Here, a **homogeneous volume target density** is desirable. With the granularity and spread of, e.g., a pellet target, an extended beam is required. [PAN12]

Furthermore, an **absence of time structures** is desirable which corresponds to a constant luminosity without peaks, leading to a constant data acquisition rate. [PAN12] Especially for studying short-lived particles and their decay products, a vertex point reconstruction with a precision well below 1 mm is required, leading to the necessity of a **pointlike interaction zone** in the order of the experimental resolution. This can be – in contrast to the previous requirement – fulfilled by the pellet target with high granularity in combination with a tracking system to reconstruct the position at time of interaction [PAN12]. Hence, neither target can fulfill all requirements presented in the last few paragraphs. Thus, apart from the different nuclear target fibers, the CJT and the pellet target will be installed alternatively at the P̄ANDA experiment. [PAN12]

With the complex detector design a strong physics case is made. The P̄ANDA experiment aims to answer questions regarding the theory of the strong force and the origin of the confinement as well as elucidates the hadronic mass generation. However, even though the detector components are nearly hermetically sealed [PAN22], a minimum distance from the target source to the IP of 2.25 m is given. The target beam dump is an additional 2.35 m distanced from the IP. This leads to a necessary minimum flight path of the cluster-jet of nearly 5 m within an ultra high vacuum. The connection between source, IP, and beam dump is designed to be a narrow beam pipe with a diameter down to 2 cm with no possibility for pumping ports. Still, for the lifetime of the antiproton beam, the minimization of background reactions, and for the very accurate luminosity determination, an ultra high vacuum needs to be retained.

All these requirements on the P̄ANDA target and the restrictions on geometry lead to an elaborate CJT design and optimization process. Even though the final MCT-P̄ANDA is build up and has been commissioned, several optimization studies can be and have been performed leading to improvements of the environmental conditions.

Chapter 3

Münster Cluster–Jet Targets in its Variations

Until today, several *Cluster-Jet Targets* (CJT) were build and commissioned in Münster by the working group of Professor Khoukaz. The most elaborate target setup is the *Münster Cluster-Jet Target* (Münster CJT or MCT) foreseen for the $\overline{\mathrm{P}}$ANDA experiment (MCT-$\overline{\mathrm{P}}$ANDA). Before this target was designed, feasibility studies were performed with the MCT-Prototype which is still in use at the Münster laboratories and was used for most of the measurements within this thesis. Measurements regarding the MCT setup, i.e., the commissioning and thorough testing of detection setups conclude the description of the MCT-Prototype in this chapter. Furthermore, the newly designed pumping station for the MCT-$\overline{\mathrm{P}}$ANDA beam dump is a setup presented here. Apart from these long distance MCTs as necessary for $\overline{\mathrm{P}}$ANDA, there are other possible experimental applications with different requirements on the (cluster-jet) target.

One example is the *MesA Gas Internal target eXperiment* (MAGIX) at *MAinz MIkrotron* (MAMI) and at the future *Mainz Energy-recovering Superconducting Accelerator* (MESA) with the *Münster Cluster-Jet Target - Mainz* (MCT-M). Here, target densities in the order of 10^{18} atoms/cm^2 are required, but the distance from nozzle to IP and from IP to jet catcher where the beam is dumped is in the order of millimeters [Gri+18, Sch+21] instead of meters as for the $\overline{\mathrm{P}}$ANDA experiment.
Another example is the collaboration between the laser working group of Professor Willi at the Heinrich Heine University in Düsseldorf and the CJT working group of Professor Khoukaz, where the MCT-D was installed in Düsseldorf. Here, also highest target densities are preferable, but due to the interaction with a laser instead of an accelerator beam, the residual gas background is neglectable. [Eic+23, Leß21]
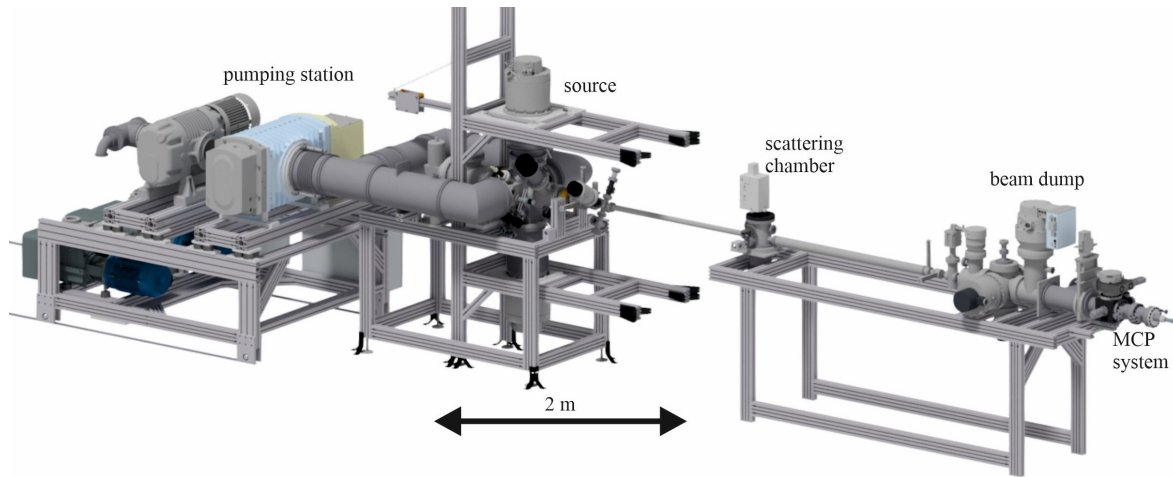
Figure 3.1: CAD drawing of the MCT-Prototype consisting of, from left to right, pumping station, cluster source, scattering chamber, and beam dump. Here, the MCP system is installed at the end of the beam dump.

The MCT-M and MCT-D are in principle a cluster-jet source with several vacuum pumps in different dedicated setups for maintaining the desired vacuum conditions. Such a cluster-jet generator consist of a gas supply, whose gas is cooled to cryogenic temperatures and fed through a nozzle which results in a cluster-jet. Even though these targets are mainly operated with hydrogen they have also been used routinely with different gases as, e.g., argon and nitrogen [Bra24, Gri18], whereas also an operation with carbon-dioxide is in preparation [Eic24].

Important to mention are the finished studies at ANKE and COSY-11 (both in operation with hydrogen or deuterium) [Dom$^+$97, Ste$^+$08] investigating a variety of hadronic reactions in proton-proton, proton-deuteron, and deuteron-proton collisions, whereas the ANKE target was in use until recently for feasibility studies and comissioning measurements for the KOALA experiment [Zho$^+$21]. Orifices to tailor the cluster-jet to the desired dimensions and to reduce residual gas background are added between the cluster-jet source and the IP, as well as a dedicated differential pumping system as beam dump for the cluster-jet.

Last but not least, the MCT-$\overline{\text{P}}$ANDA and the MCT-Prototype share a very similar setup with only minor modifications. Most prominent is the change of jet direction, as the MCT-$\overline{\text{P}}$ANDA needs to have a vertical beam direction while the cluster-jet of the Prototype target propagates in horizontal direction. Following, the MCT-Prototype is presented in detail, as it was setup to most of the studies presented in the subsequent chapters. An overview of the MCT-Prototype is shown in figs. 3.1 and 3.2.
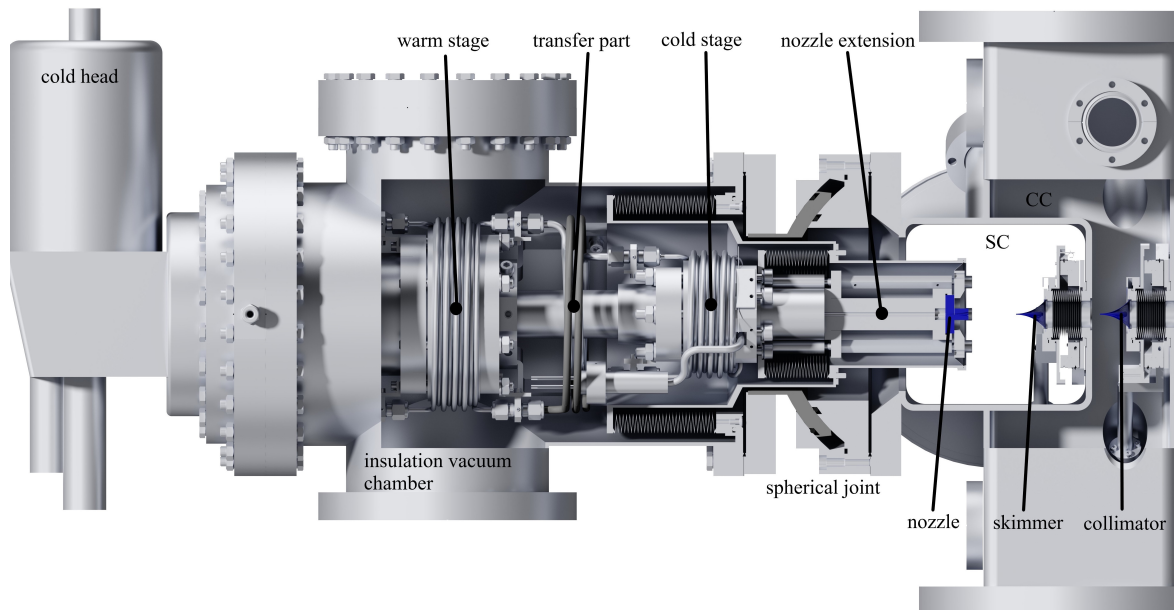
In addition to CJTs also a droplet target is in development in our working group [Har19, Man24, Wes20].
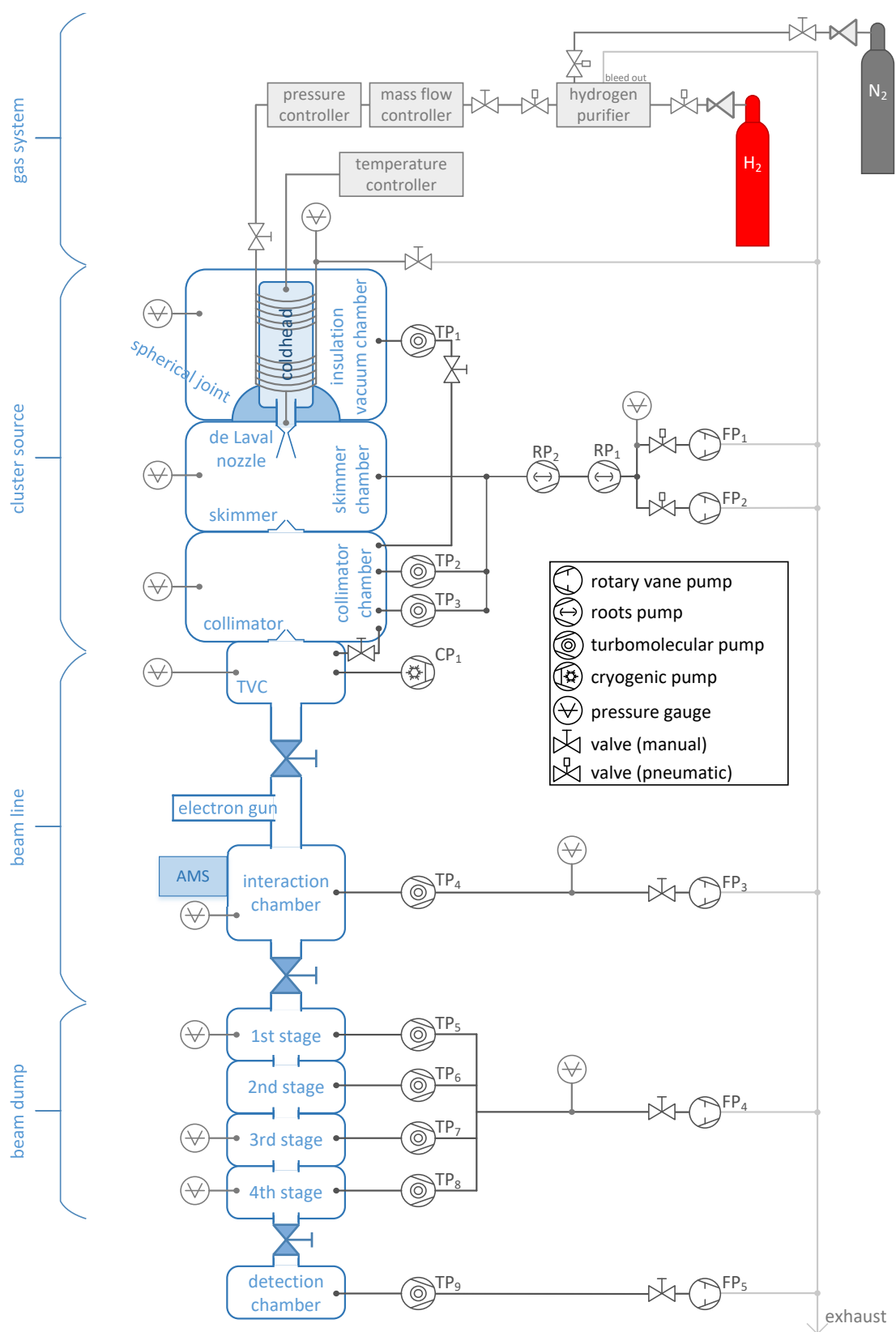
Figure 3.2: Schematic overview of the MCT-Prototype. Depicted are from top to bottom the gas system, the cluster source, the beam line with the scattering chamber, and the beam dump with the detection chamber.

3.1 Cluster Source

Figure 3.3: Cross section of the MCT-Prototype cluster source. The gas line enters the target on the left and then winds around the two stages of the cold head. The windings at the warm and the cold stage are made out of copper to maximize the heat transfer while the transfer part is made out of stainless steel. After the cold stage the fluid reaches the nozzle where the cluster-jet is formed expanding into the *Skimmer Chamber* (SC). The parts described until now are surrounded by the insulation vacuum chamber ensuring a good vacuum to minimize heat transfer from the outside. This part is tiltable with the spherical joint. The skimmer separates the residual gas from the desired part of the cluster-jet which then enters the *Collimator Chamber* (CC). The collimator then tailors the cluster-jet to its final shape which then enters the subsequent chambers. Picture generated by D. Bonaventura, edited.
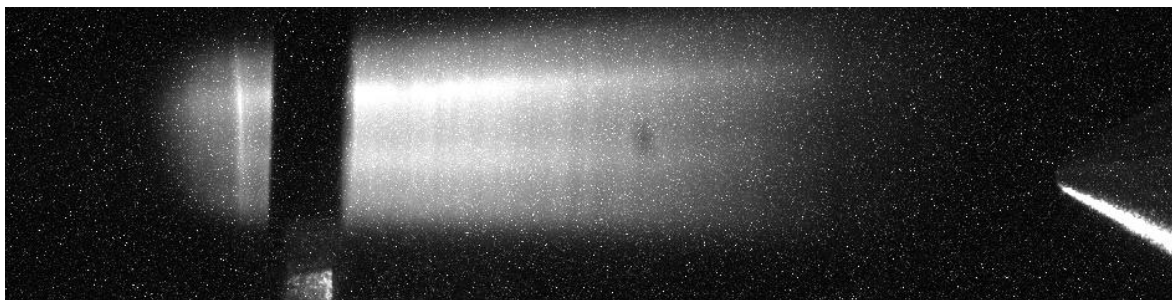
Figure 3.4: Side view of the cluster-jet within the skimmer chamber. The nozzle exit is not visible but to the left. The cluster-jet emerging from the nozzle is illuminated from the bottom, while the most left and the most right part of the jet is not visible. At the bottom the nozzle shutter is visible, blocking partly the illumination from below. On the right the skimmer tip can be seen. Important to note is that the intensity of the cluster-jet corresponds to its density. This leads to the observation that the cluster-jet is not homogeneous in density but forms highly intense "core beams".

Starting with the target material, hydrogen 5.0 is normally used. This gas is further purified with a hydrogen purifier "PS7-PD1-08-2" of the saes group to 9.0 (purity of 99.9999999%). Within the purifier a palladium membrane is heated to $300\,°C$ to $400\,°C$ where only hydrogen atoms can diffuse through the membrane. The hydrogen then passes a flow meter to measure the hydrogen flow and a pressure controller to regulate the pressure to the desired 5 bar to 20 bar. The now following components are shown in fig. 3.3. From here on the hydrogen lines are surrounded by an insulation vacuum to minimize heat transfer. This is necessary to cool the hydrogen to the desired temperatures from 20 K to 50 K. For cooling the gas a two stage cold-head "Coolpower 10 MD" with a compressor "Coolpak 6000H MD" is used. The desired temperature can be reached with heating by a heating cartridges "HTR-50" and a temperature diode "DT-670" operated with the temperature controller "Lakeshore 336". The hydrogen can at this point still be gaseous or can be liquefied, depending on the controlled stagnation conditions (temperature and pressure). The fluid is then fed through a nozzle where the cluster production process takes place. This is the most important piece of a CJT and will be described in section 4.1.1. The resulting cluster-jet expands into the first vacuum chamber, the skimmer chamber with a vacuum in the order of 10^{-2} mbar. (For the MCT-D and MCT-M the studied interactions take place here.) The cluster-jet is not only dependent on the stagnation conditions but differs strongly for different nozzles. For some nozzles the cluster-jet contains highly intense regions, so called core beams. To observe these structures an *Optical Monitoring System* (OMS) is included in the skimmer chamber. Here, a 1 mW laser illuminates the cluster-jet and under 90° a "pco.pixelfly" camera detects the scattered light. The intensity here is correlated with the density of the cluster-jet, as visible in fig. 3.4. Since the position of the core beam within the cluster-jet varies depending on the nozzle and the stagnation conditions, the preceding described setup needs to be tiltable. The ball joint allows to adjust the angle of the nozzle and thus the angle of the cluster-jet by nearly $\pm3°$. As a result, the high intense core beam can be aligned through the subsequent target beam pipes. In order to separate this core beam from residual gas a conical orifice called skimmer (thus the name skimmer chamber) with an opening diameter of 500 µm is used to inject part of the beam into the next vacuum chamber, the collimator chamber. Here, the vacuum reaches 10^{-5} mbar and the beam is further tailored by a collimator with an opening diameter of 700 µm to its final geometry. At the MCT-Prototype this collimator is currently circular, for the $\overline{P}$ANDA target it is rectangular to maximize the beam target overlap whilst minimizing the residual gas background. Generally speaking, nozzle, skimmer, and collimator are easily exchangeable to adjust to different experimental requirements. Both, skimmer and collimator, are each placed on motor driven cross-tables to adjust

the position. Hence, one is able to align the cluster-jet, together with the ball joint through the 5 m long target beam pipe. After the collimator is passed, a *Transition Vacuum Chamber* (TVC) being the last pumping port before entering the target beam line is installed. For the MCT-prototype a cryopump is installed allowing for vacuum pressures below 10^{-7} mbar whilst cluster-jet operation. The MCT-$\overline{\text{P}}$ANDA uses two turbomolecular pumps here. After the TVC, the beam line follows, in which the beam is guided to the scattering chamber. For the ANKE target the studied interactions take place only slightly behind this chamber.

3.2 Scattering Chamber and Beam Line

After a flight path of 2.1 m the cluster-jet enters the interaction chamber. This represents later on the IP of the $\overline{\text{P}}$ANDA experiment. Due to design changes the IP at $\overline{\text{P}}$ANDA will be located 2.25 m away from the nozzle. Here, for the protoype an *Absolute thickness Monitoring System* (AMS) is installed to measure the density, thickness, and expanse of the cluster-jet. After this chamber the jet enters the second beam line leading to the beam dump.

3.2.1 Absolute Thickness Monitoring System (AMS)

The AMS within the scattering chamber is shown in fig. 3.5. It consists of two rods with a diameter of 1 mm which can be moved by stepper motors. First, the horizontal orientated rod is moved vertically through the cluster-jet leading to a gradually moving, approximately rectangular overlap of cluster-jet and rod. The clusters impinging on the rod break up, resulting in a pressure increase within the scattering chamber. All other clusters have an undisturbed flight path to the beam dump. Then, the second, vertical rod is moved horizontally through the cluster-jet. Plotting the pressure against the rod position one obtains a typical pressure profile as in fig. 3.6. Due to the circular shape of the collimator, the cluster-jet is at first also circular. It can be assumed that the density within this circle is constant. However, there are a few causes leading to a smearing of this homogeneous jet over the flight path of several meters. Within the skimmer chamber only a low vacuum is present leading to the realistic possibility of scattering of the clusters with residual gas background leading to an alternation of the flight direction. Furthermore, especially in the liquid regime the cluster production process extends over probably several millimeters, leading to a variety of beam origins and thus a smeared flight direction. Thus, the density of the cluster-jet can not be
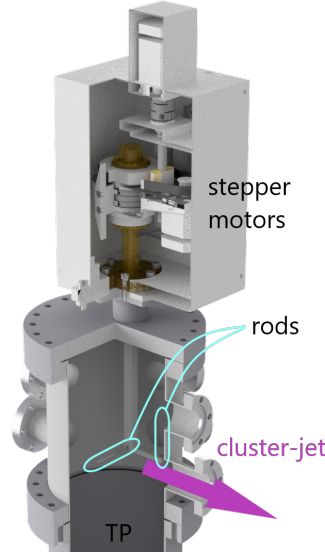
Figure 3.5: AMS within the scattering chamber. The cluster-jet enters from the left and leaves to the right. Within the chamber the vertical and the horizontal rod of the AMS can be moved one after another through the cluster-jet by means of the stepper motors placed on top. Picture generated by D. Bonaventura, edited.

assumed homogeneous in radial direction but is rather described by a convolution of a step function with a gaussian distribution:

$$
\rho(x,y) = \frac{1}{2} \left(\operatorname{erf}\left(\frac{\sqrt{(x-x_0)^2 + (y-y_0)^2} + R_c}{s} \right) \right.
$$
$$
\left. - \operatorname{erf}\left(\frac{\sqrt{(x-x_0)^2 + (y-y_0)^2} - R_c}{s} \right) \right)
\tag{3.1}
$$

with the smearing parameter s, the cluster-jet radius R_c and the error function $\operatorname{erf}(z)$ as given in [Köh15]. In order to get from the two-dimensional density to the pressure profile, one needs to integrate over the area of the rod with the diameter d and a length significantly larger than the cluster-jet diameter. Thus, the fit function for the pressure profile equals

$$
p(x) = p_{0/a} \int_{x-d/2}^{x+d/2} dx' \int_{-\inf}^{+\inf} dy' \rho(x', y') + p_{\text{back}}.
\tag{3.2}
$$

The scaling factor $p_{0/a} = \frac{vRT}{SM}$ considers the dependency on the pumping speed S, the gas properties, and the cluster velocity v. Furthermore, a constant background is added. Finally, the cluster-jet thickness is given by

$$
\rho_{\text{H}} = 2 \cdot \frac{p_{0/a} S N_A}{vRT}
\tag{3.3}
$$
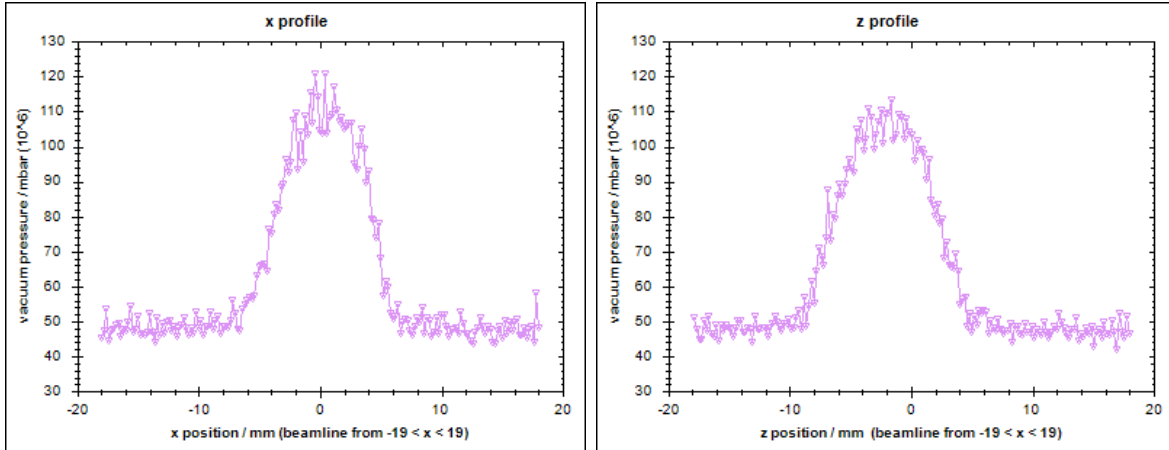
Figure 3.6: Pressure profiles of a thickness determination measurement in x- and z-direction. The cluster-jet propagates in y-direction and later on the accelerator beam propagates in z-direction. When the rod moves through the cluster-jet the impinging clusters lead to a pressure increase. The measured pressure is plotted against the rod position to obtain the one dimensional jet profile.

with the universal gas constant $R = 8.314\,51\,\text{J}/(\text{mol\,K})$, the Avogadro constant $N_A = 6.022 \times 10^{23}\,\text{mol}^{-1}$, the measured pumping speed at the interaction chamber $S = 194.6\,\text{l}_\text{n}/\text{min}$ [Klo20], the velocity v, and the temperature T [Köh15].

3.3 Beam Dump

The four-stage beam dump is shown in fig. 3.7. The cluster-jet has an undisturbed flight path into the last beam dump stage or in the subsequent detection chamber, leading to the highest pressure in this chamber. To achieve this optimal flight path a dedicated alignment process is necessary, performed best with a *Micro Channel Plate* (MCP) sytem. The preceding differentially pumped stages gradually improve the vacuum conditions and thus minimize the gas backflow into the beam line and scattering chamber. The vacuum within the beam dump is in the order of $10^{-6}\,\text{mbar}$. For the MCT-$\overline{\text{P}}$ANDA the beam dump includes three stages and the detection chamber is replaced by an additional turbomolecular pump allowing for optimal vacuum conditions. Additionally the orifices between the beam dump stages are adjustable [Bra24, Ded24]. Typical detector types installed in the detection chamber of the MCT-Prototype are the channeltron detector [Köh15, Ves20] or the MCP system [Obs23, Ves20].
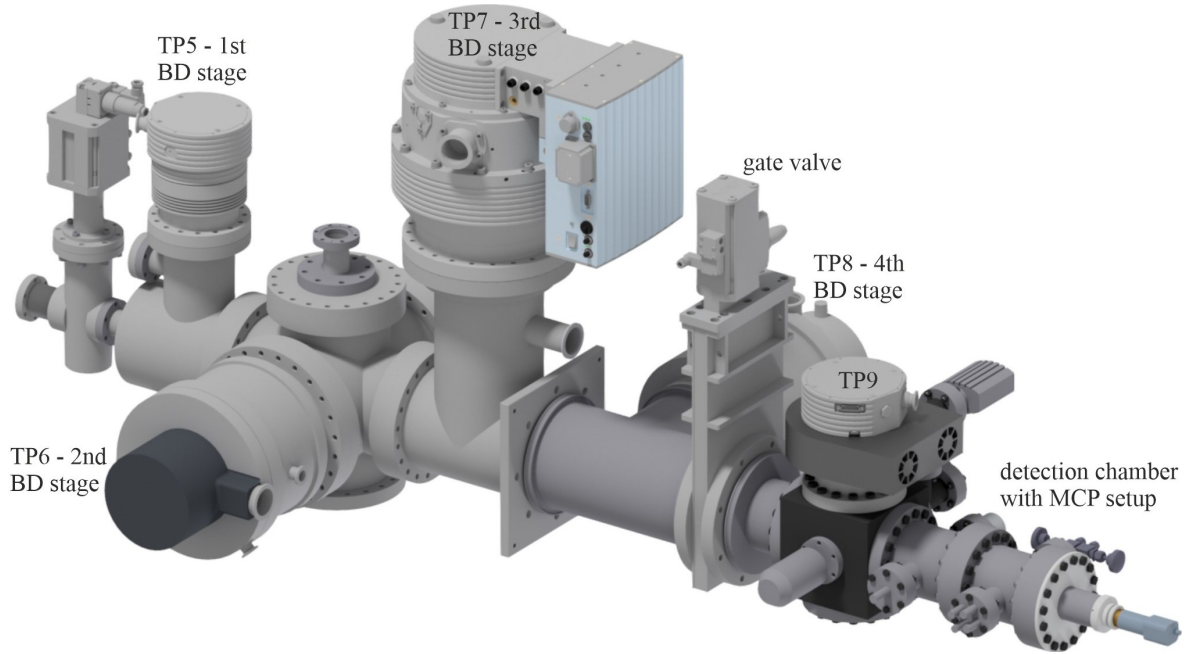
Figure 3.7: CAD drawing of the beam dump. For the MCT-Prototype it consists of four differentially pumped stages equipped with a turbomolecular pump each. The cluster-jet enters from the left. On the right behind the gate valve the detection chamber in MCP configuration is shown.

3.3.1 Time-of-Flight (TOF) Measurements

For TOF measurements, which are needed for the determination of cluster velocity distributions, a start signal and a stop signal are used to calculate the flight time for a given distance. The start signal is given by ionizing single clusters with an electron gun, which is located between the cluster source and the scattering chamber and shown in fig. 3.8. The filament is powered with $6\,\mathrm{V}$ to $11\,\mathrm{V}$ so that electrons are released. These electrons are accelerated by a reflector electrode which has a potential of $-150\,\mathrm{V}$. In order to not allow the electrons to pass the extraction orifice, which is located between filament/reflection electrode and cluster-jet, is at $-170\,\mathrm{V}$ to $-200\,\mathrm{V}$. For a short time of, e.g., $t_\mathrm{d} = 20\,\mathrm{\mu s}$ with a repetition of, e.g., $20\,\mathrm{Hz}$ the extraction orifice is grounded so that the electrons escape the e-gun and reach single clusters with an energy of up to $150\,\mathrm{eV}$. This is sufficient to ionize a cluster by scattering and thus releasing an additional electron. For shielding the variable electrical field of the extraction orifice towards the cluster-jet, a grounded grid is implemented here. Due to the pulsed operation the start time t_start is defined. The stop signal is generated by the ionized cluster after a defined flight path, reaching the corresponding detector installed in the detection chamber. Here, the ionized cluster triggers an electron avalanche in, e.g., the channeltron or the MCP system, leading to a negative voltage pulse at the readout.
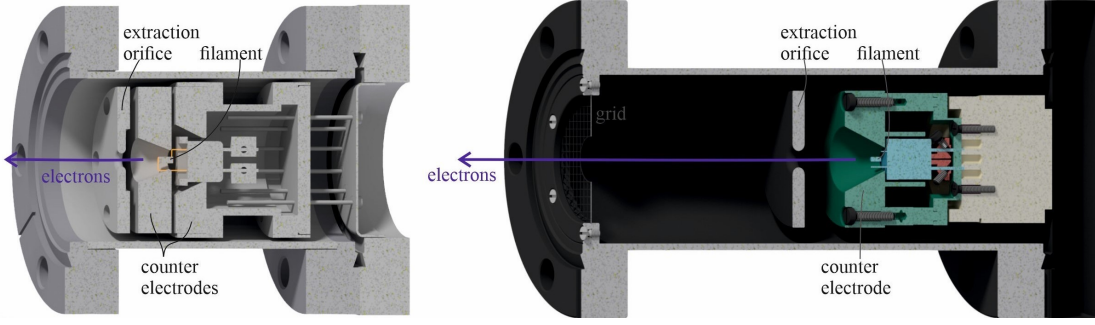
Figure 3.8: Cross section of the electron guns used at the MCT-Prototype. *Left:* Old e-gun. *Right:* New e-gun developed in [Hum21]. Both consist of a filament powered to generate free electrons. Surrounding the filament is a counter electrode to accelerate the electrons and an extraction orifice which can be used to pulse the electron flow. For the new e-gun a grounded grid is implemented to shield the electrical potential towards the cluster-jet.

This pulse is then amplified and discriminated to reduce background noise and then fed as stop signal to the TOF device to determine the stop time t_{stop}. With the known flight path between point of ionization and point of detection of $s = (4.43 \pm 0.02)\,\text{m}$ in channeltron and $s = (4.67 \pm 0.02)\,\text{m}$ in MCP configuration, the velocity can be calculated by

$$v = \frac{s}{t_{\text{stop}} - t_{\text{start}} - t_{\text{offset}}}. \tag{3.4}$$

The time offset induced by electronics was determined together with C. Fischer to $t_{\text{offset}} = (14.1 \pm 5.8)\,\text{µs}$ [Fis21] according to the first calibration in [Täs12]. With a new detection setup implemented with M. Scharpey [Sch24] a new offset was determined to $t_{\text{offset}} = (16.0 \pm 7.4)\,\text{µs}$ with a similar but slightly different method. When changing the duration of grounding the extraction orifice this value needs to be varied, as it refers to the offset corresponding to the average start time. Following, the uncertainty in velocity can be calculated by

$$u(v) = v \cdot \sqrt{\left(\frac{u(s)}{s}\right)^2 + (u(t_{\text{start}})^2 + u(t_{\text{offset}})^2)\frac{v^2}{s^2}}. \tag{3.5}$$

the uncertainty in t_{start} scales with the duration t_{d} of the (smeared) rectangular pulse for grounding the extraction orifice, which has to be kept in mind when varying the duration. For a perfect rectangular pulse this would be $u(t_{\text{start}}) = \frac{t_{\text{d}}}{\sqrt{12}}$. However, the capacity of the electrode gives a smearing, so that the duration of grounding would need to be remeasured. Depending on the stop detector a white noise of background signals can be introduced to the TOF spectrum, which results in a $f(v) \propto {}^1\!/v^2$ background in the velocity spectrum. When determining the mean velocity, which is needed for most of the measurements, this background is subtracted accordingly.
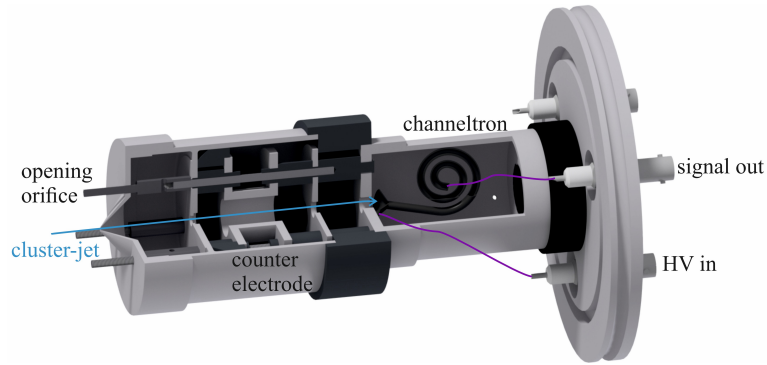
Figure 3.9: CAD Drawing of the channeltron detector setup. The cluster-jet enters through an opening orifice and passes a counter electrode (not used in this thesis and hence grounded) until the opening of the channeltron is reached. Front and end of the channeltron are each connected to the outside so that high voltages can be applied and signals can be read out. Picture generated by D. Bonaventura, edited.

3.4 Cluster-Jet Detection Setups

Within the last years and especially the last beam time, the MCP system showed great performance but a rapid aging process followed by reduced sensitivity was observed. Thus, within this thesis the development of a detector setup with results as good as the MCP system but more chemically inert and less susceptible to aging effects was started. First, the detectors currently routinely in use are presented here. Afterwards, some tested setups are shown as well. Important for the evaluation of a setup is mainly the possibility to get a pulse for the TOF measurement and to obtain a two-dimensional image of the cluster-jet cross section for the alignment.

3.4.1 Channeltron Detector

A channeltron as used in the channeltron detection setup shown in fig. 3.9 is a highly resistant lead glass tube, which is winded like a snail. As charged particles (here: ionized clusters) impinge onto the throat shaped front, electrons may be released from the channeltron. Due to an voltage gradient applied between front and end of the channeltron, these electrons are accelerated into the tube. Mostly, a negative voltage of 1600 V to 2000 V is applied to the front, while the end is at ground potential. For special setups, it is also possible for the front to be at ground and the end to be at positive high voltage. Due to the large voltage gradient, the primary electrons accelerated into the channeltron have enough energy to release secondary electrons as they impinge onto the channeltron walls. Further impacts of these electrons lead to an electron avalanche which is detectable at the end of the channeltron. For this
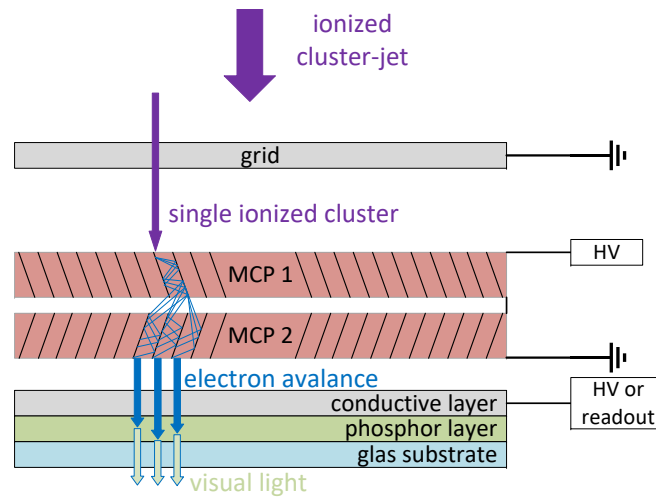
Figure 3.10: Schematic overview of the MCP assembly. The ionized cluster-jet enters from the top and first crosses a grounded grid. A single ionized cluster can trigger an electron avalance within a MCP. The second MCP is mounted directly onto the first one. The electrons leaving the first MCP spread into a few channels of the second plate where an additional gain is obtained. A few millimeters behind the MCPs the phosphor screen consisting of a conductive layer, a phosphor layer, and a glass substrate is mounted. The electron avalanche leaving the MCPs can either be detected as voltage pulse at the conductive layer of the screen or further accelerated with a positive high voltage applied at this conductive layer. When the electrons pass through the conductive layer, they interact with the phosphoric material and generate photons which can be detected as visual light by, e.g., a camera.

operation, good vacuum conditions (better than 10^{-4} mbar, for reduced background signals and an improved lifetime even better) are necessary.

With this detection setup, an excellent timing of the detection is possible. The uncertainty of $5.8\,\mu s$ [Fis21] is mainly due to the width of the grounding time span and small in comparison to the typical flight times in the order of several milliseconds. In comparison to the later presented MCP system, less background and significantly higher rates in the TOF measurement are apparent. Also, the gain is larger than for the MCP setup which results in larger signals. However, no two-dimensional profile of the cluster-jet can be obtained.

3.4.2 MCP System

The *MicroChannel Plate* (MCP) System can be used for TOF measurements as introduced in [Ves20] but also a two-dimensional visualization of the cluster-jet is obtainable. Here, even better vacuum conditions than for the channeltron are needed (better than 10^{-4} mbar is mandatory for short term operation but would lead to a fast degradation, 10^{-6} mbar is recommended for long term operation).

Directly in front of the MCP, a grounded grid is placed to shield the electrical field (see fig. 3.10). The used MCP is in chevron assembly and thus consisting of two single MCPs. One of these plates consists of many highly resistant, densely packed glass tubes arranged to a disk, each with a small bias angle. An electrode is mounted on each face of the disk so that voltages can be applied. Similar to the functionality of a channeltron, ionized clusters impinging on the channel wall release electrons, which are accelerated further into the channel. At the opposite wall, the accelerated electrons release secondary electrons so that an avalanche forms. The second plate is mounted nearly directly onto the first one but with an opposite bias angle of the channels. The electron avalanche exiting the first plate spreads into only a few channels of the second plate leading to a further increase of the number of electrons [Pho94]. This chevron assembly setup enhances the gain of the setup from about 10^3 for single stage MCPs to about 10^5 for two stage MCPs [Pho20].

For detecting the electron avalanche, there are several possibilities. A single electrode can be used to detect a signal, e.g., for the TOF measurement. Already in use at MCTs are P43 phosphor screens (e.g., in [Köh15, Ves20]). Scintillating screens generally consist of a glass substrate for stability reasons, a phosphor layer for the conversion from electrons to light, and on top a conducting layer (see fig. 3.10). Commonly and also previously used is the combination of granular P43 phosphor and the semiconductor *Indium Tin Oxide* (ITO), which is transparent and colorless for thin layers. The ITO layer can be used like an anode for the TOF measurement. Here, also a high voltage can be applied to further accelerate the electrons leaving the MCP giving an additional gain factor of several tens times [Pho94]. These accelerated electrons have enough energy to pass through the ITO layer and excite the phosphor which then glows. Due to the close proximity of MCP and screen the space resolution is maintained. With this a fast and easy alignment of the cluster-jet through, e.g., the 5 m of target beam pipe later at $\overline{\text{P}}$ANDA can be performed in only a few minutes. Furthermore, instead of using an electron gun for ionizing the cluster-jet, an accelerator beam can also ionize the jet. Hence, the MCP system can also visualize the beam-target-overlap and thus the vertex zone. This may become quite handy in aligning the cluster-jet and the accelerator beam in respect to each other and thus maximizing the luminosity [Bra24].

Scintillation Screens

When operating the MCP with a P43 phosphor screen optimal performance is obtained. Nevertheless, within the last beam time at COSY, a rapid aging process of the phosphor screen was observed [Bra24]. Probably, an excessive exposure to atomic hydrogen or

ions chemically degraded the granular phosphor. As alternative a scintillation crystal of *Yttrium Aluminum Garnet activated by Cerium* (YAG:Ce) by the company Crytur [Cry24] is explored. There it is stated, that YAG:Ce is a fast and highly universal scintillator with high mechanical and chemical resistance. The degraded phosphor screen of the MCP used in [Bra24] is up-cycled by removing the phosphor and the ITO layer from the glass substrate and adding a YAG:Ce scintillating crystal together with an ITO layer and an additional aluminum layer.

For scintillation screens P43 phosphor (also called GADOX or GOS; $Gd_2O_2S:Tb^+$) is most commonly used [MY11]. The granular phosphor is coated very densely on a glass plate and forms a uniform, a few particles thick layer [Pho94]. Its efficiency and photon stopping power is among the highest of all phosphors but has a persistence, which is correlated with the time of afterglow, of $1\,ms$ to $2\,ms$ (Yagi et al. (2004); as cited in [MY11]). The P46 phosphor (also called $YAG:Ce^{3+}$; $Y_3Al_5O_{12}:Ce^{3+}$) has a lower density and a shorter persistence (Blasse and Bril (1967) as cited in [MY11]). This leads to a decrease of fluorescence intensity of the P46 by $40\,\%$ in respect to P43 phosphor [MY11]. As compensation an additional aluminum reflection layer, on top of the ITO layer, can be added to increase light efficiency by up to $100\,\%$ and to reduce stray light. Commonly, $40\,nm$ to $50\,nm$ thickness is recommended, whereas an acceleration voltage of $3\,kV$ is required for the electrons to penetrate [Pro] (depending on the thickness). The scintillation screen fabricated by Crytur contains a $100\,nm$ aluminium layer on a $20\,nm$ ITO layer.

Since the P43 phosphor of the MCP used at the last beam time degraded [Bra24], the differences between possible phosphor materials are of highest relevance. In [Lie$^+$16] a radiation hardness test was performed with crystalline powder P43 phosphor (#1 therein, comparable to the previous phosphor screen), crystalline powder P46 phosphor (#2, #3), and a single crystal YAG:Ce screen (#4, by the company Crytur as used in this thesis). In opposition to our observed degradation by ionized hydrogen, for the radiation hardness test in [Lie$^+$16] nickle ions with higher energy but in a significantly smaller amount were used, leading to a qualitative comparison for our application. It was found that for P43 granular phosphor a decrease of $5\,\%$ in light yield was observed while the granular P46 phosphor and the corresponding single crystal YAG:Ce, which is introduced in this thesis, were found to be stable [Lie$^+$16]. Furthermore, in [Tou$^+$08] the used screen is described as mechanically and chemically stable.

This leads to the reasoned assumption that the single crystal YAG:Ce screen is comparable in imaging properties and a reduction in degradation can be expected. Together with M. Scharpey the refurbished MCP system was installed at the MCT-

Table 3.1: Typical voltages applied to the MCP systems. Variations depending on the stagnation conditions of the hydrogen upstream to the nozzle are necessary. The values are obtained after a dedicated commissioning process over a few days. As soon as spikes in MCP current or a drift in screen current are observable the respective voltage needs to be decreased and additional conditioning time has to be taken (or the other voltage may be increased).

MCP setup	voltage applied at	typical voltages for		max. limit by manufacturer
		TOF setup	visualization	
by Hamamatsu with P43 screen	MCP front screen	1200 V 0 V	1000 V 2000 V	2000 V 4000 V
by TOPAG/Crytur with YAG:Ce screen	MCP front screen	1600 V 0 V	1450 V 3800 V	2000 V 5000 V

Prototype and tested after a conditioning process [Sch24].

It was found that the imaging properties are the same: The faster response time is of no relevance since the camera used for 2D acquisition has exposure times in the order of seconds. The reduced light output is compensated by the additional aluminum layer which required a higher voltage at the screen. This higher voltage is also favorable for a higher light emission. It is found, that two-dimensional cluster-jet imaging with this MCP system is successful and comparable to previous MCP systems. The operation as stop detector for the TOF measurements is also functional. The obtained signals at the aluminum layer of the screen are even higher as for other used P43 phosphor MCPs [Sch24]. An approximate orientation for the applied voltages is given in table 3.1. This leads to the conclusion that the type of phosphor screen used has no relevant influence on the daily operation except for different voltages to be applied and a different trigger height for the TOF measurement to be chosen. For chemically challenging environments like the hydrogen atmosphere created by a dumped cluster-jet ionized by the accelerator beam, the used YAG:Ce screen is promising to be more stable. However, for confirmation this would require testing at an accelerator facility, e.g., Cave C at GSI, when possible.

3.4.3 Surface Barrier Detector

As other possible cluster-jet detector, a surface barrier detector is considered. It is a p-n diode with a small depletion layer and only a thin p-layer as entry area. For now, only the first working principle needs to be proven, whereas in a second step the implementation of a segmented detector for the 2D-visualization can be addressed. As test setup a surface barrier detector (Ortec model "BA-17-25-100") is placed in the detection chamber of the MCT-Prototype with the possibility to read out the signals
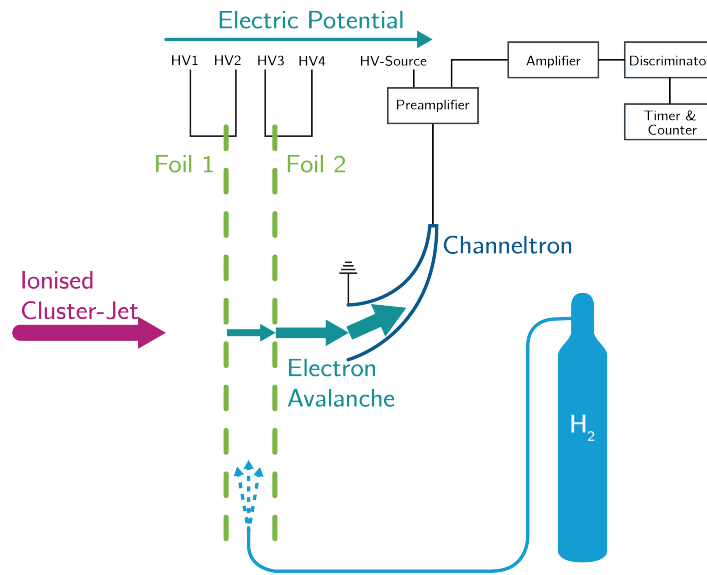
Figure 3.11: Schematic overview of the GEM setup. The ionized cluster-jet gets dumped on the first GEM foil resulting in its own multiplication gas. Additional hydrogen can be injected between the first GEM foil and a second foil. In theory, the multiplication gas gets ionized by the clusters. The resulting electrons are accelerated by the voltages applied to the foils and should get multiplied towards the channeltron. Here, an electron avalanche gets triggered, which can be measured. Drawing by M. Scharpey [Sch24].

and to apply a voltage. The detector is limited to a bias voltage of up to $50\,\mathrm{V}$. Even with this voltage not even the slightest glimpse of signal is observable when ionized clusters impinge on the detector. Probably their size and mass is to large to enter the depletion layer. This leads to the omission of this detector for the cluster-jet detection.

3.4.4 GEM Foils

As a further variation in the cluster-jet detection setup the implementation of *Gas Electron Multiplier* (GEM) foils is considered. The used GEM foils are ordered at the company Techtra [Tec24]. They consist of a $50\,\mathrm{\mu m}$ polyimide (often known as kapton) foil with a $50\,\mathrm{\mu m}$ copper coating on both sides. A network of holes with an hourglass cross section and diameters of $(70 \pm 5)\,\mathrm{\mu m}$ in the copper and $(50 \pm 5)\,\mathrm{\mu m}$ in the polyimide is etched into the foil. Between both copper planes a voltage can be applied leading to an electrical field within the holes of up to $50\,\mathrm{kV\,cm^{-1}}$, able to create an avalanche of multiplied electrons. Typically, these GEM detectors consist of several foils surrounded by a gas and a closing readout. The incident radiation ionizes the gas whereas the electrons are accelerated towards the GEM foil. Within the holes an election avalanche forms. This process is repeated at every foil leading to measurable signals.

The basic idea to the implementation at a CJT is to use a combination of GEM foils and the MCP. Due to dumping the complete cluster-jet onto the MCP surface, locally a dreadful vacuum is present, which is a possible threat to the MCP lifetime. With additional GEM foils in front of the MCP, the cluster-jet would be dumped already there and the signal would be converted into electrons. Instead of using an external gas as typical for GEM detectors, the cluster-jet produces its own multiplication gas. The 2D and timing information would be conserved while the vacuum surrounding the MCP can be improved. Due to the higher robustness in comparison to the MCP, for the first tests, the channeltron detector is used. In front of the channeltron one or two GEM foils can be mounted and between the foils additional hydrogen can be inserted to increase the multiplication capabilities (see fig. 3.11).

In order to test the working principle of this setup several measurements were performed together with M. Scharpey [Sch24]. With a relatively dense cluster-jet at liquid stagnation conditions, the clusters can be ionized by the electron gun. Step wise, no foil, one foil, and two foils are placed in front of the channeltron detector. Each foil has a front side and a back side voltage power supply with negative voltages up to 800 V. The front of the channeltron is at ground and the end is at positive high voltage.

With increasing number of GEM foils, the number of signals at the channeltron is reduced. While with one foil still some signals are measurable, with two foils only background events are observed. With one foil the clusters, which have diameters in the micrometer range, can simply fly through the holes ($\varnothing 50\,\mu m$). For two foils the holes do not align and no clusters reach the channeltron. Furthermore, with one foil and additional hydrogen gas, the number of signals is reduced. The clusters interact with the residual gas and thus also cannot reach the channeltron.

For all these measurements, the voltages applied to the foils have no noticeable effect on the signal rate, even with up to 400 V across a single foil [Sch24]. This leads to the conclusion that no electron generation and multiplication is obtained. As this detection principle is not working as expected, it is rejected.

Several cluster-jet detection setups were presented and used at the MCT-Prototype. The channeltron detector is still the best choice for background free and fast velocity spectra. The MCP has its advantages in the two-dimensional visualization of the cluster-jet. Still, velocity spectra are obtainable in acceptable time scales with only minimal background. The two scintillation screens studied give similar results in visualization and in TOF measurements, with higher stop signals for the aluminum YAG screen. However, the newly introduced YAG:Ce single crystal used as MCP

phosphor screen is expected to be chemically more stable. The two newly studied cluster-jet detection setups, the surface barrier detector and the GEM foils, were found to be not functional and are thus omitted. In possible further beam times, the degradation of the YAG:Ce screen should be tested to verify and obtain the best possible setup for future implementations and experiments as the $\overline{P}$ANDA experiment.

3.5 Pumping Station of the future MCT-$\overline{P}$ANDA Beam Dump

For the MCT-$\overline{P}$ANDA, currently a new beam dump is in development and in production [Bra24], which needs a backing pump system to allow for optimal vacuum conditions. This pumping system was built up within the scope of this thesis. The main requirement on this pumping station is to deliver a sufficient and clean fore-vacuum for the turbomolecular pumps of the differentially pumped beam dump stages and for the dedicated MCP chamber.

For a first test, the pumping station was used at the *Münster Droplet Target* (MDT-H) [Man24]. Here, only the pumping line designed for the beam dump stages was used. When operating with small gas loads typical for the droplet operation (in the order of up to $700 \, \mathrm{ml_n/min}$), an end vacuum of the pumping station in the order of $10^{-3} \, \mathrm{mbar}$ was reached.

3.5.1 Overview and Parts List

Both, the differentially pumped beam dump stages and the MCP chamber, need to be pumped and vented individually as well as together for different maintainance scenarios. An overview of the resulting pumping station is shown in figs. 3.12 and 3.13. The corresponding parts are listed in table 3.2.

The electronics included will allow for both, remote control with a computer as well as the direct control at the pumping station with hardware buttons. These controls are planned in a similar manner as for the pumping station of the MCT-$\overline{P}$ANDA source, but need to be finalized. Currently, a reduced control box is implemented, only allowing for local control.
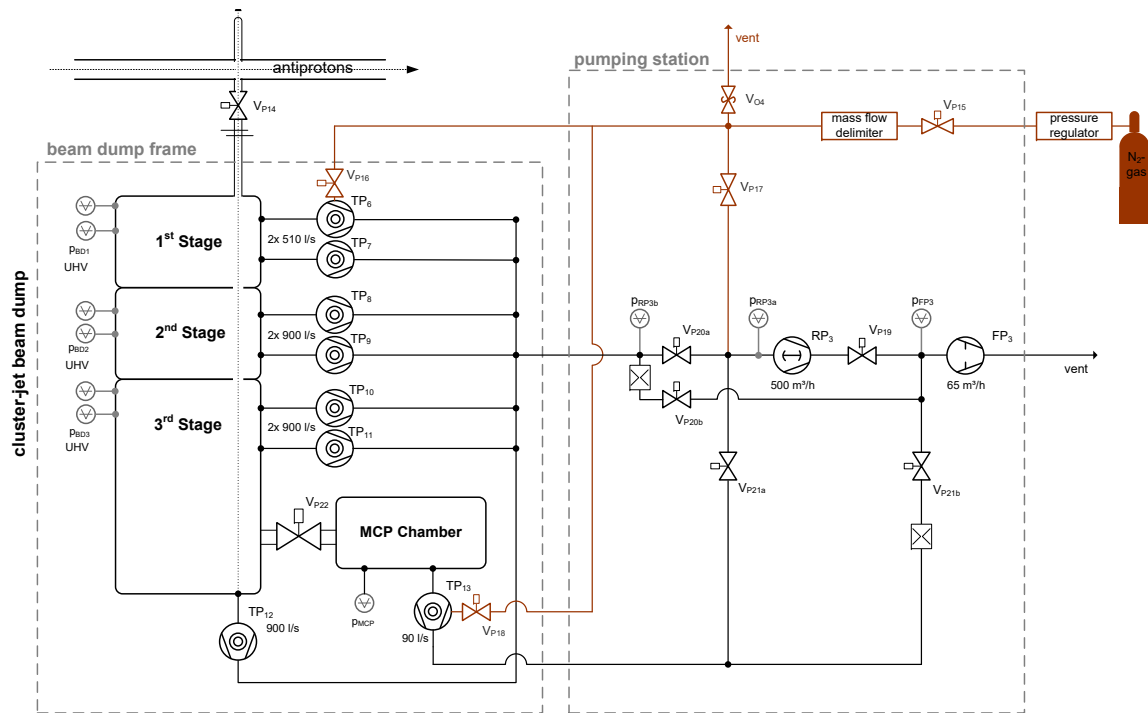
Figure 3.12: Schematic overview of the beam dump and the pumping station. The beam dump on the left includes the three differentially pumped stages each pumped by (at least) two turbomolecular pumps with a common fore-vacuum and an additional MCP chamber with its own fore-vacuum to allow for separate operation. The two fore-vacuums are both provided by the pumping station depicted on the right. Created together with P. Brand [Bra24].
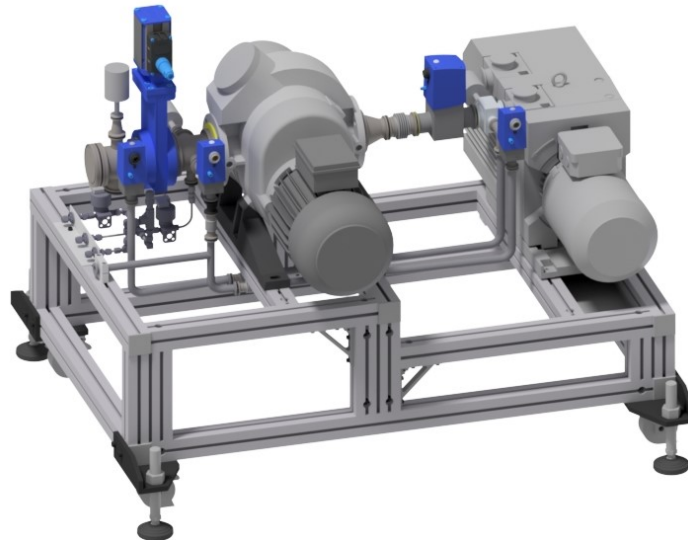
Figure 3.13: CAD drawing of the beam dump pumping station. Starting at the right the forepump Trivac D65 B ensures the fore-vacuum for the Ruvac WSU 501 (center) which further provides an excellent fore-vacuum for the subsequent turbomolecular pumps located at the beam dump. Picture generated by F. Rummler.

Table 3.2: Parts list of the BD pumping station. The label corresponds to the declaration in fig. 3.12. For the pumps the maximal pressure difference for starting and the nominal pumping speed is given, for the valves and gate valves the maximal pressure difference for opening and the nominal state in case of a power outage is given, and for the pressure gauge the measurable pressure range is given. The pressure relief valve V_{O4} serves as a safety procedure. When venting the beam dump, the MCP chamber, and/or the pumping station a pressure of 1 bar is targeted. If for some reason the pressure exceeds 1.2 bar V_{O4} is opened to prevent any damage to the vacuum system.

label	model	max. Δp	pumping speed
FP_3	Trivac D65 B	1000 mbar	$65\,\mathrm{m^3\,h^{-1}}$
RP_3	Ruvac WSU 501	80 mbar	$505\,\mathrm{m^3\,h^{-1}}$

label	model	max. Δp	normal state
V_{O4}	SS-RL3S6MM-SET	1.2 bar	pressure relief valve
V_{P15}	SS-92S6MM-O-4898 & MS-SOL-1K	20.6 bar	open
V_{P16}	SS-92S6MM-O-4898 & MS-SOL-1K	20.6 bar	open
V_{P17}	SS-92S6MM-O-4898 & MS-SOL-1K	20.6 bar	open
V_{P18}	SS-92S6MM-O-4898 & MS-SOL-1K	20.6 bar	open
V_{P19}	HV inline valve DN 40	1000 mbar	closed
V_{P20a}	HV gate valve DN 63	30 mbar	closed
V_{P20b}	HV inline valve DN 16	1000 mbar	closed
V_{P21a}	HV inline valve DN 16	1000 mbar	closed
V_{P21b}	HV inline valve DN 16	1000 mbar	closed

label	model	pressure range
p_{FP3}	Ceravac CTR 100 N - 1000Torr	1.33×10^{-1} mbar to 1332 mbar
p_{RP3a}	Ceravac CTR 100 N - 10Torr	1.33×10^{-3} mbar to 13.3 mbar
p_{RP3b}	Ceravac CTR 100 N - 10Torr	1.33×10^{-3} mbar to 13.3 mbar

3.5.2 Operating Manual

For the operation of the pumping station it is important to know how to evacuate and to vent the connected chambers. This will be presented in the following.

Pumping Both Chambers

- pumps are off, valves are closed, chambers are vented

- start FP_3, wait for it reaching operating temperature ($\approx 15\,\text{min}$)

- open V_{P20b} and V_{P21b}, wait for reaching $\approx 1\,\text{mbar}$ at p_{RP3b} and p_{MCP}

- close V_{P20b} and V_{P21b}, open V_{P19}, wait for reaching $\approx 50\,\text{mbar}$ at p_{RP3a}

- start RP_3, wait for reaching $\approx 1\,\text{mbar}$ at p_{RP3a}

- if p_{RP3b} and/or $p_{MCP} > 5\,\text{mbar}$: open V_{P20b} and/or V_{P21b} and wait until pressure is reached

- open V_{P20a} and V_{P21a}, (close V_{P20b} and V_{P21b})

- wait for p_{RP3b} and $p_{MCP} \lesssim 10^{-1}\,\text{mbar}$, start TPs

Pumping the Beam Dump Stages with MCP Chamber vented

- pumps are off, valves are closed, chambers are vented

- start FP_3, wait for it reaching operating temperature ($\approx 15\,\text{min}$)

- open V_{P20b}, wait for reaching $\approx 1\,\text{mbar}$ at p_{RP3b}

- close V_{P20b}, open V_{P19}, wait for reaching $\approx 50\,\text{mbar}$ at p_{RP3a}

- start RP_3, wait for reaching $\approx 1\,\text{mbar}$ at p_{RP3a}

- if $p_{RP3b} > 5\,\text{mbar}$: open V_{P20b} and wait until pressure is reached

- open V_{P20a}, (close V_{P20b})

- wait for $p_{RP3b} \lesssim 10^{-1}\,\text{mbar}$, start TPs

Pumping the Beam Dump Stages with MCP Chamber evacuated

- pumps are on, valves V_{P19}, V_{P21a} are open, valves V_{P20a}, V_{P20b}, V_{P21b} are closed, beam dump stages vented

- close V_{P19} and V_{P21a}

- open V_{P20b}, wait for reaching $\approx 1\,\text{mbar}$ at p_{RP3b}

- open V_{P19}

- open V_{P20a}, close V_{P20b}

- wait for $p_{RP3a} \lesssim 10^{-1}\,\text{mbar}$, open V_{P21a}

- wait for $p_{RP3b} \lesssim 10^{-1}\,\text{mbar}$, start TPs

Pumping the MCP Chamber with Beam Dump Stages vented

- pumps are off, valves are closed, chambers are vented

- start FP_3, wait for it reaching operating temperature ($\approx 15\,\text{min}$)

- open V_{P21b}, wait for reaching $\approx 1\,\text{mbar}$ at p_{MCP}

- close V_{P21b}, open V_{P19}, wait for reaching $\approx 50\,\text{mbar}$ at p_{RP3a}

- start RP_3, wait for reaching $\approx 1\,\text{mbar}$ at p_{RP3a}

- if $p_{MCP} > 5\,\text{mbar}$: open V_{P21b} and wait until pressure is reached

- open V_{P21a}, (close V_{P21b})

- wait for $p_{MCP} \lesssim 10^{-1}\,\text{mbar}$, start TP

Pumping the MCP Chamber with Beam Dump Stages evacuated

- pumps are on, valves V_{P19}, V_{P20a} are open, valves V_{P20b}, V_{P21a}, V_{P21b} are closed, beam dump stages vented

- close V_{P19} and V_{P20a}

- open V_{P21b}, wait for reaching $\approx 1\,\text{mbar}$ at p_{MCP}

- open V_{P19}

- open V_{P21a}, close V_{P21b}

- wait for $p_{RP3a} \lesssim 10^{-1}\,$mbar, open V_{P20a}

- wait for $p_{MCP} \lesssim 10^{-1}\,$mbar, start TP

Venting

For venting V_{P15} needs to be open. In order to vent the beam dump stages or the MCP chambers (individually), the pump line to the individual chamber is closed by closing V_{P20a} or V_{P21a} and the chamber is filled with nitrogen by opening V_{P16} or V_{P18}, respectively. For venting the pumping station the following steps are to be taken:

- pumps are running, all valves to the chambers are to be closed (V_{P20a}, V_{P20b}, V_{P21a}, and V_{P21b}; the b valves are probably already closed)

- stop RP_3

- close V_{P19}

- open V_{P17} for nitrogen venting

- wait for $p_{MCPRP3a} \gtrsim 10\,$mbar or out of range

- stop FP_3, open V_{P19}

- wait for $p_{MCPRP3a} \approx 1\,$bar, close V_{P19}, close V_{P17}

Note: V_{P19} needs to be closed when stopping FP_3. Otherwise this would lead to an immense amount of oil in the pumping line and the possibility of venting through the fore pump.

Chapter 4

Nozzle Studies

Due to the formation of the cluster-jet inside the nozzle, it is the centerpiece of every CJT. The nozzles have a very specific geometry, which is necessary to ensure the cluster formation processes. The small narrowest diameter compared to the large nozzle dimensions lead to a challenging production process. Even small deviations of the nozzle, e.g., size of the narrowest diameter or irregularities, lead to a large impact on the cluster-jet properties, especially on the core beam, which is a highly intense part within the residual cluster-jet. In this chapter the basics of de Laval nozzles for CJT will be unfolded with the cluster production processes. Further, two possible nozzle production processes are described, tested, and optimized. Furthermore, investigations on the manufactured nozzles are performed and presented here.

4.1 Cluster Production Processes and Nozzle Geometry

The inner geometry of nozzles used in MCTs is very specific. It is convergent-divergent, which is called de Laval nozzle. This shape is necessary for the cluster production process and furthermore is used due to the excellent cluster-jets resulting.

4.1.1 Cluster Production Processes

The fluid entering the nozzle can cluster via two different mechanisms, depending on the state of the fluid upstream of the nozzle. These mechanisms are valid for a broad variety of elements and compounds, while MCTs mainly use hydrogen. For gaseous hydrogen an accumulation of atoms occurs via three-body interactions which is the
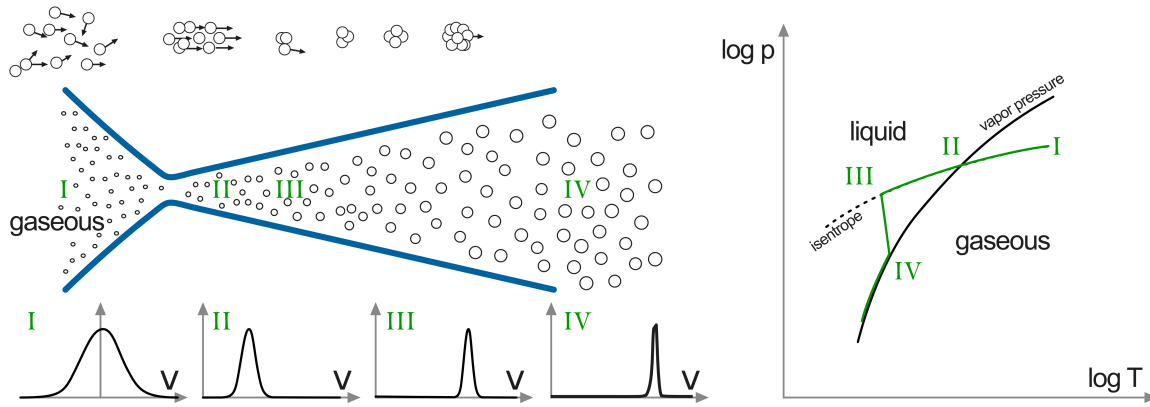
Figure 4.1: Cluster production starting with a gaseous fluid. Adapted and combined from [Dem16, Hag92, VFK22]. On the left a schematic nozzle is shown together with four markers and the microscopic description of the cluster production process. On the right a pT-diagram of the macroscopic description is shown.

breakdown of the supersaturated state while for liquid hydrogen an atomization process takes place, both leading to spherical clusters in the nanometer to micrometer regime (as will be investigated in section 6.1). For these cluster production processes to take place the resulting cluster-jet needs to expand in a chamber with a pressure only slightly below the pressure upstream to the nozzle [Täs12]. For a cluster-jet stable over several meters however, the pressure needs to be better than approximately 10^{-1} mbar [Täs12]. Otherwise shock waves could occur, leading to the breakup of clusters [Pau00a].

The thermophysical observables of a fluid flowing through a convergent-divergent de Laval nozzle can be described using the model of a quasi-one dimensional flow [Pau00a, Täs12]. As presented by A. Täschner [Täs12] due to the given areal cross section of the nozzle one can calculate, e.g., the pressure, temperature, and velocity of the fluid along the nozzle axis, depending on the stagnation conditions (pressure and temperature of the fluid upstream to the nozzle). This firstly becomes relevant while considering the cluster production processes as well as later on in calculating the mean velocity of the resulting clusters [Täs12]. These one dimensional calculations neglect, e.g., turbulence or friction at the nozzle walls. However, it has been shown that the performed, simplified calculations deliver excellent approximations [Täs12].

Gas upstream to the Nozzle

Assuming gaseous hydrogen upstream to the nozzle, the cluster production process is performed via the stepwise accumulation of hydrogen atoms. One can use a macroscopic or a microscopic approach to describe the accumulation process, which is depicted in fig. 4.1.

Starting with a laminar flow of the gas towards the nozzle (I), within the convergent inlet the gas is accelerated towards the smallest diameter up to its local velocity of sound. The mach number Ma, which is the ratio between the fluid velocity and its local speed of sound, equals 1. Within the divergent outlet of the nozzle the gas is further accelerated ($Ma > 1$). Here, the pressure and temperature decrease adiabatically along an isotrope towards the vapor pressure curve (II). The ongoing adiabatic expansion into the liquid regime leads to a supersaturation until an "onset" (III), where the gradual formation of clusters sets in. Due to the released condensation energy the expansion curve returns to the vapor pressure curve (IV) resulting in the small liquid droplets or clusters within the surrounding vacuum. [Hag92, Pau00a]

Microscopically speaking, the velocity v of the gas molecules upstream to the nozzle is Maxwell-Boltzmann distributed around $v = 0$ (I). Within the convergent inlet the molecules are accelerated to the local speed of sound. The adiabatic expansion within the divergent outlet of the nozzle leads to the reduction of the relative velocity between the gas molecules and to the alignment of the flight directions (II). This allows for three-body interactions to set in (III). Two gas atoms combine to a nucleation core while a third impact partner compensates the excess energy and momentum. With further impacts additional atoms can accumulate. At a later stage within the nozzle (IV), as the cluster concentration is no longer small compared to the molecule density, also cluster-cluster collisions occur and contribute to the cluster growth until finally a macroscopic cluster forms. [Dem16, Pau00a] The clusters have a shifted Maxwell-Bolzmann velocity distribution and binding energies in the order of a few tenths of eV [Pau00b]. These clusters are very similar in velocity and flight direction [Pau00a], leading to a collimated and very stable cluster-jet.

The resulting clusters have diameters in the nanometer range and can be described by the Hagena law [Hag87, Hag92, HO72]. Hagena gives a scaling parameter [Hag87]

$$\Gamma = n_0 d^q T_0^{0.25q-1.5} \tag{4.1}$$

with the number density n_0, the narrowest nozzle diameter d, and the parameter $0.5 < q \leq 1$, which has been experimentally determined to $q = 0.085$ [Hag92]. For different nozzle shapes the adaption

$$d_{\text{eq}}/d = 0.74/\tan\left(\alpha_{1/2}\right) \tag{4.2}$$

was found [Hag92] with the effective diameter d_{eq} which is reduced compared to the narrowest diameter d due to the conical outlet with a half-opening angle of $\alpha_{1/2}$.

Together with a generalization for different gasses (gas dependent coefficient $k_{H_2} = 184$) [SDT98], eq. (4.1) can be written as

$$\Gamma^* = \frac{k\frac{p_0}{\text{mbar}}\left(\frac{0.74\frac{d_n}{\mu\text{m}}}{\tan\left(\alpha_{1/2}\right)}\right)^{0.85}}{\left(\frac{T_0}{\text{K}}\right)^{2.29}} \qquad (4.3)$$

with the stagnation pressure p_0 in mbar, the narrowest diameter of the nozzle d_n in μm, the half-opening angle $\alpha_{1/2}$, and the stagnation temperature T_0 in K. The scaling parameter Γ^* gives a probability of cluster formation: For $\Gamma^* < 200$ there is no production of clusters. Within $200 < \Gamma^* < 1000$ cluster production begins, while for $\Gamma^* > 1000$ many clusters exceeding 100 atoms per cluster are observed [Hag87]. With the boundary of typical operating conditions of MCTs ($d_n = 30\,\mu\text{m}$, $p_0 > 5000\,\text{mbar}$, $T_0 < 100\,\text{K}$, $\alpha_{1/2} = 3.5°$) $\Gamma^* > 3500$ is always given. Thus, for typical MCT operation conditions significant cluster generation is evident.

Furthermore, one can calculate an average cluster size N with the Hagena scaling law [Hag92]

$$N = A_N \left(\frac{\Gamma^*}{1000}\right)^{\gamma_N} \qquad (4.4)$$

with $A_{\text{N,Hagena}} = 33$ and $\gamma_N = 2.35$ for $\Gamma^* > 1000$. From the number of atoms in a single cluster, its diameter can be calculated, assuming (at first) liquid droplets. In [Köh15], the mean number of atoms per clusters for gaseous stagnation conditions was determined to be approximately in the range of 10^4 to 10^5 atoms/cluster for stagnation conditions of 7 bar to 10 bar and 46 K to 80 K leading to diameters of roughly 2 nm to 10 nm. This will further be considered in section 6.1 with additional measurements and adaptions by C. Mannweiler [Man19].

Liquid upstream to the Nozzle

Before elaborating on the disintegration of a liquid jet into a cluster-jet some fluid mechanics need to be introduced. When talking about flow characteristics one can distinguish between laminar and turbulent flow. Here, the Reynolds number Re is introduced. It describes the ratio between the inertial force and the friction force and thus characterizes the similarity of internal disturbance of flows within, e.g., a pipe. [Sch16] The Reynolds number is defined by

$$Re = \frac{\rho v d}{\eta} \qquad (4.5)$$

with the density ρ, the flow velocity v, the characteristic length, here the nozzle diameter d, and the dynamic viscosity η. It was found, that below $Re \approx 2300$ the flow is layered, meaning that layers of the fluid within a pipe move with different velocities without exchanging many fluid particles. The layers close to the pipe wall move slower due to friction, while the inner layers move faster. This type is labeled laminar flow. With rising velocity, the Reynolds number exceeds the critical value of 2300 and the flow becomes turbulent. The flow has now an irregular, fluctuating motion superimposing the regular basic flow. [Sch16]

The Weber number describes the ratio between the momentum force to the surface tension force [LM17]. It is defined over [LM17]

$$We = \frac{\rho v^2 d}{\sigma} \tag{4.6}$$

with the surface tension σ. To obtain a dimensionless number which is not dependent on the flow velocity Ohnesorge derived the Ohnesorge number Z [LM17]

$$Z = \frac{\sqrt{We}}{Re} = \frac{\eta}{\sqrt{\rho \sigma d}} \tag{4.7}$$

which is an indicator of the jet stability [LM17].

With this, Ohnesorge originally defined three regions of jet disintegration, which was extended by a fourth region by Miesse [Mie55]. Here, measurement series of a liquid jet emerging into gases through nozzles were made. With varying the jet velocity and nozzle diameter, the disturbance wavelength, the breakup length, and the maximum droplet diameter were measured. The easiest way to determine which region a given breakup falls into is by contemplating the resulting jet. From this, Ohnesorge and Miesse derived boundaries based on Re and Z [LM17], whereas in the following only the last boundary condition derived by Miesse will be presented. The four regions of jet disintegration as presented in [LM17] are:

1. **Rayleigh jet breakup** This is the favored region for droplet formation in droplet and pellet targets. Axis-symmetric oscillation disturb the initial liquid filament and lead to a breakup. The predominant drop formation mechanism is the surface tension. Ideally, the resulting droplets are identical spheres, which is due to the minimization of surface area. Nevertheless, the actual resulting droplets vary slightly in size and geometry. [LM17] The size differences can be minimized by applying an external oscillation, e.g., with a piezo element [Eks+96, Man24].
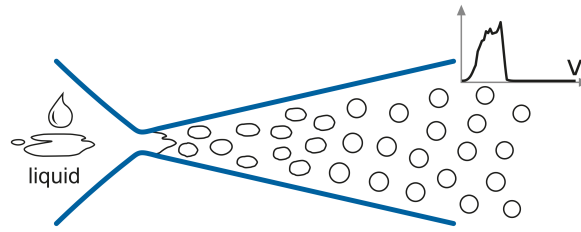
Figure 4.2: Cluster production starting with a liquid fluid. The liquid enters the nozzle from the left and is accelerated towards the narrowest diameter. Within the diverging outlet atomization takes place forming the clusters. Originally published in [VFK22].

2. **First wind-induced breakup** With rising jet velocity the effect of air friction is no longer neglectable. The breakup due to surface tension is supported by the dynamic pressure of the ambient air leading to an accelerated breakup process which still occurs several jet diameters downstream to the nozzle. The resulting drop diameters are in the same order as the jet diameter. [LM17]

3. **Second wind-induced breakup** As the jet velocity is further increased the relative motion between jet and ambient gas is increased as well as its influence on the drop formation. The effects of surface tension is reduced leading to droplets much smaller than the jet diameter. The breakup still occurs several jet diameters downstream to the nozzle. [LM17]

4. **Atomization** With even higher jet velocities an atomization occurs directly at the nozzle exit in a chaotic, irregular manner. (Note: the nozzles used by Miesse and Ohnesorge have no diverging outlet, which needs to be taken into account for the following nozzle studies.) The exact predominant drop formation mechanisms are not known, yet. [LM17, Mie55] Miesse found, that for atomization the square root of the Weber number needs to exceed an atomization boundary W_atom

$$\sqrt{We} > W_\mathrm{atom} = \frac{150}{\sqrt{2}} \cdot Z^{-0.087}. \tag{4.8}$$

Starting now with a liquid in front of the convergent-divergent MCT nozzle, it is accelerated within the convergent inlet to its local speed of sound at the narrowest cross section just as with gas. Within the divergent outlet the liquid is further accelerated until the disintegration takes place (see fig. 4.2). Based on calculations from A. Täschner [Täs+13, Täs12] one can obtain the resulting mean cluster velocities. Together with fluid data by [NIST] one obtains, that eq. (4.8) is fulfilled to at least down to 22 K (colder temperatures were not tested) and thus the jet breakup is performed by atomization.

The atomization process is sometimes subdivided into a primary and a secondary atomization. The primary atomization is responsible for the first break up already at the nozzle exit (Note: for the convergent-divergent de Laval nozzles this breakup is performed between the narrowest diameter and the nozzle exit). The resulting spray is in the form of a cone with a given opening angle and the vertex within the nozzle [RB82]. The opening angle and the virtual beam origin were already determined in [Köh15, Ves20]. Various processes of drop formation mechanism are suggested, but none can be clearly identified as predominant [LM17, RB82]. One possible theory for atomization is liquid turbulence, but this is not the only reason because the most turbulent nozzles do not generate the most instable jets. An other possibility is atomization due to cavitation phenomena, but atomization also occurs in cavitation-free nozzles [RB82]. Furthermore, there are other atomization mechanism like, e.g., aerodynamic surface wavegrowth, rearrangement of the jet's velocity profile, liquid supply pressure oscillations, or wall boundary layer velocity profile relaxation, which all in combination explain atomization observations [RB82].

Further aspects of the exact atomization process also remains unknown. It is impossible to predict the size or size distribution of the unstable waves at the time of breakup or the time between successive ruptures. However, it has been found that the resulting droplets are much smaller than the diameter of the nozzle [RB82].

In secondary atomization, additional processes may further break up the clusters generated by primary atomization. Since the former described (primary) atomization processes can also lead to a stepwise breakup of initially large to smaller droplets, it is difficult to define a clear boundary between primary and secondary atomization.

One process to consider solely for secondary atomization is the break up by **aerodynamic forces**. The generated clusters enter the skimmer chamber with residual gas background. The gas molecules could collide with the clusters causing them to break up into smaller clusters. The resulting maximum stable cluster diameter is [Mes04]

$$D_{\mathrm{max,A}} = \frac{8\sigma}{c_{\mathrm{W}}\rho_{\mathrm{vac}}v_{\mathrm{c}}^2}. \qquad (4.9)$$

For a cluster-jet at $25\,\mathrm{K}$ and $10\,\mathrm{bar}$ with the surface tension $\sigma = 0.0011\,\mathrm{N\,m^{-1}}$ [NIST], the drag coefficient of a sphere $c_{\mathrm{W}} = 0.45$ [Leß21], the vacuum density at room temperature at the worst $\rho_{\mathrm{vac}}(1\,\mathrm{mbar}) = 8.4 \times 10^{-5}\,\mathrm{kg\,m^{-3}}$ [NIST], and the cluster velocity $v_{\mathrm{c}} \approx 400\,\mathrm{m/s}$, this gives a maximum stable cluster diameter of $D_{\mathrm{max,A}} = 1.5\,\mathrm{mm}$, becoming even larger for better vacuum.

Second process to consider is the breakup of the clusters by **shock waves**. Generally, for a converging nozzle a pressure difference between the fluid upstream and down-

stream to the nozzle (nozzle pressure p_0 and pressure in the skimmer chamber p_{SK}, respectively) large enough needs to be present for a free jet to form. The ratio is given by $p_{SK} < p_0 \cdot (2/\kappa+1)^{\kappa/(\kappa-1)}$ [Pau00a]. The adiabatic index is given by $\kappa = f+2/f$ with $f = 3$ degrees of freedom for cryogenic hydrogen. (The two rotational degrees of freedom freeze out while the three translational degrees of freedom remain.) This leads to the condition $p_a > p_0 \cdot (3/4)^{5/2} \approx 0.487 \cdot p_0$ for which no cluster-jet forms. For de Laval nozzles however, the adiabatic expansion in the diverging outlet gives an additional factor. Simulations by A. Täschner [Täs12] determine the boundary for stagnation conditions of 50 K and 10 bar to be at $p_{SK} < 9.999\,999\,989$ bar for a jet to form. For pressures below this boundary the process within the diverging outlet is supersonic and hence independent of the ambient pressure within the skimmer chamber. In this case the supersonic jet is abruptly stopped and compressed to the ambient pressure at the nozzle exit. Under usual conditions the resulting jet can no longer be considered as continuous medium. [Pau00a]

The resulting pressure at the nozzle exit can be given by simulation with the van der Waals gas model of A. Täschner. At stagnation conditions of 50 K and 10 bar a pressure of 1.5×10^{-2} mbar is obtained [Täs12]. The same value is simulated in [Ves18] for the Peng Robinson gas model. For liquid stagnation conditions of 25 K and 10 bar a pressure of 9.5×10^{-2} mbar is present at the nozzle exit [Täs12]. Here it is to note, that using a real gas model for liquid conditions is a possible source of errors. In the MCT-Prototype skimmer chamber, vacuum conditions in the order of 1.3×10^{-2} mbar and 5.0×10^{-2} mbar were measured, respectively. Since the measured pressures are smaller than the simulated pressure at the nozzle exit, shock waves are of no relevance here. For significantly less pumping speed and thus worse vacuum conditions, this needs to be reevaluated.

Additionally to different atomization processes, the influence of coflowing air has been studied in literature [LM17]. Here, the liquid jet is surrounded by an air stream. An important result is the effect on the intact core length. With increased relative velocity between gas and liquid, the intact core length of the liquid filament shortens [LM17]. This effect will become again relevant later on in this chapter while studying core beams in section 4.3.3.

Summarizing, the liquid hydrogen atomizes within the nozzle, leading to clusters with diameters much smaller than the narrowest diameter of the nozzle. In comparison to clusters originating from gaseous hydrogen, clusters from liquid hydrogen are larger in diameter. This will become relevant for studying the cluster size distributions in section 6.1. Furthermore, the clusters at liquid stagnation conditions are slower. This
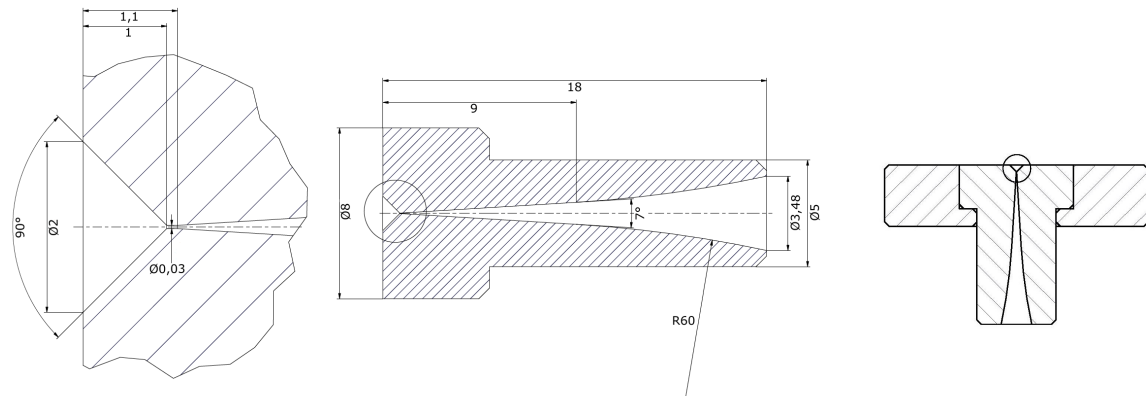
Figure 4.3: Geometry of cluster-jet de Laval nozzles. All lengths are given in mm. *Left:* Enlargement of the nozzle inlet and the narrowest diameter as marked in the center and right drawing. *Center:* De Laval nozzle with "small" outer nozzle geometry. *Right:* The outer nozzle geometry can be adapted to fit into a larger nozzle bed. Application specific differences between the small (center) and the large (right) outer nozzle geometry will become relevant in section 4.3. Drawings by D. Bonaventura.

leads to significantly higher cluster-jet densities which is favorable for, e.g., the $\overline{\mathrm{P}}$ANDA experiment. Furthermore, the velocities have a much broader spread, which will become a tool in determining the Widom line in chapter 5. Still, the flight direction is well defined and thus the cluster-jet tailored by skimmer and collimator is stable over a flight path over 5 m, sufficient for a variety of experiments as, e.g., $\overline{\mathrm{P}}$ANDA.

## 4.1.2 Geometry of de Laval Nozzles for Münster Cluster-Jet Targets

The desired convergent divergent inner nozzle geometry is shown in fig. 4.3 where both possible outer geometries (small and large) are also shown. The convergent inlet of the nozzle is 1 mm with an opening angle of 90°. The subsequent narrowest cross section is typically, depending on the exact nozzle, between 25 μm and 40 μm. The divergent outlet starts with a linear section over 8 mm with an opening angle of 7°. Tangentially adjacent is a radius with a diameter of 60 mm. The full length of the nozzle is 18 mm. This geometry was designed for the cluster production process in the gaseous regime. As the operation parameters of the MCT were moved into the liquid regime, it was observed that the resulting cluster-jet densities are significantly higher. Here, it was obtained, that the presented geometry works for the cluster production in the liquid regime as well. However, there are several possible alternations to this geometry, which can and partly already have been studied. E.g., shortening the divergent nozzle outlet

has no influence on the resulting cluster-jet [Ves18]. In addition, nozzles with nominally nearly the same geometry result in completely different cluster-jets, considering, e.g., achievable thickness, velocity, and density profile (see [Gri18] and section 4.3). Thus, developing a totally in house nozzle production technique is one aim of this thesis. This will give the possibility to investigate the optimal nozzle geometry and shed light upon the cluster production process in the liquid regime which is of highest interest.

4.2 Nozzle Production Techniques

Within this thesis two possible nozzle production techniques are considered. First, glass nozzles produced by *Selective Laser-induced Etching* (SLE) by the company LightFab are tested. This process allows producing nozzles with complex geometries and thus would enhance the possibility of testing a variety of nozzle geometries. The second production process is the galvanization of the already established copper nozzles. The process developed at the University of Münster is further optimized within this thesis and first nozzles are produced completely in the institute of nuclear physics and its mechanical workshop. Both nozzle types are installed in the MCT-Prototype to test their performances.

4.2.1 Investigating Glass Nozzles
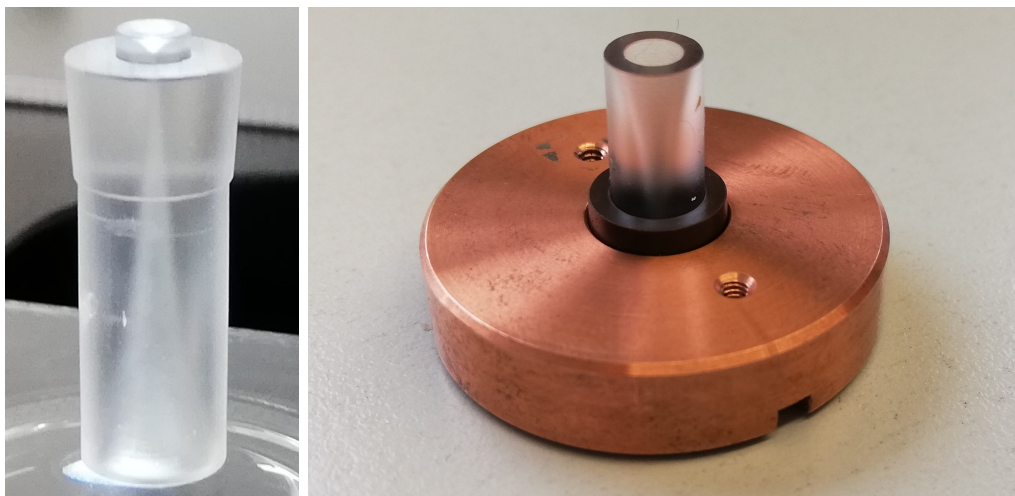
Figure 4.4: Pictures of the glass nozzle. *Left:* Glass nozzle illuminated from below with the inlet at the top. The inner surface is slightly visible. *Right:* Glass nozzle placed inside the copper bracket. The nozzle inlet is at the bottom and is hidden behind the copper bracket.

In previous theses [Gri18, Ves20] the possibility of glass nozzles was already explored. The glass nozzles are produced by LightFab by *Selective Laser-induced Etching* (SLE) [Lig20] according to CAD drawings from our working group. For this two-step process an ultra-short laser pulse is focused very precisely in order to modify the transparent material internally. Afterwards a wet chemical etching is applied at the surface of the workpiece to remove only the modified material. [Lig20] At first, glass nozzles with a length of only 3 mm were manufacturable (tested in [Gri18]). With time the fabrication process developed, allowing for production of up to 10 mm (tested in [Ves20]) and finally up to the desired total nozzle length of 18 mm (tested in this thesis). The two shorter nozzles were also tested with an aluminum nozzle extension for a total length of 18 mm. None of these 3 mm or 10 mm and the compound nozzles were working like the established copper nozzles. Within the gaseous and supercritical regime a stable cluster-jet was formed with properties comparable to the ones formed by a copper nozzle. As soon as the vapor pressure curve or its elongation into the supercritical regime, the Widom line (see chapter 5), is crossed and the hydrogen in front of the nozzle is liquid or liquid-like, additional frozen micro-particles inside the cluster-jet or one big ice chunk in front of the nozzle were formed.

Analogously to the 10 mm glass nozzle in [Ves20], the glass nozzle with a length of 18 mm is now placed in a copper bracket (see fig. 4.4) and tested at the MCT-Prototype. Due to measuring at the identical setup the measurements are perfectly comparable.

The result of the 18 mm glass nozzle is nearly the same as for the shorter one. As soon as the liquid(-like) regime in front of the nozzle is reached additional frozen micro-particles form. After some time, an ice chunk totally blocks the nozzle but is removed on its own after some further time. As already proposed in [Ves20] two possible remedies, a nozzle heating and polishing the surface, are tested and presented in the following.

Measurements with an Additional Nozzle Heating

Silicon glass has a thermal conductivity two orders of magnitude smaller than copper in the considered temperature region [Abd+00, Ho+09]. This leads to a colder inner surface in the glass nozzle and thus an even faster cooling process in the nozzle outlet. The smaller final temperature would lead to the formation of frozen hydrogen particles. Applying an external nozzle heating (see fig. 4.5) may resolve this. The result is shown in fig. 4.6 where the cluster-jet within the skimmer chamber without external nozzle heating is compared to the cluster-jet at the same stagnation conditions upstream to the nozzle with maximal nozzle heating. No improvement can be seen.
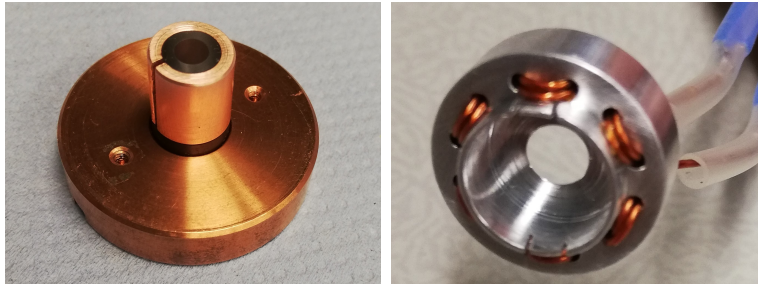
Figure 4.5: Pictures of the nozzle heating. *Left:* Glass nozzle with an additional copper casing to allow for an optimal heat transfer onto the nozzle. *Right:* The nozzle heating is basically a thin coated copper wire threaded through an aluminum holder which can be placed on the nozzle. The thin wire is connected to a larger wire which is then connected to a power supply.
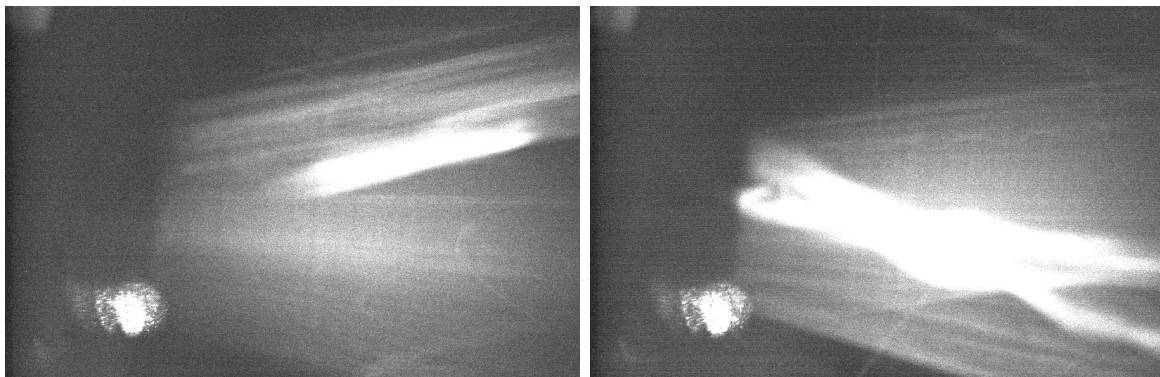
Figure 4.6: Pictures of the resulting beam in the skimmer chamber. Not visible is the nozzle exit to the left and the skimmer to the right of the pictures. *Left:* Without additional nozzle heating. *Right:* With full additional nozzle heating. For both measurements no stable cluster-jet is obtainable. As this is a snapshot of 1 s the frozen micro-particles are visible as big white line without stable direction. This blot changes from picture to picture (which cannot be shown here). Thin lines emerging from the nozzle are also visible in the background which are smaller particles. Furthermore, lines crossing the picture from, e.g., bottom to top show the chaotic flight paths of the micro-particles.

Measurements with a Polished Inner Surface

The inner surface of the glass nozzle can be seen in fig. 4.7. Due to the fabrication process the surface is not smooth but consists of many crates (diameter of approximately 5 µm) with little tips. This roughness can lead to turbulence of the hydrogen and thus no cluster-jet can form. The glass nozzle was polished several hours in an ultrasonic bath in a solvent of microparticles with a diameter of 3 µm leading to a smother inner surface. Since the particles are an order of magnitude smaller than the narrowest diameter of the nozzle, the particles can be presumed to polish even close to and in the narrowest sections. The roughness of the (polished) inner surface of the nozzle outlet
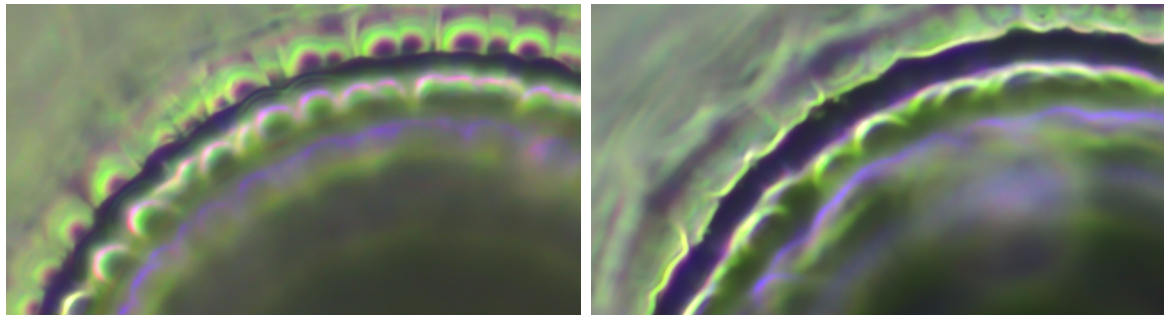
Figure 4.7: Pictures of the glass nozzle outlet. Both pictures are taken with the same magnification and are focused on the same position. *Left:* Before polishing. *Right:* After polishing. On the left the circular shape of the laser focus point with which the glass is prepared for the etching procedure by LightFab is apparent. On the right the circles are larger in diameter and thus not that prominent. A smoother surface is obtained.

cannot be measured qualitatively at our institute but investigated by light microscopy (see fig. 4.7). The two pictures show the before and after of the exact same position of the inner surface of the tested glass nozzle. A smoother surface for the polished nozzle is apparent. The nozzle was then tested again but still no difference can be seen.

Measurements with Optimized Glass Nozzle

On basis of an optimization in fabrication a smoother surface can be achieved and three nozzles with this improved surface finishing are produced. The most promising nozzle has a slightly smoother surface than the already tested glass nozzle after polishing. This new nozzle was inserted into the MCT-Prototype and tested. The resulting cluster-jet in the gaseous and gas-like supercritical region is also stable and comparable to cluster-jets formed by other (copper) nozzles (see section 4.3). Still, as soon as the vapor pressure curve or its elongation, the Widom line (see chapter 5), is crossed, frozen micro-particles are formed and no stable cluster-jet is observable, comparable to the previous tests.

As still no way was found to achieve a fully functional glass nozzle, this nozzle production technique is no longer considered for cluster-jet de Laval nozzles. For other applications where only an operation in the gas(-like) regime is foreseen, the glass nozzles can be used as comparable cluster-jets are obtained with an easier nozzle production process and a broad variety in possible nozzle geometries. Also for the use at droplet targets such glass nozzles should be reconsidered.
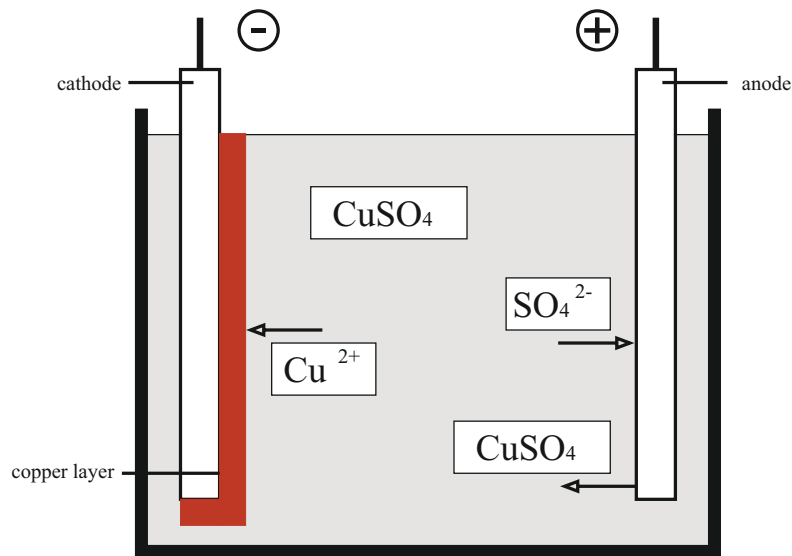
Figure 4.8: Schematic overview of the galvano bath. Figure by D. Bonaventura [Bon20], according to [Jel13], edited.

4.2.2 Optimizations in Producing Monolithic Copper Nozzles

Copper nozzles were produced serially at CERN (*Conceil Européen pour la Recherche Nucléaire*) [CER83], where the first nozzles used by the AG Khoukaz originated. One of these nozzles is currently still the best available nozzle and often referred to as CERN Nozzle. Unfortunately, the CERN production process was discontinued some time ago leading to the necessity of developing a nozzle production process at the University of Münster itself. Before this process is explained in detail and the resulting nozzles are shown, a section about galvanization will provide the necessary basics.

Basics of Galvano Forming

Galvano forming describes the process of creating a thick layer of material onto a negative mold which is afterwards removed (mechanically or chemically) leading to the formation of the complete workpiece by galvanic means [Jel13]. For the nozzle production a sulfuric acid copper bath consisting mainly of de-ionized water, copper sulfate, and sulfuric acid is used. The cathode of the electrolytic reaction is given by the negative molds fabricated by the mechanical workshop out of an aluminum alloy. For the anode two solvable copper plates are utilized. By applying a DC current positive copper ions can be detached from the copper anode, migrate to the negative cathode, and deposite here forming the new copper workpiece. This can be seen in fig. 4.8. Whilst galvano forming several reactions run simultaneously [Jel13]:

Anode reaction: $Cu \rightarrow Cu^{2+} + 2e^-$

Secondary anode reaction: $Cu^{2+} + SO_4^{2-} \rightarrow CuSO_4$

Dissociation: $CuSO_4 \rightarrow Cu^{2+} + SO_4^{2-}$

Cathode reaction: $Cu^{2+} + 2e^- \rightarrow Cu$

At the anode two reactions can occur. Copper can be ionized directly giving two electrons into the electric circuit leading to copper ions within the solvent or the copper can be extracted by means of the sulfate (anode reaction and secondary anode reaction). The copper sulfate then will be separated within the watery solution into copper ions and sulfate ions (dissociation). Both cases result in positive copper ions which then are hydrated, meaning water molecules surround the ion with the contrasting partial charge pointing to the ion. These hydrated copper ions then migrate to the cathode, making the bath an ion conductor. At the cathode electrons are added to the copper ions letting them crystallize (cathode reaction) and thus form the copper layer. [Jel13] In order to achieve a high quality copper layer a cathodic current density, which is the ratio between current and cathode area, in the right range is needed. For a cathodic current density too low, the copper deposition process takes way too long leading to instabilities in the copper bath and thus a bad coating. On the other hand, with a cathodic current too high, not enough copper ions can reach the cathode leading to the deposition of hydrogen instead. This results in a dark, non sticking layer, called combustion. This can be avoided by reducing the current or by moving the workpiece or electrolyte to enhance the redelivery of ions. Furthermore, the bath temperature can be increased or auxiliary anodes can be placed in the desired region. [Jel13] Important for the quality of the deposited layer are mainly four bath properties: **Opacity** describes the capability to totally cover the workpiece especially in depressions. The layer thickness distribution is given by the **macro scattering** of the electrolyte. For an even surface on the atomic scale gloss additives are added. Organic substances ensure an increased nucleation rate leading to shiny surfaces, which is also called **gloss depth scattering**. Finally, the **micro scattering or leveling** defines the capability to compensate for roughness in the surface. [Jel13] All these bath properties can be traced back to the bath composition. During the galvano process bath ingredients are consumed. A close monitoring of process properties, e.g., current and voltage, as well as the visual appearance of the galvanized workpiece helps to refill the needed bath components. The obstacle in this is the subjective quantification of the appearance which has to be gained with experience.

Copper Nozzle Production at CERN and the University of Münster until 2020

In 1983 the need of fine de Laval nozzles with narrowest diameters of 15 µm to 50 µm formed for special experiments at CERN. At the time, the industry was not interested to fulfill the need of such fine de Laval nozzles. Instead the CERN central workshops developed a galvano forming process: A negative of the nozzle outlet was fabricated out of aluminum and coated with a thin layer of tin. This pin was then galvanized to a sufficiently thick copper layer to permit the making of a core by spark erosion. After mechanical and chemical extraction of the pin the nozzle was completed. [CER83] This development process was "not all plain sailing" [CER83] and "was possible only through close collaboration between skilled craftsmen at the central workshops" [CER83], which already gives a small insight into the complexity of producing such narrow de Laval nozzles. One of these nozzles, internally called CERN nozzle, is currently in use by the AG Khoukaz at the MCT-$\overline{\text{P}}$ANDA. With this nozzle the highest target thickness of $(4.85 \pm 0.24) \times 10^{15}$ atoms/cm^2 was reached in a distance of 2.1 m [Gri18].

Since this is the only nozzle which fulfills the needs of the $\overline{\text{P}}$ANDA experiment and there is the reasonable possibility that this nozzle could be blocked permanently, new nozzles need to be fabricated. Due to the discontinuation of the nozzle production at CERN a production line needed to be developed at the University of Münster. Furthermore, with a production line at the University of Münster not only the production of more, even better nozzles will become possible but also changes to the nozzle geometry are possible and with that a better understanding of the cluster production process is obtainable. In general, the basic nozzle production principle from CERN was adopted, but all explicit steps need to be redesigned due to the lack of details in literature.

The first nozzle production process at the University of Münster was established in 2012 [Bon12, KBT13]. Here, the nozzle outlet negative was made out of *PolyMethyl MethAcrylate* (PMMA) acrylic glass, around which a workpiece was galvanized by an external company. Outer geometry and inlet were fabricated by the mechanical workshop of the institute of nuclear physics of the University of Münster. Finally, the narrowest diameter was fabricated by an other external company by an ultra short pulse laser [Bon12]. In [Gri18] a fabricated nozzle was cut in half to get a look at the connection between inlet and outlet. It was observed that inlet and outlet are displaced to each other which lead to an incline connection channel. It is assumed that the acrylic glass bends while galvanization leading to the incline and displacement [Gri18]. This also leads to a high rejection rate of 60 % to 80 % [Bon20]. In the following years until today, a series of optimizations were studied and changes to the process were applied leading to an intermediate production process as described by D. Bonaventura [Bon20].

Optimizations in the Copper Nozzle Production in Münster since 2020

The given nozzle production technique as derived in [Bon20] and utilized in this thesis not only uses an outlet negative but also an inlet negative. Both negatives are fabricated by the mechanical workshop out of an aluminum alloy, are vaporized with a thin silver layer (approximately $500\,\mathrm{nm}$), and are then aligned axially as well as at a distance below approximately $0.1\,\mathrm{mm}$ within a holder made by 3D printing. (In principle a distance of $0.3\,\mathrm{mm}$ should be sufficient, but would not be reliable enough.) This can be seen in fig. 4.9, top. Here, already the later introduced auxiliary anode can be seen. In the holder, also the electrical connection is ensured. This can then be placed in a sulfuric acid copper bath together with two copper anodes where the galvanization takes place over a time period of one to two weeks. Within this time period one needs to check the workpiece at least twice a day, later on only every second day to keep the bath properties in the desired range. After a few days the auxiliary anode is removed. Snapshots are shown in fig. 4.9, bottom. The post-processing is then again performed by the mechanical workshop of the nuclear physics institute. For all produced nozzles the "small" outer nozzle geometry was chosen. The galvanized workpiece within [Bon20] and also the first three of this thesis were cut along the nozzle axis to check the derived inner geometries. Only if this cross section fulfills the desired boundary conditions the production of nozzles can start. Due to the inside notch of the narrowest nozzle section where the inlet and outlet nearly meet the copper ions are not redelivered fast enough. Thus, combustion occurs here, leading to a rough inner surface which would probably degrade the performance of fabricated nozzles. That is why in [Bon20] an additional ring-shaped copper anode surrounding the inlet-outlet connection was proposed enhancing the copper deposition here and thus reducing the combustion, as often suggested by galvanization booklets [Jel13]. The first attempt in [Bon20] was not successful which is why these ring-shaped auxiliary anodes were studied in this thesis together with M. Weide [Wei21].

The explicit geometry and position of an auxiliary anode needs to be determined. Due to the very elaborate galvanization process testing every possibility would not be target-orientated. Instead together with M. Weide [Wei21] several simulation studies on geometry and position of the auxiliary anode were performed in OpenFOAM, ParaView, and Python. The trajectories of single copper ions are calculated based on the given electrical field. From this the end point at the nozzle negatives are obtained from which the relative local growth rate can be derived.

Starting first with ions from the two anode plates without an auxiliary anode, one can see that the ions are deflected away from the narrowest diameter as visualized in fig. 4.10

Figure 4.9: Example of a galvanization process, here for the cross section Q2103. *Upper left:* Adjustment of the two nozzle negatives under a microscope. The inlet negative (left) is fixed while the outlet negative (right) can be adjusted in distance and in both directions. *Upper right:* Placement of the auxiliary anode close to the narrowest diameter. As only ions from the inner face of the ring should detach, a yellow insulation lacquer covers the other faces. It is also used to attach the ring to the holder as there is no dedicated fixture. This piece is then galvanized. *Lower left:* Galvanized workpiece after a few days. The auxiliary anode is removed. Only a small notch close to the narrowest diameter of the nozzle forms which is already an improvement to previous galvanizations. The even and shiny surface shows that the bath properties were kept in the right range. *Lower right:* Final galvanization workpiece. The outer geometry is now manufactured by the mechanical workshop.

(upper left). This corresponds to what is observed in the experiment: at the connection between inlet and outlet negative where later on the narrowest diameter is located, a notch forms. By adding an auxiliary anode the ions are even more deflected away (see fig. 4.10, upper right), but this anode also generates ions leading to a presumably better result. Still, the anode plates are needed to maintain the copper ion concentration of the bath. The additional workpiece movements and also the bath composition is of relevance, not only the ion trajectories.

Testing now different auxiliary anodes, M. Weide simulated 50000 ions to start at the tested anode which then travel to the nozzle negatives For the optimal auxilliary anode geometry this is shown in fig. 4.10, lower left. The positions at which the ions reach the negative are filled into a histogram (see fig. 4.10, lower right). With varying position, inner diameter, and thickness of the ring tested as auxiliary anode the resulting histogram with the positions at the nozzle negative vary. Most favorable is the geometry leading to the most ions close to the narrowest diameter, which is a ring with inner diameter of 2 mm and a width of 1 mm at a position close to the narrowest diameter but slightly shifted to the outlet.
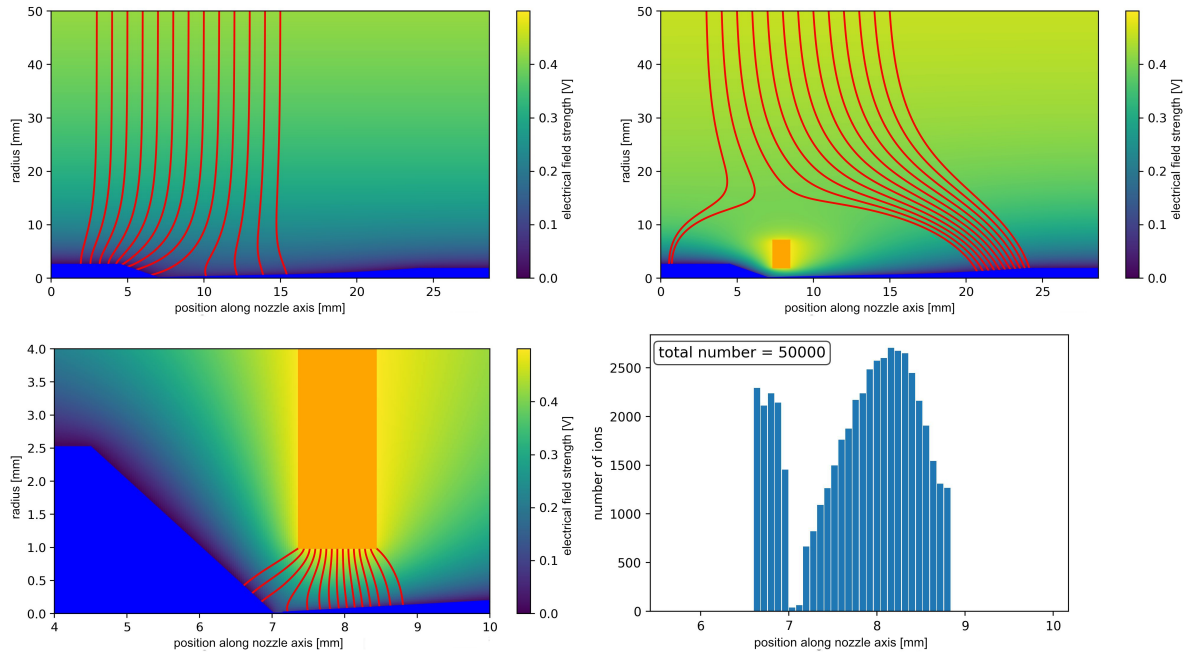
Figure 4.10: Exemplary simulation results obtained together with M. Weide [Wei21], edited.
The color code shows the electrical field strength while in blue the nozzle negatives and in
orange the auxiliary copper anode is shown. *Upper left:* Simulating 13 ions starting at the top
at the anode plate they are accelerated towards the nozzle negative as can be seen with their
red trajectories. Close to the nozzle negatives they are deflected and are preferably deposited
at protruding edges rather than the inside notch at the narrowest diameter. *Upper right:*
When adding an auxiliary anode the ions from the plate anodes do not reach the narrowest
diameter. Still, they are needed to re-deliver copper ions and thus maintain the favorable
bath properties. *Lower left:* Especially ions starting from the inside face of the ring anode
reach the narrowest diameter. Thus, later at the galvano process the other faces are covered
with insulation lacquer. *Lower right:* Histogram of the obtained deposition position of 50000
simulated ions starting from the inside face of the auxiliary anode. At $7\,\mathrm{mm}$ the narrowest
diameter is located. Here, directly no ions can accumulate in the simulation since there is a
small gap between inlet and outlet. Still, in close proximity most of the ions are deposited.
This is the best obtainable result using an anode with an inner diameter of $2\,\mathrm{mm}$ and a width
of $1\,\mathrm{mm}$ at a position close to the narrowest diameter but slightly shifted to the outlet.

Together with [Wei21] two galvanization processes each lead to a cross section of the
galvanized workpiece and one galvanization process had to be terminated. Afterwards,
a further galvanization workpiece was cut in half. Together with the first galvanization
of D. Bonaventura [Bon20], these four cross sections are depicted in fig. 4.11. With
these the optimizations derived in this thesis will be explained in the following.

The first cross section, manufactured in [Bon20], shows significant combustion. Remedy
is an auxiliary anode whereas a first version is tested in *Q2101*. Here, an auxilliary
anode with an inner diameter of $4\,\mathrm{mm}$ and a width of $1\,\mathrm{mm}$ is placed centrally around
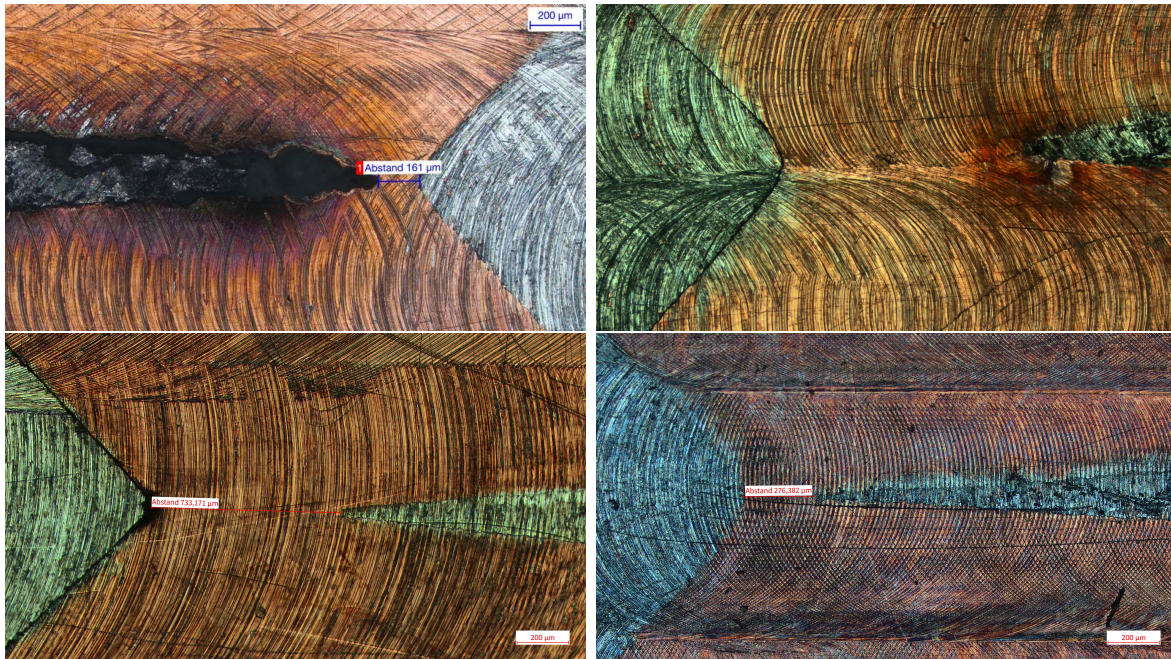
Figure 4.11: *Upper left:* Cross section manufactured in [Bon20]. In silver the negative aluminum molds are visible surrounded by copper. Here, no auxiliary anode was used leading to large combustion at the tip of the outlet negative (left) which is recognizable by the dark color and the cavities. *Upper right:* Cross section Q2101 as in [Wei21]. Using an auxiliary anode reduces the combustion. *Lower left:* Cross section Q2102 as in [Wei21]. The adaption of the auxiliary anode prevents all combustions. Unfortunately the distance between inlet and outlet is too large to be connected by micro drilling. *Lower right:* Cross section Q2103. All parameters are within specifications: No combustion visible, necessary drilling depth is below $300\,\mu m$, and it is homogeneous copper workpiece without cavities.

the narrowest diameter. The combustion is reduced but still the color of the copper surrounding the outlet negative is too dark. With the optimized auxiliary anode derived from simulations (smaller inner diameter of $2\,mm$, width of $1\,mm$, slightly shifted to the outlet; as shown in fig. 4.10), a very significant notch forms in the galvanization process at the narrowest diameter, which leads to the rejection of this workpiece and auxilliary anode. Probably, the inner diameter is to small for the bath and, e.g., its gloss additives, to be redelivered to the narrowest diameter. Going back to the auxilliary anode with an inner diameter of $4\,mm$ as for the Q2101, a placement with a small shift to the nozzle outlet is promising in the simulations. The nozzle cross section *Q2102* from this galvanization shows no signs of combustion. Unfortunately, the 3D printed holder absorbs water and expands, even though it was put into water before the alignment. This leads to an increase in distance between aligned inlet and outlet while galvanization. Possibly also the alignment itself was not optimal. A further optimization is applied in changing the inlet negative slightly, which results in a reduction of the notch and a rounding of the corner. Additionally the bath

Table 4.1: Ingredients of the Copper-Galvanobath. Compared to previous nozzle production processes only 90 % of the bath is used leading to a lower bath height and thus less space beneath the nozzle.

ingredient	amount
H_2O (de-ionized)	900 ml
copper sulfate ($CuSO_4$)	252 g
sulfuric acid (H_2SO_4)	72 g
salt (NaCl)	78.3 mg
thiourea (CH_4N_2S)	7.02 mg
gloss additive LED-A	9 ml
gloss additive LED-B	13.5 ml

level is reduced. The bath composition is listed in table 4.1. This leads to less space beneath the nozzle and thus less deposition at the nozzle inlet, which is at the bottom whilst galvanization. With the last cross section *Q2103* the alignment was performed even more carefully which resulted in a distance between inlet and outlet negative of 276 µm which can be drilled. With this the requirements on the galvanization process are fulfilled. Since a few things additional to the auxilliary anode were changed, at this point again the galvanization without an additional ring anode was tested. Since there is no dedicated fixture for the ring and it needs to be coated with insulation lacquer, this would significantly reduce the preparation time. However, the galvanization process shows a significant notch at the narrowest section. Thus, the auxiliary anode is definitively needed. Next step is the production of "real" nozzles.

At first, two nozzles were galvanized parallel resulting in nozzle *S/N 2021-01* and nozzle *S/N 2021-02*. Until the micro drilling process everything seemed fine. However, the surface the nozzle inlet negative leaves is quite rough. To remedy this, a very short pilot drill with $\varnothing 30$ µm is used first to even the surface out. Afterwards the fragile $\varnothing 30$ µm drill with a drilling depth of up to $10 \cdot d = 300$ µm is used. Due to the large ratio of drilling depth to diameter together with a drilling diameter in the order of the machine precision this step is quite challenging. This brings that much stress onto the drill to shatter. After a few tries the remainders of the drill were locked in the nozzle inlet so that it was no longer possible to drill again. The unfinished nozzle was then kept upright and nitric acid was gradually dripped into the inlet to etch a channel to the outlet. This was regularly interrupted to see if the connection is formed. Since this process is not easily manageable, the resulting diameters are in the range of 100 µm instead of the desired 30 µm.

Even with some experience, the process of assembling the negatives, the auxiliary anode and the electrical connection into the holder, coating parts with the insulation lacquer,

Table 4.2: Eight nozzles were produced within three batches from in total 13 galvanized work pieces. Five of these nozzles have diameters in the desired range (2202 nozzle and batch of 2023) while three were fully tested at the MCT-Prototype.

year of batch	final nozzles	omitted nozzles	technique
2021	2021-01 and -02	0	with etching
2022	2202 and 2203	1	one drilled, one etched
2023	2301 to 2304	4	with radial shift

and starting the galvano bath in total one working day is needed. Together with the coating of the negative molds and the daily checks on the growing galvano workpiece an immense amount of time is necessary not even taken the time of the mechanical workshop into account. Here, several tries of drilling the connection failed due to the rough inner surface of the nozzle inlet.

At this point a look back to the CERN production lead to getting back to the basics and simplicity. Galvanizing only the outlet cuts the workload at least in half: no aligning, no inlet and auxilliary anode fabrication, and the galvanization process is faster and does not need as much monitoring. On the other hand, the inlet needs to be found before drilling. In the first batch of outlet only galvanization three negatives were galvanized. At first, a 90° inlet with a depth of 1 mm was drilled. The geometry of the drill leaves an uneven surface in the center which was smoothed out with a $\varnothing 100\,\mu m$ drill. Then, the $\varnothing 30\,\mu m$ pilot drill smoothed the surface for the last drilling step of $\varnothing 30\,\mu m$ for the connection. The first nozzle 2201 was not successful, but the nozzle 2202 was obtained with an nearly perfectly circular narrowest diameter close to 30 µm. For the third nozzle, the 2203, the drill again shattered, leaving remainders in the nozzle. With the etching process, again a narrowest diameter of approximately 100 µm was obtained. Thus, from this production line, the two nozzles *2202* and *2203* were fabricated out of three galvanizations.

As drilling the $\varnothing 30\,\mu m$ still resulted mostly in breaking the drill, another method is tested. Since the inlet needs to be drilled anyway, the conical drill is advanced in steps. After a few tens micrometer the nozzle is viewed under a microscope to see if the outlet was reached. If not, additional tens of micrometer are drilled. From this process, the four nozzles *2301*, *2302*, *2303*, and *2304* result with additional four rejections where the outlet was not reached.

During the course of this thesis eight nozzles were produced successfully. With intermediate testing in total 17 nozzle inlet negatives were used, whereas only 13 nozzle galvanization processes were finished. This leads to a rejection rate of in total 36 %. Here it is to note, that only five of the eight nozzles are in the right narrowest diameter

range and from these only three were tested in the MCT-Prototype for highest densities. Currently, two of the "too large" nozzles are in operation at the droplet target for the droplet jet bending tested in [Fro24, Hau24, Man24]. Importantly, eight out of 13 nozzle productions were successful and can be used for de Laval nozzle studies and/or for gas- or cluster-jet experiments. Also, they can be used for other fluids like argon or carbon dioxide. Compared to the previous rejection rate of 60 % to 80 % a significant improvement was obtained. Furthermore, the production process is now totally in-house so that every challenge emerging can directly be tackled. This is also one reason why the rejection rate decreased.

Additionally, an orifice with conical inlet and a diameter of 30 µm which is commercially available is welded in a copper workpiece with the desired outer geometry and tested. This orifice nozzle thus has no diverging outlet. The fabricated nozzles are now to be optically assessed and tested at the MCT-Prototype to evaluate their quality.

4.3 Investigating Nozzle Properties

As several nozzles were successfully produced in the previous section, now it is important to test their quality. There are several quantities with which nozzles can be characterized: E.g., the narrowest diameter, the visual appearance of the cluster-jet within the skimmer chamber, and most importantly the highest achieved thickness. All these characteristics as well as several others depend on each other. The visual appearance of the cluster-jet, e.g., displays if a core beam is present which significantly enhances the available thickness. Now, for studying the manufactured nozzles, they are installed at the MCT-Prototype where images of the cluster-jet are taken and velocity spectra and density measurements are performed. For comparison also the properties of the already existing A19 nozzle and the Düsseldorf nozzle (DD-nozzle; long time used for experiments in Düsseldorf) are compiled.

Additionally, studies on core beams and the angle dependence are performed with two nozzles. Also the outer nozzle geometry and its influence on heat transfer is investigated.

4.3.1 Comparing Produced Nozzles

In testing the produced nozzles there are dedicated steps in which the assessment is most useful. First, having a look at the inlet and narrowest cross section with light microscopy is the easiest step (see fig. 4.12 for the 2202 nozzle). Anomalies in the inlet
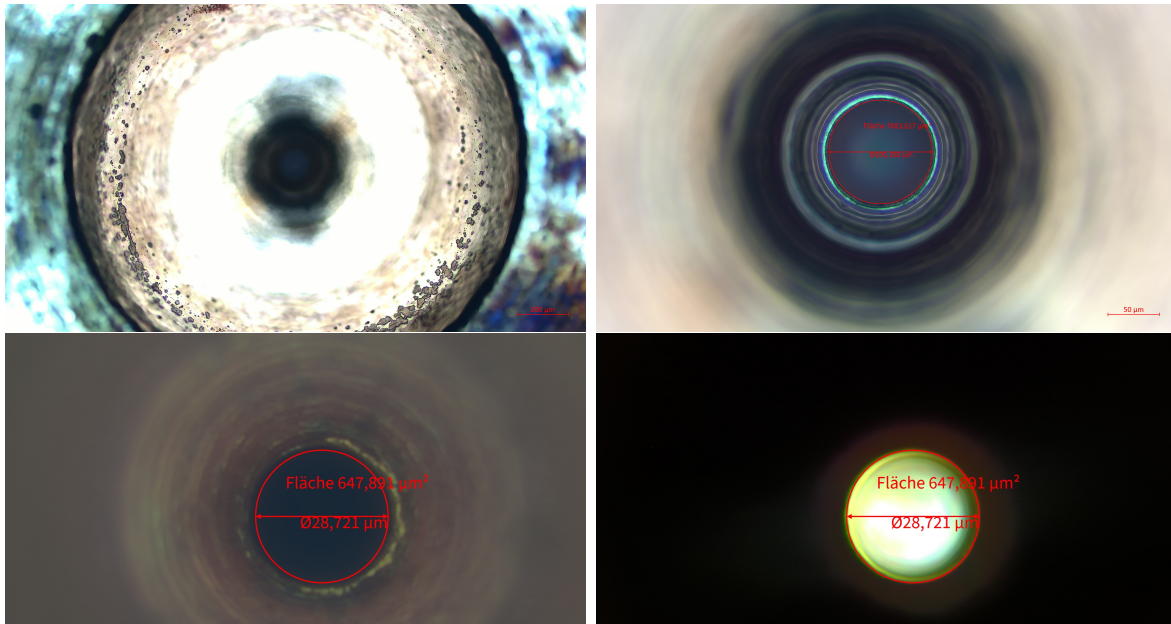
Figure 4.12: Microscopic images of the 2202 nozzle. *Upper left:* Nozzle inlet. *Upper right:* Step within the nozzle inlet due to the additional 100 μm drilling. *Lower left and right:* Narrowest section illuminated with incident and with transmitted light. The narrowest cross section forms a perfect circular shape. The estimated nozzle diameter is 28.7 μm which is interestingly slightly smaller than the diameter of the drill.
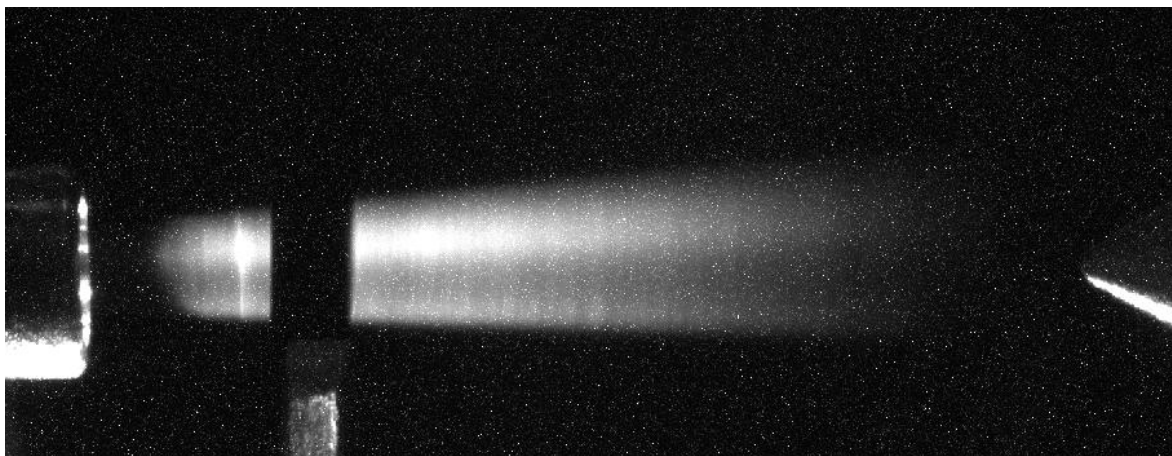
Figure 4.13: Cluster-jet resulting from 2202 nozzle at 24 K and 16 bar within the skimmer chamber. On the left the nozzle exit is visible, in the lower left the nozzle shutter can be seen blocking parts of the illumination from below. On the right the skimmer tip is visible. Slight core beam structures are visible as the cluster jet is more collimated and more intense in the center.

can be detected and the narrowest diameter can be measured. The derived diameters are listed in table 4.3. For the third batch of produced nozzles (2301-2304) a radial shift of the inlet center to the connection to the outlet is apparent (see fig. 4.14). This can be traced back either to machine tolerances or a asymmetry in the nozzle outlet negative used in galvanization, which both result in a shifted inlet. The shift is only 2 to 3 times the narrowest diameter. Hence, there is the possibility that this does not effect the resulting cluster-jet. When the diameter is close to the desired $30\,\mu\mathrm{m}$ the nozzle is tested in the MCT-Prototype. Here, a visual evaluation of the resulting cluster-jet with liquid hydrogen being upstream to the nozzle gives a first impression. It is important, that a stable jet forms without any disturbances perpendicular to the propagation direction as, e.g., observed for the glass nozzles. Within the first liquefying process after cooling down from room temperature instabilities are typical whereas the cluster-jet typically becomes stable over time. For highest densities, a core beam needs to be visible, as can be seen in fig. 4.13 for the 2202 nozzle and slightly in fig. 4.15 for the 2302 nozzle. After a few days of operation, partly in the liquid regime, a reproducible stable cluster-jet is obtained and a density mapping is conducted. Here, several stagnation conditions are set and the velocity, density, and thickness of the resulting cluster-jet are measured. The obtained values for all produced and some already existing nozzles are listed in appendix A. Again, most important is the highest achievable density and thickness, which is thus listed in table 4.4.

Evaluating now the success of the nozzle production, we start with the simplest nozzle consisting only of an orifice in a dedicated holder. No real cluster-jet is formed and the obtained thickness in a distance of $2.1\,\mathrm{m}$ is very small (order of $10^{11}\,\mathrm{atoms/cm^3}$). This nozzle geometry is used in droplet targets with much smaller pressures. There, the liquid filament leaves the nozzle. For the operation with higher pressures in the liquid regime as typical for CJTs this geometry is omitted, leading to the conclusion that the nozzle outlet has a significant role in the cluster production process.

The glass nozzles tested obtained a better result. Within the gaseous regime, the same behavior with similar densities and velocities as previous copper nozzles have been observed. Unfortunately, no stable cluster-jet from liquid hydrogen can be formed. Thus, for MCTs these nozzles are no alternative to copper nozzles. Still, with other fluids or for other experiments where an operation in the gaseous regime is desired, they are perfectly suited. Also for the operation at droplet targets with coflowing gas they should be reconsidered.

The three copper de Laval nozzles produced and tested all delivered a stable cluster-jet. The density is comparable to other nozzles fabricated before this thesis (A19 nozzle and

Table 4.3: Properties characterizing different nozzles. Important are the narrowest nozzle diameter and the radial shift observed for some nozzles. The nozzle diameter can be determined either with optical microscopy in transmitted light or with the flow of hydrogen when installed at, e.g., the MCT-Prototype. At room temperature the flow is rather small so that the calibration of the flow meter is not guarantied. For different nozzles there are different discrepancies between the 290 K and the 50 K measurement. At 290 K the accuracy is enough to check the proper sealing, whereas at 50 K the real diameter is obtained.

nozzle	narrowest diameter determined with...			radial shift of narrowest diameter
	... microscopy	... flow through the nozzle at		
		290 K, 5 bar	50 K, 5 bar	
2021-01	66.2 µm	x	x	x
2021-02	97.3 µm	x	x	x
2202	28.7 µm	27.3 µm	24.5 µm	x
2203	106.5 µm	x	x	x
2301	45.6 µm	x	x	124 µm
2302	34.7 µm	43.3 µm	31.4 µm	67 µm
2303	41.5 µm	52.7 µm	43.5 µm	99 µm
2304	47.1 µm	x	x	137 µm
orifice	31.4 µm	39.8 µm	28.8 µm	x
glass	34.6 µm	34.0 µm	29.9 µm	x
DD	37.6 µm	46.5 µm	36.4 µm	x
A19	35.5 µm	41.9 µm	34.8 µm	x

Table 4.4: Maximal measured volume densities and thicknesses (in a distance of 2.1 m) for the tested nozzles at different stagnation temperatures and pressures together with the core beam visibility.

nozzle	max. volume density [atoms/cm^3]	max. thickness [atoms/cm^2]	core beam(s) visible
2202	$(1.0 \pm 0.1) \times 10^{14}$	$(1.2 \pm 0.1) \times 10^{14}$	yes
2302	$(4.6 \pm 0.1) \times 10^{13}$	$(5.5 \pm 0.1) \times 10^{13}$	slightly
2303	$(1.1 \pm 0.1) \times 10^{14}$	$(1.3 \pm 0.1) \times 10^{14}$	no
orifice	$(7.1 \pm 0.4) \times 10^{11}$	$(9.6 \pm 0.5) \times 10^{11}$	no / only spraying
glass	$(4.5 \pm 0.2) \times 10^{13}$	$(4.9 \pm 0.3) \times 10^{13}$	only gas(-like)
A19	$(2.4 \pm 0.4) \times 10^{14}$	$(2.5 \pm 0.1) \times 10^{14}$	yes
DD	$(2.1 \pm 0.1) \times 10^{14}$	$(2.3 \pm 0.1) \times 10^{14}$	yes
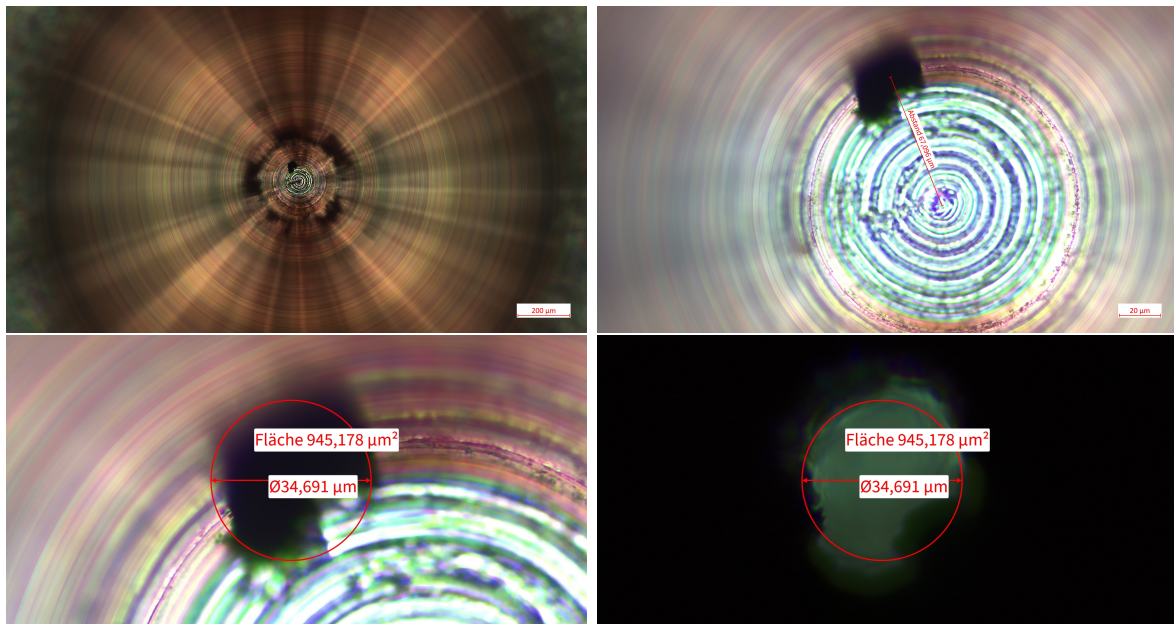
Figure 4.14: Microscopic images of the fabricated nozzle 2302 *Upper left:* Nozzle inlet. Centered circles show the traces of the conical drill. *Upper right:* Enlargement of the center of the inlet. Due to the illumination with incident light, the connection to the outlet, which forms the narrowest cross section is black. It can be seen that this narrowest section is not centered as desired but shifted radially by 67 μm. *Lower left:* Enlargement of the narrowest section illuminated with incident light. *Lower right:* Enlargement of the narrowest section illuminated with transmitted light. The narrowest cross section does not form a circular shape but has an irregular shape. The estimated nozzle diameter is 34.7 μm.
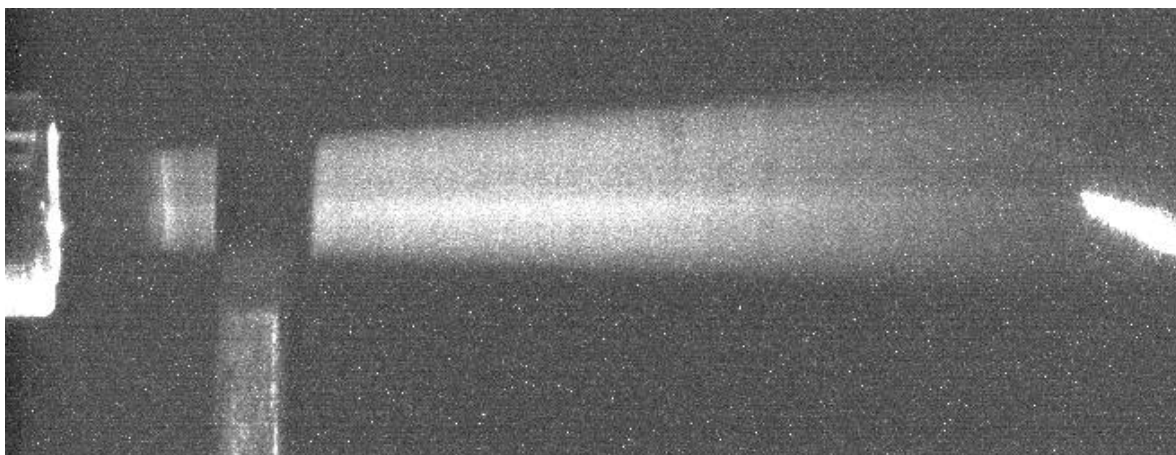
Figure 4.15: Cluster-jet resulting from nozzle 2302 at 24 K and 12 bar within the skimmer chamber. On the left the nozzle exit is visible, in the lower left the nozzle shutter can be seen blocking parts of the illumination from below. On the right the skimmer tip is visible. Only slight core beam structures are visible.

Figure 4.16: The two different outer nozzle geometries and the adaption with a nozzle adapter are depicted. *Left:* Small nozzle 2202 in nozzle adapter with the tightening nut aside and large A19 nozzle. The A19 nozzle was shortened in [Ves18], so that it only has a total length of 14 mm. *Right:* CAD drawing of a small nozzle in the nozzle adapter. Nozzle adapter and large nozzle can be placed in the nozzle holder within MCTs. The sealing for all nozzles used in this thesis and the nozzle adapter is made of polyimide. For other nozzles, e.g., the CERN nozzle a sealing with indium is foreseen. The small nozzle is sealed in the nozzle adapter with a further polyimide layer and tightened with a nut.

Düsseldorf nozzle) while the desired density achieved with the CERN nozzle was still missed by an order of magnitude. One important aspect to reach these high densities is the presence of core beams. The three tested nozzles partly showed these structures which is also an important step. These core beams need to be analyzed further for additional optimizations in the nozzle production techniques.

As next step a compound nozzle is proposed, using the orifice used for the simple orifice nozzle and combining it with a nozzle outlet obtained from galvanization. For this, the nozzles of the 2023 batch which could not be turned into final nozzles are used. These nozzles are tested in [Wei24], where M. Weide will further study and optimize the nozzle production process. Furthermore, for all nozzle batches a major challenge is to find the nozzle outlet either with the inlet negative or with the inlet drilling. Thus, generating the narrowest diameter is a major challenge. Since this seems to not depend on the process used further investigation on the outlet negatives used for galvanization seems to be interesting and will also be performed in [Wei24].

The most important result obtained regarding nozzle production is the production process being totally in-house. With this, every aspect of the final product can be studied and varied.

4.3.2 Influence of the outer Nozzle Geometry

The outer geometry can vary between the "small" and "large" outer nozzle geometry (see fig. 4.16). Since for the cluster production, the outer geometry is of no relevance, new nozzles are fabricated with the smaller outer nozzle geometry. As advantage, one

production step is omitted. However, for the installation at MCTs a nozzle adapter is needed, which is also shown in fig. 4.16. With the adapter, changing the nozzle in the MCT is simpler, which is a further advantage. On the other hand, with this adapter an additional heat barrier is introduced between nozzle and cold head. Important to answer is, if this additional heat barrier has a negative influence on the target performance.

Generally, when a nozzle temperature is set, the desired temperature is maintained at the temperature diode placed at the cold stage of the cold head and the heating power of the heating cartridge close by is varied accordingly. Shortly after, the temperature controlled fluid reaches the nozzle, so that only a small temperature difference can be present, depending on external heating effects and the heat conductivity between cold head and nozzle. When studying the different nozzles, it was found that the heating power differs between the nozzle shutter being closed or open. It is apparent, that the cold cluster-jet is reflected from the closed nozzle shutter onto the nozzle, leading to an additional cooling and thus an increase in heating power. This increase in heating power thus gives an estimation on the heat conductivity between the cold head and the nozzle. The measurement was performed with the A19 nozzle and the 2202 nozzle so that the difference based on the outer nozzle geometry can be studied.

In order to normalize the difference in heating power Δh, two differences of the two studied nozzles can be taken into account: First, the A19 nozzle has a larger narrowest diameter, which results in a larger flow f through the nozzle, which further results in an increased cooling by the reflected clusters. Second, due to the placement of the smaller 2202 nozzle in the nozzle adapter, the nozzle outlet is closer to the nozzle shutter, leading to a smaller distance for the clusters to be traveled. This results in a smaller spread of the cluster-jet and thus a larger cooling power for the given nozzle area which is not covered by the stainless steel holder plate, which is only a simple assumption. Since the cluster-jet expands radially with the distance a, the area is proportional to a^2 and the cooling power thus is proportional to $1/a^2$.

The measured values are listed in table 4.5. Assuming at first, that the distance between nozzle and nozzle shutter has no relevant influence, $\Delta h/f$ equals $0.303\,\mathrm{W\,min/l_n}$ for the A19 nozzle and $0.499\,\mathrm{W\,min/l_n}$ for the 2202 nozzle, which gives an unexpected result: the heat conductivity for the large outer nozzle geometry is smaller than for the small geometry with adapter. Taking now the distance into account, the values of $\Delta h \cdot a^2/f$, which is $9.26\,\mathrm{kg\,m\,s^{-2}}$ for the A19 nozzle and $0.48\,\mathrm{kg\,m\,s^{-2}}$ for the 2202 nozzle show the smaller heat conductivity for the 2202 nozzle due to the placement in the nozzle adapter. The additional copper work piece and polyimide sealing as heat barrier hinder the heat transfer between the cold head and the nozzle. Thus, it may be assumed that

Table 4.5: Comparison of the heating power with open and closed nozzle shutter for the A19 nozzle and the 2202 nozzle. Full power of the heating cartridge ($100\,\%$) equals $50\,\mathrm{W}$. The difference in nozzle flow f and in distance between nozzle shutter and nozzle a is accounted for in an empirical approach.

|	A19	2202
closed shutter	$(20.5 \pm 0.5)\,\%$	$(27.5 \pm 0.7)\,\%$
open shutter	$(15.8 \pm 0.5)\,\%$	$(24.4 \pm 0.7)\,\%$
difference Δh	$4.7\,\%$	$3.1\,\%$
difference in W	$2.35\,\mathrm{W}$	$1.55\,\mathrm{W}$
nozzle flow f	$7.75\,\mathrm{l_n/min}$	$3.11\,\mathrm{l_n/min}$
distance a	$22.5\,\mathrm{mm}$	$4.0\,\mathrm{mm}$
$\Delta h/f$	$0.303\,\mathrm{W\,min/l_n}$	$0.499\,\mathrm{W\,min/l_n}$
$\Delta h \cdot a^2/f$	$154.4\,\mathrm{W\,mm^2 min/l_n}$ $= 9.26\,\mathrm{kg\,m\,s^{-2}}$	$8.0\,\mathrm{W\,mm^2 min/l_n}$ $= 0.48\,\mathrm{kg\,m\,s^{-2}}$

the 2202 nozzle is warmer than the temperature measured by the temperature diode located at the cold head.

Since there are differences in the two studied nozzles, which were not taken into account and their influence and even the influence of the considered differences is not definitely known, the extend of the heat shielding has to be measured by calibrating the temperature diode with means of the vapor pressure curve as performed in chapter 5, as already performed for the A19 nozzle together with M. Scharpey [Sch24]. The result of this measurement is an important input for the further development of the nozzle production. If the heat barrier of the nozzle adapter is too large, it has to be returned to the larger outer nozzle geometry.

4.3.3 Studying Core Beams and Cluster-Jet Angle Dependencies

In operating and testing these nozzles, the core beam is one of the quality features. It is directly apparent in observing the cluster-jet in the skimmer chamber. When hunting for highest densities, the angle of the spherical joint is aligned that the core beam is extracted by skimmer and collimator. The questions on where these core beams originate from and subsequently how to produce nozzles with stable core beams are of highest interest. To systematically study this, for two nozzles with core beam structures angle dependent velocity and density measurements were performed.

Together with H. Eick [Eic23] velocity and density of the cluster-jet were measured with an angular tilt of the the Düsseldorf nozzle. One of the measurements is shown in fig. 4.17. For the middle measurement, the density is maximal with the velocity being
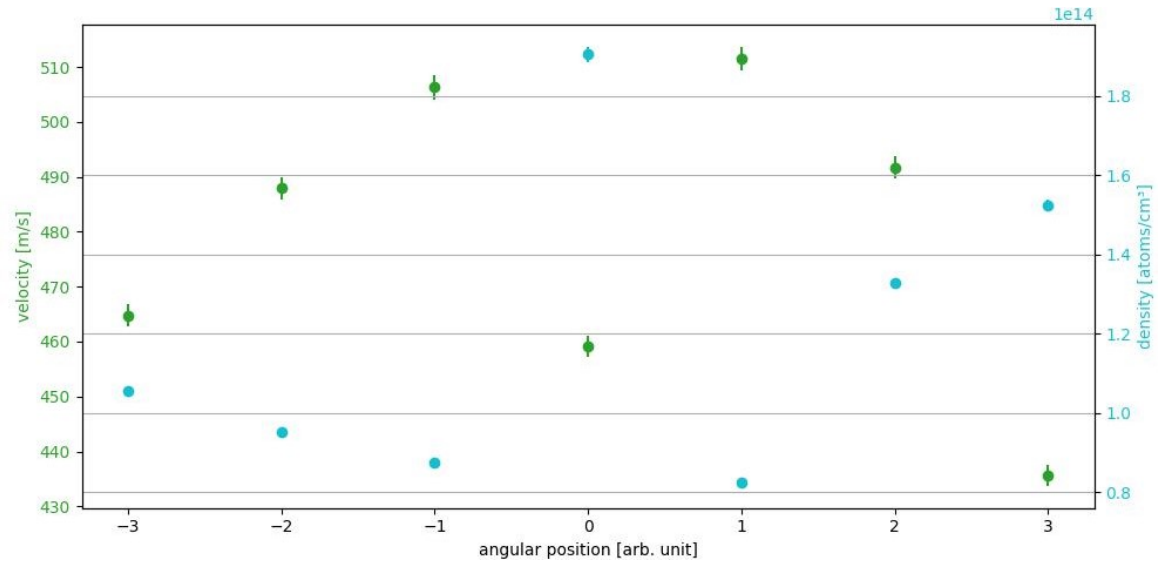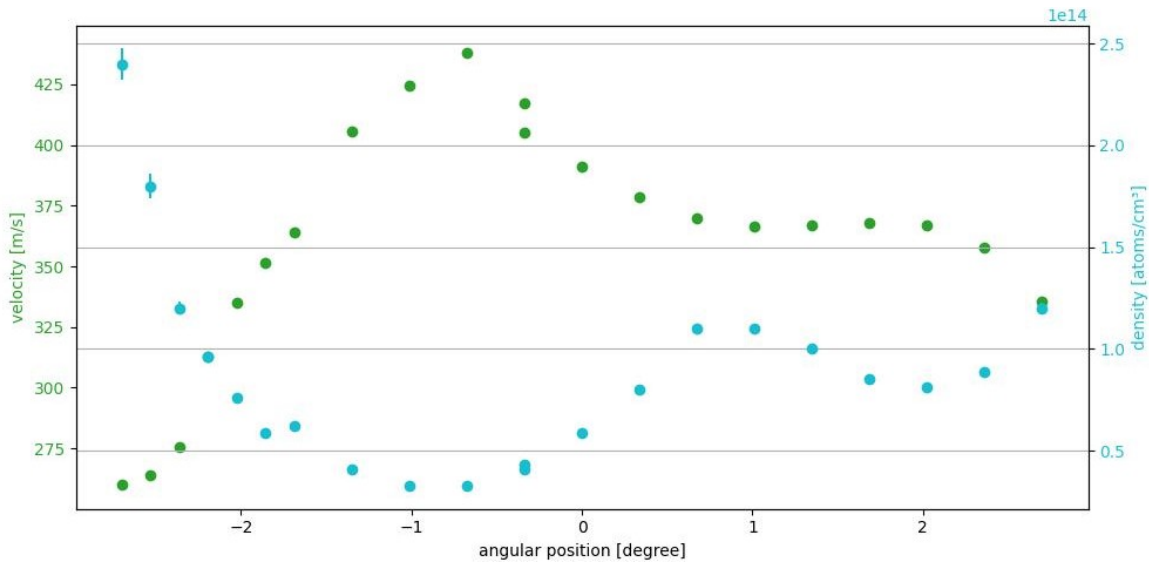
Figure 4.17: Angular dependent measurement of velocity and density of the Düsseldorf nozzle at 24 K and 12 bar. For the center measurement a significant step towards a large density and a small mean velocity is apparent. Data obtained with H. Eick [Eic23].

minimal. Here, the core beam is extracted. This gives the idea, that the core beam is the same as the residual cluster-jet, but slower, which leads to a larger density and thickness.

This measurement is repeated here with the A19 nozzle with a smaller step size. In fig. 4.18 the density and the mean velocity of the cluster-jet also show the exact opposite course to each other. For the highest density the smallest velocity is measured. Unfortunately, the source cannot be tilted far enough to measure the total core beam. Still, with tilting the source a factor of 5 in density and a factor of nearly 2 in velocity is obtained. This again stresses the importance of a tiltable source. Furthermore, the dependence of density on the velocity is apparent. However, there has to be another influence, since velocity and density are not directly anti-proportional to each other. One possibility are different cluster sizes dependent on the angle.

In [Gri18] the spherical joint allowed for the highest achieved thickness ever with the CERN nozzle. However, there no systematic angular dependent velocity and density studies were performed, so that the velocity was calculated based on [Täs12]. As with this nozzle the most significant core beam structures are apparent, for the future, measuring the angular dependent velocity and density of the CERN nozzle is important in further understanding core beams and also producing nozzles with highest densities.

Furthermore, in the course of this thesis it was observed, that for some nozzles the velocity spectra show double peaking structures as in fig. 4.19. A sharp slow velocity

Figure 4.18: Angular dependent measurement of velocity and density of the A19 nozzle at 24 K and 16 bar. The course of velocity and density is opposite. For the largest density the smallest velocity was measured. Unfortunately, the source could not be tilted further to negative angles, where the core beam was located. Since the measurement was performed over two days, the connecting measurement was performed on both days (slightly below 0°). Important to note is the factor of 5 in density which can be obtained by tilting the source.

peak together with a broader second peak at larger velocities is apparent. After some other measurements the nozzle was installed again at the MCT-Prototype and the same measurement was performed. Here, only one peak with larger velocities was apparent. For both measurements the nozzle was operated for several days in the liquid regime and the flow through the nozzle was the same, meaning only the orientation of the nozzle was changed.

Similar double peaking structures were already found in [Gri18, Köh15, Täs12] but close to the vapor pressure curve. Here, a narrow peak at faster velocities was combined with a broader peak at slower velocities. As interpreted there, this is due to the two cluster production processes within the gaseous and in the liquid regime. In opposition to the
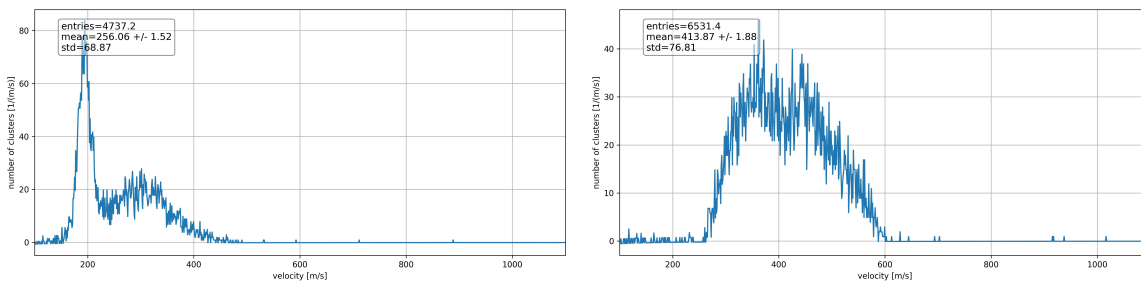
Figure 4.19: Measurement of the velocity of the 2202 nozzle at 24 K and 16 bar. There was some time between the measurements but for both a stable cluster-jet was observable.

measurement in chapter 5 where a clear step-like transition within an interval of $0.1\,\mathrm{K}$ occurred, a region of transition where both processes seem to be running in parallel was observed. Maybe some kind of instability which was not measurable back then lead to the coexistence of fluid and gaseous hydrogen over a broader temperature range. This instability seems to be no longer apparent due to optimizations of the cluster source, since this double peaking structure is not observed within this thesis.

Still, the same concept may be the basis to the double peaking structure observed in this thesis at smaller temperatures. The broad peak in the velocity spectrum is obtained by the cluster production based on atomization as observed for most of the cluster-jet, while for the core beam an other (but maybe still similar) process leads to the narrow peak at smaller velocities. Possible is the atomization at a position closer to the narrowest diameter, where the fluid is not yet accelerated so much or the atomization is performed into larger clusters that are slower with the same kinetic energy. An other possibility is, that a liquid filament is surrounded by already atomized fluid, which could be interpreted as a cluster-jet providing its own coflowing gas. In general, coflowing air (here: atomized liquid hydrogen) leads to an increase in breakup length, due to the decreased relative velocity between the intact core and the coflowing air [LM17].

In [Fra15] a formation of a liquid filament was observed depending on the inlet angle for conical-cylindrical nozzles. For a half-opening angle below 35° a diffuse spray with a small breakup length is obtained. With a half-opening angle of 45° or above a clear filament with a large breakup length is obtained, which further rises above 60°. With the geometry used for MCT de Laval nozzles (inlet half-opening angle of 45°) this decoupling of a liquid filament is possible, whereas an even larger inlet angle would be favorable. However, the influence of the additional divergent outlet is not studied there, but may include the atomization process and/or the proposed possibility of a cluster-jet providing its own coflowing gas.

The general increase in breakup length favors larger cluster sizes [LM17]. This could also lead to smaller velocities for clusters obtained from the primary intact filament (later detected as core beam) and larger velocities for the primary clusters serving as coflowing air (later detected as residual cluster-jet).

To completely determine the reason and effects of core beams and their velocity, an angle dependent measurement of cluster sizes is necessary. Importantly, for the measured region of the cluster-jet, simultaneously the velocity and density needs to be measured to give further insights into the origin of core beams. For this optimally the CERN nozzle will be measured and compared to other nozzles to obtain insights into the differences leading to the world record of target thickness.

4.4 Conclusion of the Performed Nozzle Studies

Elaborate studies on de Laval nozzles have been conducted in this chapter. Starting with the cluster production processes, the differences between cluster-jets originating from liquid or gaseous hydrogen have been presented whereas cluster production in the liquid regime is not fully understood yet. Still, important aspects of the atomization process are obtained.

Glass nozzles have finally been omitted for the use at MCT operating with fluid hydrogen. For droplet targets and CJT operating with gases they are still considered. Within this thesis, copper de Laval nozzles were successfully produced totally in-house for the first time. Additionally, a reduction in rejection rate compared to previous, partly external production batches was obtained. The newly produced nozzles (here: 2202, 2302, and 2303) are comparable in performance to previously produced nozzles (A19 and Düsseldorf nozzle), but still miss an order of magnitude in density compared to the CERN nozzle. This and the rejection rate still not being close to zero, leads to further necessary optimizations in the nozzle production.

In [Wei24] the further optimization in the nozzle production is aimed at. As a first step, a compound nozzle is proposed using a simple orifice with conical inlet welded onto a galvanized copper nozzle outlet. First promising results are obtained there. Which method of copper nozzle production is finally chosen, will probably be determined by M. Weide. [Wei24]

With a totally in-house nozzle production, the influence of the geometry can further be tested. The length of the nozzle outlet seems to have no influence on the performance [Ves18], whereas it is definitely needed for stable cluster-jet operation. Here, the outlet angle would be an interesting variable to study. Furthermore, the inlet angle is promising to have an influence on the core beam generation. Also the influence of the outer nozzle geometry needs to be finally determined by temperature calibration with the vapor pressure curve. The temperature offset for the large outer nozzle geometry was already studied with M. Scharpey [Sch24], but a comparative measurement needs to be performed with a small nozzle to determine the influence of the additional heat barrier of the nozzle adapter.

Important for the final assessment of the nozzle production process is the quality of the nozzles produced. One of the most important factors for this is the presence and quality of core beams. Angle dependent density and velocity studies within this thesis gave insights into their nature. The significantly smaller velocity of clusters in the core beam compared to clusters in the residual cluster-jet hint towards a different but maybe similar cluster production process. For this the angle dependent velocity and density

of the CERN nozzle but also of further newly produced nozzles will be interesting.

In addition to these measurements, the measurement of cluster sizes is very important as it will give further insights into, e.g., the breakup length, and with this into the nature of the cluster production process and core beams, which is further relevant for producing optimal nozzles. The general measurement of cluster sizes is discussed in section 6.1. At this point it is already to note, that the study of cluster sizes should additionally be performed in combination with the proposed angular dependent velocity and density measurement.

Chapter 5

Determination of the Widom Line Using Cluster-Jets

Working with CJTs not only includes investigating their properties and behavior in respect to possible optimizations but also utilizing them, e.g., for characterizing properties of the used fluid. Within this chapter a newly developed method for measuring the widom line is presented. It was conducted at the MCT-Prototype using the TOF setup (see section 3.3.1) in channeltron configuration and the AMS (see section 3.2.1) together with C. Fischer [Fis21] and was first published in [VFK22]. For now, only measurements with hydrogen were performed as thus a proof of principle is given.

5.1 Widom Line and Gas Theory

Each fluid has its characteristic vapor pressure curve, melting point, critical point, and so on. For the operation of a MCT with hydrogen, especially the temperature region $20\,\mathrm{K}$ to $50\,\mathrm{K}$ and pressure region $5\,\mathrm{bar}$ to $20\,\mathrm{bar}$ including the vapor pressure curve is of highest interest (see fig. 5.1). This vapor pressure curve describes a first order phase transition between liquid and gaseous hydrogen and is classically described as ending in the critical point (at $T_c = 33.145\,\mathrm{K}$, $p_c = 12.964\,\mathrm{bar}$ [NIST]). The region above the critical point ($T > T_c$ and $p > p_c$) is commonly referred to as supercritical where a continuous transition from a gas-like to a liquid-like behavior occurs [Bra$^+$11, MS10]. Another possibility is to consider the transition as higher order phase transition. This so-called Widom line is defined as loci of maxima in correlation length [MS10]. The correlation length gives a scale on which atoms in the fluid are correlated; high
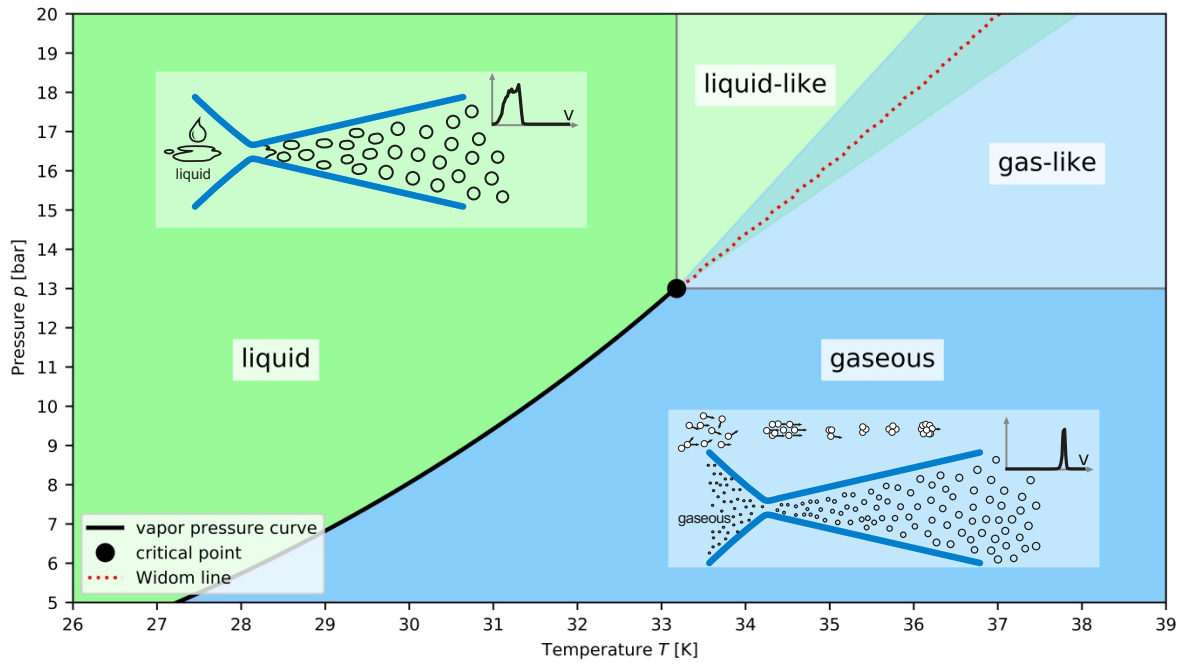
Figure 5.1: pT-diagram with the vapor pressure curve separating liquid (green) and gaseous (blue) hydrogen. The supercritical region above the critical point can be separated into liquid-like (light green) and gas-like (light blue) regions separated by the Widom line (red). The cluster production processes are strongly connected to the phase of the fluid in front of the nozzle. Originally published in [VFK22].

correlation length meaning highly correlated on a large scale, small correlation length meaning only slightly correlated on a small scale. In close vicinity of the critical point all thermodynamical response functions as, e.g., the specific heat capacity, density fluctuations, or the isothermal compressibility are expressible in terms of correlation length. Here, in the so-called scaling region, their local isotherm or isobaric maxima coincide [Bra+11, MS10, Xu+05].

When moving away from the critical point the lines of maxima in thermodynamic response functions diverge from one another and the maxima themselves are smeared and become broader. This region can be described as "Widom delta" [Ha+18]. In [Bra+11] the maxima in thermodynamic response functions were calculated theoretically for Lenard-Jones systems. Here, the single Widom line ends at a temperature 10% above the critical temperature, which is for hydrogen $T = 1.1 \cdot T_c = 36.46\,\mathrm{K}$, while the quantitative results are reported to be sensitive to the type of potential used.

Alternatively, another approach is performed in [PJ05], where it is stated that states with an infinite network of bonded molecules and states with small oligomers are separated by the elongation of the vapor pressure curve. Considering two different definitions of molecule binding, 1000 water molecules are Monte Carlo simulated. It is

stated that with increasing temperature the size difference of these hydrogen bonded clusters of water molecules decreases. This is likely correlated to the smearing of the maxima in the thermodynamic response functions. But, the exact position in the pT-plane of the transition between small oligomers and infinite network is strongly dependent on the details of the definition of the van der Waals binding.

Apart from theory, the experimental determination of the Widom line and its position in the pT-diagram is challenging and dependent on the substance probed.

By utilizing inelastic X-ray scattering (IXS) one can analyze the sound dispersion [Gor$^+$06, Sim$^+$10]. While for liquids it is expected to have a positive dispersion, i.e., increasing speed of sound as a function of wavelength from the continuum limit to the short-wavelength limit, this should vanish as crossing the critical temperature. But, even for the deep supercritical region with $T > 2\,T_c$ and $p > 100\,p_c$ liquid-like behavior was observed [Gor$^+$06], while at $T = 6\,T_c$ and $p \approx 100\,p_c$ gas-like behavior was reported [Sim$^+$10]. It was found that the amount of positive dispersion has a sharp slope crossover transition on crossing the Widom line [Sim$^+$10]. Nonetheless, for the measurement of one pT-point a measurement time of 12 h to 15 h is reported to be necessary, whereas several points are necessary to determine the boundary [SG08].

Further on, studies with small-angle neutron scattering (SANS) have been performed in [Sat$^+$08]. This is used to measure the skewness of the number density distribution of the molecules in the supercritical regime. When applying a reverse Monte Carlo analysis, liquid-like and gas-like regions can be distinguished. Though, these measurements are typically performed at larger, complex accelerator facilities which are needed for the required high-quality neutron beams.

In comparison to these methods, a new and experimentally simple method of determining the position of the Widom line was developed in this thesis. Within section 4.1.1 two completely different cluster production mechanisms for liquids and gases were presented. As the dynamic and transport properties of liquid-like and gas-like fluids differ strongly from each other [Gor$^+$06], the mechanisms of cluster production are extended from the liquid and gaseous region into the corresponding liquid-like or gas-like supercritical region. The properties of the resulting cluster-jets differ strongly. The desired property difference in the use for MCTs in particle physics is the significant increase in cluster-jet density. This is accompanied by an even more obvious difference in velocity distribution as it will become observable in the course of the following measurements. Thus, the cluster-jet density, the mean cluster velocity, and the standard deviation of the cluster velocity are simple and excellent tools to study the phase of the fluid before passing through the nozzle.

5.2 Measurements

For studying the Widom line in total nine isobar measurement series are performed. For each pressure several temperatures close to the vapor pressure curve or the expected Widom line are encountered, close to the phase transition with a temperature stepsize of down to 0.1 K. For each pT-point it is waited for the cluster-jet to stabilize for a few minutes until the density and the velocity distribution were measured. This took approximately 1 h per measurement point. With an upgrade of the TOF setup introduced later on [Sch24], now this measurements only take 10 min or less.

The pressure of the fluid upstream to the nozzle is regulated by a pressure controller. In close proximity to the nozzle a baratron is used to measure the fluid inlet pressure even more precisely. According to its manual, it has an uncertainty of 1% of the measured pressure. The temperature diode utilized by the temperature controller to determine the actual temperature at the nozzle and thus also to regulate it has a calibration uncertainty from the manufacturer of 0.5 K with a reproduction uncertainty of 0.01 K. For determining the exact pressure and temperature, within the measurement time both were monitored and the mean and standard deviation were determined.

Firstly, three isobaric measurement series were performed at $p = 6$ bar, 10 bar, and 12 bar below the critical point crossing the vapor pressure curve. With this, the validity of the measurement principle can be shown at a first order phase transition and a temperature offset can be determined to reduce the systematic error of the temperature determination. In the course of the evaluation it was observed, that the standard deviation of the velocity distribution opposed to the mean velocity and the density of the cluster-jet shows the clearest step at the corresponding phase change temperature. Thus, this is used to calibrate the temperature diode. The three obtained evaporation temperatures can now be compared with the corresponding temperatures from literature [NIST], whereas the uncertainty from literature is neglectable. From this a temperature calibration can be performed by minimizing the deviation from the nominal evaporation temperatures and thus shifting all measured temperatures by (0.31 ± 0.11) K. Hence, an additional uncertainty due to the standard deviation of the mean temperature offset is introduced, which is the largest contribution to the overall uncertainty. This leads to the smallest useful step size in temperature of 0.1 K which could be reduced if the calibration would be improved.

For the explicit measurement of the Widom line, series of isobaric measurements were performed at 13 bar, 14 bar, 15 bar, 16 bar, 17 bar, and 18 bar, above the critical point. With an exemplary measurement at 14 bar which is shown in figs. 5.2 and 5.3 the general procedure of evaluation is presented. It is to note that the pressure controller regulating
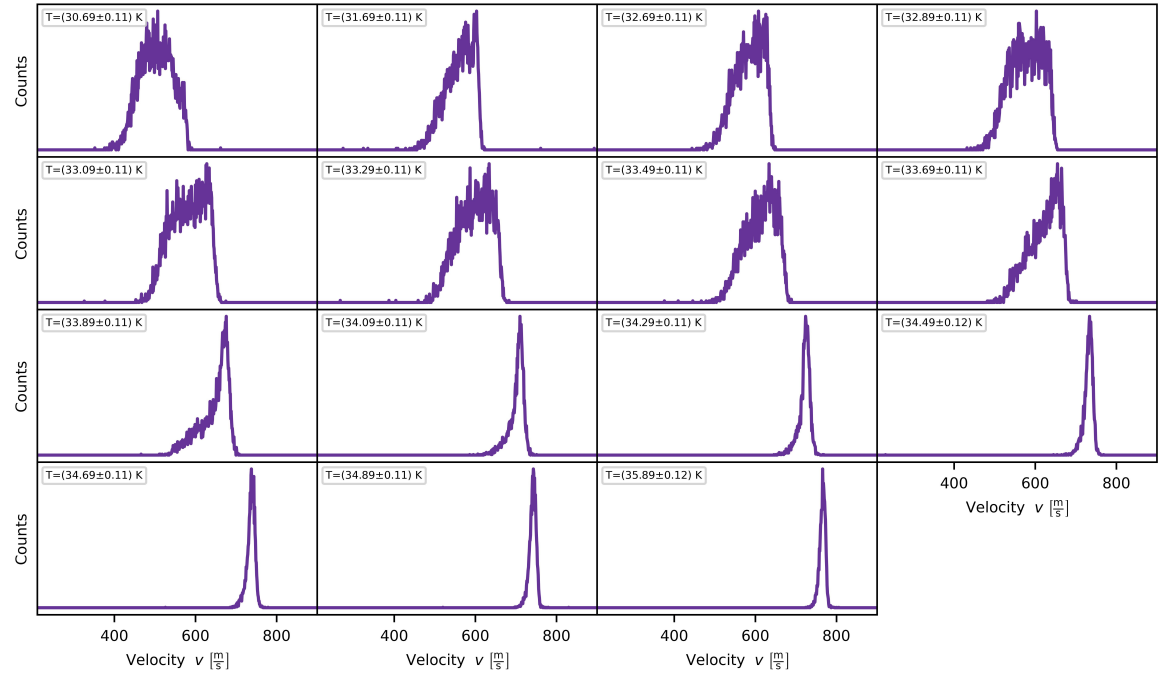
Figure 5.2: Velocity distributions of the cluster-jet with a constant pressure of 14.22 bar and gradually rising temperatures from 30.69 K to 35.89 K (top left to bottom right) as published in [VFK22]. Clearly visible is the increasing velocity and the decreasing standard deviation of the velocity with rising temperature.

the pressure upstream to the nozzle is not calibrated. The obtained pressure measured with the calibrated baratron is slightly above the nominal value, here (14.22 ± 0.15) bar.

Starting with a low temperature of 30.7 K the hydrogen upstream to the nozzle is even liquid. The velocity distribution (see fig. 5.2, upper left) exhibits a broad width with a comparatively small mean value. With rising temperature the velocity distribution becomes gradually smaller in width and shifted to higher velocities until for the highest measured temperature of 35.9 K a very narrow distribution at highest mean values is obtained (see fig. 5.2, lower right). The evaluated standard deviation and the mean velocity of the distribution are plotted against the corresponding hydrogen input temperature in fig. 5.3 in the top and center, respectively. This highlights the steep transition of the respective observable within a temperature interval of approximately 1 K. Thus, the temperature step size of 0.1 K is neglectable to the phase transition interval. Considering the cluster-jet density a similar transition is apparent. With rising nozzle input temperature, the cluster-jet density decreases and at the higher order phase transition a steep decrease is observable (see fig. 5.3, bottom). For some pressures a small increase in standard deviation directly below the transition temperature is
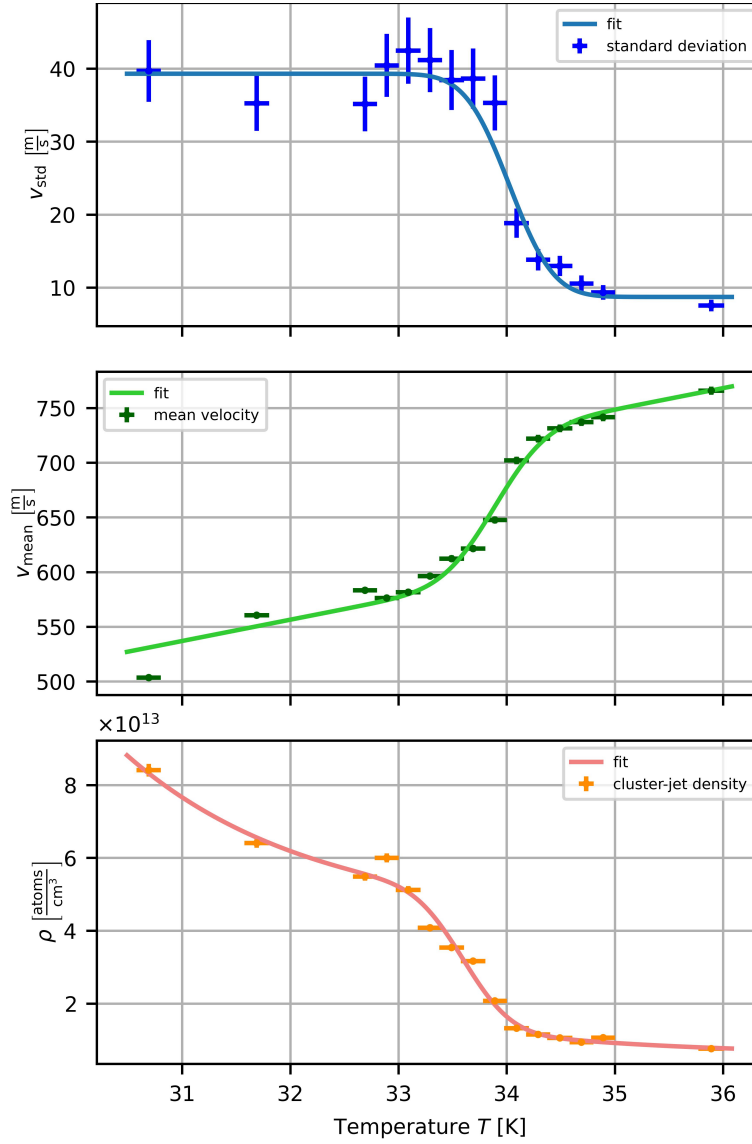
Figure 5.3: Fits of the standard deviation of the velocity distribution (top), the mean velocity (center), and the cluster-jet density (bottom) at 14.22 bar with rising temperature from 30.69 K to 35.89 K as published in [VFK22]. For each individual fit a step-like increase or decrease is observable at approximately 34 K.

observable. Since it is not significant and only present for some measurement series it is not further considered. Regarding the uncertainties, the uncertainty in velocity standard deviation is proportional to the value itself but scaled in a way that the reduced chi-squared χ^2_{red} of the up-following fit equals 1. For the mean velocity and the cluster-jet density the uncertainties are determined by the uncertainty of the TOF-setup and the AMS with taking error propagation into account.

For determining the exact phase transition temperatures the measured values for the standard deviation $v_{\text{std}}(T)$, the mean velocity $v_{\text{mean}}(T)$, and the cluster-jet density $\rho(T)$ must be described by a suitable function each.

In general, the step-like increase (or decrease) can be described with a step function at the transition temperature T_{t}. This step function is convoluted with a Gaussian to account for the limited experimental resolution, the higher order of the phase transition, and the possibility of a "Widom delta". The convolution results in an error function $\text{erf}(x)$ with a smearing parameter s. Apart from the step function with its smearing the general trend of the observables without the presence of a phase transition needs to be taken into account. The velocity standard deviation is for a limited temperature region constant while the mean velocity rises linear close to the phase transition. For the cluster-jet density several different previous studies (e.g. [Gri18, Täs12]) showed a nearly exponential behavior in dependence of the temperature. This results in the empiric fit functions:

$$v_{\text{std}}(T) = A_1 - \frac{B_1}{2} \cdot \text{erf}\left(\frac{T - T_{\text{std}}}{s}\right) \tag{5.1}$$

$$v_{\text{mean}}(T) = A_2 + B_2 \cdot T + \frac{C_2}{2} \cdot \text{erf}\left(\frac{T - T_{\text{mean}}}{s}\right) \tag{5.2}$$

$$\rho(T) = A_3 + B_3 \cdot \exp(C_3 \cdot T) - \frac{D_3}{2} \cdot \text{erf}\left(\frac{T - T_{\text{den}}}{s}\right) \tag{5.3}$$

with A, B, C, and D being further fit coefficients. For the resulting phase change temperatures T_{std}, T_{mean}, and T_{den} the uncertainties are scaled with $\sqrt{\chi^2_{\text{red}}}$. With this an error based on possible wrongly describing fit functions is introduced which could be analyzed in further measurements.

The velocity distributions and the temperature dependent standard deviation, mean velocity, and density as presented here for 14 bar can be found in appendix B for the other measurements series.

Table 5.1: Phase transition temperatures determined with the three presented methods as published in [VFK22]. For subcritical pressures only the velocity standard deviation was used and for 18 bar an instability in the cluster-jet occurred leading to larger uncertainties and the impossibility to determine a phase change temperature with means of the cluster-jet density. Results are also shown in fig. 5.6.

pressure p in bar	phase change temperatures in K determined with...		
	... standard deviation T_{std}	... mean velocity T_{mean}	... beam density T_{den}
6.08 ± 0.06	28.29 ± 0.16	x	x
10.17 ± 0.10	31.39 ± 0.16	x	x
12.19 ± 0.13	32.88 ± 0.16	x	x
13.21 ± 0.14	33.59 ± 0.17	33.39 ± 0.17	33.28 ± 0.17
14.22 ± 0.15	34.03 ± 0.17	33.89 ± 0.18	33.60 ± 0.16
15.25 ± 0.16	34.60 ± 0.17	34.48 ± 0.17	34.21 ± 0.17
16.28 ± 0.17	35.02 ± 0.17	34.92 ± 0.16	34.56 ± 0.16
17.27 ± 0.18	35.47 ± 0.17	35.38 ± 0.17	35.11 ± 0.16
18.27 ± 0.19	35.63 ± 0.35	35.86 ± 0.39	x

5.3 Results and Discussion

Based on the fits, for each pressure measured the phase change temperature T_{t} is determined with the three different methods. The results are given in table 5.1 and later on shown in fig. 5.6 together with the vapor pressure curve and different approximations of the Widom line for hydrogen. For the three measurements below the critical point only the velocity standard deviation was used to determine the phase change temperature, because it was used to calibrate the temperature diode and is thus the only one shown. For the measurement series at 18 bar the cluster-jet became unstable meaning that the core beam changed position and thus a different part of the cluster-jet was used for the following measurements. This leads to larger systematic uncertainties especially in the density measurement and to the omission of the determination of the phase change temperature by the density measurement.

Comparing the results of the three different methods, the phase change temperatures determined by the velocity information, i.e., the standard deviation and the mean velocity differ by only 0.1 K and thus agree within their uncertainties. Using on the other hand the cluster-jet density for the phase change temperature, a difference of up to 0.6 K is obtained. Even though these and the velocity values agree within 2.5 standard deviations, an average systematic shift of 0.4 K ($= 1.7\sigma$) towards lower temperatures is obtained. One possible reason is that the temperature dependence of the cluster-jet density is not accurately described by an exponential formula as this was only an empiric approximation based on previous measurements. Thus, the phase change temperatures based on the cluster-jet density need to be considered as less exact. With an even more elaborate investigation of the cluster-jet density dependence
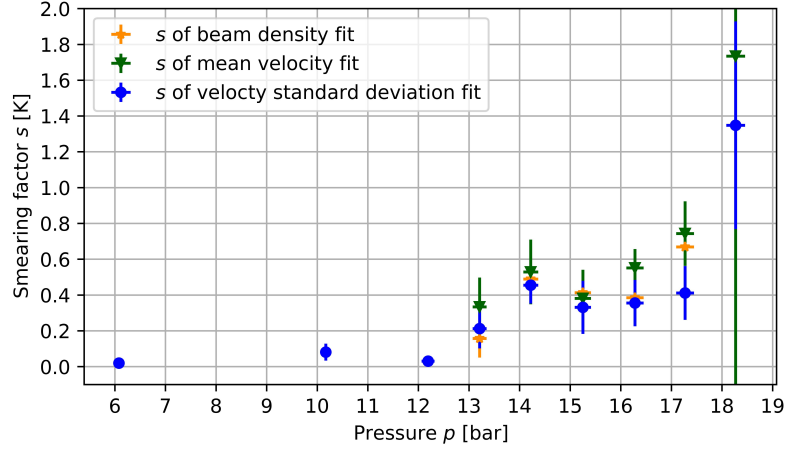
Figure 5.4: Determined smearing parameter s in dependence of the pressure p for all performed fits. The smearing in the subcritical region of below $0.1\,\mathrm{K}$ is reasoned in the chosen temperature step size. Within the supercritical region the smearing rises with rising pressure showing the presence of a higher order phase transition and the formation of a "Widom delta".

on the temperature a more accurate description would be possible.

The determined smearing parameter s, i.e., the width of the Gaussian function convoluted with the step function is shown in fig. 5.4 for all performed fits. For the three subcritical measurements the determined smearing parameter remains below $0.1\,\mathrm{K}$. This corresponds to the limited resolution based on the chosen temperature step size of $0.1\,\mathrm{K}$. For the measurements with supercritical pressures the smearing is larger than the temperature step size. Even disregarding the measurement at $18\,\mathrm{bar}$ where an instability in the cluster-jet occurred, all five measurements have an increase in smearing parameter for all three methods. It is to note, that the smearing at $14\,\mathrm{bar}$ leaps slightly out of line. This general increase hints towards the presence of a higher order phase transition and thus towards the formation of a "Widom delta" with rising pressure [Ha+18]. Still, the exact phase change temperature can be determined with an accuracy below $\pm 0.2\,\mathrm{K}$. It has to be noted that the uncertainty of the results presented here and above is not based on the method itself, but primarily arises from the quality of the temperature measurement and its calibration. For even more precise measurements an independent temperature calibration has to be taken into account in the future.

In order to compare the determined results with literature and/or theory, in the scope of this work the isobaric and isothermal values of c_p and c_V (data from [NIST]) were each used to determine altogether four approximations for the Widom line [Bra+11, LS19, MS10] which are shown in fig. 5.5. The maxima of $c_p(T)$, $c_p(p)$, $c_V(T)$, and
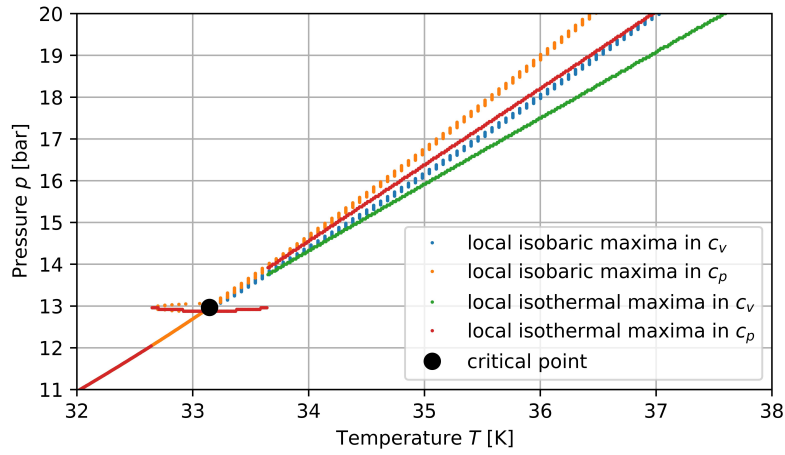
Figure 5.5: The local isothermal and isobaric maxima of c_p and c_V each give an approximation for the Widom line. The data is taken from [NIST]. Below the critical point (black) the four approximations coincide exactly at the vapor pressure curve. As the data was generated with measurements at significantly higher temperatures and extrapolated [NIST], close to the critical point inaccuracies occur. Above 14 bar the divergence of the four approximations is observable with up to ±0.5 K in the considered region. For comparing theory and experiment in fig. 5.6 only one of the mean approximations, i.e., the isothermal maxima in c_p is used $(c_p(T)^{\max})$.
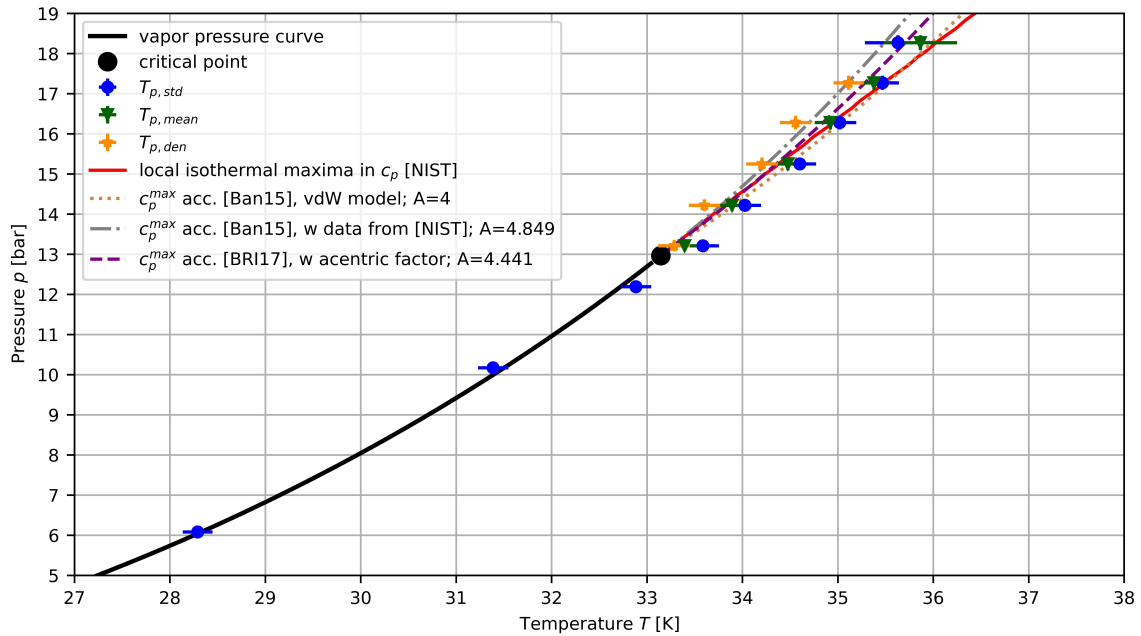
Figure 5.6: Obtained results of the phase change temperatures as presented in table 5.1 and as published in [VFK22], modified. Also shown is the vapor pressure curve, the critical point, and four theoretical predictions of the Widom line.

$c_V(p)$ should coincide as describing the Widom line [LS19]. The used heat capacity information is only a theoretical extrapolation from measured data from a significantly higher temperature range due to the absence of data for the region of interest. It is found that the four approximations differ by only up to $\pm 0.5\,\text{K}$ in the considered region. This can be considered as approximation error of the literature values. For clarity only one of the four lines of maxima $c_p(T)^{\text{max}}$ is shown in fig. 5.6 as it is the middle of the lines.

Another theoretical derivation for the line of maxima in c_p is given by [Ban15]

$$p(T) = p_c \cdot \exp\left(A\left(\frac{T}{T_c} - 1\right)\right) \tag{5.4}$$

with

$$A = \frac{T_c}{p_c}\left(\frac{\mathrm{d}p}{\mathrm{d}T}\right)_{\text{cr}}. \tag{5.5}$$

One can use different approaches to determine A. With the van der Waals equation of state one obtains $A = 4$ (beige, dotted line in fig. 5.6) and using data from [NIST] on the slope of the vapor pressure curve one obtains $A = 4.849$ (gray, point-dash line in fig. 5.6). A generalization beyond simple fluids was derived in [BRI17] with taking the acentric factor into account to describe all fluids equally. For hydrogen this approach leads to $A = 4.441$ (purple, dashed line in fig. 5.6). When comparing these three theoretical descriptions a difference of up to $1\,\text{K}$ within the considered region is apparent. This shows the high model dependence of these theoretical predictions. To resolve this, there is a pressing need for new quality experimental data. Especially since in the course of this thesis no direct measurement of the Widom line for hydrogen has been found in literature. This makes the here presented method the first measurement ever performed to determine the Widom line of hydrogen experimentally.

Comparing now the obtained data with the derived theoretical descriptions it is found that the first two of the four presented descriptions (with data from [NIST] and with the van der Waals model leading to $A = 4$) of the local maxima in c_p coincide and agree well with the determined phase change temperatures. For the results from the velocity standard deviation the temperatures agree within one standard deviation.

The presented method gives a new and experimental simple method to determine the Widom line using the formation of cluster beams. In this thesis, the Widom line was measured for the first time for hydrogen, but also other fluids (elements and composite materials) could be probed. Recent publications [Mou+22] show the large interest in determining the Widom line, in that case for CO_2 and binary or ternary mixtures.

The used MCT-Prototype would require only minor modifications to accommodate for the different fluids due to the different pressure and temperature regions. Because of the steady flow of material through the de Laval nozzle a recuperation system is recommended when rare or expensive fluids are studied. Hence, even in these cases the presented measurements are feasible which makes cluster-jets an universal analytical tool in determining Widom lines of a wide range of substances.

Chapter 6

Properties of Clusters and Cluster-Jets

For the operation and especially for the optimization of CJTs it is important to know the properties of the generated clusters and cluster-jets. Several probing methods were developed by previous researchers and are already in standard use, as can be seen in the previous chapters. Still, there are additional properties to be determined for further optimizations in MCTs.

Within this thesis, a study on the origin of residual gas background via outgassing simulations was supervised [Wei23]. This information is valuable in developing methods to improve vacuum conditions, however, its precision is currently limited by an incomplete knowledge of the cluster size. The cluster size (distribution) is not only relevant for residual gas background simulations, but also for, e.g., laser cluster interactions [Leß21, Man24], target-accelerator beam interaction simulations (energy loss and small angle scattering of the accelerated protons) [Eic23], and the data rates at $\overline{\text{P}}$ANDA. Here, a small amount of large clusters would lead to jumps in luminosity whereas many small clusters give a smooth luminosity and data rate. Also in the study of core beams, the cluster size can give insights on their nature and production process. As the following chapter will unfold, the cluster size is not easy to determine, but first measurements are presented here. Furthermore, measurements of the cluster-jet temperature directly after leaving the nozzle are presented, providing an important cross check to the values given by simulations.

6.1 Examining the Size of Clusters

Measurements of the cluster size were already performed a few times with different methods. These measurements were only partly successful and are presented shortly in the following. Based on the gained insights of these measurements, different methods are tested within this thesis. One method is using a short laser pulse to generate momentary snapshots of the clusters (together with [Eic23]). Further methods are based on Mie scattering. The angle dependent Mie scattering was already investigated in [Man19] for all but small angles. Focusing on small angles, the three-Wavelength Extinction Measurement (3-WEM) (together with [Hal23]) as well as the angle dependent Mie scattering in forward direction (together with [Gök23]) is investigated.

6.1.1 Appraisal and Previous Measurements on Cluster Sizes

When investigating cluster sizes, there needs to be a differentiation between clusters resulting from gaseous and from liquid hydrogen. The accumulation from hydrogen gas towards clusters results in significantly smaller clusters (nanometer range) than by the atomization from liquid hydrogen (micrometer range), as described in section 4.1.1. Valid for both cluster production processes is that not a single cluster size is obtained but a size distribution.

Cluster Size Distribution Functions

In general, for the vast majority of aerosols and dispersed systems like crystallization phenomena, condensation nuclei, raindrops, pharmalogical aerosols, or photographic emulsions, the particle diameter can be represented by the **logarithmic-normal distribution** (lognormal distribution) [Oum+03, RH51, SJ64]. The lognormal distribution is given by [Oum+03, RH51]

$$p(D) = \frac{1}{\sigma\sqrt{2\pi}D} \exp\left(-\frac{(\ln(D) - \ln(D_{\text{av}}))^2}{2\sigma^2}\right) \tag{6.1}$$

with the diameter D, the average diameter D_{av}, and the standard deviation σ [Oum+03]. Such lognormal distributions have thus been used to describe cluster size distributions, e.g., in [Köh15, Man19], mainly for stagnation conditions in the gaseous regime. Furthermore, the size distribution for a sequential breakup process where mother drops are split up into daughter drops, which further split up can also be

described by a lognormal distribution [Vil07].

Another approach for size distributions of aggregation scenarios as the cluster production process for gaseous hydrogen is the **exponential distribution** as presented in [Vil07]. Initially, small particles like the clusters collide and merge, following Smoluchowski's kinetic aggregation process, even taking evaporation of the drops into account. If this aggregation process has enough time, the cluster volume distribution is given by [Vil07]

$$p(v) = \frac{1}{v_{\mathrm{av}}} \exp\left(-\frac{v}{v_{\mathrm{av}}}\right) \tag{6.2}$$

with the cluster volume v and the mean cluster volume v_{av}. This exponential distribution can also be used for fragmentation scenarios (Knuth and Henne (1999) as cited in [Fra15]).

A third size distribution which can often be found in literature for sprays is the **gamma distribution**. It is found to represent size distributions when the drops are formed from ligaments or thin sheets of fluid breaking up [EV08, Vil07] and is given by

$$p(D) = \frac{n^n}{\Gamma(n)} \left(\frac{D}{D_{\mathrm{av}}}\right)^{n-1} \exp\left(-n\frac{D}{D_{\mathrm{av}}}\right) \tag{6.3}$$

with the scaling parameter n.

The reasoning in choosing one of these or even other functions to describe the size distribution is difficult. Most important is the consistency with the physical phenomena involved. Further possible reasons as given by [LM17] could be the mathematical simplicity or the ease of manipulation in computations. These two become relevant when the analysis can only take, e.g., the mean and width into account. Whenever possible the comparison between theoretical prediction and obtained cluster size distribution data gives the final assessment on the correct distribution function. Previous measurements on cluster size distributions at MCTs, as will be presented in the following, mostly use a lognormal distribution to describe the cluster sizes. Even though this gives valid or at least promising results, the other possible distributions should not be omitted without further testing.

Previous Measurements on Cluster Sizes and Cluster Size Distributions

In previous theses on MCTs the cluster size distributions were measured with varying success. To give a starting point for the cluster size measurements within this thesis, a short overview of the previous results in chronological order follows here.

E. Köhler [Köh15] used a retardation potential to stop ionized clusters. With the e-gun (also used in this thesis, but in [Köh15] with a smaller distance of 1 m to the MCP) the clusters can be single positively charged. With this, it is possible that the clusters break up so that the measured values are more of a lower limit in cluster sizes. Using an MCP system (with a P43 phosphor screen) in visualization mode, the intensity obtained from the camera is proportional to the number of ionized clusters hitting the MCP surface. In comparison to the MCP setup used in this thesis (as described in section 3.4.2), an additional grid for a retardation potential and a second grounded grid were installed in front of the MCP setup. Different retardation potentials were applied to the grid. Only clusters with kinetic energies larger than the potential energy of the electric field can pass this grid. From [Täs12] the nominal cluster velocity was calculated and with the assumption of single positively charged clusters the energy can be converted to the cluster mass. The total beam image intensity of the MCP in dependence of the applied retardation voltage of up to 4 kV can thus be transformed into a transmission spectrum dependent on the cluster size [Köh15].

The measurements were performed with the CERN nozzle (narrowest diameter of 28 µm) and cover only the gaseous region at pressures of 7 bar to 10 bar and temperatures below 80 K. For temperatures below approximately 60 K not all clusters could be reflected by applying 4 kV, but still the cluster size distribution is obtainable down to 50 K. It is found, that the mean cluster size is in the order of 10^4 atoms to 10^5 atoms with an increase towards lower temperature [Köh15]. This equals cluster diameters of 2 nm to 10 nm.

Comparing these results with Hagena's scaling law as shown in eq. (4.4), the cluster sizes were 2.6 times larger than predicted, which is small in respect to the determination over several orders of magnitude. With a fit the updated scaling parameter of $A_{\mathrm{N,Köhler}} = 86 \pm 3$ was found (compared to the previous factor of $A_{\mathrm{N,Hagena}} = 33$) [Köh15]. Beside these promising results, the determination of the size of clusters originating from colder hydrogen gas or even from liquid hydrogen is not possible. This leads to the necessity of a completely different method.

In cooperation with the laser plasma working group of Professor Willi at the Heinrich Heine-Universität Düsseldorf, C. Mannweiler performed Mie measurements [Man19]. As Mie scattering will become relevant later on, the theoretical basis to these measurements is presented below. For now, it is important that detecting the angular dependent intensity of laser light scattered at individual clusters gives insight on the cluster size. In [Man19] the scattered laser light was measured at angles from 9° to 165° for both polarizations (S1 and S2 polarized).

While cooling down the target the scattered intensity at a angle of 21° was monitored. The amount of light increases significantly below 65 K which is interpreted as an increase in clustering, consistent with the measurements of E. Köhler. While for E. Köhler the measurements were not feasibility for temperatures below 50 K, for C. Mannweiler a plateau in scattered light was found. Unfortunately, with the Mie scattering setup as used by C. Mannweiler, he states that the cluster sizes in this region are too small to be measured [Man19].

The further measurements performed in [Man19] focus on stagnation conditions below 45 K within the gas(-like) and within the liquid regime. For the analysis of measurement data of clusters from stagnation conditions in the gaseous regime two different size distributions are considered. The lognormal distribution as also used by E. Köhler and the Nukiyama-Tanasawa distribution. The obtained mean diameters are within one standard deviation, while the lognormal distribution is compressed basically to a delta peak, so that the Nukiyama-Tanasawa distribution is preferred [Man19]. The obtained mean cluster diameters are in the range of 20 nm to 120 nm. Here it is to note that E. Köhler measured clusters from gaseous hydrogen above 60 K while C. Mannweiler measured below 45 K. While E. Köhler found larger clusters than predicted by Hagena, C. Mannweiler found smaller clusters. The respective scaling factors are $A_{\mathrm{N,Hagena}} = 33$, $A_{\mathrm{N,Köhler}} = 86 \pm 3$, and $A_{\mathrm{N,Mannweiler}} = 25 \pm 5$. Again to note is the correct order of magnitude this measurement obtained. The difference between E. Köhler and C. Mannweiler of below a factor of 4 for two completely different size determination methods is remarkable.

For the liquid regime the obtained data below 13° was not reliable, leading to difficulties in the analysis. Still, C. Mannweiler gives a mean cluster size in the order of tens of nanometers, but it is also stated that a few extremely massive clusters with sizes above 1 µm are present [Man19].

To resolve this for the liquid regime, L. Leßmann [Leß21] started with the totally different method of shadowgraphy [Leß21]. For these measurements, the cluster jet is illuminated with an ultra short laser pulse (also provided by the working group of Professor Willi) as background illumination. Due to the short illumination time the clusters do not move and appear as small dark spots. Within his doctoral thesis only 160 snapshots were taken for liquid conditions and the depicted clusters were counted and measured by hand. A significant number of clusters with sizes from 1 µm to 10 µm were found [Leß21]. One of the results of these measurements was the feasibility of visualizing clusters by means of shadowgraphy. Due to the limited statistics, this measurement is repeated in this thesis together with H. Eick [Eic23].
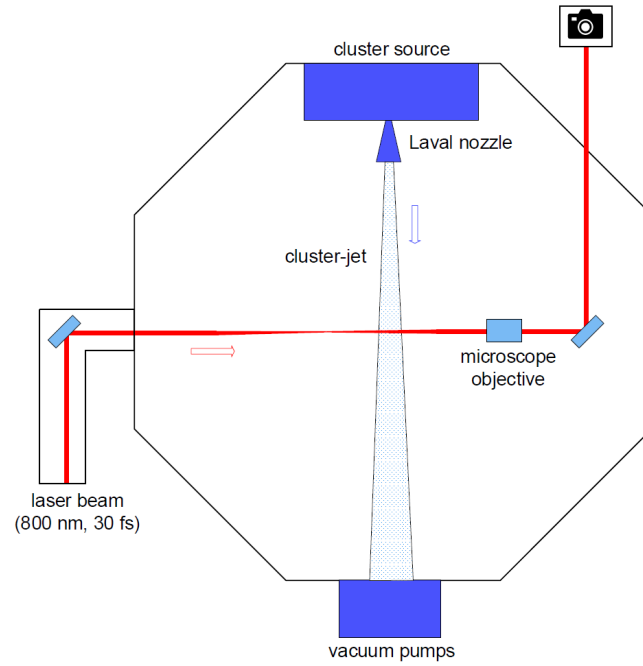
Figure 6.1: Setup for the shadowgraphy measurements viewed from top. The cluster-jet propagates from top to bottom. The laser beam illuminates the cluster-jet from the left. With a microscope objective the shadowgraph is directed onto a camera. Figure by H. Eick [Eic23].

To summarize, for gaseous hydrogen the resulting clusters are in the order of 1 nm to 100 nm [Köh15, Man19]. For liquid stagnation conditions the size is not that clearly given. Values between tens of nanometers up to a few micrometer seem valid. Thus, especially for the liquid regime new data is necessary.

6.1.2 Shadowgraphy

For shadowgraphy measurements as first performed in [Leß21] and here together with H. Eick [Eic23], the ARCTURUS laser system is used to background illuminate clusters of the MCT-D, which is shown in fig. 6.1. The MCT-D generates a cluster-jet that moves horizontally through the interaction chamber and is directly pumped by a large roots pump. The ARCTURUS laser system provides ultra short laser pulses (30 fs) at a wavelength of 800 nm crossing the cluster-jet perpendicular at a distance of 2.8 cm behind the nozzle exit. With a maximum velocity of 1000 m/s the clusters move 3×10^{-5} µm at most, which is unnoticeable little compared to the cluster sizes, so that the clusters are not smeared. The laser is focused in front of the cluster-jet to obtain a homogeneous background illumination. After crossing the cluster-jet, the laser light is

guided through a microscope objective onto a camera to obtain the shadowgraph. This microscope objective has a limited focus depth. With moving the objective in steps of $1\,\mathrm{mm}$ in laser direction (z-direction) the focus spot scans the cluster-jet obtaining a profile. The given setup has a Abbe diffraction limit of $2.9\,\mathrm{\mu m}$ [Eic23] so that only clusters larger in diameter can be resolved.

With this setup, ten stagnation conditions are measured at at least seven z-positions where 1000 snapshots are taken each. Since these pictures cannot be analyzed by hand, H. Eick developed a routine to find potential clusters, determine whether they are real, and determine their diameter. In general, clusters with diameters from $3\,\mathrm{\mu m}$ to $10\,\mathrm{\mu m}$ are found, as can be seen for $28\,\mathrm{K}$, $16\,\mathrm{bar}$, and $z = 0$ in fig. 6.2. The blue histogram shows these cluster sizes without further calculations. Interestingly, the left hand side of the distribution is much steeper than the right hand side. Circling back to the Abbe diffraction limit of $2.9\,\mathrm{\mu m}$ the left hand side of the distribution is probably cut off since smaller clusters cannot be resolved. This implies that not the total distribution is measured but only the high end tail.

Additionally to the cluster measurements and the development of the analysis program, the determination of the focus depth has to be carried out. For this, toner particles with a diameter in the order of micrometers are placed in the focal plane of the microscope objective. By moving the particles in the z-direction in $1\,\mathrm{\mu m}$ steps and analyzing the obtained snapshots with the analysis program developed by H. Eick, the region in which a single particle can still be found, is determined to $(53 \pm 9)\,\mathrm{\mu m}$, which equals the focus depth. A second, very important aspect found with this measurement is that the particle appears to be larger when moving only slightly out of the focal plane. The measured toner particle, which is $6\,\mathrm{\mu m}$ in diameter, is determined to be up to $3\,\mathrm{\mu m}$ enlarged towards the border of the focus region. Inferring back from this to the cluster measurements, in average the clusters are smaller than they appear in the pictures. This means further, that the obtained diameters need to be de-convoluted to determine the real size distribution.

In fig. 6.2 not only the measured distribution is shown, but also the real distribution. Since only the high end of the size distribution is measurable and the lower end is cut off, in principle a lognormal distribution (for the real sizes) with a cut off by a step function (for the Abbe limit) should be used. However, with this the mean and standard deviation are not determinable because most data is below the cut off limit and thus no fit can be performed. Instead a symmetric Gaussian distribution is used. This distribution is convoluted with the distribution obtained by the toner measurement. By varying the Gaussian distribution the convolution is optimized to have minimal differences to the measured distribution. From this, the mean
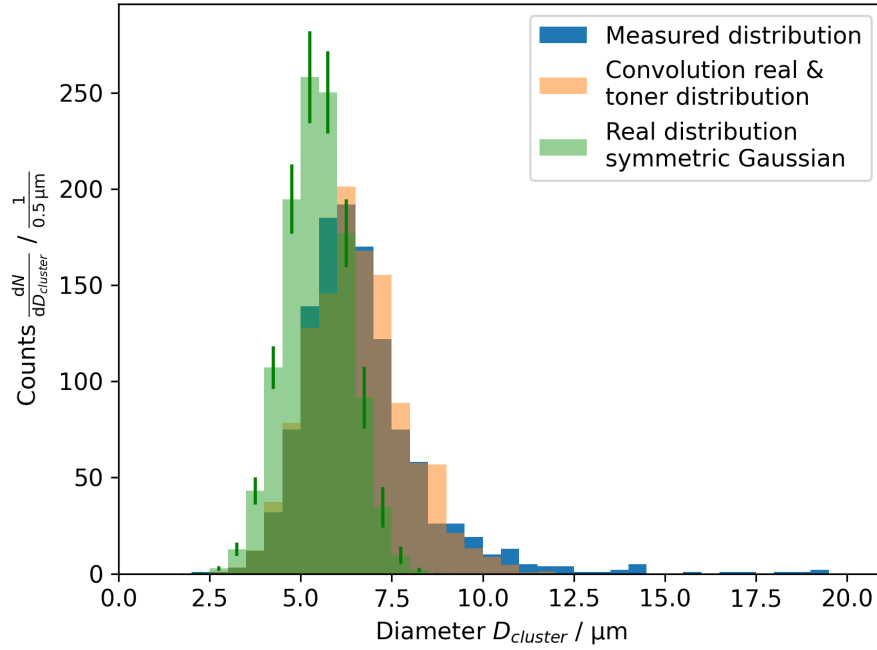
Figure 6.2: Histogram of the cluster size diameters at target settings of $28\,\mathrm{K}$ and $16\,\mathrm{bar}$ in the center of the cluster-jet obtained from 1000 pictures. The blue histogram shows the measured distribution and gives a mean diameter of $6.63\,\mu\mathrm{m}$. The green histogram shows the assumption of the real cluster size distribution which is convoluted with the toner distribution to obtain the orange histogram. The green histogram is varied so that blue (real) and orange (convoluted) histogram align as well as possible. The mean of the real diameters (green histogram) is $5.45\,\mu\mathrm{m}$. Figure from [Eic23].

$\mu = (5.45 \pm 0.07)\,\mu\mathrm{m}$, the standard deviation $\sigma = (0.88 \pm 0.05)\,\mu\mathrm{m}$, and the total number of clusters $A = (1183 \pm 76)$ in 1000 pictures is obtained for $28\,\mathrm{K}$, $16\,\mathrm{bar}$, and $z = 0$ [Eic23].

Comparing the different stagnation conditions, only slight differences in mean cluster size and standard deviation are observable. With rising pressure and decreasing temperature the mean cluster size and the standard deviation is larger. The mean cluster sizes obtained in [Eic23] range from $4.6\,\mu\mathrm{m}$ to $5.6\,\mu\mathrm{m}$ with standard deviations of $0.73\,\mu\mathrm{m}$ to $1.16\,\mu\mathrm{m}$.

Furthermore, with H. Eick [Eic23] different methods to determine the volume density of the cluster-jet are considered, i.e., the flow through the nozzle, the AMS (see section 3.2.1), and the observed clusters with shadowgraphy. When comparing, only $(46.8 \pm 6.4)\,\%$ to $(78.3 \pm 12.4)\,\%$ of the flow through the nozzle is accounted for in the clusters seen with shadowgraphy, depending on the stagnation conditions but without a significant trend. This leads to the conclusion that remaining hydrogen flowing through the nozzle is in clusters smaller than the Abbe limit and furthermore, that the obtained mean diameters give more of an upper limit than exact values.

For future measurements using shadowgraphy, the Abbe limit needs to be pushed towards smaller diameters. This is either possible by using a laser with a smaller wavelength or/and using a microscope objective with larger magnification. This measurement will be performed in [Eic24, Fis24]. The other possibility is to use Mie scattering, as it is also sensitive to smaller objects.

6.1.3 Mie Scattering

Mie scattering was already used by C. Mannweiler [Man19] to determine cluster sizes. It gives insight into the size of the particle based on the angular dependent intensity of scattered light. In [Man19] it was found, that a few very large clusters dominate the scattering pattern in the forward region, which was not measured fully. In this region two possible measurement concepts are now tested in this thesis. First, the wavelength dependent extinction with the three-Wavelength Extinction Measurement (3-WEM) is tested together with L. Halstenberg [Hal23]. Second, a setup for measuring Mie scattering in the region, which was not measured in [Man19] is commissioned together with E. Göktas [Gök23]. Afterwards a preliminary measurement of Mie scattering in forward direction is performed. As basis for this, the theory of Mie scattering is presented first.

Theory of Mie Scattering

When an electromagnetic wave with the wavelength λ encounters a spherical particle, e.g. a cluster, the electrons within this particle are perturbed periodically which induces a dipole moment. This dipole moment is a source of electromagnetic radiation itself resulting in scattered light with mostly the same frequency as the incident wave [Hah09]. Generally, this complex interaction is dependent on the particle size and can be described by Mie scattering (after Gustav Mie [Mie08]). For small particles (significantly smaller than $\lambda/2\pi$) it can be simplified to Rayleigh scattering whereas for large particles (larger than $20 \cdot \lambda$) it converges to geometric optics [Hah09, Hul57]. Starting with the incident light with the intensity I_0 being scattered at the spherical object the resulting intensity at a distance r at the angle θ can be described by [Hul57]

$$I_{\mathrm{scat}} = \frac{I_0}{k^2 r^2} i_{1,2}(\theta) \tag{6.4}$$

with $k = 2\pi/\lambda$. $i_{1,2}(\theta)$ is the squared complex amplitude function $|S_{1,2}(\theta)|^2$. The index 1 or 2 refers to the polarization S1 where the electrical field oscillates orthogonal to

the plane of incidence or S2 where the electrical field oscillates parallel to the plane of incidence. Mixtures of both polarizations are also possible, but will not be discussed here, since it is not of relevance. Further, the complex amplitude functions are given by [Hah09, Hul57]

$$S_1 = \sum_{n=1}^{\infty} \frac{2n+1}{n(n+1)} [a_n \pi_n(\cos\theta) + b_n \tau_n(cos\theta)] \tag{6.5}$$

$$S_2 = \sum_{n=1}^{\infty} \frac{2n+1}{n(n+1)} [b_n \pi_n(\cos\theta) + a_n \tau_n(cos\theta)]. \tag{6.6}$$

Therein π_n and τ_n are defined over the Legendre polynomials P_n^1 with

$$\pi_n(\cos\theta) = \frac{P_n^1(\cos\theta)}{\sin\theta} \tag{6.7}$$

$$\tau_n(\cos\theta) = \frac{dP_n^1(\cos\theta)}{d\theta}. \tag{6.8}$$

Further, a_n and b_n are given by [Hah09, Hul57]

$$a_n = \frac{\Psi_n'(mx)\Psi_n(x) - m\Psi_n(mx)\Psi_n'(x)}{\Psi_n'(mx)\xi_n(x) - m\Psi_n(mx)\xi_n'(x)} \tag{6.9}$$

$$b_n = \frac{m\Psi_n'(mx)\Psi_n(x) - \Psi_n(mx)\Psi_n'(x)}{m\Psi_n'(mx)\xi_n(x) - \Psi_n(mx)\xi_n'(x)} \tag{6.10}$$

with $x = \frac{2\pi a}{\lambda}$, the radius a of the spherical object, and m being the refractive index of the particle material. The so called Riccati-Bessel functions are further defined over the half-integer-order Bessel function of the first kind $J_{n+1/2}$ and the half-integer-order Hankel function if the second kind $H_{n+1/2}$ according to [Hah09, Hul57]

$$\Psi_n(z) = \left(\frac{\pi z}{2}\right)^{1/2} J_{n+1/2} \tag{6.11}$$

$$\xi_n(z) = \left(\frac{\pi z}{2}\right)^{1/2} H_{n+1/2}. \tag{6.12}$$

With this, the angular dependent intensity can be plotted for a given wavelength, particle size, and refractive index ($m = 1.333$ for hydrogen) which is exemplary shown in fig. 6.3 for three particle sizes and the three wavelengths used in this thesis. It is to note that these angular plots are symmetrical to the laser propagation axis, leading to the possibility to plot the S1 polarized intensity in the upper half and the S2 polarization in the lower half. The main difference in the intensity for both polarizations is at 90° where for the S2 polarization no light is emitted since the induced dipole
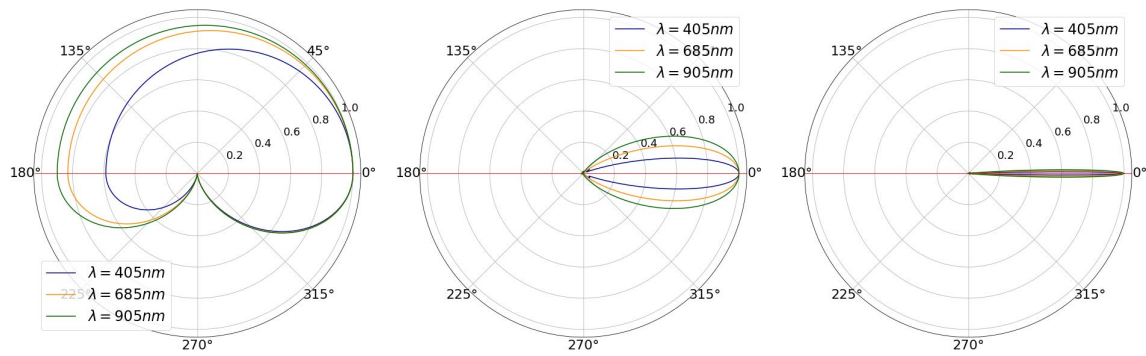
Figure 6.3: Polar plots for the intensity of scattered light normalized to its intensity at 0°. The laser enters from the left (180°) and scatters on the spherical particle located in the center. The upper half shows the scattered intensity for S1 polarized light, the lower half for S2 polarized light. The particle diameter is 0.1 μm (left), 1 μm (center), and 10 μm (right). With rising particle size and with smaller wavelength the intensity is more forward directed. Figures from [Hal23].

oscillates in this direction. This asymmetry is reduced for larger particle sizes and is only of minor relevance in the forward direction. For both polarizations the intensity scattered in forward direction is larger than scattered backwards, especially with rising particle size. The shown intensity plots are each normalized to its maximum at 0°, but it is to note, that with rising particle size also the total amount of light scattered is increased.

3-WEM

The three-Wavelength Extinction Measurement (3-WEM) is an optical measurement based on Mie scattering [Oum$^+$03]. Instead of measuring the scattered intensity for several angles, the transmitted intensity (and with this the extinction) for three wavelengths is measured. Depending on the particle size the extinction ratio between the wavelengths differs [Oum$^+$03].

The corresponding setup is depicted in fig. 6.4, left. Three lasers with the wavelengths 405 nm, 685 nm, and 905 nm and their respective intensities 100 mW, 40 mW, and 7 mW (Laser Components, models FP-D-405-100-E-F, FP-D-685-40-E-F, and FP-D-905-7-E-F) are each collimated and aligned onto a common volume within the jet. After crossing the measurement volume each laser intensity is measured with a silicon photodetector (Thorlabs, model PDA36A2). The output is connected to an 1 kHz low-pass filter (Thorlabs, model EF110) and subsequently to an oscilloscope. To measure the extinction, the full laser intensities $I_{0,i}$ without jet are measured. When the jet now enters the measurement volume, all three laser intensities are attenuated to the
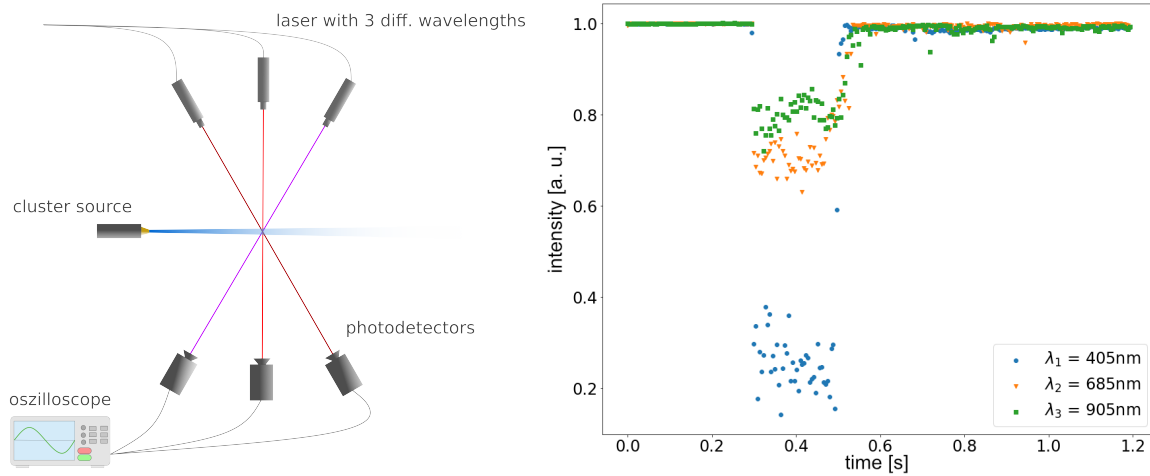
Figure 6.4: *Left:* Setup for the 3-WEM. Three lasers are aligned to cross a common volume within the jet. Each laser intensity is measured with a photodetector. Figure from [Hal23], edited. *Right:* Example for the measured data. The incident intensity is attenuated by different factors depending on the wavelength. Plot by L. Halstenberg, edited.

intensities I_i by different amounts. The obtained intensity curves from the oscilloscope can be seen in fig. 6.4, right.

The attenuation can now be described by the Lambert-Beer type expression [Oum$^+$03]

$$I_i = I_{0,i} \exp\left(-NL \int_0^\infty p(D)\pi(D/2)^2 Q_{\text{ext}}(D, \lambda_i, m)dD\right) \tag{6.13}$$

with the particle density N, the path length within the measurement volume L, the particle size distribution $p(D)$, the diameter D, and the extinction coefficient Q_{ext}, which holds for each wavelength individually. By transforming this equation and setting it into relation for the different wavelengths, the extinction ratios can be found: [Oum$^+$03]

$$\text{ER}_{1,2} = \frac{\ln(I/I_0)_{\lambda_1}}{\ln(I/I_0)_{\lambda_2}} = \frac{\int_0^\infty p(D)D^2 Q_{\text{ext}}(D, \lambda_1, m)dD}{\int_0^\infty p(D)D^2 Q_{\text{ext}}(D, \lambda_2, m)dD} \tag{6.14}$$

$$\text{ER}_{2,3} = \frac{\ln(I/I_0)_{\lambda_2}}{\ln(I/I_0)_{\lambda_3}} = \frac{\int_0^\infty p(D)D^2 Q_{\text{ext}}(D, \lambda_2, m)dD}{\int_0^\infty p(D)D^2 Q_{\text{ext}}(D, \lambda_3, m)dD} \tag{6.15}$$

With this, the dependence on N and L is removed, assuming them to be constant for all three lasers. From this system of equations with two independent input parameters ($\text{ER}_{1,2}$ and $\text{ER}_{2,3}$), the particle size distribution $p(D)$ determined by, e.g., mean diameter and width, can be obtained.

For this determination, the extinction coefficient has to be calculated based on Mie

theory. At 0° the angle and polarization dependency of the intensity pattern is canceled
and eqs. (6.5) and (6.6) collapse to [Hul57]

$$S(0) = S_1(0) = S_2(0) = \frac{1}{2} \sum_{n=1}^{\infty} (2n + 1)(a_n + b_n).$$ (6.16)

From this the extinction coefficient is defined over [Hul57]

$$Q_{\text{ext}} = \frac{4}{x^2} \operatorname{Re}\{S(0)\} = \frac{2}{x^2} \sum_{n=1}^{\infty} (2n + 1) \operatorname{Re}\{a_n + b_n\}$$ (6.17)

with $x = \pi D/\lambda$ and with a_n and b_n as in eq. (6.9). The calculation cannot be numerically
performed to $n \to \infty$, but is carried out up to $n_{\max} = \lfloor 2 + x + 4x^{1/3} \rceil$ [Man19, Mät02].
With this, the theoretical foundation for the determination of the particle or cluster
size distribution is laid. The calculations for this are performed in python based on
[Man19] which is in turn based on [Mät02]. For details of the derived analysis program
refer to [Hal23].

To test the possibilities of 3-WEM together with L. Halstenberg [Hal23] different water
sprays were measured as this is easier to setup and align. Several measurements were
performed and averaged for each setup. For the particle sizes a lognormal distribution
is assumed. For the water spray a typical pressure sprayer (Gloria prima 5), a medical
inhalation device (Pari boy Type 038), a convergent pressure nozzle ($\varnothing(277 \pm 5)\,\mu\mathrm{m}$),
and a hollow-cone nozzle (Lechler model 220.004) were used. With each device the
setup and the analysis program were optimized and more significant results could be
gained.
The measurement with the pressure sprayer prove the general feasibility of 3-WEM. For
this device no reference value for the spray sizes can be given. The obtained diameters
in the range of micrometers seem reasonable. Unfortunately, the uncertainties are in
the same order of magnitude or even larger, which needs to be improved for more
detailed measurements.
Using the medical inhalation device, only a reference value for the follow-up model
can be found, where the mass median aerodynamic diameter is $2.6\,\mu\mathrm{m}$ to $4.0\,\mu\mathrm{m}$ for
salbutamol [PAR19]. Assuming a similar size for water, at least a rough size validation
can be obtained. The measurements give a mean diameter of $732^{+1262}_{-257}\,\mathrm{nm}$ and a
standard deviation of $0.3^{+0.6}_{-0.3}\,\mathrm{nm}$ [Hal23]. The uncertainties of the mean diameter allow
for the range $475\,\mathrm{nm}$ to $1994\,\mathrm{nm}$. Accounting for the determination over possibly
several orders of magnitude, this range is an acceptable result. The uncertainties of

Table 6.1: Calculated upper limit in particle size based on aerodynamic forces and measured mean particle sizes for the three measured pressures. As the breakup for 10 bar is performed after the measurement volume, the calculated upper limit is exceeded by the measurement. For the other two pressures, the upper limit is valid. Values obtained together with L. Halstenberg [Hal23].

pressure p [bar]	theoretical upper limit [nm]	mean diameter [nm]
10.0 ± 0.2	718 ± 15	1267^{+3231}_{-516}
12.0 ± 0.2	587 ± 11	451^{+1807}_{-200}
14.0 ± 0.2	497 ± 9	463^{+796}_{-174}

the standard deviation however are still too large. One reason for this is that the mist of the inhalation device is not very located and fill in a large volume. With this the lasers not only cross the mist in the common volume but a length an order of magnitude larger. Since this path is different for each laser the cancellation of L and N in eq. (6.14) is no longer valid.

For the convergent pressure nozzles the spray is comparable to the cluster-jet, as desired. For a pressure of 10 bar, 12 bar, and 14 bar the resulting jet is measured. With a beaker the jet can be blocked for the full intensity measurement. While measuring it is observed that for 10 bar the jet is possibly not fully atomized, different to the 12 bar and 14 bar measurement. This leads to the assumption that the breakup is performed by aerodynamic forces as presented in section 4.1.1. With this, an upper limit in particle size can be given. The results are given in table 6.1. For 10 bar, as the breakup is performed after the measurement volume was crossed, the diameter obtained is larger than the calculated upper limit. For 12 bar and 14 bar the measured mean diameter is below this upper limit. This reinforces the performed measurement. However, for some measurements an unphysical large diameter is obtained which were not taken into account for the presented results.

Finally, the hollow-cone nozzle is measured. For this nozzle, the size distribution of the resulting spray was measured by the producing company Lechler, so that a precise comparison and thus possible validation of the measurement concept is aimed at. With this spray there are difficulties in obtaining the correct mean diameter. An attempt to optimize this is made by pulsing the spray by periodically, shortly blocking it with a beaker. With this, the extinction of each laser can again be unambiguously determined. Unfortunately, the measurements cannot be brought to a valid diameter. Further literature research showed a limitation for 3-WEM. In [SSZ94] the limitation of the diameter D to

$$0.1 < \frac{\pi D}{\lambda} < 10 \qquad (6.18)$$

and thus to approximately $0.013\,\mu m$ to $3\,\mu m$ is given. The size of the spray from the hollow-cone nozzle is in the range of $50\,\mu m$ and thus the non-accessibility of valid diameters with 3-WEM is apparent.

The obtained insights in 3-WEM show the general possibility to measure the particle size distribution of a spray, but the obtainable size is limited to $0.013\,\mu m$ to $3\,\mu m$. Since this feasibility study was performed in parallel to the shadowgraphy measurements presented in section 6.1.2 the necessity for measuring particles above this limit was not known in the beginning. Unfortunately, the larger clusters would mask the signal of the clusters in the measurable diameter range. With this, no cluster sizes in the liquid regime can be measured with 3-WEM. For the gaseous regime the cluster sizes from $1\,nm$ to $100\,nm$ [Köh15, Man19] partly fall below the lower boundary of the possible size range so that a measurement would also not be successful. With this, the 3-WEM needs to be omitted for cluster size determinations at CJTs.

Mie Scattering in Forward Direction

Measuring the Mie scattering of clusters was already partially successful in [Man19]. The angular range of $9°$ to $165°$ was measured in Düsseldorf. For the large clusters present when operating an MCT in the liquid regime it was found that smaller angles are of higher relevance than large angles (see fig. 6.3). Thus this method is again tested in this thesis together with E. Göktas [Gök23] in Münster at the MCT-Prototype.
The general setup is depicted in fig. 6.5. At the position of the e-gun of the MCT-Prototype and thus behind skimmer and collimator a laser and a Mie detection chamber are installed. The measurement of cluster sizes after the collimator and thus in such large distances is highly relevant for experiments like $\overline{P}$ANDA since here the clusters are most likely already frozen and thus no large differences to the IP or the scattering chamber are expected. Furthermore, only that part of the cluster-jet that is used for further measurements (density, velocity, or later at $\overline{P}$ANDA) is analyzed which allows for angle depended studies. At these distances, the thickness of the cluster-jet is orders of magnitude smaller than directly behind the nozzle as for the measurements in Düsseldorf (thickness $\propto 1/r^2$). Since the intensity scales with the thickness this gives the first challenge in this setup. The laser FP-D-685-40-E-F by LaserComponents ($\lambda = 685\,nm$, $I_0 = 40\,mW$) is placed within vacuum, perpendicularly crossing the cluster-jet, defining the scattering center. Clusters illuminated by the laser generate Mie scattering. In a distance of $74.4\,cm$ the scattered light is coupled into a glass fiber by an optical collimator (see fig. 6.5). It consists of a $1''$-lens, a polarization filter,
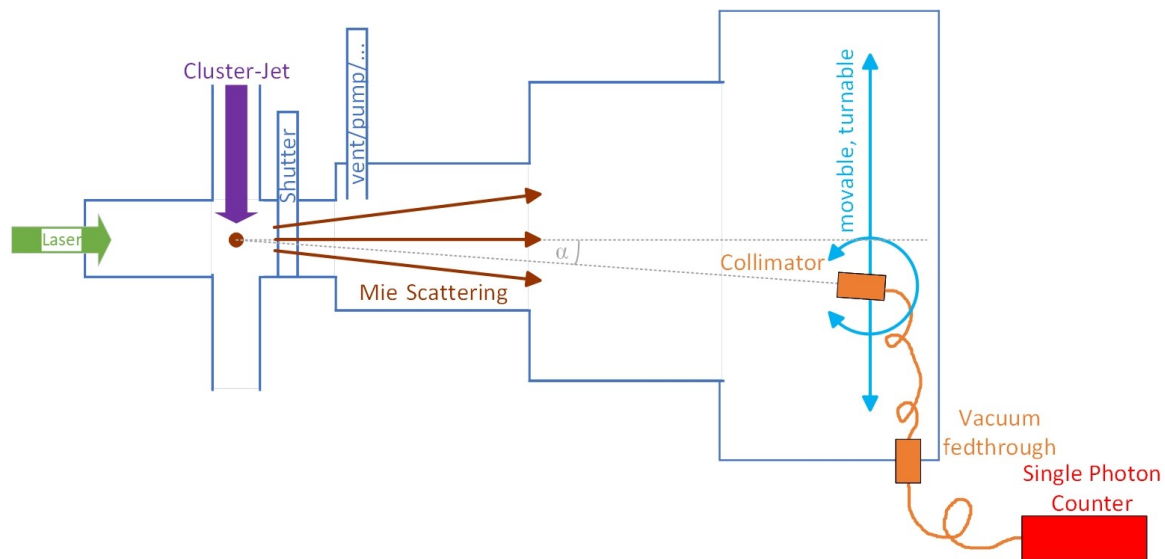
Figure 6.5: Setup for measuring Mie scattering in forward direction. The laser is placed perpendicular to the cluster-jet within vacuum. Their crossing forms the scattering center from which Mie scattering emerges. In a large distance a movable and turnable collimator is placed to couple the light into a glass fiber. The intensity is measured with a single photon counter connected to a rate meter.

and a fiber holder connected by an adjustable lens holder for varying the focus length according to the distance to the scattering center to maximize the light coupled into the fiber. This collimator is movable by hand to measure different angles and turnable by the motorized rotation stage PDR1/M by Thorlabs (with KIM101 controller) to be adjusted towards the scattering center. The glass fiber guides the light to a single photon counter (Model COUNT-10C-FC by LaserComponents). This detector gives a TTL signal each time a photon is detected. The TTL signal is then connected to a ratemeter for the measurements.

The two main challenges in this Mie setup are to reduce scattered background light and to align everything accurately. For the reduction of background light the inner surface of the used chamber is coated with black paint. Additionally, black cardboard is used at the surfaces that cannot be covered with paint. Also a laser beam dump is installed at 0°. For the alignment a wire is placed in the scattering center, where normally the cluster-jet would be illuminated. With this, the alignment can be performed at atmosphere. For the first alignment of the collimator a powermeter is used measuring the light output after the glass fiber. The focal length of the collimator and the vertical angle are aligned precisely and fixed for all measurements. For the alignment of the horizontal angle, for each position the collimator is turned, scanning the relevant region once with and once without the wire. The position of the wire can be unambiguously determined and with this the collimator is aligned towards the scattering center. For
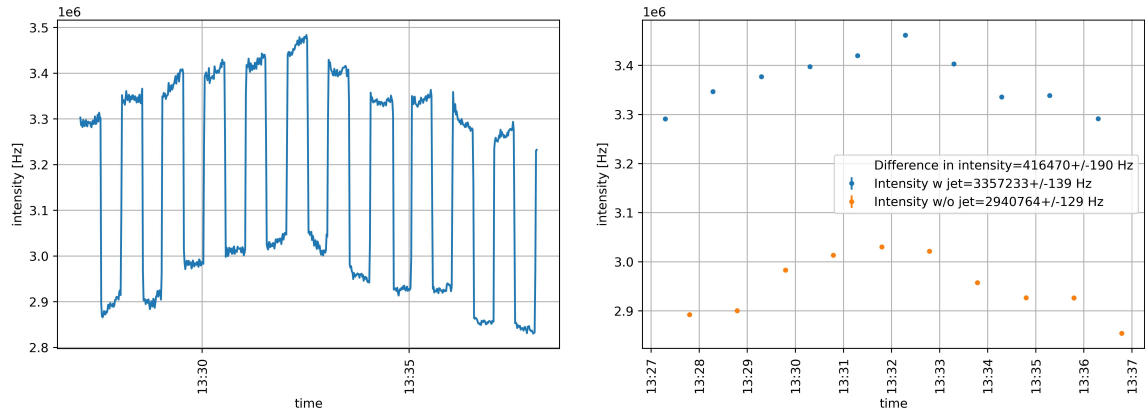
Figure 6.6: Exemplary measurement of Mie scattered light at 1.2°. *Left:* Raw data from the ratemeter measuring the number of photons detected by the single photon counter. In intervals of 30 s the nozzle shutter is closed and opened. Each time a significant drop or increase in photon rate is observed. Over the total time of 10 min the instability in intensity is observable, which is still smaller than the difference between cluster-jet and no cluster-jet being present. *Right:* Mean intensity for each interval from 10 s to 25 s. The uncertainties in the mean intensity vanish in the data points. The total difference in photon rate is $(416\,470 \pm 190)\,\mathrm{Hz}$ which is directly proportional to the intensity of scattered light.

the real measurements later on, this angular alignment is optimized slightly with the cluster-jet instead of the wire.

Still, there is a non-negligible amount of background light and significant fluctuations in intensity. These fluctuations are not present in the laser intensity itself, but only in the scattered light at small angles. For this the laser intensity was monitored together with E. Göktas [Gök23] with a silicon detector, showing stable behavior. For this reason the cluster-jet is pulsed: Alternating, the nozzle shutter is opened and closed for 30 s each. Of this measurement time only the region of 10 s to 25 s is used, so that boundary effects, e.g., due to stabilization of the cluster-jet, are excluded. An exemplary measurement is shown in fig. 6.6. The clear difference between the intensities with and without a cluster-jet is apparent as well as the intensity fluctuations over the total measurement time. With this result a systematic measurement is conducted in this thesis.

Firstly, the thickness dependency of the intensity is tested. The measurement presented above is performed for different stagnation conditions. By putting the measured background subtracted intensity in relation to the thickness, an approximate linear behavior can be seen in fig. 6.7. Since the measurement was performed for different stagnation conditions a possible different cluster size distribution can lead to deviations from this proportionality of intensity and cluster-jet thickness.

After the general feasibility of this method was shown, the angle dependent intensity for one target setting is measured. For each position the collimator needs to be placed by
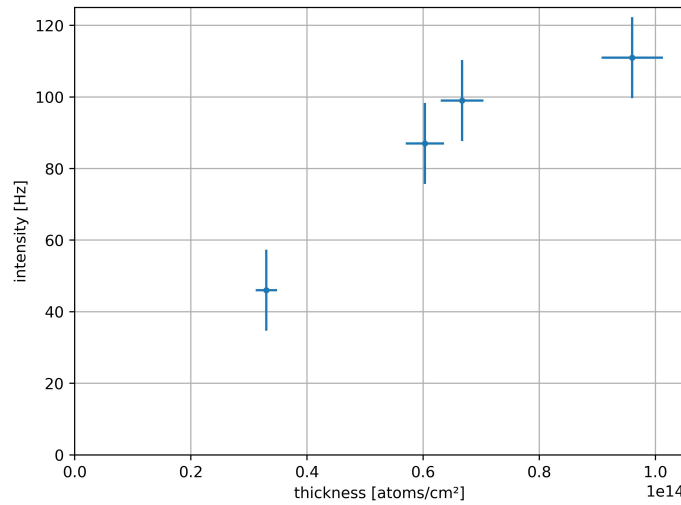
Figure 6.7: Exemplary measurement of Mie scattered light at 1.2° in dependence of the cluster-jet thickness. The intensity is approximately proportional to the thickness.

hand and its horizontal angle needs to be aligned with the wire accordingly. This leads to possible error sources, which has to be kept in mind for the analysis. Furthermore, only one position can be measured per day, leading to slight differences in the cluster-jet (density and especially cluster sizes) for each measurement. A further error source is the geometric expansion of the scattering center and the collimator. With the 1″-lens a broad region of scattered light is coupled into the fiber. A slit would improve this, but lead to significantly less intensity. This would need an easier alignment process for reliable intensity measurements. Still with the presented setup, a first measurement can be performed. For each collimator position a 10 min measurement with 30 s pulsed cluster-jet operation is performed and the difference in intensity is determined. The obtained data is shown scaled in fig. 6.8. As expected, a decrease in intensity with larger angle is observable.

Additionally to the data, several intensity patterns for single cluster sizes are shown, each scaled to fit one data point, keeping in mind, that the absolute intensities are larger for larger cluster sizes. For clarity the intensity patterns are divided into two plots. On basis of the obtained cluster sizes from shadowgraphy (section 6.1.2, [Eic23]) cluster sizes below 10 μm seem reasonable. The corresponding intensity patterns are too large for large angles and/or too small for small angles (see fig. 6.8, left). Even with different scaling or the composition of several cluster sizes, the measured data cannot be described.

In the shadowgraphy measurements in [Leß21] single clusters above 10 μm have been observed. The intensity patterns of such cluster sizes above 10 μm are shown in fig. 6.8,
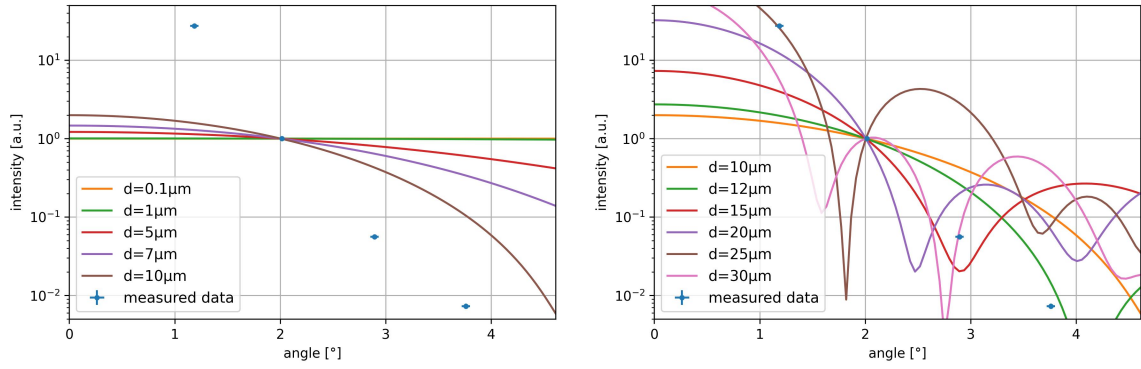
Figure 6.8: Mie scattered light for different cluster sizes. The error bars of the measured intensities partly vanish in the markers. The intensity patterns for different cluster sizes are shown. *Left:* Cluster sizes 0.1 μm to 10 μm. *Right:* Cluster sizes 10 μm to 30 μm. Here, the effects of geometric optics become visible. For $d \gtrsim 20 \cdot \lambda = 13.7$ μm Mie theory still describes the intensity pattern fully, but it can be simplified to geometric optics.

right. Due to the large size of the clusters compared to the wavelength of the laser, multiple maxima and minima are obtained. Even though no single cluster size is able to describe the measured data, combining different cluster sizes, as it is demanded by the atomization processes obtaining cluster size distributions, a proper description of the measured data is imaginable. Due to the complexity of such cluster size distribution models together with the complex scattering patterns for cluster sizes above 10 μm, the still large systematical uncertainties, and the limited number of data points, a proper fit to the data is not possible at this point. Still, the measurements show the general feasibility at such large distances and hence small cluster-jet densities together with a first cluster size estimation.

Preliminary, the measured Mie scattering hints towards the presence of clusters with diameters above 10 μm. Explicit size distributions cannot be obtained here. Instead, two possibilities are considered: First, cluster size distributions with significantly larger mean diameter than obtained by shadowgraphy, or second, the presence of single clusters with diameters above 10 μm additionally to the cluster size distribution obtained by shadowgraphy. In the first evaluation step in [Eic23], cluster candidates with sizes from 2.3 μm to 10.3 μm are selected. Since these boundaries are far away from the obtained size distributions, this seemed reasonable. However, with the newly gained knowledge a reevaluation allowing for larger cluster sizes is necessary and will be considered in future measurements in [Eic24]. Still, the images taken together with H. Eick [Eic23] only cover in total a measurement time of

$$30 \, \text{fs/image} \cdot 1000 \, \text{images/position} \cdot 7 \, \text{positions/setting} \cdot 10 \, \text{settings} = 2.1 \, \text{ns}$$

whereas the sampling rate in this measurement of $1\,\mathrm{s}$ is $5 \cdot 10^8$ times as large. Single large clusters would thus not be statistically present in the perfomed shadowgraphy measurement but still permanently present in the Mie measurement presented here.

Circling back to an interpretation already presented in section 4.3.3: The hydrogen exiting the nozzle first forms a liquid filament surrounded by already atomized fluid which serves as coflowing gas. The filament later on breaks up into larger clusters with smaller velocity compared to the coflowing residual cluster-jet, leading to the large density in core beams. When such a cluster-jet is now studied, a cluster size distribution in the micrometer range as obtained in [Eic23] for the residual cluster-jet would be combined with some additional large clusters in the core beam. The measurement presented in this section would support this, even though the obtained data is not significant yet. Hence, an angle dependent measurement of cluster sizes with shadowgraphy (then allowing for clusters larger than $10\,\mathrm{\mu m}$) and especially with Mie scattering in the forward direction is of high importance.

Within this thesis, the general feasibility of small angle Mie scattering in a large distance to the nozzle was proven. This allows for future Mie measurements with larger cluster sizes compared to [Man19] and with larger statistics compared to [Eic23]. Since the measurement is performed after the extraction of the cluster-jet with the collimator, a measurement in dependence of the cluster-jet angle is possible and with this the differentiation between residual cluster-jet and core beam. For such elaborate measurements, significant changes to the setup need to be established. The angle scan and the alignment of the optical collimator need to be performed motorized. Furthermore, the general alignment needs to be performed once and then kept for all measurements. With this, faster scans become possible, reducing systematical errors. The optical collimator further should be equipped with a slit to enhance the angular resolution. Most important, a significant reduction of background intensity is necessary. Furthermore, an elaborate cluster-jet angle dependent shadowgraphy measurement with a smaller Abbe limit and the possibility for larger clusters is additionally beneficial, as planned in [Eic24, Fis24]. With such updated setups, a significant step beyond the results achieved here in terms of cluster size distribution and the nature of core beams would become possible.

6.2 Temperature of the Cluster-Jet

Not only the cluster size distribution but also their temperature can give further insight into the cluster production process and their behavior within an accelerator vacuum. In [Wei23] simulations on the evaporation of clusters in vacuum were performed. One parameter simulated is the temperature of these clusters. For a cross check, the temperature of the clusters close to the nozzle exit needs to be determined.

6.2.1 Placement of a Temperature Diode within the Cluster-Jet

For measuring the temperature of the cluster-jets resulting from the A19 nozzle and the Düsseldorf nozzle a temperature diode is installed at the nozzle shutter. The distance from the nozzle exit to the temperature diode is 22.5 mm for the A19 nozzle and 4 mm for the Düsseldorf nozzle. With a heat barrier of polyimide the heat transfer from the nozzle shutter and the vacuum chmabers at room temperature towards the diode and its cabling is minimized. As this diode nevertheless cannot be perfectly isolated, the measured temperatures are more an upper limit in temperature than an exact value. With the installation at the nozzle shutter, three measurement positions are available: First, the nozzle shutter is moved out of the cluster-jet, i.e., the cluster-jet is undisturbed, second, the nozzle shutter is moved into, i.e., totally blocking the cluster-jet, and third, the nozzle shutter is moved even further so that the diode is moved into the cluster-jet, i.e., only the temperature diode is partly blocking the cluster-jet and hence measuring the temperature. With this, an easy movement for measuring reference values is available.

6.2.2 Performed Temperature Measurements

A first measurement was performed at room temperature. Since the gas is also at room temperature, intention was to see the effect of the gas impinging onto the temperature diode: Is there a temperature increase based on the velocity of the gas molecules? To answer this, the düsseldorf nozzle is kept at room temperature and the temperature diode at the nozzle shutter is read out outside the jet and read out when moved into the jet. While the temperature diode at the cold head shows $T_{\text{nozzle}} = 295.0\,\text{K}$, the temperature diode at the nozzle shutter, not being in the jet, measures $T_{\text{diode}} = 296.1\,\text{K}$, meaning there is nearly no difference between the diodes. After moving the diode into the jet, there is a steep temperature rise that flattens out further to $T_{\text{diode}} = 330.0\,\text{K}$. With studying the literature, the Joule-Thomson effect can explain this large

difference. For many gases (CO_2, nitrogen, oxygen, air, ...) at room temperature an adiabatic expansion, as performed in the diverging nozzle exit, leads to a decrease in temperature [Dem08]. This is also valid for hydrogen at typical CJT operation temperatures. However, for each gas, there is an individual inversion temperature above which the adiabatic expansion leads to an increase in temperature. The inversion temperature of hydrogen is 200 K [Dem08] so that at room temperature the hydrogen is warmed. The extent of this warming cannot be calculated easily due to the complex nozzle geometry. The calculations of A. Täschner commonly adapted and used [Täs12] do not account for this effect. If this Joule-Thomson effect is the only contribution to the temperature increase cannot be validated at this point.

For measuring the cluster-jet temperature, a measurement series in the gaseous regime and in the liquid regime was performed each with the A19 nozzle and the Düsseldorf nozzle. In the gaseous regime, at a temperature of 50 K, different pressures are set between 2 bar and 19 bar. After a few minutes of stabilizing the temperature can be read off. With a larger pressure, the flow through the nozzle increases and the effect of heat conductivity and heat radiation onto the temperature diode is relatively reduced. In the liquid regime, at 25 K pressures between 5 bar and 19 bar are set. Upon hitting the temperature diode it can be clearly seen visually that a condensation nucleus is given and the clusters freeze onto the diode. This shows that close to the nozzle exit an undercooled liquid (below 14 K, apparent in the data) is present. The freezing process releases energy resulting in a steep increase to a temperature of 14 K, the freezing temperature. For measuring the real temperatures, the diode is moved out of and into the cluster-jet five times, and the coldest temperature measured is determined, as this possibly is the temperature before the freezing process started.

Additionally, the temperature at the nozzle exit can be simulated based on calculations by A. Täschner [Täs12].

6.2.3 Determined Temperatures of the Cluster-Jet close to the Nozzle Exit

Starting with the measurements at 50 K, for both nozzles a significant decrease in temperature with rising pressure is apparent (see fig. 6.9). With rising pressure the flow through the nozzle and thus the cooling power onto the temperature diode rises. The constant heating effects like the heat conductivity and the heat radiation towards the diode thus become less significant. To describe the flattening behavior of the temperature and obtain a final temperature for an infinite flow, different fit functions
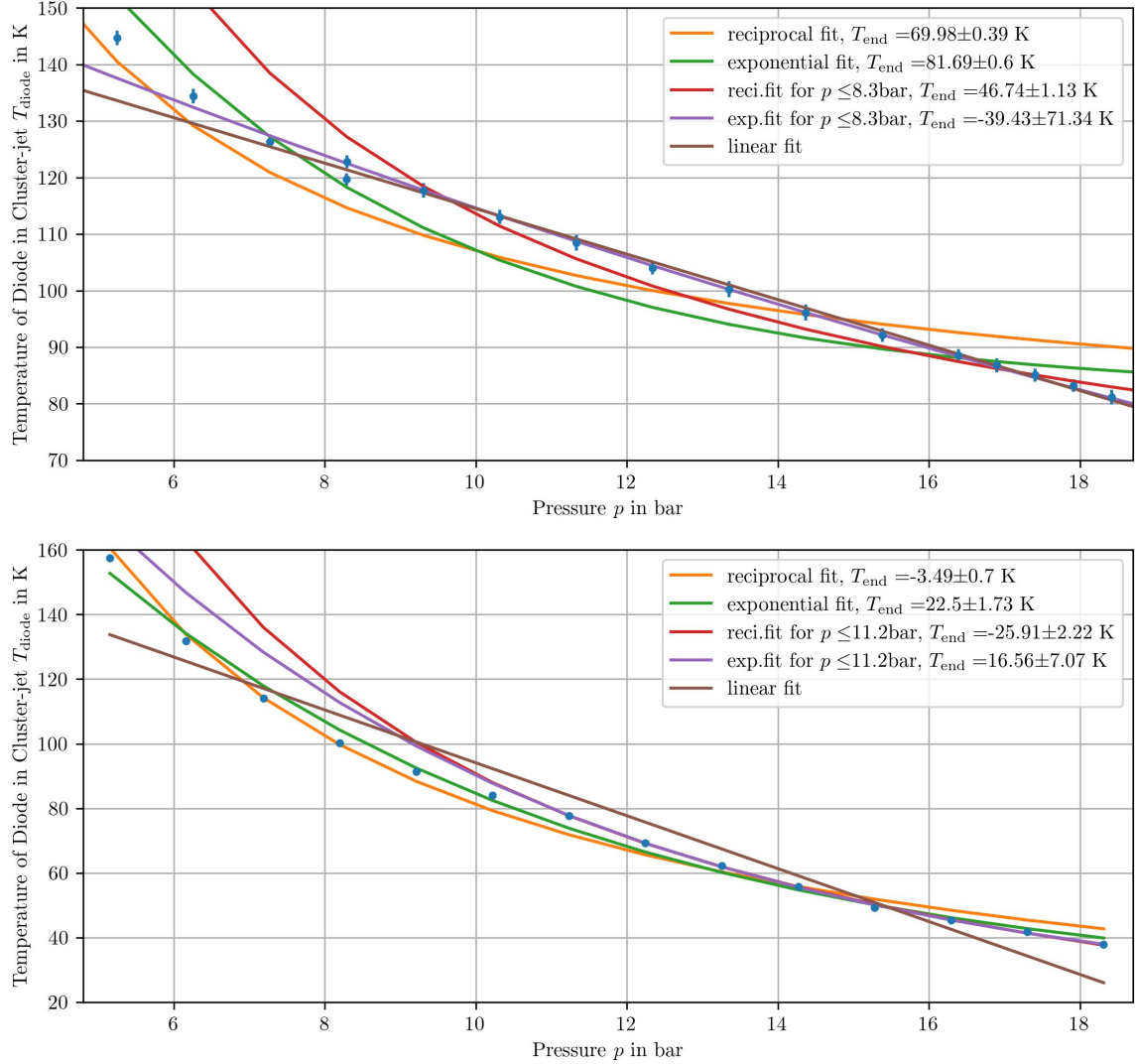
Figure 6.9: Measured temperatures with the Düsseldorf nozzle (top) and the A19 nozzle (bottom) at 50 K. With rising pressure the flow through the nozzle rises and thus the cooling power onto the temperature diode rises leading to lower temperatures. Still, heating effects have a significant influence on the measured temperatures. As an attempt, an exponential and a reciprocal fit with a temperature offset was performed over the total pressure range and also over the high end pressure range. The strong model dependency leads to a broad variety of resulting temperatures. Hence, a determination of the real temperature of the cluster-jet is not possible with this setup. Due to the exchange of the nozzle between the measurements also other boundaries may have changed leading to possible differences in heating. This implies that also a comparison between the measured temperatures for the different nozzles is not meaningful.

are tested. No fit function was found to be suited perfectly for the given course. The obtained temperatures range for the Düsseldorf nozzle from $-39\,\mathrm{K}$ to $82\,\mathrm{K}$ and for the A19 nozzle from $-26\,\mathrm{K}$ to $23\,\mathrm{K}$. The negative temperatures are highly nonphysical and the large differences between the fit functions show that the determination of the real temperature is not possible with this method, whereas the values fluctuate near zero. The corresponding simulated temperatures based on [Täs12] are only slightly dependent on the pressure and equal $(7.6\pm0.4)\,\mathrm{K}$ and $(7.9\pm0.4)\,\mathrm{K}$, respectively. This shows hat this measurement method is generally feasibly once the heat sources are reduced.

The influence of the heat radiation and heat conductance seems to be too large to be neglected. Also the used fit functions for an extrapolation seem to be not suitable. Heat shielding or investigations on the effects that heat the diode are necessary to determine the real cluster-jet temperature in the gaseous regime.

The measurements in the liquid regime are more revealing and can be seen in fig. 6.10. For the Düsseldorf nozzle no direct pressure dependency of the cluster-jet temperature is apparent. In the measurements the diode freezes nearly directly when moved into the cluster-jet. Due to the limited sampling rate, this leads to a larger uncertainty in the temperature determination as the coldest temperature may not have been read out. On average, a temperature close to $10\,\mathrm{K}$ is obtained, which is approximately $2\,\mathrm{K}$ warmer than simulations of the temperature at the nozzle exit based on [Täs12]. For the A19 nozzle, a slight pressure dependency of the temperature is apparent. The simulations based on [Täs12] show a slight increase in temperature for rising pressure, especially in the low pressure regime. This increase is also visible in the measured temperatures in the distance of $22.5\,\mathrm{mm}$ to the nozzle exit. The measured temperatures are close to $10\,\mathrm{K}$ and in average shifted by $2\,\mathrm{K}$ compared to the simulations.

Simulations performed by M. Weide [Wei23] for a stagnation temperature upstream to the nozzle of $24\,\mathrm{K}$ show an additional temperature decrease of the clusters based on evaporation. The temperatures fall below $9\,\mathrm{K}$ before the freezing process is started and an increase in temperature is observed. In these simulations the freezing is finished within $10^{-4}\,\mathrm{ms}$ to $10^{-2}\,\mathrm{ms}$ and thus already within the nozzle outlet. Here it is to mention, that a vacuum pressure of $10^{-5}\,\mathrm{mbar}$ is assumed [Wei23]. Considering real pressures within the nozzle outlet and within the skimmer chamber, the process is probably slowed down. Based on the presented temperature measurements, it can be assumed that the clusters exiting the nozzle are still under-cooled and freeze out upon impacting the temperature diode or otherwise (when there is no temperature diode) within the skimmer or collimator chamber.

Since for the measurements additional heat is introduced by heat conductance and heat radiation, only an upper limit in cluster-jet temperature is given. This upper limit generally strengthens the simulation results by A. Täschner and by M. Weide. Most importantly, the cooling of the clusters below freezing temperature has been measured. Even though starting with a temperature of $25\,\mathrm{K}$ upstream to the nozzle, the resulting clusters are significantly below $14\,\mathrm{K}$ and thus freeze out in their flight path through vacuum. This is an important property in order to maintain the high vacuum conditions of, e.g., an accelerator.
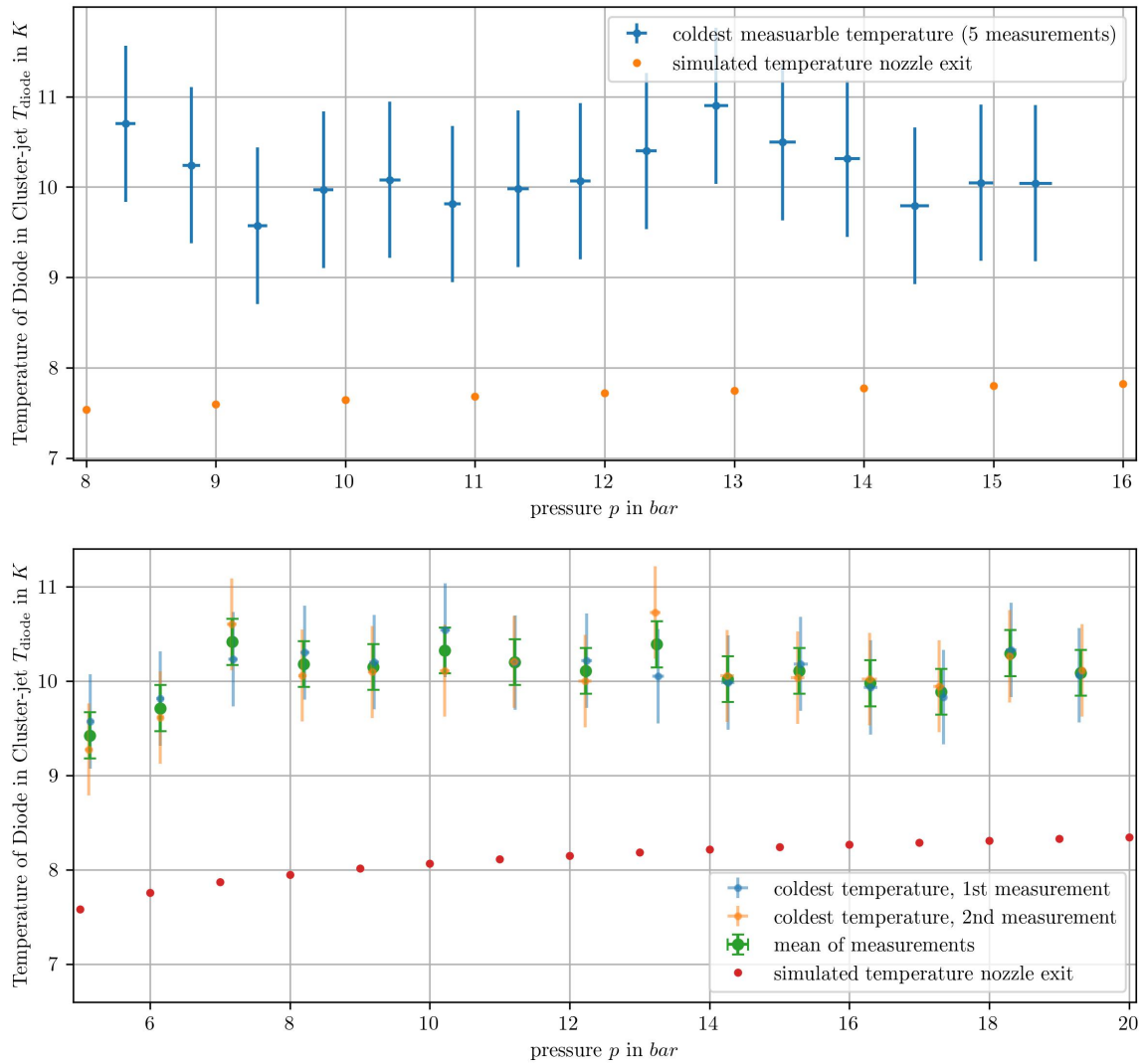
Figure 6.10: Measured and simulated temperatures with the Düsseldorf nozzle (top) and the A19 nozzle (bottom) at $25\,\mathrm{K}$. Only for the A19 nozzle a slight pressure dependency of the measured temperatures is apparent. The course follows the simulated temperatures based on [Täs12]. Here, a shift of in average $2\,\mathrm{K}$ is present.

Chapter 7

Conclusion and Outlook

This thesis focused on the study and optimization of existing MCT parts in combination with the characterization of the resulting cluster and cluster-jet properties.

For the final MCT-$\overline{\text{P}}$ANDA with its new beam dump (designed in [Bra24]) a **new pumping station** was designed and built up. With this, a clean fore vacuum is provided for the differential beam dump stages and the MCP chamber. Both chambers can be pumped and vented together as well as individually. For intermediate testing this pumping station was used at the MDT-H, where a fore vacuum below 10^{-3} mbar has been confirmed. Currently the pumping station is operated locally, but a more complex control system is in preparation which additionally allows for remote control as necessary for $\overline{\text{P}}$ANDA.

In this new beam dump several cluster-jet diagnostic tools are foreseen as they are in regular use at the MCT-Prototype. One of these handy tools is the **MCP system** consisting of two microchannel plates in chevron assembly with a scintillation screen, which is used for two dimensional cluster-jet visualization and velocity measurement. Such MCP systems have achieved good results as their norm, but their scintillation screens showed significant degradation with exposure to hydrogen ionized by an accelerator beam. As alternative a surface barrier detector was tested, but found to be not sensitive to clusters and thus omitted. Furthermore, an extension of the MCP system by GEM foils was tested to enhance the vacuum surrounding the MCP. In the setup tested the GEM foils did not generate electron avalanches. Applying higher voltages was not found to be successful and additional gas had even a deteriorating influence. Thus, GEM foils were also omitted.

As a third option, the degraded screen of the MCP was up-cycled by replacing the

degraded P43 phosphor with a P46 YAG:Ce phosphor, renewing the ITO layer, and adding an aluminum layer. The used YAG:Ce single crystal is promising to be more chemical and mechanical stable. The MCP was then tested at the MCT-Prototype. It has been found that due to the additional aluminum layer larger voltages are needed for the cluster-jet visualization. With this, the same possibilities as with previous MCP systems were found. A good spatial resolution and intensity is obtained. It was found further, that the TOF measurement is also possible. The obtained signals at the scintillation screen even exceeded the signal height of previous MCP systems, probably due to the additional aluminum layer. With this possibly a measurement with even less background is possible. In the curse of this thesis the new screen did not show any degradation. However, the chemical and mechanical stability against hydrogen ionized by an accelerator beam needs to be finally measured. Still, the additional aluminum layer already proved its potential in enhancing visual intensity and signal strength and thus definitely should be added to upcoming MCP systems.

With the MCT-Protoype **the Widom line has been measured** for the first time for hydrogen. The two completely different cluster production mechanisms in the gaseous and in the liquid regime provide a great tool to study the phase of the fluid upstream to the nozzle with an MCT. The processes extend into the liquid-like and the gas-like regime which are separated by the Widom line. In order to distinguish between these two cluster production processes the cluster-jet density, the mean velocity, and the velocity standard deviation were investigated. All three properties show a significant step with the phase transition. Especially **the standard deviation of the cluster-jet velocity distribution separates the liquid(-like) and gas(-like) phases** being present upstream to the nozzle. With this not only the Widom line as higher order phase transition can be measured but also the vapor pressure curve as first order phase transition. Further, this allows for a precise **temperature calibration** of the temperature diode at its complex surroundings of the cold stage in the cluster source. This was already used together with M Scharpey [Sch24] in a slightly adapted manner to determine the temperature offset with a precision of $0.0011\,\text{K}$.

For the nozzle production for MCT some advances were obtained in this thesis. Glass nozzles had to be omitted for the use at CJTs but should be reconsidered for solely gaseous target materials or the use at droplet targets. For the first time copper de Laval nozzles were produced totally in-house. With this, great possibilities open up considering variations on the nozzle design. Within this thesis **eight nozzles were successfully produced** starting from 13 galvanization processes leading to a rejection

rate of 36 % which is a great improvement to previous batches. Since only five of these eight nozzles are in the desired narrowest diameter range, further optimization of the process is necessary, also in respect to the obtained cluster-jet properties from these nozzles. Still, also the three "too large" nozzles can be used, e.g., for MCTs with other gases or for the bending system of the MDT-H.

There are a few possibilities on how to advance the nozzle production. The first proposition is to build a compound nozzle using nozzles with galvanized outlet which cannot be turned into working nozzles. This outlet shall be used together with an orifice including a conical inlet as was used for the orifice nozzle within this thesis. This is currently already tested in [Wei24] with first promising results. Furthermore, one consistency in the difficulties of manufacturing copper nozzles is finding the nozzle outlet negative from the inlet side. Further investigations on this could provide important insights.

Additionally, investigation on the influence of the outer nozzle geometry was started. Since small nozzles need to be placed in an adapter to fit in the same nozzle holder as the large nozzles, an additional heat barrier is introduced. A first measurement showed, that this heat barrier has an influence on the nozzle temperature. Whether this also has a temperature influence on the fluid, cannot be determined here. The measurement of the temperature offset based on the Widom line measurement presented here can answer this question. A complementary measurement to the measurement with large outer nozzle geometry as performed with M. Scharpey [Sch24] needs to be performed with a nozzle with small outer geometry. Based on the results the outer geometry for new nozzles can be specified, whereas the smaller geometry is preferable.

In order to **characterize optimal nozzles** core beam structures were analyzed. The core beams are the most important quality feature since these provide the largest densities. Angle dependent velocity and density studies showed, that for the core beams as the density maximizes the mean velocity is minimized. Studying the velocity distribution within and outside of the core beam, significant differences were observed. The double peaking structure hints towards two different cluster production processes for core beam and residual cluster-jet. One possible explanation is the formation of a liquid filament as the liquid hydrogen that has been accelerated in the inlet decouples from the nozzle walls. This filament would be surrounded by already atomized hydrogen serving as coflowing gas. With this, the breakup length of the filament is enlarged leading to a stable, slow cluster-jet with larger clusters. To further study this, the measurement of cluster sizes is important.

To determine **which size(-distribution) the clusters within the cluster-jet have**, several methods were tested, especially in the liquid regime. With shadowgraphy a limited size distribution has been determined. The 3-WEM was performed successfully with water sprays, but unfortunately found to be not sensitive to cluster-jets. A setup measuring Mie scattering in forward direction was set up for the first time in Münster and shown to be sensitive enough.

The performed measurements using shadowgraphy are limited to cluster sizes larger than the Abbe diffraction limit of 2.9 μm and smaller than approximately 10 μm due to the selection criteria, which is afar from the determined distribution. The mean cluster sizes obtained with H. Eick [Eic23] range from 4.6 μm to 5.6 μm with standard deviations of 0.73 μm to 1.16 μm. This accounts for $(46.8 \pm 6.4)\,\%$ to $(78.3 \pm 12.4)\,\%$ of the flow through the nozzle in the clusters. There are a significant amount of clusters below the Abbe diffraction limit but possibly there could be single clusters larger than the considered region. For a future setup in Münster in [Eic24, Fis24] the Abbe limit needs to be pushed towards lower cluster sizes and the region above 10 μm should also be considered. A reevaluation of the analyzed shadowgraphy data regarding larger clusters should also be performed.

The performed measurements of the Mie scattering in forward direction prove most importantly the general feasibility at large distances from the nozzle. This is necessary to perform cluster size studies dependent on the nozzle angle, especially in combination with velocity and density studies. A significant background reduction was performed and the proportionality between scattered light and cluster-jet thickness was measured. A first measurement of Mie intensity at several forward angles hint towards clusters exceeding 10 μm in diameter. Further background reduction and especially a motorized angle measurement is needed for more significant studies.

Furthermore, the **cluster-jet temperature close to the nozzle exit** was measured. In the gaseous region the influence of heat radiation and conductance is too large to be neglected and prevents the determination of the cluster-jet temperature. In the liquid regime the heat radiation and conductance also has an influence, but this seems to be neglectable. Here, cluster-jet temperatures of approximately 10 K and thus below freezing temperature are measured. On impact on the temperature diode used for the measurement, a rapid freezing process has been observed. This shows that a few millimeters behind the nozzle outlet, the cluster-jet is in an undercooled state. This confirms the temperatures obtained in simulations [Wei23], even though slight differences were observed. An additional measurement of the cluster-jet temperature at larger distances to the nozzle would be interesting.

Within this thesis several milestones were reached and interesting knowledge was gained. The pumping station for the $\overline{\text{P}}$ANDA CJT beam dump was set up, a possibly more robust MCP system was tested, and the Widom line was measured. A new method for temperature calibration of the cluster source was found and the temperature of the cluster-jet gave insight into the undercooled state of the clusters close to the nozzle exit. For the first time nozzles with narrowest diameters close to 30 μm have been produced totally in-house and further core beam studies were performed. Important advances in cluster size measurement have been obtained, which will be further refined in the future in respect to enlarging the range in obtainable diameters. Steps towards the origin of core beams were taken but this need to be studied further. Especially the angle dependent velocity, density, and most importantly cluster size measurement will be an important tool to better understand cluster-jets and especially the nature of core beams. With this the possible interpretation of core beams resulting from a liquid filament surrounded by coflowing atomized hydrogen can be confirmed or rejected. Here, the study of the CERN nozzle, reaching the highest densities, is of high relevance. With these results, a further optimization in nozzle production is obtainable allowing for the production of high class nozzles exceeding the current expectations.

A Supplemental Material for Produced and Tested Nozzles

In chapter 4 different nozzles were produced, ordered, and tested. Here, the supplementary material will be presented. First, microscopic images of the glass nozzles produced by LightFab as presented in section 4.2.1 and of the in section 4.2.2 described copper nozzles are shown together with already existing copper de Laval nozzles for comparison are shown. Furthermore, interesting properties of the nozzles are listed.

A.1 Microscopic Images of the Nozzle Inlets and Images of the Cluster-Jet within the SC

The investigation of nozzles with light microscopy is an important every day tool. It is used for a first investigation of the fabricated nozzle but also used to determine if the nozzle is clogged. The estimated diameter can be used to determine if the nozzle is installed correctly without leakage and without clogging by comparison with the determined flow through the nozzle.

From the microscopic images of the produced nozzles the most prominent were chosen to be tested in the MCT-Prototype. At first, the visual appearance of the cluster-jet within the skimmer chamber gives a first impression on the nozzle performance. Especially the stability of the resulting cluster-jet can be seen here, as well as the core beam structures.
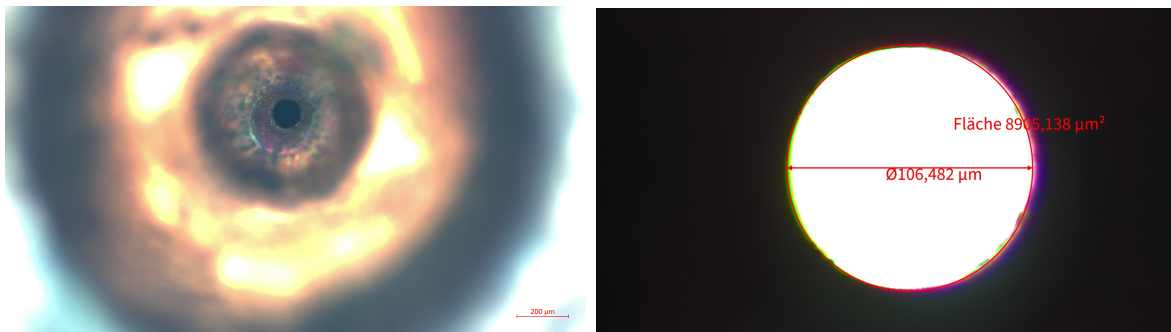
Figure A.1: Microscopic images of nozzle 2203. *Left:* Nozzle inlet. No drilling marks can be seen, but a rather smooth inlet surface. This is due to the follow up processing by acid to achieve a connection between inlet and outlet. *Right:* Narrowest section illuminated with transmitted light. The estimated nozzle diameter is 106.5 µm.
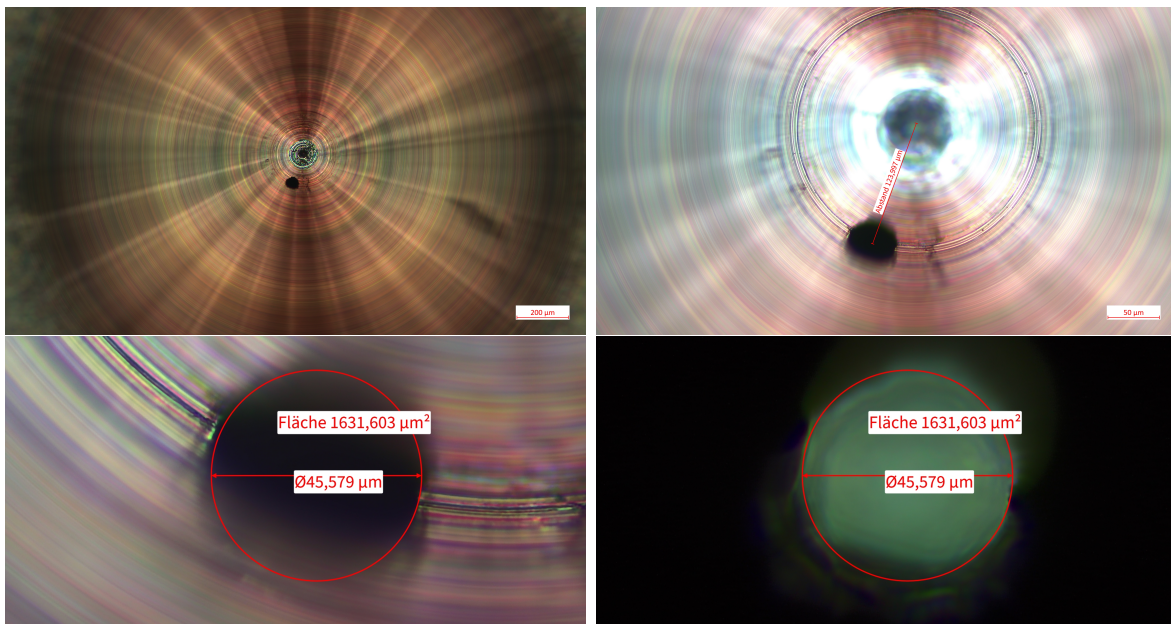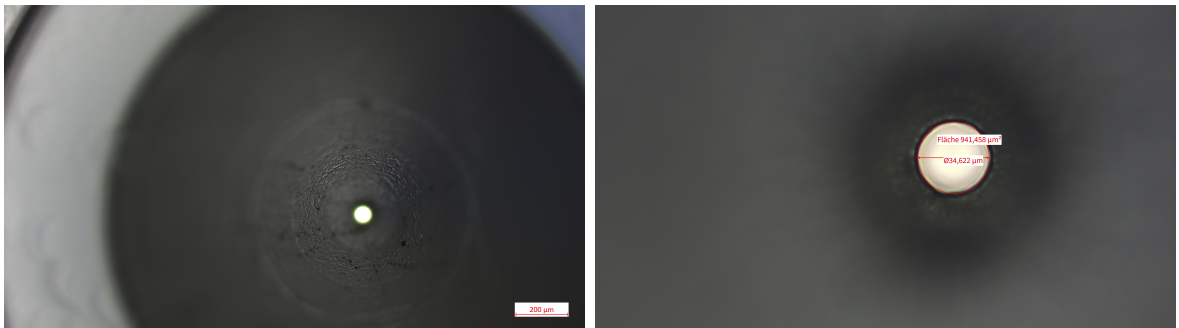

Figure A.2: Microscopic images of nozzle 2301. *Upper left:* Nozzle inlet. *Upper right:* Center of the inlet. The narrowest section is shifted radially by 124 µm. *Lower left:* Narrowest section illuminated with incident light. *Lower right:* Narrowest section illuminated with transmitted light. The narrowest cross section does not form a circular shape but has an irregular shape. The estimated nozzle diameter is 45.6 µm.
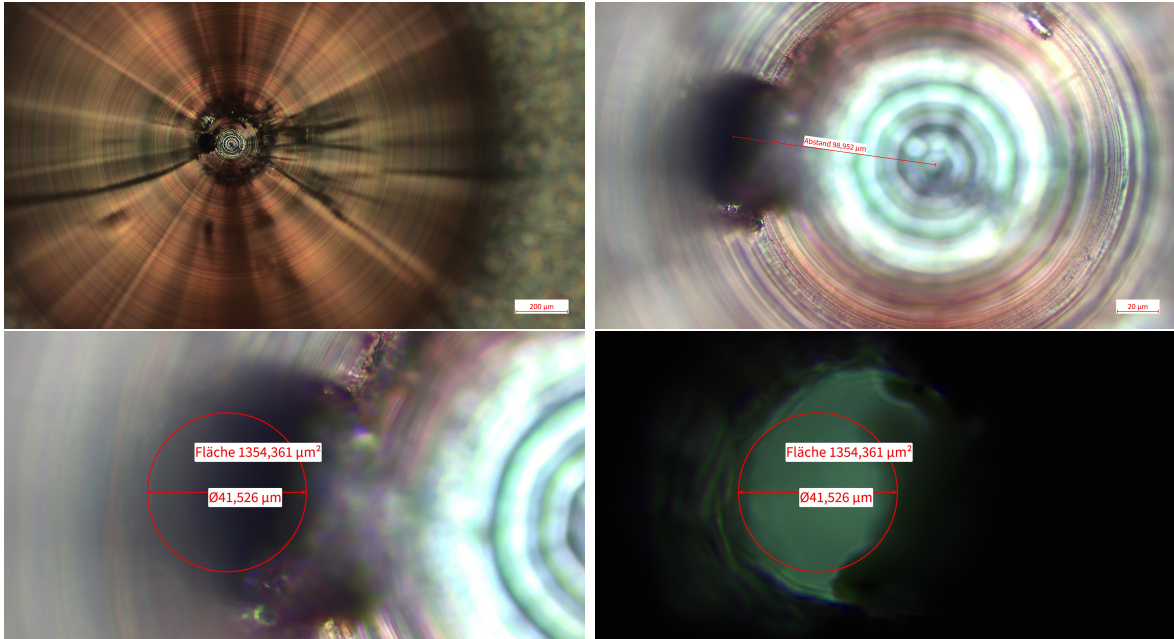
Figure A.3: Microscopic images of nozzle 2303. *Upper left:* Nozzle inlet. *Upper right:* Center of the inlet. The narrowest section is shifted radially by 99 μm. *Lower left:* Narrowest section illuminated with incident light. *Lower right:* Narrowest section illuminated with transmitted light. The narrowest cross section does not form a circular shape but has an irregular shape. The estimated nozzle diameter is 41.5 μm.
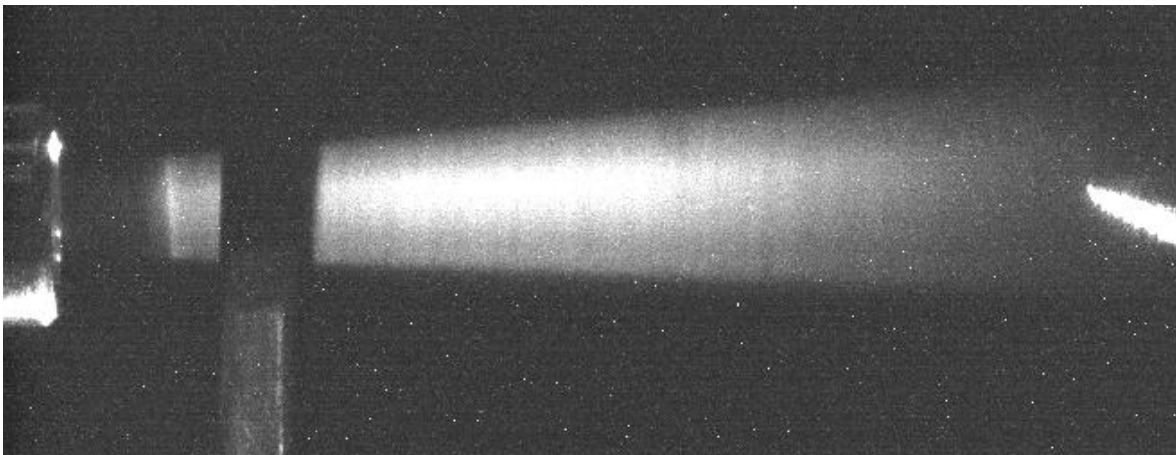
Figure A.4: Cluster-jet resulting from nozzle 2303 at 27 K and 16 bar within the skimmer chamber. On the left the nozzle exit is visible, in the lower left the nozzle shutter can be seen blocking parts of the illumination from below. On the right the skimmer tip is visible. No significant core beam structures are visible.
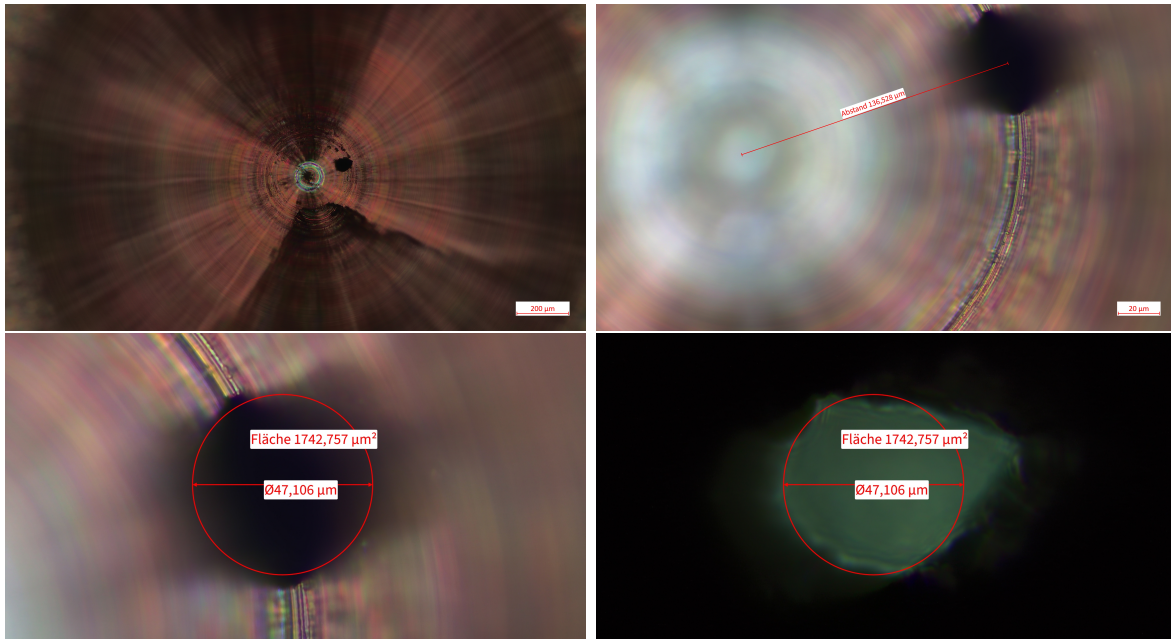
Figure A.5: Microscopic images of nozzle 2304. *Upper left:* Nozzle inlet. *Upper right:* Center of the inlet. The narrowest section is not centered as desired but shifted radially by 137 μm. *Lower left:* Narrowest section illuminated with incident light. *Lower right:* Narrowest section illuminated with transmitted light. The narrowest cross section does not form a circular shape but has an irregular shape. The estimated nozzle diameter is 47.1 μm.
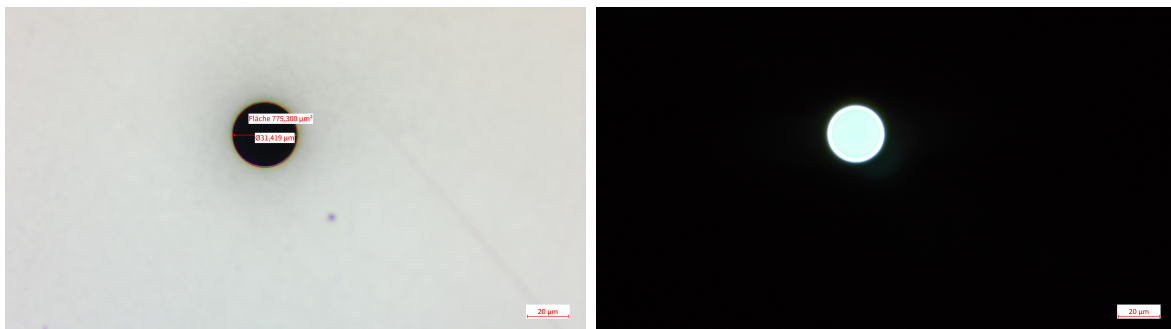
Figure A.6: Microscopic images of orifice nozzle. *Left:* Nozzle inlet in incident light. The nozzle diameter is 31.4 μm. *Right:* Nozzle inlet in transmitted light. The perfect circular shape is apparent.

Figure A.7: Cluster-jet resulting from orifice nozzle at $25\,\mathrm{K}$ and $13\,\mathrm{bar}$ within the skimmer chamber. On the left the nozzle exit is visible, in the lower left the nozzle shutter can be seen blocking parts of the illumination from below. On the right the skimmer tip is visible. A significantly larger divergence of the jet and a border not as prominent compared to other nozzles is apparent.

Figure A.8: Microscopic images of $18\,\mathrm{mm}$ glass nozzle. *Left:* Nozzle inlet. *Right:* Narrowest section. The estimated nozzle diameter is $34.6\,\mathrm{\mu m}$.
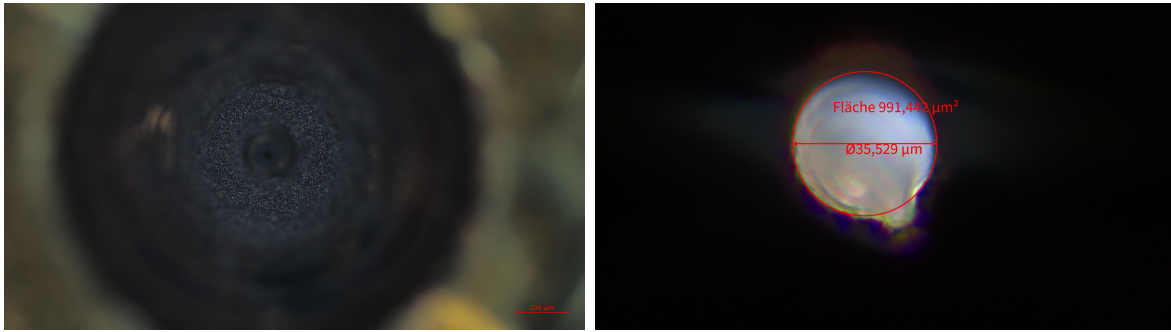
Figure A.9: Microscopic images of A19 nozzle. *Left:* Nozzle inlet. *Right:* Narrowest section illuminated with transmitted light. The narrowest cross section does not form a circular shape but has an irregular shape. The estimated nozzle diameter is $35.5\,\mu$m.
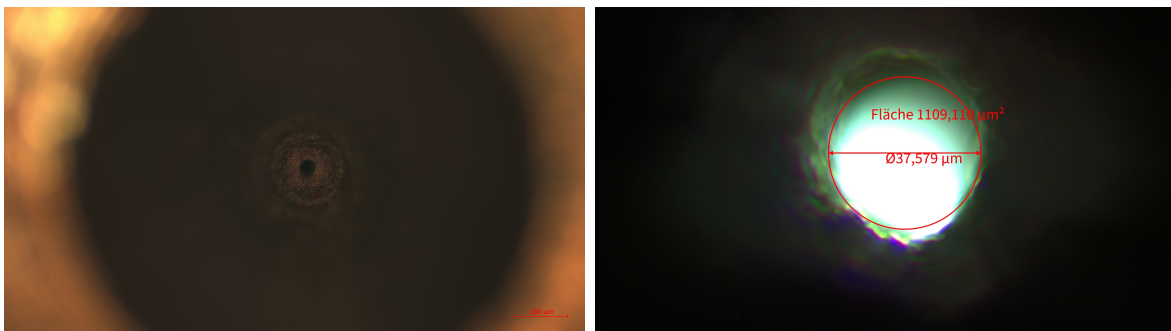
Figure A.10: Microscopic images of the düsseldorf nozzle. *Left:* Nozzle inlet. *Right:* Narrowest section illuminated with transmitted light. The narrowest cross section does not form a circular shape but has an irregular shape. The estimated nozzle diameter is $37.6\,\mu$m.
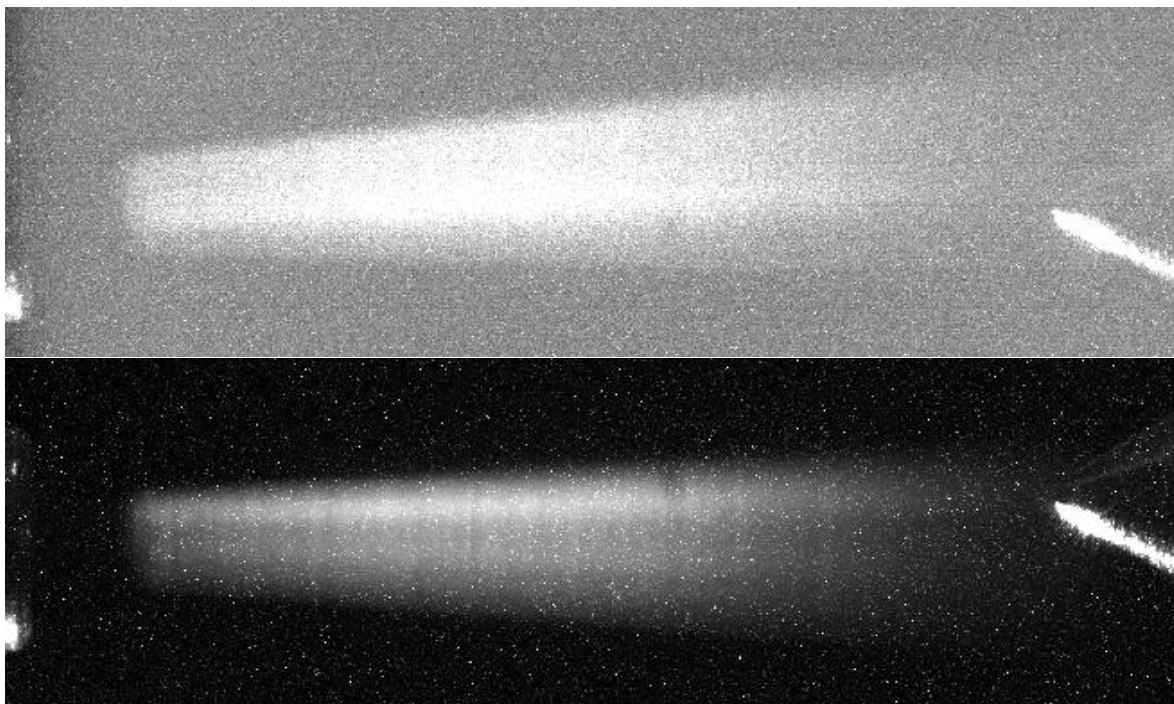
Figure A.11: Cluster-jet resulting from DD-nozzle at 24 K and 10 bar (top) and 28 K and 10 bar (bottom) within the skimmer chamber. On the left the nozzle exit is visible, and on the right the skimmer tip. Due to different illumination times the contrast for the bottom picture is enhanced. The temperature difference of 4 K results in totally different core beam structures and location.

A.2 Obtained Velocities and Densities

For the final assessment of the nozzle performance, quantifying properties need to be taken into account. First, the nozzle diameter is important as it quantifies the hydrogen consumption and the residual gas background. But, most important are the reached densities. These properties are listed here for all tested nozzles.

Table A.1: Measured mean velocities v_{mean} with its standard deviations $\mathrm{std}(v)$, volume densities, and thicknesses (in a distance of $2.1\,\mathrm{m}$) for different stagnation temperatures T and stagnation pressures p for the nozzle 2202. The measurements marked with * are measured with the YAG:Ce-MCP system in the second BD stage and the other measurements with the channeltron system directly behind the gate valve. For the * measurements the e-gun did not work perfectly leading to enlarged uncertainties in the start time. With this possible slower velocities than measured were actually present, which would lead to even higher densities. The highest obtained density is highlighted.

stagn. cond.		state of fluid	v_{mean} [m/s]	$\mathrm{std}(v)$ [m/s]	volume density [atoms/cm^3]	thickness [atoms/cm^2]
T [K]	p [bar]					
21	7	liquid	380 ± 15*	64.6	$(1.9 \pm 0.1) \times 10^{13}$	$(2.4 \pm 0.1) \times 10^{13}$
21	10	liquid	375 ± 15*	54.8	$(2.9 \pm 0.2) \times 10^{13}$	$(3.4 \pm 0.2) \times 10^{13}$
21	13	liquid	365 ± 15*	49.8	$(3.0 \pm 0.1) \times 10^{13}$	$(3.9 \pm 0.2) \times 10^{13}$
21	16	liquid	345 ± 15*	74.7	$(3.9 \pm 0.2) \times 10^{13}$	$(4.9 \pm 0.2) \times 10^{13}$
21	19	liquid	385 ± 15*	53.0	$(3.2 \pm 0.1) \times 10^{13}$	$(4.0 \pm 0.2) \times 10^{13}$
24	10	liquid	365 ± 15*	61.9	$(3.5 \pm 0.2) \times 10^{13}$	$(4.2 \pm 0.2) \times 10^{13}$
24	13	liquid	315 ± 15*	67.6	$(9.1 \pm 0.5) \times 10^{13}$	$(1.1 \pm 0.1) \times 10^{14}$
24	16	liquid	260 ± 15*	68.9	$(8.2 \pm 0.5) \times 10^{13}$	$(1.1 \pm 0.1) \times 10^{14}$
double peak at 190 and 300 m/s						
27	10	liquid	400 ± 20*	76.2	$(1.4 \pm 0.1) \times 10^{13}$	$(1.8 \pm 0.1) \times 10^{13}$
27	13	liquid	410 ± 20*	73.2	$(1.9 \pm 0.1) \times 10^{13}$	$(2.4 \pm 0.1) \times 10^{13}$
27	16	liquid	370 ± 15*	74.3	$(6.2 \pm 0.3) \times 10^{13}$	$(7.2 \pm 0.3) \times 10^{13}$
30	16	liquid	470 ± 20*	50.7	$(1.6 \pm 0.1) \times 10^{13}$	$(1.8 \pm 0.1) \times 10^{13}$
40	7	gas	795 ± 70*	97.1	$(2.1 \pm 0.2) \times 10^{11}$	$(2.7 \pm 0.2) \times 10^{11}$
40	16	gas-like	705 ± 70*	83.1	$(4.8 \pm 0.5) \times 10^{11}$	$(7.3 \pm 0.7) \times 10^{11}$
24	7	liquid	408.5 ± 1.9	75.6	$(3.6 \pm 0.1) \times 10^{13}$	$(4.2 \pm 0.1) \times 10^{13}$
24	10	liquid	407.8 ± 1.9	73.9	$(3.9 \pm 0.1) \times 10^{13}$	$(4.8 \pm 0.1) \times 10^{13}$
24	13	liquid	411.5 ± 1.9	80.0	$(3.7 \pm 0.1) \times 10^{13}$	$(4.5 \pm 0.1) \times 10^{13}$
24	16	liquid	413.9 ± 1.9	76.8	$(1.0 \pm 0.1) \times 10^{14}$	$(1.2 \pm 0.1) \times 10^{14}$
27	10	liquid	455.4 ± 2.1	84.6	$(3.9 \pm 0.2) \times 10^{13}$	$(4.5 \pm 0.1) \times 10^{13}$
27	13	liquid	475.1 ± 2.2	75.0	$(4.0 \pm 0.1) \times 10^{13}$	$(4.9 \pm 0.1) \times 10^{13}$
27	16	liquid	484.2 ± 2.2	73.8	$(4.2 \pm 0.1) \times 10^{13}$	$(5.1 \pm 0.1) \times 10^{13}$
40	7	gas	911.5 ± 4.3	9.2	$(7.6 \pm 0.2) \times 10^{11}$	$(9.5 \pm 0.2) \times 10^{11}$
40	10	gas	859.9 ± 4.0	11.4	$(6.3 \pm 0.1) \times 10^{11}$	$(9.1 \pm 0.1) \times 10^{11}$
40	16	gas-like	794.2 ± 3.7	17.4	$(8.7 \pm 0.1) \times 10^{11}$	$(1.3 \pm 0.1) \times 10^{12}$
50	16	gas-like	876.7 ± 4.1	19.4	$(1.3 \pm 0.1) \times 10^{11}$	$(1.8 \pm 0.1) \times 10^{11}$

Table A.2: Measured mean velocities v_{mean} with its standard deviations $\mathrm{std}(v)$, volume densities and thicknesses (in a distance of $2.1\,\mathrm{m}$) for different stagnation temperatures T and stagnation pressures p for the nozzle 2302. The highest obtained density is highlighted.

| stagn. cond. | | state | v_{mean} | $\mathrm{std}(v)$ | volume density | thickness |
T [K]	p [bar]	of fluid	[m/s]	[m/s]	[atoms/cm^3]	[atoms/cm^2]
24	10	liquid	540.3 ± 2.4	71.6	$(4.5 \pm 0.1) \times 10^{13}$	$(5.4 \pm 0.1) \times 10^{13}$
24	12	liquid	566.3 ± 2.5	51.8	$(4.6 \pm 0.1) \times 10^{13}$	$(5.3 \pm 0.2) \times 10^{13}$
24	13	liquid	554.2 ± 2.5	66.6	$(4.6 \pm 0.1) \times 10^{13}$	$(5.5 \pm 0.1) \times 10^{13}$
24	16	liquid	620.7 ± 2.8	52.7	$(2.6 \pm 0.1) \times 10^{13}$	$(3.2 \pm 0.1) \times 10^{13}$
27	13	liquid	678.0 ± 3.0	50.4	$(1.5 \pm 0.1) \times 10^{13}$	$(1.8 \pm 0.1) \times 10^{13}$
27	16	liquid	646.3 ± 2.9	66.1	$(2.7 \pm 0.1) \times 10^{13}$	$(3.2 \pm 0.1) \times 10^{13}$
30	16	liquid	705.3 ± 3.2	36.9	$(3.0 \pm 0.1) \times 10^{13}$	$(3.4 \pm 0.1) \times 10^{13}$

Table A.3: Measured mean velocities v_{mean} with its standard deviations $\mathrm{std}(v)$, volume densities, and thicknesses (in a distance of $2.1\,\mathrm{m}$) for different stagnation temperatures T and stagnation pressures p for the nozzle 2303. The highest obtained density is highlighted.

| stagn. cond. | | state | v_{mean} | $\mathrm{std}(v)$ | volume density | thickness |
T [K]	p [bar]	of fluid	[m/s]	[m/s]	[atoms/cm^3]	[atoms/cm^2]
24	6	liquid	490.9 ± 2.2	54.5	$(7.3 \pm 1.1) \times 10^{13}$	$(7.0 \pm 0.2) \times 10^{13}$
24	9	liquid	468.2 ± 2.1	49.8	$(9.6 \pm 0.2) \times 10^{13}$	$(7.0 \pm 0.2) \times 10^{13}$
24	12	liquid	587.7 ± 2.6	58.5	$(4.7 \pm 0.2) \times 10^{13}$	$(4.5 \pm 0.1) \times 10^{13}$
27	6	liquid &	783.3 ± 3.5	128.5	not possible as pulsating beam	
		gaseous	double peak at 650 and 900 m/s			
27	9	liquid	628.2 ± 2.8	42.8	$(3.7 \pm 0.2) \times 10^{13}$	$(4.1 \pm 0.1) \times 10^{13}$
27	12	liquid	664.1 ± 3.0	50.5	$(3.4 \pm 0.2) \times 10^{13}$	$(3.1 \pm 0.1) \times 10^{13}$
27	15	liquid	687.9 ± 3.0	43.4	$(3.1 \pm 0.2) \times 10^{13}$	$(3.4 \pm 0.1) \times 10^{13}$
30	12	liquid	628.4 ± 2.8	48.1	$(1.1 \pm 0.1) \times 10^{14}$	$(1.3 \pm 0.1) \times 10^{14}$
30	15	liquid	681.0 ± 3.1	44.8	$(9.8 \pm 0.2) \times 10^{13}$	$(1.1 \pm 0.1) \times 10^{14}$
30	17	liquid	680.9 ± 3.1	39.2	$(8.8 \pm 0.2) \times 10^{13}$	$(1.1 \pm 0.1) \times 10^{14}$
40	10	gaseous	1109.3 ± 5.1	16.7	$(1.2 \pm 0.1) \times 10^{12}$	$(1.5 \pm 0.1) \times 10^{12}$
40	15	gas-like	1058.3 ± 4.9	17.5	$(3.5 \pm 0.2) \times 10^{12}$	$(4.0 \pm 0.1) \times 10^{12}$

Table A.4: Measured volume densities and thicknesses (in a distance of $2.1\,\mathrm{m}$) for different stagnation temperatures T and stagnation pressures p for tested nozzles. Since velocity measurements were not performed, the mean velocities v_{mean} are calculated based on [Täs12]. Especially for the simple orifice nozzle these calculations are dubious since there is no diverging outlet which is basis to the calculations.

| stagn. cond. | | state | v_{mean} | volume density | thickness |
T [K]	p [bar]	of fluid	[m/s]	[atoms/cm^3]	[atoms/cm^2]
Converging inlet orifice without outlet					
23	17	liquid	266.2 ± 13.5	$(7.1 \pm 0.4) \times 10^{11}$	$(9.6 \pm 0.5) \times 10^{11}$
25	13	liquid	268.1 ± 13.6	$(5.0 \pm 0.3) \times 10^{11}$	$(7.0 \pm 0.4) \times 10^{11}$
Glass nozzle with full length					
35	16	gas-like	710.8 ± 36.1	$(4.5 \pm 0.2) \times 10^{13}$	$(4.9 \pm 0.3) \times 10^{13}$

Table A.5: Measured mean velocities v_{mean} and thicknesses (in a distance of $2.1\,\mathrm{m}$) for different stagnation temperatures T and stagnation pressures p for the A19 nozzle. The highest obtained density is highlighted. The data was obtained from [Ves18] (*) and together with M. Scharpey [Sch24] at the "new Prototype source". The highest thickness was measured by S. Grieser in [Gri18] (**).

stagn. cond. T [K]	p [bar]	state of fluid	v_{mean} [m/s]	thickness [atoms/cm^2]
27	16	liquid	480 ± 2*	$(2.5 \pm 0.1) \times 10^{14}$
25	10	liquid	425 ± 2*	$(2.5 \pm 0.1) \times 10^{14}$
30	14	liquid	560 ± 3*	$(7.8 \pm 0.1) \times 10^{13}$
35	15	liquid-like	782 ± 3*	$(1.7 \pm 0.1) \times 10^{13}$
45	15	gas-like	962 ± 4*	$(3.5 \pm 0.1) \times 10^{12}$
30	7	gaseous	846 ± 4*	$(9.4 \pm 0.1) \times 10^{12}$
45	10	gaseous	1000 ± 4*	$(3.1 \pm 0.1) \times 10^{12}$
27	16	liquid	589.9 ± 2.5	$(5.0 \pm 0.1) \times 10^{13}$
25	10	liquid	524.2 ± 2.2	$(5.0 \pm 0.1) \times 10^{13}$
30	14	liquid	647.6 ± 2.8	$(3.7 \pm 0.1) \times 10^{13}$
35	15	liquid-like	897.8 ± 3.9	$(4.7 \pm 0.1) \times 10^{12}$
45	15	gas-like	989.6 ± 4.3	$(2.2 \pm 0.1) \times 10^{12}$
30	7	gaseous	888.7 ± 3.8	$(2.8 \pm 0.1) \times 10^{12}$
45	10	gaseous	1024.3 ± 4.5	$(1.8 \pm 0.1) \times 10^{12}$
25	18	liquid	**	$(5.36 \pm 0.37) \times 10^{14}$

Table A.6: Measured mean velocities v_{mean} with its standard deviations std(v), volume densities, and thicknesses (in a distance of $2.1\,\mathrm{m}$) for different stagnation temperatures T and stagnation pressures p for the DD-nozzle. The highest obtained density is highlighted. The data was obtained by H. Eick [Eic23].

stagn. cond. T [K]	p [bar]	state of fluid	v_{mean} [m/s]	std(v) [m/s]	volume density [atoms/cm^3]	thickness [atoms/cm^2]
24	6	liquid	522.9 ± 2.5	81.2	$(3.4 \pm 0.1) \times 10^{13}$	$(4.2 \pm 0.1) \times 10^{13}$
24	8	liquid	536.6 ± 2.6	76.9	$(5.6 \pm 0.1) \times 10^{13}$	$(6.8 \pm 0.1) \times 10^{13}$
24	10	liquid	533.3 ± 2.6	60.6	$(8.0 \pm 0.1) \times 10^{13}$	$(9.8 \pm 0.1) \times 10^{13}$
24	12	liquid	510.3 ± 2.5	58.5	$(1.1 \pm 0.1) \times 10^{14}$	$(1.4 \pm 0.1) \times 10^{14}$
24	14	liquid	479.8 ± 2.3	46.9	$(1.6 \pm 0.1) \times 10^{14}$	$(1.8 \pm 0.1) \times 10^{14}$
24	16	liquid	256.1 ± 1.5	68.9	$(2.1 \pm 0.1) \times 10^{14}$	$(2.3 \pm 0.1) \times 10^{14}$
26	16	liquid	506.4 ± 2.4	55.2	$(1.2 \pm 0.1) \times 10^{14}$	$(1.4 \pm 0.1) \times 10^{14}$
28	16	liquid	523.4 ± 2.5	55.1	$(6.6 \pm 0.1) \times 10^{13}$	$(8.2 \pm 0.1) \times 10^{13}$
30	16	liquid	538.9 ± 2.6	45.7	$(5.7 \pm 0.1) \times 10^{13}$	$(6.8 \pm 0.1) \times 10^{13}$
32	16	liquid	597.9 ± 2.9	38.5	$(3.1 \pm 0.1) \times 10^{13}$	$(3.5 \pm 0.1) \times 10^{13}$
40	10	gas	1041.9 ± 5.2	13.1	$(3.0 \pm 0.1) \times 10^{11}$	$(3.9 \pm 0.1) \times 10^{11}$
40	16	gas-like	975.7 ± 4.8	10.9	$(1.7 \pm 0.1) \times 10^{12}$	$(2.4 \pm 0.1) \times 10^{12}$

B Supplemental Measurement Results for the Widom line

In chapter 5 the determination of the Widom line was presented. There, only the measured data and fits for 14 bar were shown. Here, the full set of velocity measurement data is shown as well as the resulting temperature dependent fits together with the determined phase change temperatures.
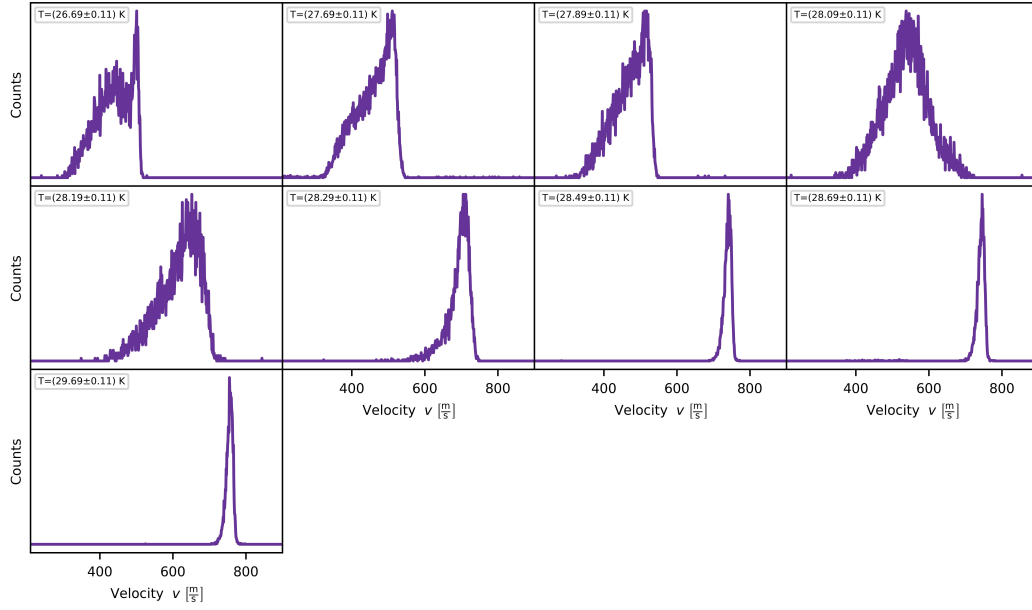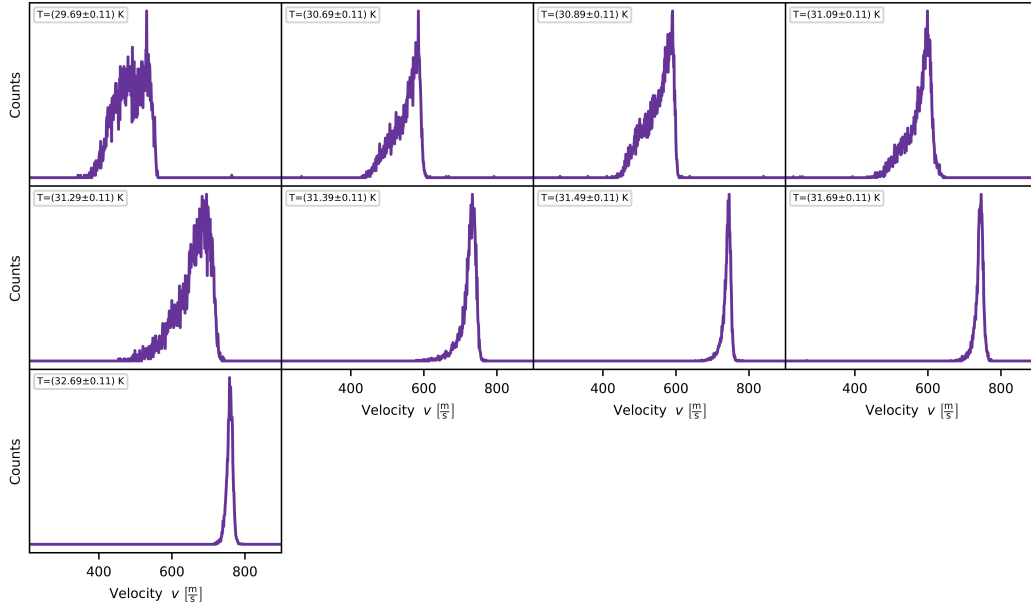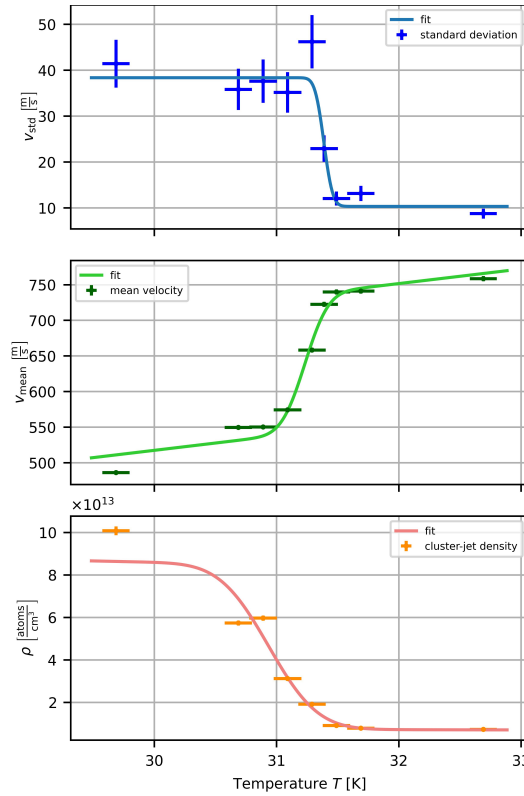
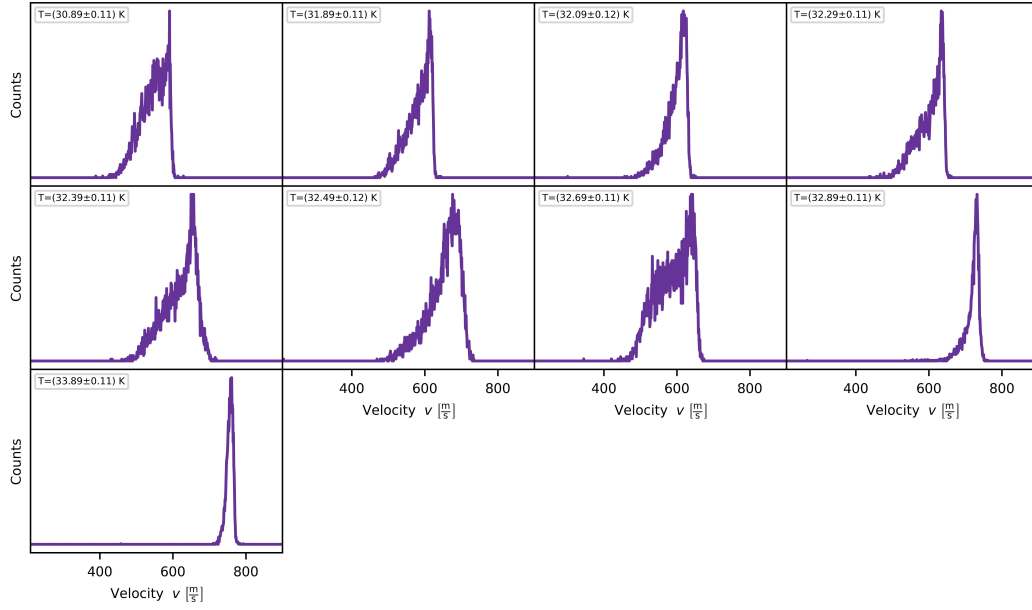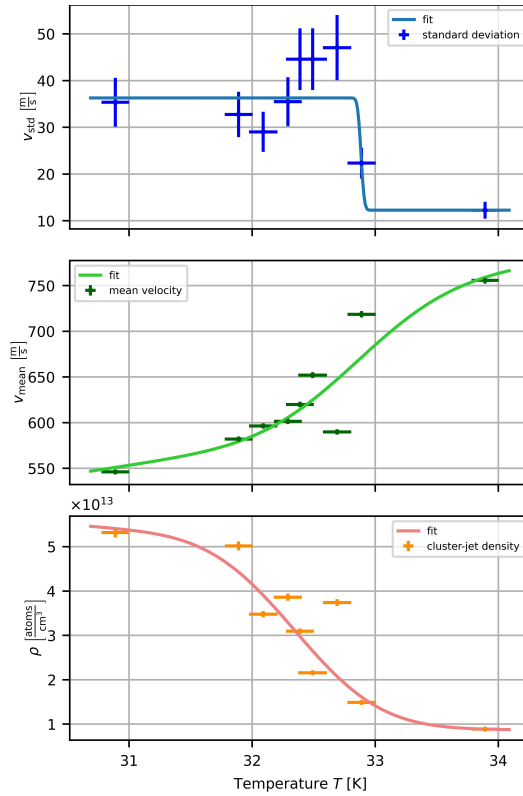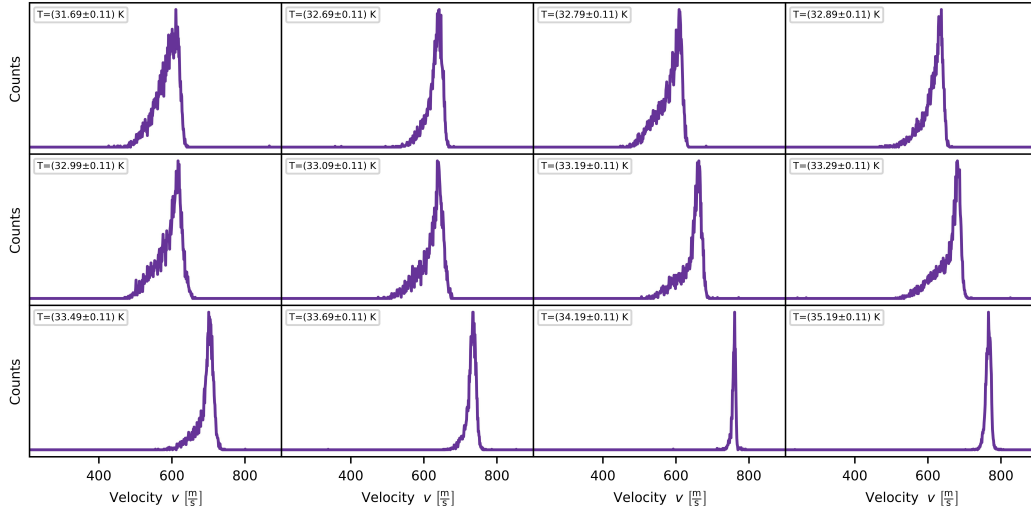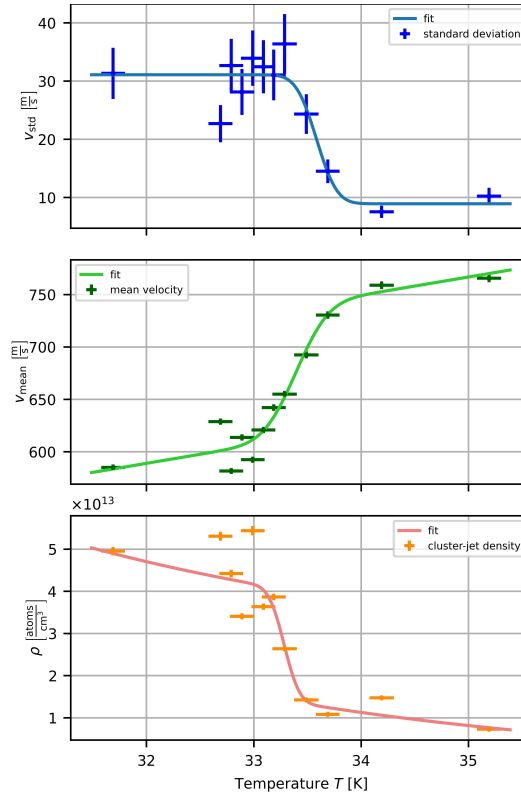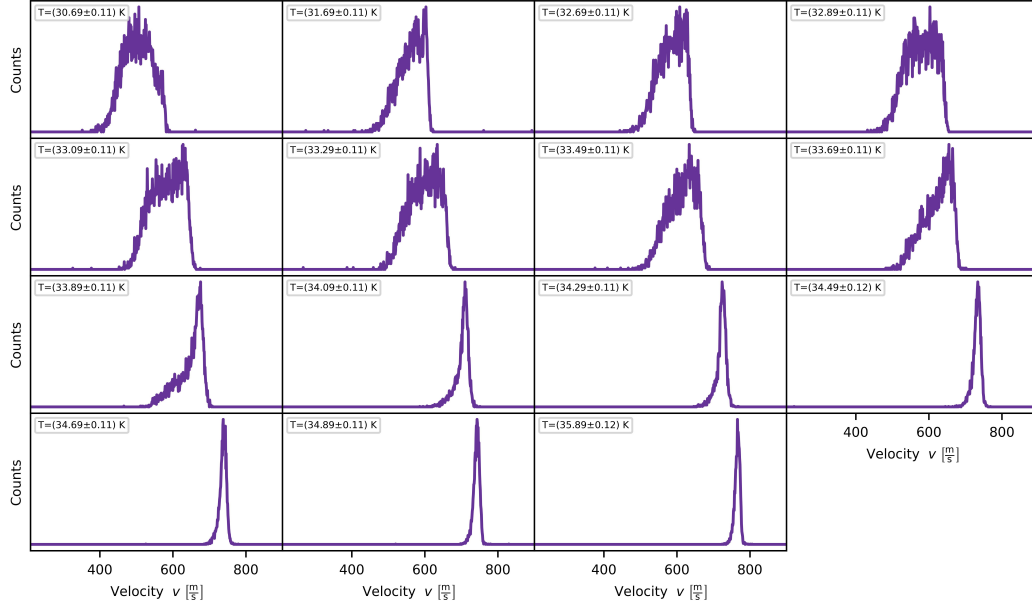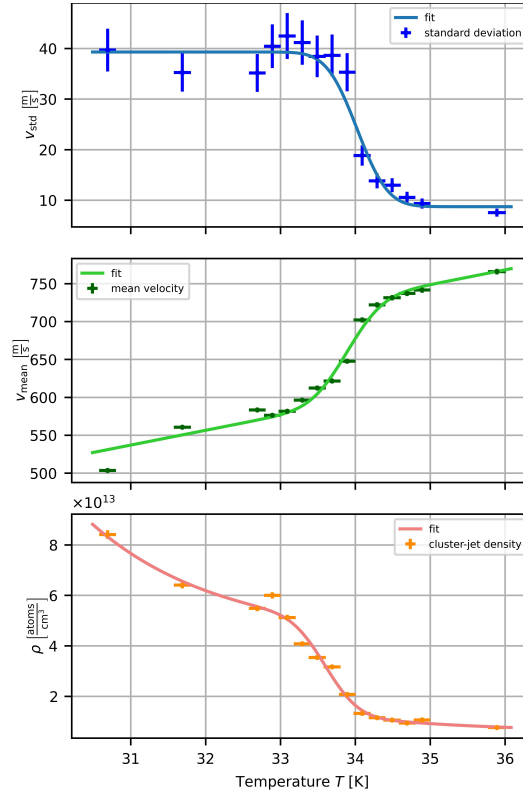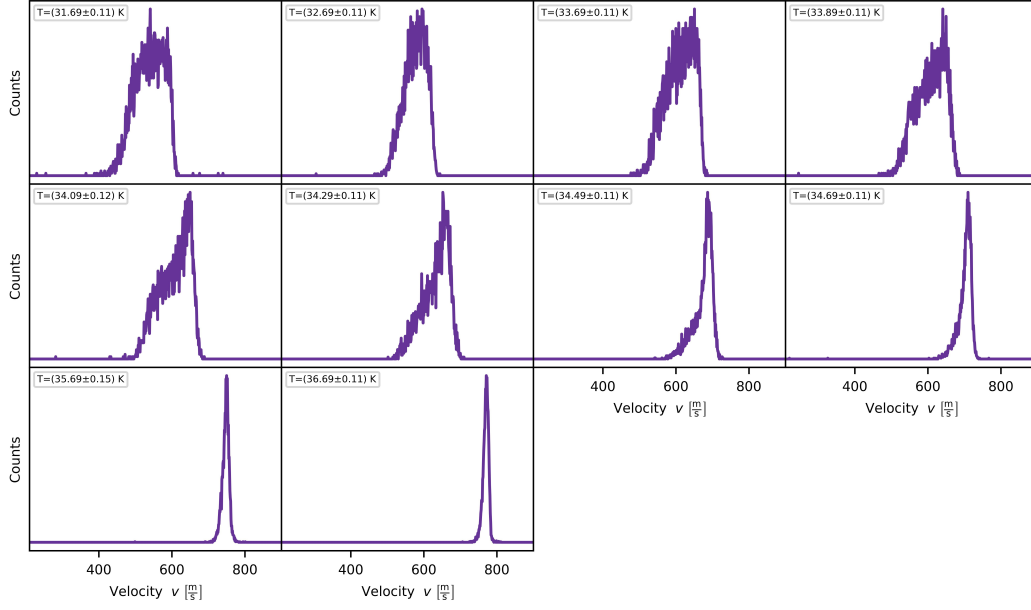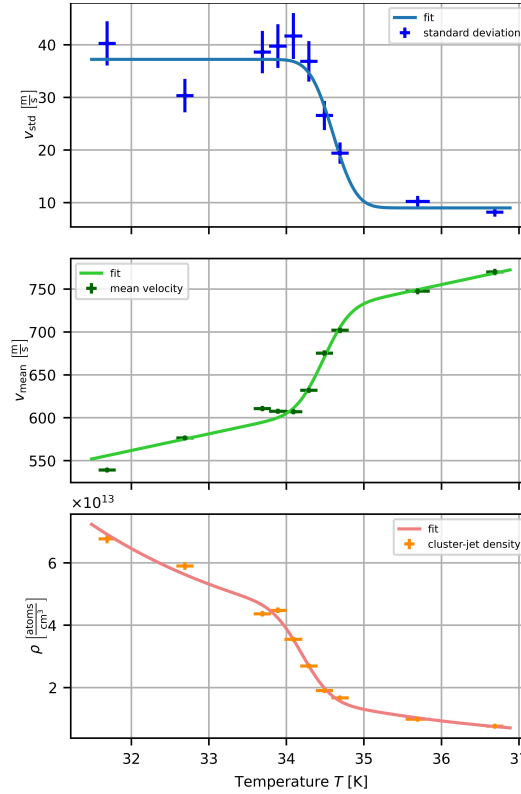**Figure B.1:** Temperature dependent velocity distributions of the isobar measurement series at (6.08 ± 0.06) bar as published in [VFK22].
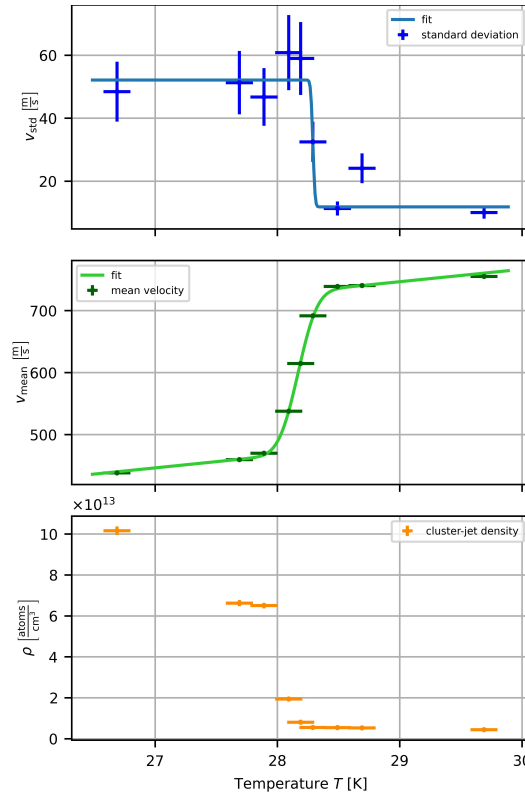
Figure B.2: Fits and/or data of the velocity standard deviation, the mean velocity, and the cluster-jet density in dependence of the temperature for the isobar measurement series at (6.08 ± 0.08) bar as published in [VFK22]. The determined phase change temperature by velocity standard deviation is $T_{\mathrm{std}} = (28.29 \pm 0.16)$ K.

Figure B.3: Temperature dependent velocity distributions of the isobar measurement series at (10.17 ± 0.10) bar as published in [VFK22].
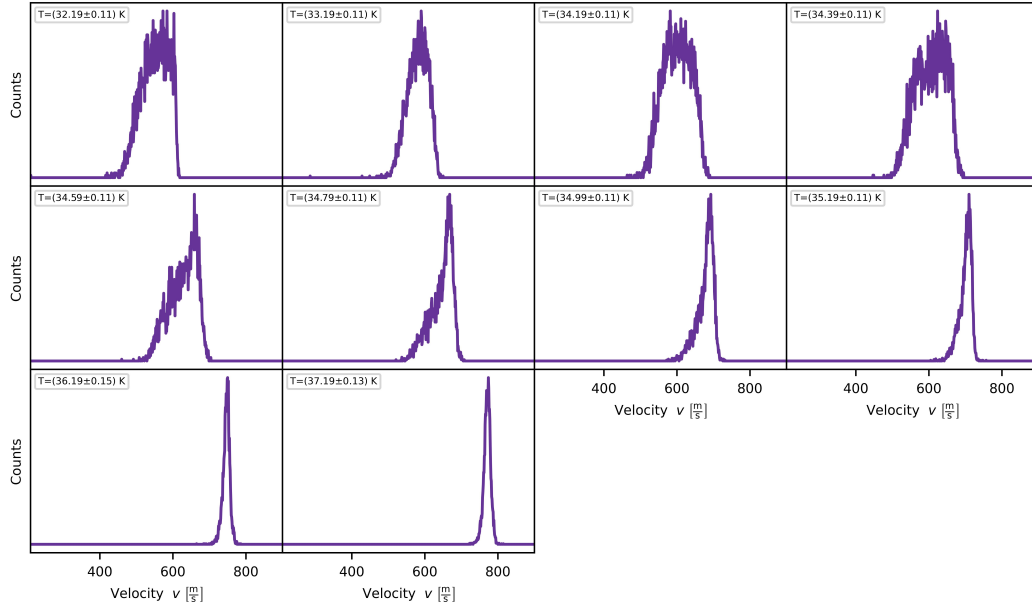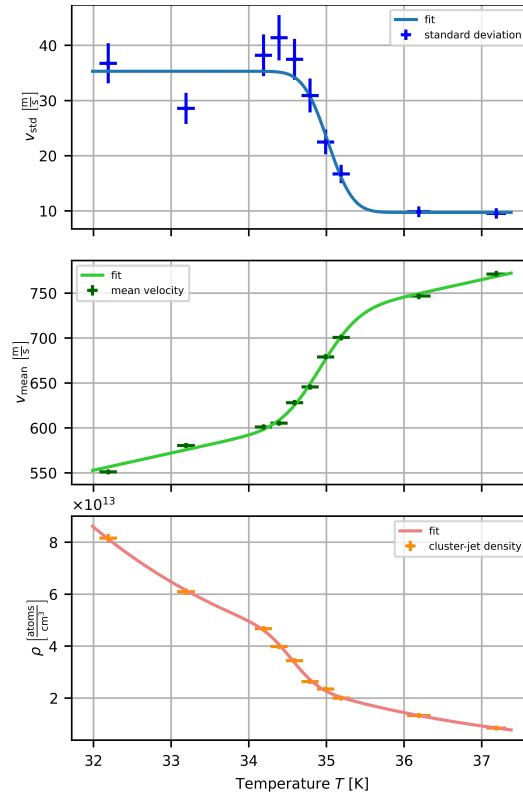

Figure B.4: Fits of the velocity standard deviation, the mean velocity, and the cluster-jet density in dependence of the temperature for the isobar measurement series at (10.17 ± 0.10) bar as published in [VFK22]. The determined phase change temperature by velocity standard deviation is $T_{\mathrm{std}} = (31.39 \pm 0.16)$ K.

Figure B.5: Temperature dependent velocity distributions of the isobar measurement series at (12.19 ± 0.13) bar as published in [VFK22].
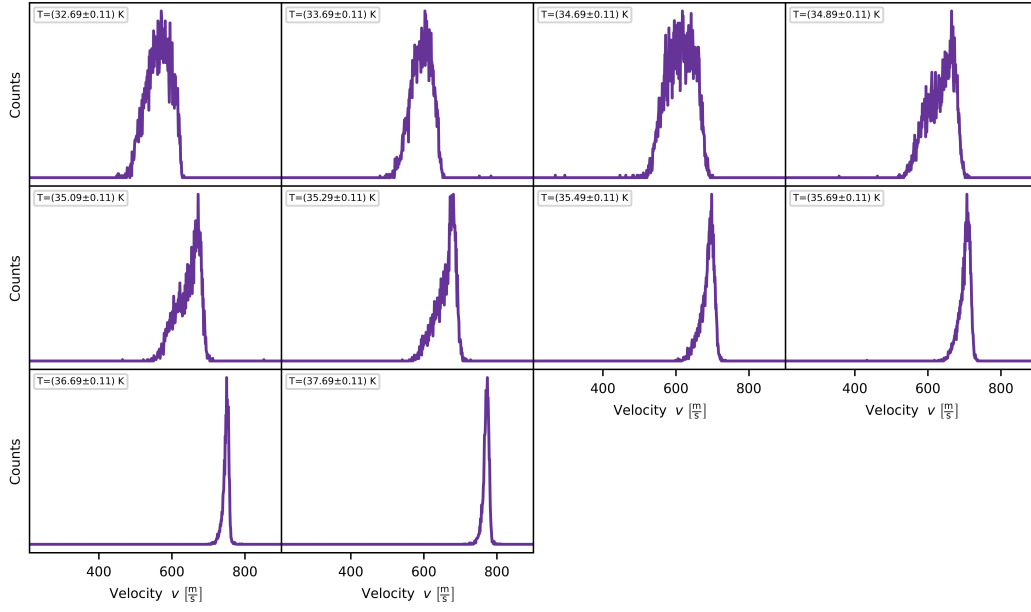

Figure B.6: Fits of the velocity standard deviation, the mean velocity, and the cluster-jet density in dependence of the temperature for the isobar measurement series at (12.19 ± 0.13) bar as published in [VFK22]. The determined phase change temperatures are $T_{\mathrm{std}} = (32.88 \pm 0.17)$ K.
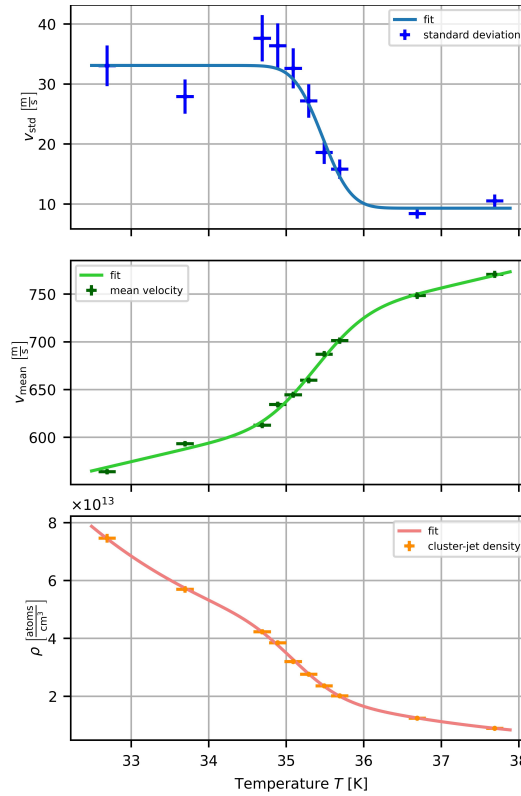
Figure B.7: Temperature dependent velocity distributions of the isobar measurement series at (13.21 ± 0.14) bar as published in [VFK22].

Figure B.8: Fits of the velocity standard deviation, the mean velocity, and the cluster-jet density in dependence of the temperature for the isobar measurement series at (13.21 ± 0.14) bar as published in [VFK22]. The determined phase change temperatures are $T_{\mathrm{std}} = (33.59 \pm 0.17)$ K, $T_{\mathrm{mean}} = (33.39 \pm 0.17)$ K, and $T_{\mathrm{den}} = (33.28 \pm 0.17)$ K, respectively.
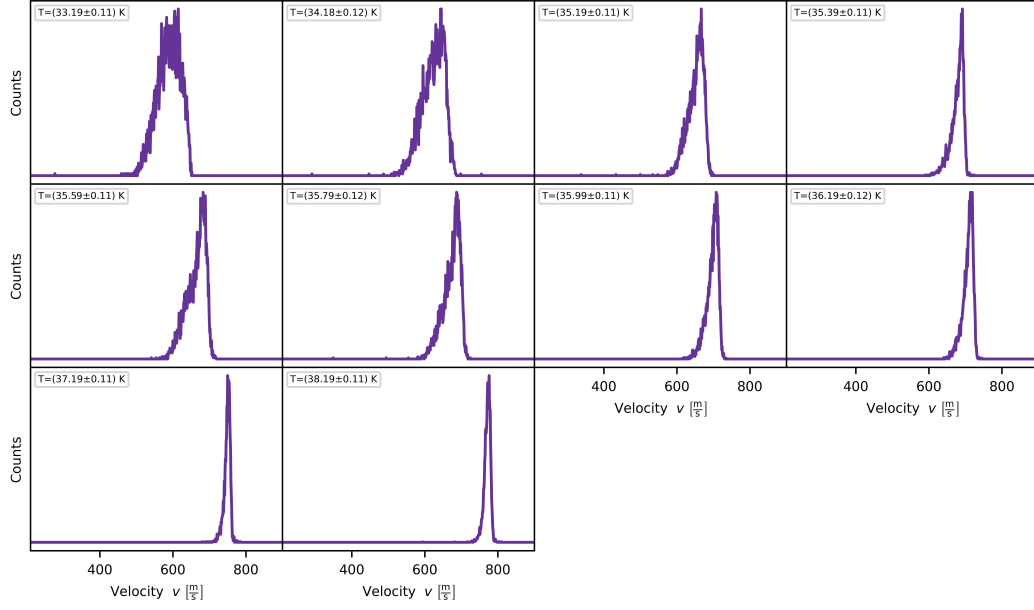
Figure B.9: Temperature dependent velocity distributions of the isobar measurement series at (14.22 ± 0.15) bar as published in [VFK22].

Figure B.10: Fits of the velocity standard deviation, the mean velocity, and the cluster-jet density in dependence of the temperature for the isobar measurement series at (14.22 ± 0.15) bar as published in [VFK22]. The determined phase change temperatures are $T_{\mathrm{std}} = (34.03 \pm 0.17)$ K, $T_{\mathrm{mean}} = (33.89 \pm 0.18)$ K, and $T_{\mathrm{den}} = (33.60 \pm 0.16)$ K, respectively.

Figure B.11: Temperature dependent velocity distributions of the isobar measurement series at (15.25 ± 0.16) bar as published in [VFK22].
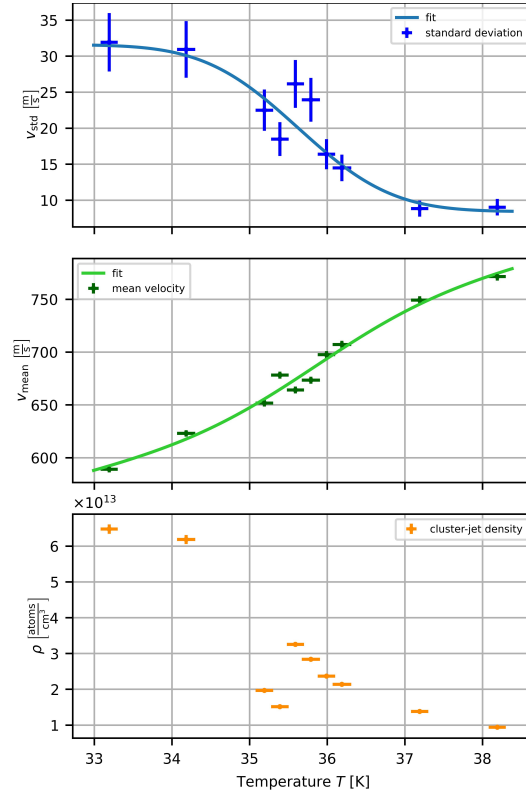

Figure B.12: Fits of the velocity standard deviation, the mean velocity, and the cluster-jet density in dependence of the temperature for the isobar measurement series at (15.25 ± 0.16) bar as published in [VFK22]. The determined phase change temperatures are $T_{\mathrm{std}} = (34.60 \pm 0.17)$ K, $T_{\mathrm{mean}} = (34.48 \pm 0.17)$ K, and $T_{\mathrm{den}} = (34.21 \pm 0.17)$ K, respectively.

Figure B.13: Temperature dependent velocity distributions of the isobar measurement series at (16.28 ± 0.17) bar as published in [VFK22].

Figure B.14: Fits of the velocity standard deviation, the mean velocity, and the cluster-jet density in dependence of the temperature for the isobar measurement series at (16.28 ± 0.17) bar as published in [VFK22]. The determined phase change temperatures are $T_{\mathrm{std}} = (35.02 \pm 0.17)\,\mathrm{K}$, $T_{\mathrm{mean}} = (34.92 \pm 0.16)\,\mathrm{K}$, and $T_{\mathrm{den}} = (34.56 \pm 0.16)\,\mathrm{K}$, respectively.

Figure B.15: Temperature dependent velocity distributions of the isobar measurement series at (87.27 ± 0.18) bar as published in [VFK22].

Figure B.16: Fits of the velocity standard deviation, the mean velocity, and the cluster-jet density in dependence of the temperature for the isobar measurement series at (17.27 ± 0.18) bar as published in [VFK22]. The determined phase change temperatures are $T_{\mathrm{std}} = (35.47 \pm 0.17)$ K, $T_{\mathrm{mean}} = (35.38 \pm 0.17)$ K, and $T_{\mathrm{den}} = (35.11 \pm 0.16)$ K, respectively.

Figure B.17: Temperature dependent velocity distributions of the isobar measurement series at (18.27 ± 0.19) bar as published in [VFK22].

Figure B.18: Fits and/or data of the velocity standard deviation, the mean velocity, and the cluster-jet density in dependence of the temperature for the isobar measurement series at (18.27 ± 0.19) bar as published in [VFK22]. The phase change temperatures are $T_{\mathrm{std}} = (34.03 \pm 0.17)$ K and $T_{\mathrm{mean}} = (33.89 \pm 0.18)$ K. The phase change temperature based on cluster-jet density was not determinable.

Bibliography

[Abd⁺00] I. Abdulagatov et al., *Thermal conductivity of fused quarz and quarz ceramic at high temperatures and pressures*. Journal of Physics and Chemistry of Solids 61, 779–787. 2000.

[Abl⁺17] T. Ablyazimov et al. (CBM Collaboration), *Challenges in QCD matter physics – The scientific programme of the Compressed Baryonic Matter experiment at FAIR*. The European Physical Journal A 53.3. DOI: `10.1140/epja/i2017-12248-y`. URL: `http://arxiv.org/pdf/1607.01487.pdf`. 2017.

[Abl⁺22] M. Ablikim et al., *First Observation of the Direct Production of the χ_{c1} in e^+e^- Annihilation*. Physical review letters 129.12, 122001. DOI: `10.1103/PhysRevLett.129.122001`. 2022.

[Ban15] D. T. Banuti, *Crossing the Widom-line – Supercritical pseudo-boiling*. The Journal of Supercritical Fluids 98, 12–16. DOI: `10.1016/j.supflu.2014.12.019`. 2015.

[Bar⁺21] G. Barucca et al. ($\overline{\text{P}}$ANDA Collaboration), *PANDA Phase One*. The European Physical Journal A 57.6. DOI: `10.1140/epja/s10050-021-00475-y`. 2021.

[Bon12] D. Bonaventura, *Verfahren zur Herstellung von monolithischen Laval-Mikrodüsen (MTec-Verfahren). Verfahrensanweisung*. Institut für Kernphysik, Westfälische Wilhelms-Universität Münster. 2012.

[Bon20] D. Bonaventura, *Analyse und Verbesserung eines Verfahrens zur Herstellung von Mikrolavaldüsen aus Kuper mit kleinsten Querschnitten von 30 Mikormeter Durchmesser*. Bachelor's thesis. Fachhochschule Münster. 2020.

[Bra⁺11] V. V. Brazhkin et al., *Widom line for the liquid-gas transition in Lennard-Jones system*. The journal of physical chemistry. B 115.48, 14112–14115. DOI: `10.1021/jp2039898`. 2011.

[Bra24] P. Brand, *in progress*. Doctoral thesis. Universität Münster. 2024.

[BRI17]   D. T. Banuti, M. Raju, and M. Ihme, *Similarity law for Widom lines and coexistence lines.* Physical review. E 95.5-1, 052120. DOI: `10.1103/PhysRevE.95.052120`. 2017.

[CER83]   CERN, *By a hairsbreadth.* bulletin 1983.45/83, 1. URL: `https://cds.cern.ch/record/1720922/files/45-1983.pdf`(visited on 24.10.2024). 1983.

[Cry24]   Crytur, *Integrated crystal based solutions.* URL: `https://www.crytur.com/`(visited on 12.5.2024). 2024.

[Ded24]   L. Deda, *New Motors for the PANDA Cluster-Jet Target: Programming and Implementation into the local EPICS Slow Control System.* Master's thesis. Westfälische Wilhelms-Universität Münster. 2024.

[Dem08]   W. Demtröder, *Experimentalphysik 1, Mechanik und Wärme.* Vol. 5. Springer Verlag. 2008.

[Dem16]   W. Demtröder, *Experimentalphysik 3, Atome, Moleküle und Festkörper.* Vol. 4. Springer Verlag. 2016.

[Dom+97]   H. Dombrowski et al., *The Münster cluster target for the COSY-11 experiment.* Nuclear Physics A, 427–433. DOI: `10.1016/S0375-9474(97)00565-4`. 1997.

[Eic+23]   H. Eick et al., *Cluster size determination using shadowgraphy measurements.* EPJ Web of Conferences 285, 02001. DOI: `10.1051/epjconf/202328502001`. 2023.

[Eic23]   H. Eick, *Cluster-jet beams: Size distributions and effects on a stored accelerator beam.* Master's thesis. Westfälische Wilhelms-Universität Münster. 2023.

[Eic24]   H. Eick, *in progress.* Doctoral thesis. Universität Münster. 2024.

[Eks+96]   C. Ekström et al. (WASA Collaboration), *Hydrogen pellet targets for circulating particle beams.* Nuclear Instruments and Methods in Physics Research Section A: Accelerators, Spectrometers, Detectors and Associated Equipment 371.3, 572–574. DOI: `10.1016/0168-9002(96)00009-5`. 1996.

[EV08]   J. Eggers and E. Villermaux, *Physics of liquid jets.* Reports on Progress in Physics 71.3, 036601. DOI: `10.1088/0034-4885/71/3/036601`. 2008.

[FAI24]   FAIR, *FAIR - The Facility for Antiproton and Ion Research in Europe.* URL: `https://fair-center.eu/`(visited on 29.3.2023). 2024.

[Fis21]   C. Fischer, *Identification of the Widom line by time of flight distributions of a cluster-jet beam.* Bachelor's thesis. Westfälische Wilhelms-Universität Münster. 2021.

[Fis24]   C. Fischer, *in progress.* Master's thesis. Universität Münster. 2024.

[Fra15]   R. A. C. Fraga, *Entwicklung und Charakterisierung mikroskopischer, kryogener Tröpfchentargets für die Anwendung in Experimenten der Laserplasma- und Atomphysik.* Doctoral Thesis. Frankfurt am Main: Johann Wolfgang Goethe-Universität. 2015.

[Fri17]   M. Fritsch ($\overline{P}ANDA$ Collaboration), *General $\overline{P}ANDA$ material for slides, logos, detector drawings, etc.* 2017.

[Fro24]   J. Froning, *in progress.* Doctoral thesis. Universität Münster. 2024.

[FSS12]   V. E. Fortov, B. Y. Sharkov, and H. Stöker, *European Facility for Antiproton and Ion Research (FAIR): the new international center for fundamental physics and its research program.* Physics-Uspekhi 55.6, 582–602. DOI: 10.3367/UFNe.0182.201206c.0621. 2012.

[GHN12]   J. Gerl, A. Herlert, and T. Nilsson (NUSTAR Collaboration), *NUSTAR Progress Report: NUSTAR at FAIR.* URL: https://fair-center.de/fileadmin/FAIR/experiments/NUSTAR/Pdf/NUSTAR_ProgressReport_SC_Nov2012_final.pdf(visited on 3.1.2024). 2012.

[Gök23]   E. Göktas, *Machbarkeitsstudie zur Bestimmung der Clustergrößenverteilung eines Münsteraner Cluster-Jet Targets mittels Mie-Streuung.* Bachelor's thesis. Universität Münster. 2023.

[Gor+06]   F. Gorelli et al., *Liquidlike behavior of supercritical fluids.* Physical review letters 97.24, 245702. DOI: 10.1103/PhysRevLett.97.245702. 2006.

[Gri+18]   S. Grieser et al., *A Cryogenic Supersonic Jet Target for Electron Scattering Experiments at MAGIX@MESA and MAMI.* Nuclear Instruments and Methods in Physics Research Section A: Accelerators, Spectrometers, Detectors and Associated Equipment 906, 120–126. DOI: 10.1016/j.nima.2018.07.076. URL: http://arxiv.org/pdf/1806.05409v1. 2018.

[Gri18]   S. Grieser, *Cluster-Jet Targets for the $\overline{P}ANDA$-, MAGIX- and CryoFlash-Experiments at Hadron-, Lepton- and Laser-Facilities.* Doctoral thesis. Westfälische Wilhelms-Universität Münster. 2018.

[GSI]   GSI Helmholtzzentrum für Schwerionenforschung GmbH, *FAIR - Das Universum im Labor.* URL: https://www.gsi.de/en/researchaccelerators/fair(visited on 19.12.2023).

[GSI22]   GSI Helmholtzzentrum für Schwerionenforschung GmbH, *Statement on the war of agression by Russia on Ukraine.* URL: www.gsi.de/en/about_us/geschaeftsfuehrung/stellungnahme-zum-angriffskrieg-von-russland-auf-die-ukraine(visited on 17.9.2024). 2022.

[Ha+18]   M. Y. Ha et al., *Widom Delta of Supercritical Gas-Liquid Coexistence*. The journal of physical chemistry letters 9.7, 1734–1738. DOI: `10.1021/acs.jpclett.8b00430`. 2018.

[Hag87]   O. F. Hagena, *Condensation in Free Jets: Comparison of Rare Gases and Metals*. Zeitschrift für Physik D - Atoms, Molecules and Clusters 4, 291–299. DOI: `10.1007/BF01436638`. 1987.

[Hag92]   O. F. Hagena, *Cluster ion sources (invited)*. Review of Scientific Instruments 63.4, 2374–2379. DOI: `10.1063/1.1142933`. 1992.

[Hah09]   D. W. Hahn, *Light Scattering Theory*. PhD thesis. Florida: University of Florida. 2009.

[Hal23]   L. Halstenberg, *Machbarkeitsstudie über das Drei-Wellenlängen-Extinktionsverfahren zur Bestimmung der Clustergrößenverteilung von Cluster-Jet Targets*. Bachelor's thesis. Westfälische Wilhelms-Universität Münster. 2023.

[Har19]   C. Hargens, *Development and Set-up of a Droplet Generator for Cryogenic Fluids*. Master's thesis. Westfälische Wilhelms-Universität Münster. 2019.

[Hau24]   E. Hausch, *in progress*. Master's thesis. Universität Münster. 2024.

[Ho+09]   C. Ho et al., *Thermal conductivity of then selected binary alloy systems*. Journal of Physical and Chemical Reference Data 7. 2009.

[HO72]   O. F. Hagena and W. Obert, *Cluster Formation in Expanding Supersonic Jets: Effect of Pressure, Temperature, Nozzle Size, and Test Gas*. The Journal of chemical physics 56.5, 1793–1802. DOI: `10.1063/1.1677455`. 1972.

[Hul57]   H. C. van de Hulst, *Light Scattering by Small Particles*. New York: Dover Publications. 1957.

[Hum21]   N. Humberg, *Entwicklung einer Elektronenkanone für das PANDA Cluster-Jet Target*. Bachelor's thesis. Westfälische Wilhelms-Universität Münster. 2021.

[Jel13]   T. W. Jelinek, *Praktische Galvanotechnik*. Vol. 7. Bad Saulgau: Leuze Verlag. 2013.

[KBT13]   A. Khoukaz, D. Bonaventura, and A. Täschner, "Verfahren zur Herstellung Monolithischer Lavaldüsen". DE102013003644B4. 2013.

[Klo20]   D. Klostermann, *Studies on $\overline{P}ANDA$ vacuum conditions using simulations and a cooled beam pipe*. Master's thesis. Westfälische Wilhelms-Universität Münster. 2020.

[Köh15]   E. Köhler, *Mass spectroscopy of hydrogen cluster-jets and beam density optimisation studies*. Doctoral thesis. Westfälische Wilhelms-Universität Münster. 2015.

[Küm21]   M. Kümmel ($\overline{\text{P}}$ANDA Collaboration), *Physics Prospects of PANDA at FAIR*. International Journal of Modern Physics A. 2021.

[Leß21]   L. Leßmann, *Investigations on Laser-Cluster Interaction Concerning the Acceleration of Protons and Electrons and the Generation of X-Ray Radiation*. Doctoral thesis. Westfälische Wilhelms-Universität Münster. 2021.

[Lie$^+$16]   A. Lieberwirth et al., *Test of the Imaging Properties of Inorganic Scintillation Screens Using Fast and Slow Extracted Ion Beams*. Proc. 5th Int. Beam Instrumentation Conf. (IBIC'16), 517–520. DOI: `10.18429/JACoW-IBIC2016-TUPG70`. 2016.

[Lig20]   LightFab, *SLE with LightFab 3D Printer*. URL: `https://lightfab.de/files/Downloads/SLE_3D_printed_glass.pdf` (visited on 25.9.2020). 2020.

[LM17]   A. H. Lefebvre and V. G. McDonell, *Atomization and sprays*. Second edition. Boca Raton: CRC Press Taylor & Francis Group CRC Press is an imprint of the Taylor & Francis Group an informa business. 2017.

[LS19]   J. Losey and R. J. Sadus, *The Widom Line and the Lennard-Jones Potential*. The journal of physical chemistry. B 123.39, 8268–8273. DOI: `10.1021/acs.jpcb.9b05426`. 2019.

[Man19]   C. Mannweiler, *Commissioning and characterisation of a cluster-jet target for CryoFlash*. Master's thesis. Westfälische Wilhelms-Universität Münster. 2019.

[Man24]   C. Mannweiler, *The next generation of cryogenic hydrogen targets: Innovations surrounding target systems for particle and plasma physics (in progress)*. Doctoral thesis. Universität Münster. 2024.

[Mät02]   C. Mätzler, *MATLAB functions for Mie scattering and absorption, version 2*. IAP Res. Rep 8.1, 9. 2002.

[Mes04]   R. Messerschmid, *Zerstäubung von Flüssigkeiten in einer nicht angepassten Lavaldüse*. Doctoral thesis. Rheinische Friedrich-Wilhelms-Universit Bonn. 2004.

[Mie08]   G. Mie, *Beiträge zur Optik trüber Medien, speziell kolloidaler Metallösungen*. Annalen der Physik 1908.330, 377–445. 1908.

[Mie55]   C. C. Miesse, *Correlation of Experimental Data on the Disintegration of Liquid Jets.* Industrial & Engineering Chemistry 47.9, 1690–1701. DOI: `10.1021/ie50549a013`. 1955.

[Mou⁺22]   A. Mouahid, P. Boivin, S. Diaw, and E. Eadens, *Widom and extrema lines as criteria for optimizing operating conditions in supercritical processes.* The Journal of Supercritical Fluids 186. DOI: `10.1016/j.supflu.2022.105587`. 2022.

[MS10]   P. F. McMillan and H. E. Stanley, *Going supercritical.* Nature Physics 6.7, 479–480. DOI: `10.1038/nphys1711`. 2010.

[MY11]   T. Matsuo and N. Yagi, *Measurement of persistence in YAG:Ce(3+) scintillator with pulsed synchrotron X-rays.* Journal of synchrotron radiation 18.Pt 4, 601–604. DOI: `10.1107/S0909049511010843`. 2011.

[NIST]   E. Lemmon, M. McLinden, and D. Friend, "Thermophysical Properties of Fluid Systems". *NIST Chemistry WebBook, NIST Standard Reference Database Number 69.* Ed. by P. Linstrom and W. Mallard. Gaithersburg MD: National Institute of Standards and Technology, 20899. DOI: `10.18434/T4D303`. URL: `webbook.nist.gov/chemistry/fluid/`(visited on 7.2.2024).

[Obs23]   S. Obszerninks, *Inbetriebnahme und Charakterisierung eines MCP - Detektors für das PANDA Cluster-Jet Target.* Bachelor's thesis. Universität Münster. 2023.

[Oum⁺03]   K. Oum et al., *On-line and in situ optical detection of particles of organic molecules formed by rapid expansion of supercritical solutions (RESS) of CO2.* Physical Chemistry Chemical Physics 5.24, 5467. DOI: `10.1039/b312040f`. 2003.

[PAN12] $\overline{P}$ANDA Collaboration, *Technical Design Report for the $\overline{P}$ANDA Internal Targets: The Cluster-Jet Target and Developments for the Pellet Target.* Technical report. FAIR. 2012.

[PAN22] $\overline{P}$ANDA Collaboration, *Technical Report for the: PANDA Detector Infrastructure and Installation.* 2022.

[PAR19]   PARI GmbH, *Gebrauchsanweisung PARI BOY Junior Inhalationssystem.* URL: `https://www.pari.com/fileadmin/user_upload/PARI.com-DE/Dokumente/IFU/130D2102-Gebrauchsanweisung-PARI-BOY-Junior.pdf`(visited on 14.10.2024). 2019.

[Pau00a]   H. Pauly, *Atom, Molecule, and Cluster Beams 1.* Vol. 1. Springer Verlag. 2000.

[Pau00b] H. Pauly, *Atom, Molecule, and Cluster Beams 2*. Vol. 1. Springer Verlag. 2000.

[Pet⁺17] K. Peters, L. Schmitt, T. Stockmanns, and J. Messchendorp, *PANDA: Strong Interaction Studies with Antiprotons*. Nuclear Physics News 27.3, 24–28. DOI: 10.1080/10619127.2017.1351182. 2017.

[Pho20] H. Photonics, ed., *Image Intensifiers*. Cataloge. URL: https://www.hamamatsu.com/content/dam/hamamatsu-photonics/sites/documents/99_SALES_LIBRARY/etd/II_TII0007E.pdf (visited on 2.9.2024). 2020.

[Pho94] H. Photonics, ed., *MCP Assembly*. Technical Information. 1994.

[PJ05] L. Pártay and P. Jedlovszky, *Line of percolation in supercritical water*. The Journal of chemical physics 123.2, 24502. DOI: 10.1063/1.1953547. 2005.

[Pov⁺14] B. Povh et al., *Teilchen und Kerne*. Berlin, Heidelberg: Springer Verlag. DOI: 10.1007/978-3-642-37822-5. 2014.

[Pro] Proxivision, *Phosphor Screens: 2D, visual detection of electrons, charged particles, X-Rays, Neutrons and UV-radiation*. PR-0056E-03. URL: https://www.proxivision.de/datasheets/Phosphor-Screen-PR-0056E-03.pdf (visited on 26.7.2024).

[RB82] R. D. Reitz and F. V. Bracco, *Mechanism of atomization of a liquid jet*. The Physics of Fluids 25.10, 1730–1742. DOI: 10.1063/1.863650. 1982.

[RH51] R. A. Mugele and H. D. Evans, *Droplet Size Distribution in Sprays*. Industrial & Engineering Chemistry. 1951.

[Sat⁺08] T. Sato et al., *Structural difference between liquidlike and gaslike phases in supercritical fluid*. Physical review. E, Statistical, nonlinear, and soft matter physics 78.5 Pt 1, 051503. DOI: 10.1103/PhysRevE.78.051503. 2008.

[Sch⁺21] B. S. Schlimme et al., *Operation and characterization of a windowless gas jet target in high-intensity electron beams*. Nuclear Instruments and Methods in Physics Research Section A: Accelerators, Spectrometers, Detectors and Associated Equipment 1013, 165668. DOI: 10.1016/j.nima.2021.165668. URL: http://arxiv.org/pdf/2104.13503v2. 2021.

[Sch16] H. Schlichting, *Boundary-Layer Theory*. 9th ed. Berlin, Heidelberg: Springer Verlag. URL: http://gbv.eblib.com/patron/FullRecord.aspx?p=4710248. 2016.

[Sch24] M. Scharpey, *The Next Stage of the $\overline{P}ANDA$ Cluster-Jet Target Prototype: Cluster Source Upgrade and Beam Diagnostic Enhancements*. Master's thesis. Universität Münster. 2024.

[SDT98]   R. A. Smith, T. Ditmire, and J. W. G. Tisch, *Characterization of a cryogenically cooled high-pressure gas jet for laser/cluster interaction experiments*. Review of Scientific Instruments 69.11, 3798–3804. DOI: `10.1063/1.1149181`. 1998.

[SG08]   M. Santoro and F. A. Gorelli, *Structural changes in supercritical fluids at high pressures*. Physical Review B 77.21. DOI: `10.1103/PhysRevB.77.212103`. 2008.

[Sim+10]   G. G. Simeoni et al., *The Widom line as the crossover between liquid-like and gas-like behaviour in supercritical fluids*. Nature Physics 6.7, 503–507. DOI: `10.1038/nphys1683`. 2010.

[SJ64]   J. E. Smith and M. L. Jordan, *Mathematical and graphical interpretation of the log-normal law for particle size distribution analysis*. Journal of Colloid Science 19.6, 549–559. DOI: `10.1016/0095-8522(64)90069-8`. URL: `https://www.sciencedirect.com/science/article/pii/0095852264900698`. 1964.

[SSZ94]   K. Schaber, A. Schenkel, and R. Zahoransky, *Drei-Wellenlängen-Extinktionsverfahren zur Charakterisierung von Aerosolen unter industriellen Bedingungen*. Technisches Messen, 295–300. 1994.

[Ste+08]   H. J. Stein et al., *Determination of target thickness and luminosity from beam energy losses*. Physical Review Special Topics - Accelerators and Beams 11.5. DOI: `10.1103/PhysRevSTAB.11.052801`. 2008.

[Täs+13]   A. Täschner, E. Köhler, H.-W. Ortjohann, and A. Khoukaz, *Determination of hydrogen cluster velocities and comparison with numerical calculations*. The Journal of chemical physics 139.23, 234312. DOI: `10.1063/1.4848720`. 2013.

[Täs12]   A. Täschner, *Entwicklung und Untersuchung von Cluster-Jet-Targets höchster Dichte*. Doctoral thesis. Westfälische Wilhelms-Universität Münster. 2012.

[Tec24]   Techtra, *Technology transfer Agency*. URL: `https://techtra.pl/technology/gem-foils/` (visited on 2.8.2024). 2024.

[Tou+08]   J. Touš et al., *High-resolution application of YAG:Ce and LuAG:Ce imaging detectors with a CCD X-ray camera*. Nuclear Instruments and Methods in Physics Research Section A: Accelerators, Spectrometers, Detectors and Associated Equipment 591.1, 264–267. DOI: `10.1016/j.nima.2008.03.070`. 2008.

[Ves18]   S. Vestrick, *Impact of nozzle length on properties of Cluster Beams*. Bachelor's thesis. Westfälische Wilhelms-Universität Münster. 2018.

[Ves20]   S. Vestrick, *Feasibility Studies on Beam Visualization and Glass Nozzles at the $\overline{P}ANDA$ Cluster-Jet Target Prototype.* Master's thesis. Westfälische Wilhelms-Universität Münster. 2020.

[VFK22]   S. Vestrick, C. Fischer, and A. Khoukaz, *Crossing the Widom line: Cluster formation as sensitive probe of supercritical fluids.* The Journal of Supercritical Fluids 188, 105686. DOI: `10.1016/j.supflu.2022.105686`. 2022.

[Vil07]   E. Villermaux, *Fragmentation.* Annual Review of Fluid Mechanics 39.1, 419–446. DOI: `10.1146/annurev.fluid.39.050905.110214`. 2007.

[Wei21]   M. Weide, *Optimierung des Herstellungsverfahrens von Kuperlavaldüsen für das $\overline{P}ANDA$-Experiment.* Bachelor's thesis. Westfälische Wilhelms-Universität Münster. 2021.

[Wei23]   M. Weide, *Vacuum studies on the $\overline{P}ANDA$ cluster-jet target considering flash evaporation and cluster bursting.* Master's thesis. Universität Münster. 2023.

[Wei24]   M. Weide, *in progress.* Doctoral thesis. Universität Münster. 2024.

[Wes20]   C. Westphälinger, *Optimization of the Droplet Target Prototype for Cryogenic Fluids.* Master's thesis. Westfälische Wilhelms-Universität Münster. 2020.

[Wor$^+$22] R. L. Workman et al. (Particle Data Group), *Review of Particle Physics.* Progress of Theoretical and Experimental Physics 2022, 083C01. DOI: `10.1093/ptep/ptac097`. 2022.

[Xu$^+$05]   L. Xu et al., *Relation between the Widom line and the dynamic crossover in systems with a liquid–liquid phase transition.* The Proceedings of the National Academy of Sciences 102, 16558–16562. 2005.

[Zho$^+$21] Y. Zhou et al., *The KOALA experiment for (anti)proton–proton elastic scattering.* Nuclear Instruments and Methods in Physics Research Section A: Accelerators, Spectrometers, Detectors and Associated Equipment 1019, 165849. DOI: `10.1016/j.nima.2021.165849`. 2021.

Acknowledgments

Lebenslauf

Persönliche Daten

Name	Sophia Vestrick
Geburtsdatum	20.09.1997
Geburtsort	Borken
Nationalität	Deutsch
Eltern	Thomas Vestrick und Dagmar Vestrick (geb. Knuf)

Schulausbildung

2003 – 2007	Mariengrundschule, Heiden
2007 – 2015	Gymnasium Remigianum, Borken
20.06.2015	Allgemeine Hochschulreife

Studium

10/2015 – 03/2019	Bachelor Studium der Physik an der Westfälischen Wilhelms-Universität Münster
09/2018	Bachelorarbeit in Physik: „Einfluss der Düsenlänge auf die Eigenschaften von Clusterstrahlen"
10/2018 – 11/2020	Master Studium der Physik an der Westfälischen Wilhelms-Universität Münster
11/2020	Masterarbeit in Physik: „Feasibility Studies on Beam Visualization and Glass Nozzles at the $\overline{\text{P}}$ANDA Cluster-Jet Target Prototype"

Promotionsstudium

12/2020	Beginn der Dissertation am Institut für Kernphysik der Westfälischen Wilhelms-Universität Münster unter der Betreuung von Prof. Dr. Alfons Khoukaz

Berufstätigkeit

09/2017	Studentische Hilfskraft am Institut für Angewandte Physik, Westfälische Wilhelms-Universität Münster
10/2018 – 03/2019	Studentische Hilfskraft am Institut für Kernphysik, Westfälische Wilhelms-Universität Münster
11/2019 – 03/2020	Studentische Hilfskraft am Institut für Kernphysik, Westfälische Wilhelms-Universität Münster
06/2020 – 11/2020	Studentische Hilfskraft am Institut für Kernphysik, Westfälische Wilhelms-Universität Münster
12/2020 – heute	Wissenschaftliche Mitarbeiterin am Institut für Kernphysik, Westfälische Wilhelms-Universität Münster

Münster, 21. November 2024